MOMENTUM TRANSFER TO ATOMS BY ABSORPTION AND EMISSION OF RADIATION

by

Phillip Lloyd Gould

B.S. Bates College
(1979)

Submitted to the Department of
Physics
in Partial Fulfillment of the
Requirements for the
Degree of

DOCTOR OF PHILOSOPHY

at the

MASSACHUSETTS INSTITUTE OF TECHNOLOGY

January 1986

Signature of Author _____
Department of Physics

Certified by _____
Thesis Supervisor

Accepted by _____
Chairman, Departmental Committee on
Graduate Studies

Momentum Transfer To Atoms by Absorption

and Emission of Radiation

by

Phillip Lloyd Gould

Submitted to the Department of Physics
on January 10, 1986 in partial fulfillment of the
requirements for the degree of Doctor of Philosophy

Abstract

We report on measurement of momentum transfer to an atomic sodium beam by a standing-wave laser field. Experiments were performed in two regimes: 1) the regime in which spontaneous emission is negligible; and 2) the regime in which the effects of spontaneous decay dominate the momentum transfer process. In the first regime, we observe diffraction of the atomic beam: the near-resonant Kapitza-Dirac effect. In the second regime, spontaneous emission leads to momentum diffusion. Theoretical predictions are in good agreement with the data in both regimes.

Thesis Supervisor: Dr. David E. Pritchard

Title: Professor of Physics

Dedicated to my sister, Susan

Table of Contents

Chapter I. Introduction

This thesis describes experimental observations and theoretical interpretations of momentum transfer to an atomic beam by standing-wave laser radiation. In particular, the experiments cover two physically distinct regimes: 1) the regime in which the effects of spontaneous decay are negligible, and 2) the regime in which the effects of spontaneous decay dominate the momentum transfer process.

I.A. Introduction to Thesis

1. *Scope of Thesis*

The thesis is organized as follows: In the present chapter, (Chapter I) we define the scope of this work, our motivation in performing it, and its relation to the general field of radiative forces on atoms. Chapter II is a description of the experimental apparatus and procedure, with emphasis on the aspects of the experiment which allow us to make quantitative measurements of these radiative forces. Measurements of atomic beam diffraction, in the absence of spontaneous decay, are presented and compared to our theoretical predictions in Chapter III. In Chapter IV, we present our measurements of the induced force and induced momentum diffusion as a demonstration of the effects of spontaneous decay on the momentum transfer process.

2. *Motivation*

Our motivation in performing these experiments has its roots in three basic issues. First, the fact that current work on momentum transfer to atoms from radiation has been overwhelmingly theoretical requires definitive experiments to verify and/or challenge the many existing theories and motivate new directions for theoretical investigation. This is especially true in the case of induced processes occurring in a standing-wave. Secondly, the current interest in the use of radiative forces to cool, trap, and manipulate atoms demands quantitative investigation of these forces, both in

terms of their positive (eg. confinement by dipole force) and negative (eg. heating by induced momentum diffusion) aspects. Thirdly, the experiments we have undertaken are very convincing demonstrations of some basic physical principles. Diffraction of atoms by a light "grating" is a classic example of the wave-particle duality of quantum mechanics and the transition from atomic beam diffraction to momentum diffusion is a clear example of the effect of a stochastic process (spontaneous emission) on a simple coherent system. In addition, our momentum transfer studies are excellent probes of the interaction of an atom with a strong radiation field and demonstrate the fundamental coupling between internal and external degrees of freedom of an atom by near-resonant radiation.

I.B. Introduction to Radiative Forces on Atoms

Although the mechanical effects of light on atoms have long been recognized (LEB10, EIN17, FRI33), experimental observation of these effects was not practical until the advent of the tunable dye laser. Since that time, the field has generated a great deal of interest (see JOS85, LEM81, COO81, BJF80, ASH80, KAZ78, STE78 for reviews of the subject). Recently, extensive theoretical advances have been realized and experimental efforts have been progressing from the observational stage towards practical utility.

Radiative forces on atoms are readily classified into two types: the spontaneous (scattering) force and the induced (dipole) force. This classification is based on the type of photon exchange process responsible for the momentum transfer: absorption, stimulated emission, or spontaneous emission. Referring to Fig. 1, we see that momentum is transferred differently by the three types of exchange. The spontaneous force is due to repeated cycles of absorption followed by spontaneous emission (ASH70). The induced force, on the other hand, is the result of absorption followed by stimulated emission (ASH78). For a net force to result from these induced processes, the direction (i.e. mode) of the stimulated photon must be different than that of the absorbed photon, i.e. there

Figure 1

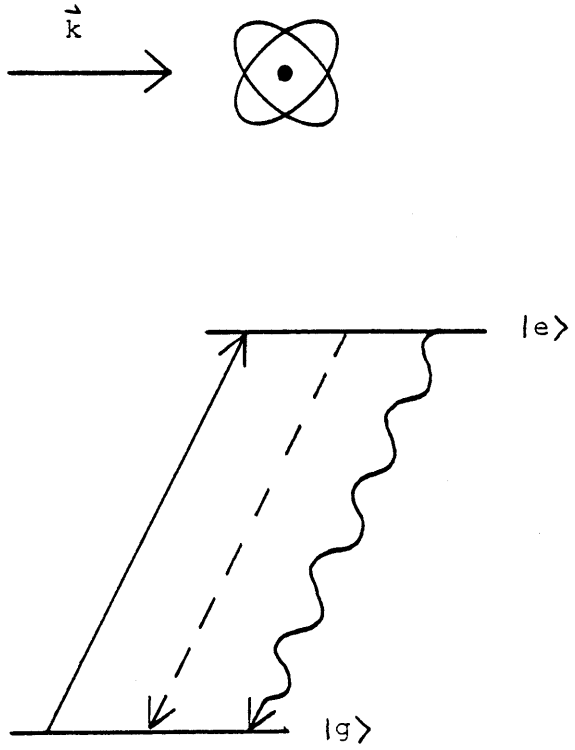

process	momentum transfer
——— absorption	$\vec{p} = \hbar\vec{k}$
— — — stimulated emission	$\vec{p} = -\hbar\vec{k}$
∿∿∿ spontaneous emission	$\begin{cases} \lvert\vec{p}\rvert = \hbar k \\ \langle\vec{p}\rangle = 0 \\ \langle\vec{p}^2\rangle = (\hbar k)^2 \end{cases}$

must be a field gradient. Alternatively, this induced force can be viewed as originating from the interaction of the induced dipole moment with the field gradient (hence the name "gradient" force). Our main goal in this thesis is to study various aspects of this gradient force using the strong field gradients found in a standing wave.

General theoretical treatments of these forces have been extensive and varied. Fully quantum mechanical (i.e. with the translational motion of the atom quantized) theories (COO80d, DAC85a) utilize the Wigner distribution for calculations while semi-classical treatments (COO79, COO80c, GOA80) generally formulate the problem in terms of the generalized optical Bloch equations. The dressed atom concept (DAC85b) is particularly useful in the case of strong fields.

Specific aspects of radiative forces have been treated by numerous authors, usually by restricting the discussion to simple examples such as plane traveling or standing wave. We will list a few major contributions which are particularly relevant to our orthogonal standing-wave experiments. Classical scattering of atoms by a standing-wave in the absence of spontaneous decay was studied (in the context of the gradient force) in the early work of Kazantsev, et. al. (KAS75, DGK78). The first quantum mechanical treatment predicting atomic beam diffraction (for the on-resonant case) was carried out by Cook and Bernhardt (COB78). Subsequent works elaborated on these results to account for spontaneous decay of atoms leaving the standing-wave in the excited state (KSY80), off-resonant excitation and the effects of adiabatic entry and exit (KSY80, BES81, MOS84, MGP85), non-orthogonal laser/atomic beam geometries (BES81, PRG85) and the effect of a small number of spontaneous decays occurring during the interaction (TRC84, KSY85).

The case of many spontaneous decays occurring during the interaction may be treated as a forced diffusion problem obeying a Fokker-Planck equation (COO80d, JAS80, KSY81, LEM81). Recently, the dressed atom concept has also been successfully applied to this situation (DAC85b) and the transition from no spontaneous decays to many has been discussed (TRC84).

The experimental situation is somewhat reversed from the theoretical one in terms of emphasis. Theoretically, the main interest in radiative forces seems to lie in the area of the induced force, due to the rich variety of related phenomena which arise (eg. velocity dependence of the force, Doppleron resonances, Bragg scattering, atomic diffraction, optical Stern-Gerlach effect, induced momentum diffusion). However, experiments on the induced force have been relatively scarce, and definitive ones non-existent, due in large part to the difficulty in creating a well-defined field gradient. Instead, experimental efforts have focused on the spontaneous force. Traveling-wave deflection has been studied extensively (FRI33, PIV72, SWW72, BFP81, WHC85) as has the slowing of atomic beams using the spontaneous force (PPM85, PMP85, EBH85). In addition, the spontaneous force has been used in laser cooling applications (CHB85, NHT80, WII81).

The induced force has been observed (in the optical domain) in two types of experiments. The first demonstration (BFA78, PFB80) used the radial intensity gradient of a Gaussian laser beam to focus and defocus a copropagating atomic beam. Later experiments (ALO79, GKN81, MGA83, GKK84, MGP85, GKN85) utilized the gradients of an orthogonal standing-wave to deflect an atomic beam. These experiments, as discussed in Sections III.A and IV.A, did not provide definitive tests of the theory.

Advances in the study of radiative forces on atoms have been accompanied by many suggested applications, some of which have already been successfully realized. Generally speaking, these advances represent another step in the historic quest for greater control over the system under experimental investigation, i.e. preparing the system according to our desires instead of simply studying the system in its naturally occurring state. Examples of control of internal degrees of freedom include our ability to selectively populate quantum levels with applied radiation and control over spin orientation through optical pumping. The mechanical forces of light afford us the possibility to control external degrees of freedom (momentum and position) of atoms and molecules.

As evidence that this phenomenon has progressed to the point of being a useful tool, we cite several examples. Of great current interest are investigations into the slowing, cooling, and confinement of atoms using radiative forces (see PPM85 for a recent review of the subject). Atomic beams have been collimated (BLM85) and focussed (BFA78) with laser light. Deflection of an atomic beam by resonance radiation has been used to separate isotopes (BDS74, BDS76), perform spectroscopy (JLP73, HLW79), measure excited state population in collision experiments (JDW80, DEV80), and study photon statistics (WHC85). Other potential applications of these forces include state and/or velocity selection (ASH70) and atomic interferometry (CDK85).

Chapter II. Apparatus and Procedure

The design of the experimental apparatus was geared towards making general measurements of momentum transfer to atoms from laser light under conditions sufficiently well-defined to allow meaningful comparisons with available theory. The ability to perform the experiments relies on the achievement of three major goals: 1) a high intensity atomic beam with well-defined velocity, internal state, and collimation; 2) a well-characterized laser/atomic beam interaction; and 3) a high efficiency, low noise neutral atom detector with high momentum resolution. The achievement of these goals will be discussed in detail in this chapter. In section A, the apparatus itself will be described, and in section B, we will discuss the general experimental procedure. Our novel method of state selection using optical pumping and the resultant radiative deflection is described in section C.

II.A. Apparatus: Mechanical Details

The experiments involve intersecting an atomic sodium beam with a laser field and measuring the deflection angle which results from momentum transfer. An overall schematic of the apparatus is shown in Fig. 1. The atomic beam is produced by seeding sodium vapor in a supersonic expansion of argon, and is optically pumped prior to the main interaction in order to prepare it as a two-state system. The deflection caused by this optical pumping eliminates atoms in the wrong ground state hyperfine level. The required high degree of collimation is accomplished with two well-separated narrow slits. The laser/atomic beam interaction takes place in an interaction region well-characterized by various diagnostic measurements. The momentum transferred in this interaction is measured with a high resolution detector with an inherently high signal-to-noise ratio. The various aspects of the apparatus will now be examined.

Figure 1: Deflection Apparatus

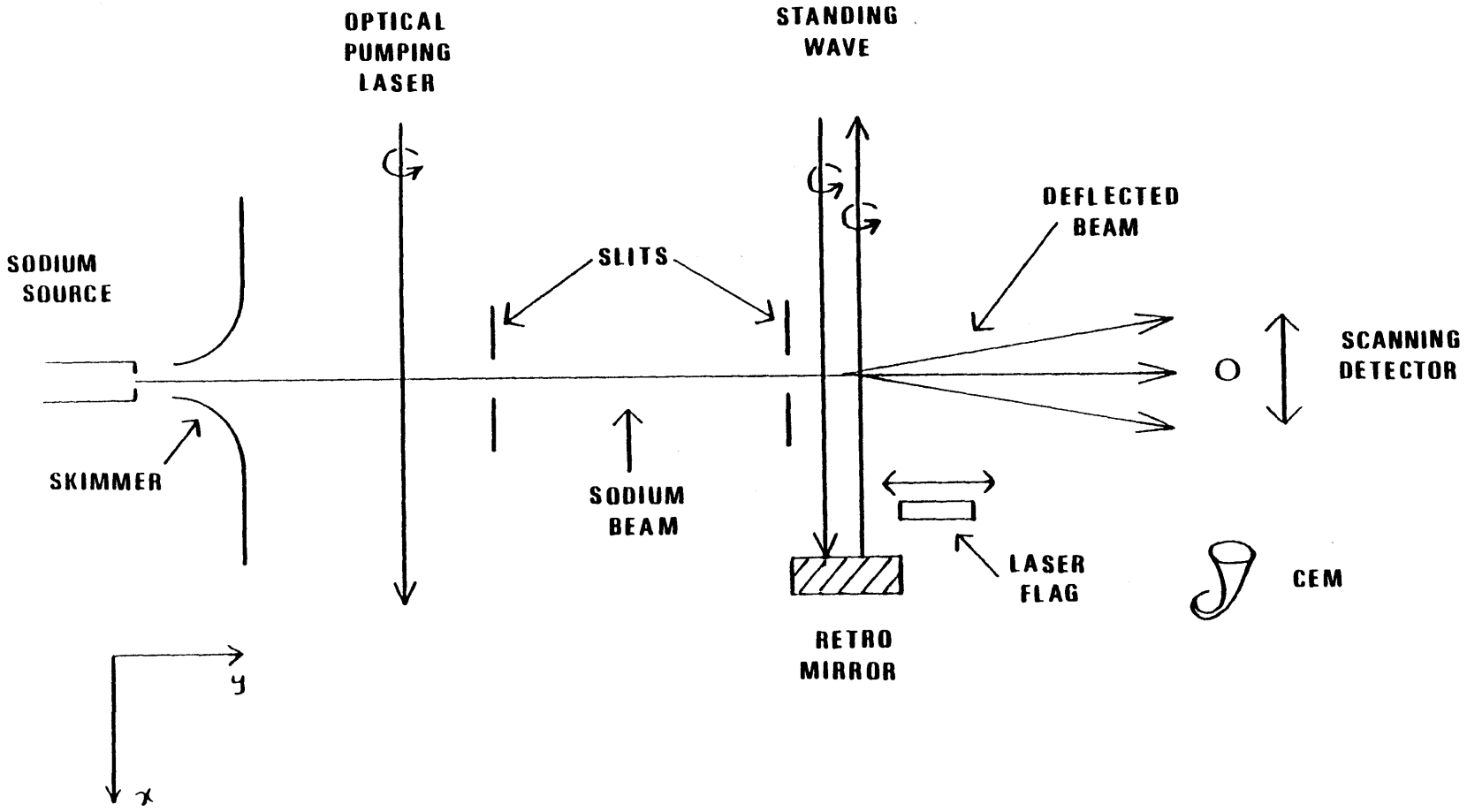

1. Vacuum System

Our use of a supersonic expansion of argon to "cool" the sodium beam places unusual requirements on the design of the vacuum system. The system must be able to handle a fairly large gas load and at the same time provide a reasonably good vacuum for the atomic beam to travel through without collisions. (The collisions are especially bothersome due to our stringent collimation requirements.) These goals are met by the use of differential pumping.

The vacuum system, shown schematically in Fig. 2, is comprised of five separate vacuum chambers: 1) source chamber; 2) first differential pumping chamber (optical pumping region); 3) second differential pumping chamber; 4) main chamber (free flight region); and 5) detector chamber. Slide valves (made of plexiglass to allow optical alignment) separate the source and differential chambers from the main chamber and the main chamber from the detector chamber so that the apparatus actually consists of three independent vacuum systems which can be connected to allow passage of the atomic beam. These valves are an important feature as they allow independent servicing of the different vacuum systems. The source requires the most service, but also pumps down to operating pressure most rapidly ($\sim$ 1 day). The main chamber requires 2 days or more to reach its ultimate pressure. The detector chamber is rarely brought up to atmosphere in order to avoid exposing the hot-wire filament to air. These independent vacuum systems will now be described in detail.

The first vacuum system consists of (in order of decreasing pressure) the source chamber and the first and second differential pumping chambers. The source chamber is a cubical aluminum chamber, 12" on a side. It is pumped by a 4" Stokes ring-jet booster pump, model 900-150-1, charged with Edwards grade 200 vapor booster pump fluid in order to give high throughput at pressures in the $10^{-3} \rightarrow 10^{-2}$ torr range (pumping speed $\sim 250\ l/s$). The two differential chambers are sections of a large stainless steel chamber which are separated by an internal flange. This flange

Figure 2: Vacuum System

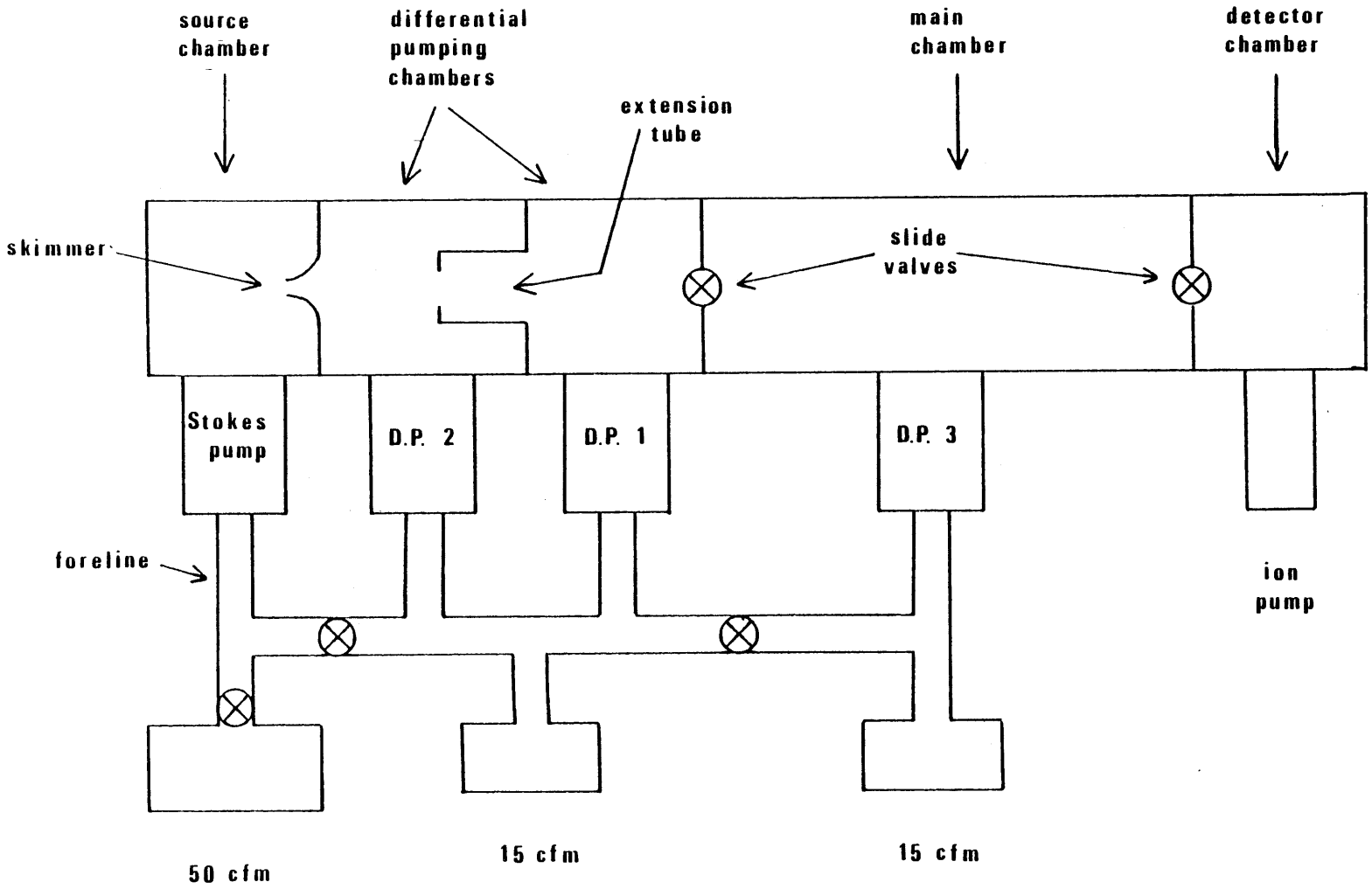

has mounted on it an extension tube which "extends" the lower pressure of the second differential region into the first in order to reduce the path length of the atomic beam in the higher pressure chamber. The first differential pumping chamber is pumped by a 10" NRC diffusion pump (D.P. #2), model HS10-4200, Type 163 (pumping speed $\sim 4200\, l/s$ for pressures up to $\sim 10^{-3}$ torr) in order to handle the moderate gas load efficiently. The second differential pumping chamber utilizes a 4" diffusion pump (D.P. #1) CVC model PMC-4B (pumping speed $\sim 700\, l/s$), as there is virtually no gas load. Both diffusion pumps are charged with DC-704 silicone oil. The three diffusion pumps on this portion of the vacuum system share a common interlock which utilizes thermal switches on each pump, flow switches on the cooling water for each pump and a thermocouple gauge set point which can monitor either the foreline pressure or the pressure in the second differential region.

The second vacuum system consists of the main chamber or free flight region, and comprises most of the length of the machine. The chamber consists of an extended 8" stainless steel six-way cross (where the interaction region is located), followed by another long straight stainless steel section. The chamber is pumped by an NRC 4" belly pump (D.P. #3), model VHS-4, charged with DC-704 oil and operated with a water cooled baffle to reduce backstreaming. The pumping speed is ~ 500 l/s (baffled). This diffusion pump is interlocked with a thermal switch, a flow switch, and a thermocouple gauge (which can monitor the chamber or foreline pressure).

All of the diffusion pumps of the first and second vacuum systems share a common foreline. The foreline itself is bolted solidly to the wall behind the apparatus and connected to the diffusion pumps via bellows in order to reduce the effect of mechanical pump vibrations. These forepumps are supported on damping pads to reduce coupling through the floor as the apparatus itself rests solidly on the floor. The foreline is pumped by three mechanical pumps in parallel: a Cenco Hyvac 150 (50 cfm) and two Welch 1397 pumps (15 cfm each). There are three butterfly valves situated in the foreline in order to allow various combinations of fore pumps and diffusion pumps

(see Fig. 2). We note here that the large Cenco pump is rarely used because of the relatively large amount of vibration associated with it, even though it is set up on inflatable mounts and has its own bellows to isolate it from the foreline. However, its use would be necessary if the source were operated at higher stagnation pressures. Under present operating conditions, the two Welch pumps operating in parallel are enough to handle the gas load.

Because of the constant flow of gas in the apparatus it is necessary to be able to monitor the pressure in the various chambers. In this paragraph we describe the various pressure monitors in each chamber. The chamber numbers in parentheses are those assigned for historical reasons and correspond to the numbers of the appropriate diffusion pumps in the interlock circuits. The source chamber pressure is monitored with a temperature controlled capacitance manometer (MKS Baratron #222AHS-A-B-10) and is typically $\sim 10\ \mu$ (10^{-2} torr) with the source at normal operating conditions. There is also a pair of thermocouple gauge tubes (DV-24) located in the source chamber and the foreline of the Stokes pump. The first differential pumping chamber (chamber #2) is equipped with a Penning (cold cathode) gauge which can be interchanged with an ionization gauge. We have found that the Penning gauge tubes are more reliable when there is a lot of backstreaming (which is the case in both differential chambers). The pressure in chamber #2 is typically $\sim 2x\,10^{-6}$ torr. There is also a pair of thermocouple gauge tubes (DV-6M), one located in the chamber and one in the foreline. The pressure in the second differential pumping chamber (chamber #1) is monitored with a Penning gauge (interchangeable with an ionization gauge) and is $\sim 10^{-6}$ torr with a typical atomic beam. The main chamber (chamber #3) pressure is monitored with both an ionization gauge and a Penning gauge, mounted on a "T" arrangement, and is typically $5x\,10^{-7}$ torr. There is a thermocouple gauge tube (DV-6M) on the chamber and one on the foreline.

The third vacuum system consists of the detector chamber which is situated at the very end of the apparatus. It is pumped by an old Vac-ion pump ($50\ l/S$) and equipped with an LN_2 cold

trap to prevent pump oil from reaching the hot-wire filament when this chamber is open to the main chamber. The pump is baffled with aluminum honeycomb to prevent any radiation given off by the ion pump from reaching the CEM. This ion pump has a built-in protection circuit which shuts the pump off when the pressure exceeds $\sim 10^{-4}$ torr. The hot-wire filament supply and the CEM high voltage supply are also interlocked to this protection circuit.

2. *Sodium Source*

Our use of a supersonic expansion of argon seeded with sodium as the atomic beam source results in a narrow velocity distribution in the beam. The distribution of velocities affects the experiment in two ways. Firstly, since the interaction time between the atom and the laser is the transit time of the atom through the focused laser waist, a faster (slower) atom spends less (more) time in the laser field. Thus, a distribution of velocities results in a distribution of interaction times. Secondly, after an atom has interacted with the laser, its deflection angle for a given transverse (i.e. perpendicular to the atomic beam) momentum transfer, depends inversely on its longitudinal (i.e. along the atomic beam) velocity. Thus, the distribution of velocities tends to wash out any structure present in the momentum distribution, especially at large momentum transfers. We would also like to point out that in proposed experiments (PRG85) where the atomic beam and laser beam(s) are not orthogonal, atoms with different velocities see the laser light at different frequencies, due to the first-order Doppler shift.

The use of a supersonic expansion of argon results in a cooling of the atomic beam with consequent *compression* of the velocity distribution. The resulting flux is greater than that obtained with velocity *selection* techniques, since the entire velocity distribution is utilized. In addition, the on-axis flux is enhanced in the supersonic (relative to the effusive) regime.

The main disadvantage of supersonic beam technology is the requirement that the vacuum system be able to handle a large gas load and still maintain a very low background pressure to

allow unperturbed atomic beam propagation. Another potential problem is that the cooling in the expansion can result in increased dimer formation.

Supersonic beams have been investigated very extensively. We certainly have no intention of discussing the relevant physics in any detail here, but a few useful facts and formulae will be quoted. For the reader interested in further details, we list the following references. Very thorough discussions of supersonic expansions can be found in AND74 and HAB77. Both of these works contain an exhaustive list of appropriate references. In addition, Appendix I of SER80 and Chap. II.B of MIG84 are good discussions of alkali seeded beams, particularly appropriate for our application. The effects of the skimmer are described in CLL76 and BIR76 and references therein.

Supersonic (as opposed to effusive) flow occurs when the mean free path becomes smaller than the diameter, D, of the nozzle. Continuum conditions hold in the nozzle but a transition to free molecular (i.e. collisionless) flow occurs downstream from the expansion. In very simple terms, the cooling in a supersonic adiabatic expansion results from the conversion of thermal energy into the kinetic energy of directed mass flow. The efficiency of this conversion, i.e. the final beam temperature (T), depends on the stagnation density (n_0) and temperature (T_0) and on the size of the nozzle (D). Restricting the discussion to a monoatomic gas ($\gamma = \frac{5}{3}$), Habets derives (HAB77, Eq. 2.2.22) the following expression for the total nozzle throughput (atoms/sec):

$$\Gamma \approx .51 \cdot n_o \alpha_o A$$

where $\alpha_o = (\frac{2kT_o}{m})^{1/2}$ is the characteristic stagnation velocity and $A = \frac{\pi}{4}D^2$ is the area of the nozzle. The flow velocity is also derived (HAB77, Eq. 2.2.9):

$$u = (\frac{5kT_o}{m})^{1/2}$$

The peaking factor, i.e. the enhancement of the on-axis intensity relative to the effusive case, is calculated (HAB77, Table 2.1) to be 2.0. The velocity distribution can be characterized by the speed ratio $S = \frac{u}{\alpha}$, where u is the flow velocity and $\alpha = (\frac{2kT}{m})^{1/2}$ is the characteristic thermal velocity of the cooled beam. Using the known potentials for Ar-Ar collisions, Habets uses a "thermal conduction model" to calculate (HAB77, Eqns. 2.3.78, 2.3.76):

$$S = (2.62 \times 10^{-8}) \cdot (n_o \cdot D \cdot T_o^{-1/3})^{6/11}$$

where n_0 is in cm^{-3}, D is in cm and T_0 is in K. We see that the internal beam temperature (αS^{-2}) goes almost inversely (i.e. to the $-\frac{12}{11}$ power) with the stagnation density. The FWHM of the velocity distribution (width of Gaussian only, i.e. ignoring multiplicative factors which are powers of velocity) is $\Delta v_{FWHM} = 2(ln\,2)^{1/2}\alpha = 1.67 \cdot \alpha$, so that the fractional FWHM can be written in terms of the speed ratio:

$$\frac{\Delta v_{FWHM}}{u} = \frac{1.67}{S}$$

The sodium is seeded in the argon (density ratio of $\sim$ 1:100) and assumes the same velocity distribution as the argon. We note that increasing the stagnation pressure (i.e. argon density) results in a larger argon flow and a higher speed ratio but does not change the sodium flux. (The sodium density depends only on the reservoir temperature.) For typical operating conditions (P_0 = 20 psiG of argon, D = 70 μ, T_0 = 650 C) we calculate a speed ratio of $\sim$ 16.5 and a fractional FWHM of $\sim$ 10%. A value of $\sim$ 11% was measured (MOS84) for these parameters, using a Doppler technique.

The sodium source itself is shown in Fig. 3. It consists of a reservoir to contain the molten sodium, an inlet for the argon gas, and a small (70 μ diameter) nozzle where the expansion occurs.

Figure 3: Sodium Source

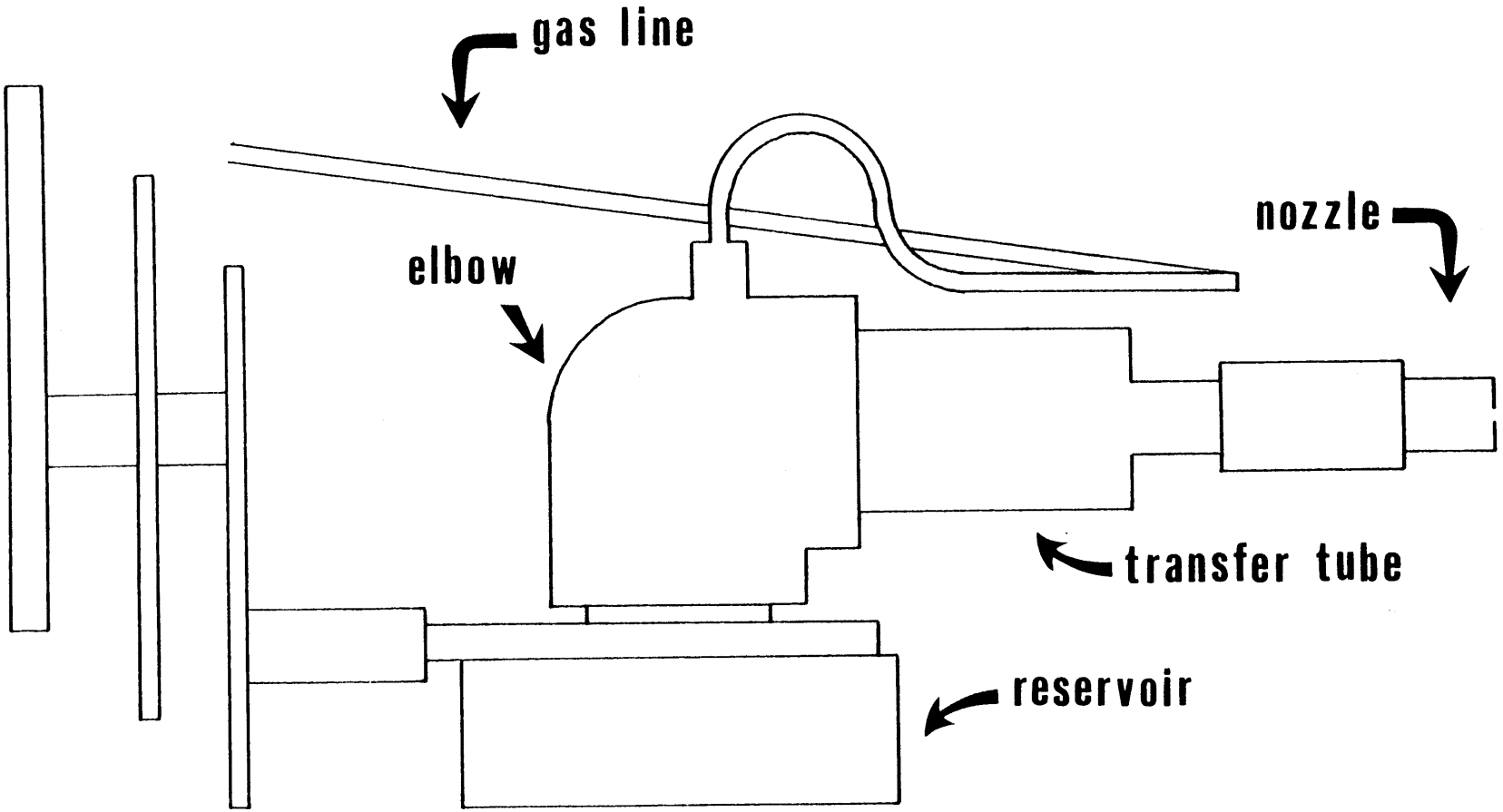

Differential heating is required to prevent clogging of the nozzle and/or gas line.

The source is a modified version of the one described in MOS84. The modifications were geared towards improvements in three major areas: 1) less frequent clogs of the gas inlet line, 2) better mixing between the sodium vapor and the argon, and 3) better thermal isolation.

The source is constructed of stainless steel, using standard parts (Swagelok) whenever possible. Stainless steel maintains its tensile strength at high temperature and is also relatively resistant to corrosion in the presence of molten sodium. Its poor thermal conductivity facilitates differential heating and thermal isolation.

The reservoir has an internal capacity of $\sim 25\ cm^3$ so that a full charge of sodium is ~ 25 g. This is sufficient for hundreds of hours of running time.

The heating of the source is accomplished by four separate heaters which are in contact with the four sections of the oven. Despite thermal connection between these sections, the temperature of each section can be controlled somewhat independently. The temperature of each section is monitored with a Chromel-Alumel (type K) thermocouple. Flexible high watt density electric heaters manufactured by ARI Industries, Inc. are wrapped tightly (to avoid hot-spots) around the various source parts. The characteristics of the heaters are shown in the following table.

Heater	*ARI part #*	*Resistance*	*Max. Power Rating*
(1) Nozzle	BXX-04B-16-10K	40Ω	300W
(2) Transfer tube	BXX-09B-35-7K	19Ω	1500W
(3) Reservoir	BXX-09B-52-3K	26Ω	2250W
(4) Swage Tee (elbow)	BXX-09B-35-4K	18Ω	1500W

It should be noted that these heaters have "K" type (epoxy) as opposed to "T"-type (ceramic) termination, so that care must be taken to keep the cold lengths behind the heat shields.

The argon carrier gas enters the oven through a $\frac{1}{8}$" stainless steel tube which couples to a Swagelok fitting welded into the top of the Swagelok elbow. This location allows adequate heating of the gas line, which is essential in avoiding clogs. In addition, the gas is pre-heated by having the gasline lie close to the source heaters for several inches after passing through the heat shields.

The effect of the size of the gas inlet was investigated in some detail in order to minimize the chronic clogging problem. A larger hole has the obvious advantage of requiring more material to obstruct it, but the disadvantage of lower argon flow velocity, thereby allowing backstreaming and subsequent condensation of sodium vapor (or other sodium compounds). Our experience with holes ranging from .020" to .085" diameter has shown that the larger holes seem more reliable, but still require unclogging every half-dozen runs or so. The source stagnation pressure is measured with an Ametek vacuum → 100 psiG gauge and the flow monitored with a Matheson rotameter (floating ball type flowmeter) with a #601 tube.

Due to the relatively large distance (5 cm) between the gas inlet and the sodium reservoir, measures must be taken to ensure good mixing between the argon and the sodium vapor. We elected to install a baffle (0.005" stainless steel shim) to obstruct the line of sight from the inlet to the nozzle and force the argon down into the reservoir. At typical operating conditions (20 psiG of argon, T=600 C→20 torr of Na), we calculate a diffusion coefficient (for sodium diffusing into the argon) of $\sim .04 \frac{cm^2}{sec}$. Thus, the diffusion time for a distance of ~5 cm is ~6 min. This is to be compared to the "refresh" time of the oven, which is ~1 min. Obviously, static diffusion alone would not produce adequate mixing. We note that the diffusion coefficient is inversely proportional to the stagnation pressure, so that less mixing occurs at higher pressures.

The heated source is supported by arms which attach to the reservoir. This ensures that any heat lost through conduction is from the reservoir, thereby maintaining it as the coolest section of the oven. These arms are stainless steel blocks which attach to a $\frac{1}{8}$" thick stainless steel back

plate via 1" long ceramic spacers. This plate in turn is attached to the tilt plate assembly via ceramic spacers for added thermal isolation. These spacers pass through a watercooled copper plate which prevents overheating of the heater terminations, electric connections, and mechanical movements. The water flow through this plate is interlocked (Proteus model 100 flow switch) with the source heaters to prevent heating without coolant.

The entire source is enclosed in a double layered heat shield (.005" and .007" stainless steel shim) to cut down on radiative losses. Even so, the source chamber gets quite warm when the source is at operating temperature. Cooling plates heat sunk to the side flanges keep the chamber at a reasonable temperature.

Small movements of the source are accomplished by the tilt plate which sits between the source and the source mounting flange. A three point arrangement using 40 tpi screws results in tilts of ~ 6 mrad/turn. This tilt corresponds to a ~ 2 mm translation of the nozzle. If all three screws are turned together the entire source is translated towards or away from the skimmer. The range of this motion is ± 4 turns (± 2.5 mm) with the center corresponding to a nozzle-skimmer distance of ~ 1 cm. This position is monitored with a mechanical counter on the pivot screw.

After emerging from the 70 μ diameter nozzle, the beam passes through the skimmer. The purpose of the skimmer is two-fold. First, the small solid angle subtended by the skimmer orifice skims off the majority (>99%) of gas expanding from the nozzle and allows it to be pumped from the source chamber. Secondly, the skimmer acts as an "aerodynamic beam extractor" by allowing attachment of a shock wave from the nozzle. This shock wave separates the supersonic (central) portion of the expansion from the background gas in the chamber and allows relatively collision-free passage into the next vacuum chamber. The efficiency in this regard depends critically on the shape of the skimmer and the sharpness of the orifice. We use a commercially available (Beam Dynamics, model 1) electroformed nickel skimmer with a .5 mm orifice diameter. This has a

specified orifice edge thickness of 5 μ (typical) but this undoubtedly degrades with use. The skimmer is mounted to the bulkhead flange which separates the source chamber from the first differential pumping region. A Macor ring ($\frac{1}{4}$" thick) thermally isolates the skimmer from this flange. A copper flange attaches to the bulkhead flange and serves to clamp the skimmer in place. This copper flange is heated with a nichrome cartridge heater to $\sim 350\ C$ to keep the skimmer free of sodium deposits. The heater is constructed from ~ 4 ft. of #24 nichrome wrapped around a ceramic rod which is slipped inside a ceramic tube and sealed with #8 Saureisen cement. The unit has a resistance of $\sim 6\ \Omega$ and requires ~ 3 A to reach operating temperature. A type K thermocouple monitors the skimmer temperature.

We should mention some interesting and potentially useful observations concerning the skimmer. We have always seen that atomic beam signals have decreased with increasing source stagnation pressure. An extensive investigation of this problem has led us to believe that this behavior is caused by "skimmer choking", i.e. a build-up of gas in the skimmer which prevents clear passage of the atomic beam. The origin of the problem lies in inadequate pumping speed for the space directly behind the skimmer. The present hole in the bulkhead (or "adapter") flange is $\sim\frac{3}{8}$" in diameter and $\sim\frac{3}{4}$" long. We constructed a new bulkhead flange and skimmer mounting assembly which completely opens up the back of the skimmer to the first differential region. Fortunately, we had enough signal with the old configuration to perform the experiments described in this thesis. However, if future experiments require more signal and/or a narrower velocity distribution (i.e. higher stagnation pressure), this new assembly may provide the necessary improvement.

According to Campargue et. al. (CLL76), the intensity of the beam emerging from the skimmer is optimized at a particular distance between the nozzle and the skimmer orifice. Using Eqn. 1 in CLL76, we calculate an optimum nozzle-skimmer distance of ~ 1 cm for our operating

conditions. This number is relatively independent of the source stagnation pressure. Experimentally, we find that this does indeed appear to be close to the optimal value.

The ability to measure momentum transfers with resolution less than $\hbar k$ calls for an extremely high degree of collimation of the atomic beam. For deflection experiments such as the ones we have performed, the relevant figure of merit is the ratio $\frac{d_\gamma}{w}$, where d_γ is the deflection from a single photon (measured at the detector), and w is the FWHM of the collimated beam. For the geometry shown in Fig. 4, we can calculate (RAM56) that $w = s \cdot \frac{y_2}{y_1}$, where we have assumed that the width of both slits, s, is much smaller than the effective size of the source. If the deflection occurs immediately after the second slit, then $d_\gamma = (y_2 - y_1)\theta_\gamma$ where $\theta_\gamma = \frac{\hbar k}{mv} = 3.0 \times 10^{-6}$ rad. is the angular deflection due to a single photon. The figure of merit is optimized when $y_1 = \frac{y_2}{2}$. However, practical considerations determined the final choice: $y_1 = 87$ cm and $y_2 = 224.8$ cm, which yield a value of w = 25.8 μ when 10 μ wide slits (Melles Griot #05 PAS 002) are used. We have convolved this with the width of the detector (25 μ) and obtained a FWHM of 29.6 μ. With optimum alignment, we have measured a FWHM of 29.4 μ, in excellent agreement with the predicted value. The deflection occurs 1.9 cm after the second slit, yielding a value of 41 μ for d_γ. This value is confirmed by measurements of the separation between diffraction peaks.

Because of the small collimation angle, slits with a high aspect ratio (10 μ wide x 3 mm high) are used to increase the flux reaching the detector. The use of this "ribbon beam" results in only one direction (horizontal) of critical alignment. However, it does require that the slits and the detector filament be parallel to a high degree. In order to achieve the narrowest beam profile, this parallelism must be of the order of the inverse of the slit aspect ratio, i.e. $\sim 3 \times 10^{-3}$ rad. Since the first slit is so close to the source, only the atoms which pass through it very close to its vertical center are able to reach the second slit. This reduced effective aspect ratio relaxes the parallelism

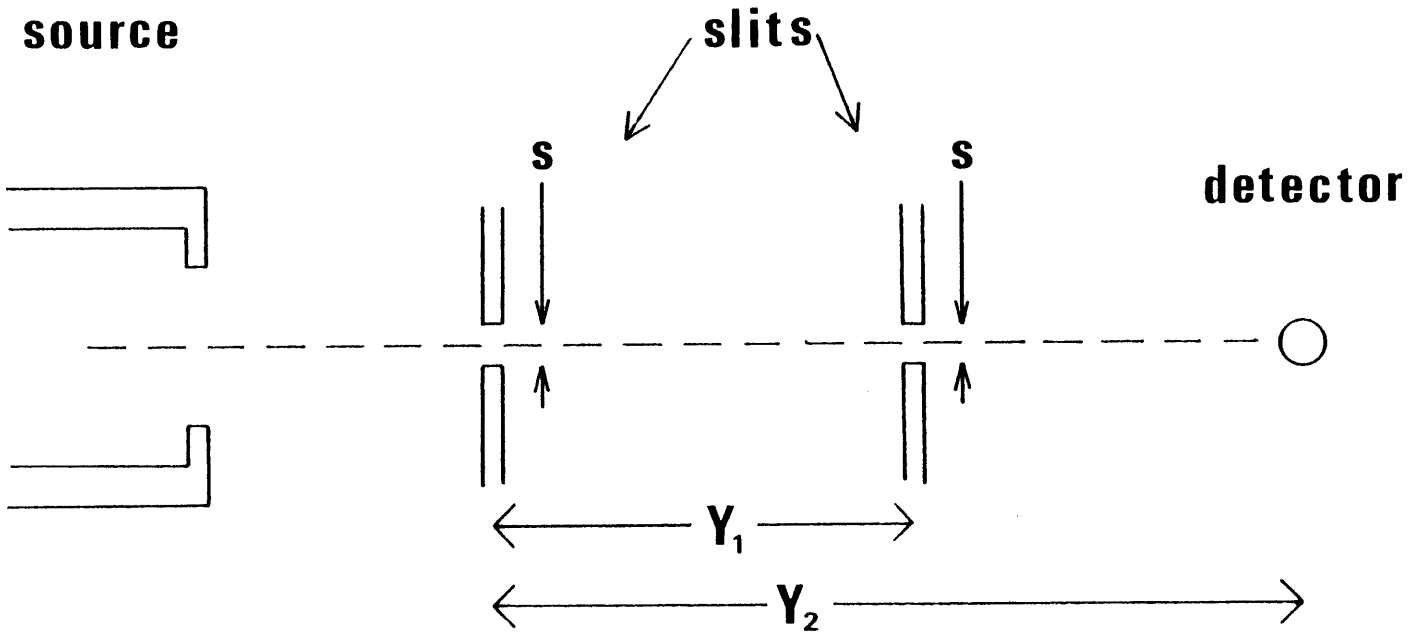

Figure 4: Collimation Geometry

requirement for the first slit.

Various diagnostics and initial beam alignment require larger signals than are typically present with the collimating slits in place. Therefore each of the two slits can be translated off axis and replaced with an open aperture ($\frac{3}{16}$" diameter).

The first slit sits on a translator assembly at the end of the extension tube which separates the first and second differential pumping chambers. This translator (Daedal #4507) moves horizontally to allow either the slit or open aperture to be aligned on axis. The two alignment positions differ by 0.5" or 32 turns of the 64 tpi screw. This motion is accomplished with a rotatary feedthrough on the rear (plexiglass) flange of the first differential pumping chamber and the position is monitored with a mechanical counter (.1 turn = 40 μ resolution) on the rotating shaft. When the slit is in position, the open aperture is obscured by a sheet metal flag to prevent the extra argon from entering the second differential pumping chamber.

The second slit is mounted on an assembly which allows rotation as well as vertical and horizontal translation. This assembly is attached to the bottom flange of the six-way cross where the interaction region is located. Vertical motion is achieved with a Daedal #4007 translator whose 64 tpi screw is coupled to a Ferrofluidic rotary feedthrough. The slit and $\frac{3}{16}$" diameter aperture are offset vertically by 0.5" or 32 turns of the feedthrough (monitored with a mechanical counter). The horizontal motion of the slit is accomplished with a Daedal #4505 translating stage. A drive system consisting of an Airpax #K82501-P2 stepper motor (48 steps/rev.), a gear and chain drive (24:25 reduction ratio), and a Klinger BM17.04 micrometer (2 threads/mm, 4 mm travel) is controlled by a lab built electronic driver/counter (MOS84) to provide horizontal motion in 10 μ steps. An Oreil #2501 rotator is mounted on the horizontal translator to allow for rotation of the slit located at its center. A spring-loaded lever arm attached to the inner rotating ring is driven by a TRW Globe DC Motor (#43A106-5) through a worm gear. For +20 V, the rotation rate is

$\sim 0.25°/sec$ and the direction is CCW as viewed from the source. The slit itself is mounted (with vacuum grease) on an aluminum pedestal to bring it as close as possible (~ 1.9 cm) to the interaction region while keeping the relatively bulky translators out of the way.

3. Detector

The momentum transferred to the atomic beam is measured with a scanning hot-wire detector. This detector is almost identical to the one described in MOS84, so we will not discuss it in detail here. The heart of the detector is a heated 25 μ diameter filament on which incident sodium atoms are ionized. According to our experience, Pt(92%)/W(8%) (alloy #479, Sigmund Cohn, Co.) yields the most consistent results in terms of high efficiency and low noise. Much experimental work has been done on surface ionization of alkali metals but consistent and reproducible results are rare. For the reader interested in the details of surface ionization, we recommend the following works and the references contained therein: DAT56, WII64, and KAM65.

In simple terms, surface ionization occurs when a neutral atom (sodium in our case) is incident on a heated metal surface and gives up its valence electron to the surface. The probability for this process depends on the difference between the magnitudes of the ionization potential (I) of the incident atom and the work function (Φ) of the filament material, as well as the filament temperature. If the difference $\Delta=I-\Phi$ is negative, the surface will more likely than not strip the electron from the incident atom. The Pt/W alloy is efficient because of its high work function (5.30 eV according to WII64) relative to the ionization potential of sodium (5.14 eV). We have found that a filament current of 35 mA (corresponding to T $\approx$ 1500 K according to WII64) gives good ionization efficiency (absolute efficiency is difficulty to determine) low background, and fast response. In fact, the background is so low (after a long aging period) that we have removed the $\vec{E}x\vec{B}$ filter described in MOS84 and still have background signals of only 5 $\rightarrow$ 10 cts/sec (cf. peak

signals in undeflected beam of $\sim 10^5$ cts/sec). We note that filament efficiency is very dependent on detector chamber pressure and contamination (since the process occurs on a surface), so the detector is kept closed off when not in use and always cold-trapped when exposed to the atomic beam.

The filament is situated approximately midway between two parallel plates which are biased to provide the electric field which accelerates the ions into the multiplier. The plate between the filament and the multiplier (which has a grid to allow passage of the ions) is at ground potential, while the filament and back plate are biased at V_F and V_B respectively. A uniform field is obtained for $V_F/V_B \approx \frac{1}{2}$, but small tilts of the filament and the voltage drop across the filament (typically ~ 1.5 V for a current of 35 mA) affect this ratio as well as the individual voltages. We find that $V_F/V_B \approx$ 50V/100V is usually the optimum range. The uniformity of these accelerating fields is important as the ions must travel ~ 14 cm from the filament to the multiplier. We note that the filament is mounted under tension (Be-Cu spring) to prevent thermal distortions which would adversely affect the detector resolution.

The multiplier is a Galileo model 4039C Channeltron Electron Multiplier (CEM) with an input orifice diameter of 1 cm and a gain of $\sim 10^8$ at an operating voltage of 2.8 kV. This gain drops by an order of magnitude for a count rate of 10^6 cts/sec, so care should be taken to avoid signal levels much in excess of 10^5 cts/sec. The pulse from the CEM are coupled to a 50 Ω cable with an impedance matching transformer and amplified by a Mechtronics 511 amplifier/discriminator. The output pulses are then either fed to the computer interface (CAMAC) or converted to analog for display on an X-Y recorder. There is a metal flag between the filament and the CEM to allow background measurements and to prevent material buildup on the CEM when not in use.

The assembly consisting of the filament and accelerating electrodes is mounted on a

translating stage (Daedal #4505) which is driven by a stepper motor/micrometer arrangement. The drive system is very similar to that used for the horizontal movement of slit #2, except that a Klinger BM12.16 micrometer is used as it has a larger translation range (16 mm). The same electronic driver/counter provides motion in 10 μ steps.

For subsequent analysis, it is essential that the deflection data be recorded and stored on the laboratory computer system. The software, developed by Susie Atlas, runs on the PDP 11/20 after downloading from the PDP 11/34. The interface to the experiment utilizes CAMAC hardware, in particular, a Kinetic Systems 3655 timing pulse generator and an EG&G 5424B quad scalar which step the detector (in conjunction with the stepper motor driver) and count the CEM pulses. Some features of the data-taking programs are described in MOS84. We choose not to elaborate here, as we are currently in the process of changing over to an IBM AT system, whereby the present hardware and software will be obsolete.

Besides the scanning hot-wire detector (designated HWD #3) located at the very downstream end of the apparatus, there are two other hot wire detectors along the beam path to monitor the atomic flux at their respective positions. The first (HWD #1) is situated in the first differential pumping chamber $\sim$9.3 cm from the nozzle and the second (HWD #2) is located in the main chamber between the interaction region and the detector chamber, $\sim$ 179.4 cm from the nozzle. Both detectors employ iridium (Φ=5.27 eV) ribbon filaments (.028" wide x .0018" thick) and collectors biased at -30 V with respect to the filament. Ion currents are measured with a Keithley 601 electrometer. HWD #1 is mounted on a rotating shaft to allow its placement alternatively in or out of the beam path. The shaft rotates in a pair of ball bearings and is driven by a rotary feedthrough on the rear (plexiglass) flange via a gear/chain drive. Optimum filament current is $\sim$2.5 amps AC. HWD #2 is mounted on a shaft which goes through a rotary feedthrough on the top flange of the vacuum section which follows the six-way cross. There is also a beam flag on this shaft to block the beam from HWD #3. The optimum current for HWD #2 is $\sim$3.0 amps AC.

Both HWD #1 and HWD #2 are of limited use in beam flux measurements because of low and unknown efficiency (probably due to filament contamination). However, they are fairly reliable in measuring *relative* beam intensities.

4. Optical Pumping Optics

The preparation of the atomic beam as a two-state system requires the use of another laser to do the necessary optical pumping. We use a Coherent 699-21 scanning single-mode ring dye laser for this purpose. This laser is pumped by a Spectra Physics 171 argon ion laser and uses R6G dye since we do the optical pumping on the D_2 line of sodium (589.0 nm). Typically, an output power of $\sim$ 200 mW (linewidth <1 MHz) is obtained for $\sim$ 5 W (all lines) of pump power.

Unfortunately, this laser is located in a different room than the main apparatus, so the light must be transported between these locations. In the past, we have unsuccessfully attempted this with wall-mounted mirrors (too much vibration) and a multimode 200 μ core optical fiber (excessive loss of brightness). Success has been achieved using a single-mode polarization-preserving optical fiber. A single-mode fiber is necessary for good spatial quality of the output beam (i.e. high intensity and low divergence). The high birefringence of the fiber preserves the polarization by minimizing the effects of environmentally induced birefringence.

We use $\sim$ 25 m of York VSP #HB530 high birefringence fiber which has a core diameter of $\sim 4\ \mu$ and a beat length (distance over which the polarization rotates by 360°) of <2 mm. This fiber has an attenuation of <22 dB/km (i.e. 6% loss for 25 m). The high mechanical precision and stability required to couple the light into the fiber are achieved with an NRC model F-916 coupler, which has the capability for fiber rotation (in order to ensure alignment of the incident polarization with the principle axis of the fiber). A 20X microscope objective seems to provide optimal input coupling when situated $\sim$1 m from the 699 laser. The fiber output is collimated with either a 15X or 6X microscope objective, depending on the desired beam diameter ($\sim$ 1.2 mm or

$\sim$3 mm FWHM, respectively). The fiber and output objective are mounted in an NRC model F-916T coupler with rotation capability in order to allow adjustment of the angle of the linearly polarized output. The overall transmission efficiency of the fiber and microscope objectives is $\sim$60%.

The path of the optical pumping beam is shown in Fig. 5. After collimation it passes through a pyrex flat which picks off $\sim$10% of the light for the sodium reference cell (discussed in section II.A.7). The remainder of the light passes through a linear polarizer (Melles Griot 03 FPG 003) followed by a $\lambda/4$ plate (Optics For Research #RZ-1/4-589.6, zero-order quartz, anti-reflection coated) which converts the polarization to circular (estimated degree of circular polarization > 99%). The handedness is chosen to induce Δm=+1 transitions.

The power of the optical pumping laser is adjusted with a pair of linear polarizers located before the input to the fiber. The first polarizer is rotated relative to the second to give a variable attenuation with a fixed output polarization.

After passing through (with $\sim$10% power loss) the large glass vacuum window (heated to prevent condensation of diffusion pump oil), the laser intersects the atomic beam in the center of the five-way cross shown in Fig. 6, and exits through a heated anti-reflection coated window mounted on the rear (plexiglass) flange. Here, the optical pumping power is monitored with a photodiode. The purpose of the five-way cross is to spatially define the optical pumping interaction and allow monitoring of the resulting fluorescence with the split photodiode.

Since the optical pumping beam is of relatively low intensity (i.e. no power broadening) and is orthogonal to the atomic beam (i.e. no Doppler broadening), the laser frequency must be within the natural linewidth (10 MHz FWHM) for effective pumping. The long term drift of the 699 (specified to be < 100 MHz/hr) is intolerable in this regard. Therefore, this laser must be actively locked to the atomic transition, using a signal from the optical pumping process itself, as described

Figure 5: Optical Pumping Optics

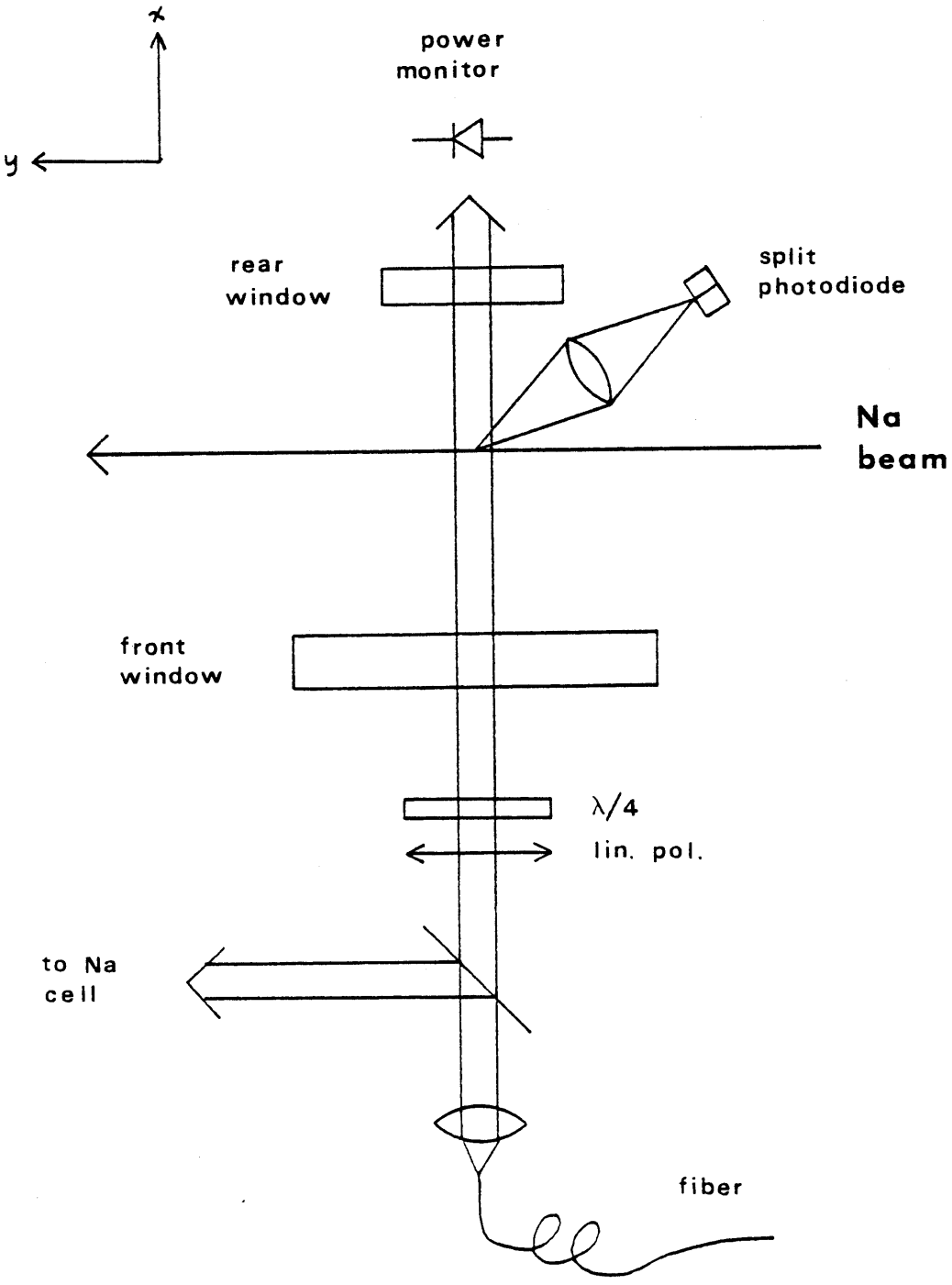

Figure 6: Optical Pumping Interaction Region

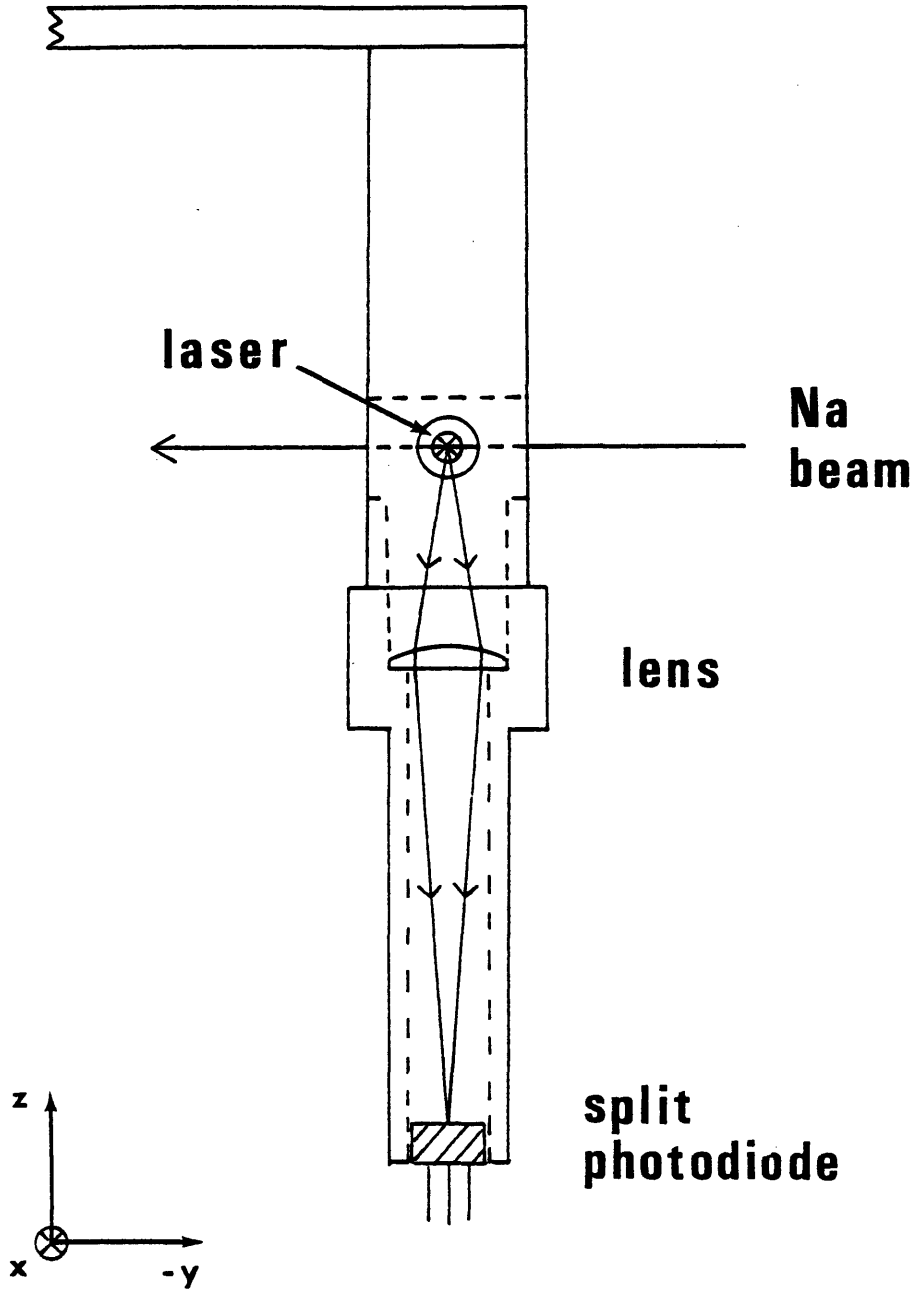

below.

The locking technique (JIT84, MCK85) utilizes the spatial dependence of the Doppler shift in an uncollimated atomic beam. As shown in Fig. 7, the laser intersects an atomic trajectory at a distance x from the axis which depends on the angle θ which this trajectory makes with the axis. The Doppler shift depends on θ: $\Delta_D = \vec{k} \cdot \vec{v} \approx kv\theta$ (for θ<<1), resulting in a spatial dependence of the resonant frequency. As the laser frequency is swept from red to blue, the point along the laser which is resonant travels in the direction of positive x. The unshifted resonance occurs exactly on axis. For a narrow velocity distribution and low laser power, the angular width of the resonance corresponds to the natural linewidth: $\Delta\theta = \frac{2\pi \cdot 10\ \text{MHz}}{k \cdot v} \approx \frac{10\ \text{MHz}}{1.7\ \text{GHz}} \approx 6 \times 10^{-3}$ rad where we have used $v \approx 10^5$ cm/sec and $k/2\pi = 1.7 \times 10^4\ \text{cm}^{-1}$. For our geometry (L~ 20 cm) this corresponds to a spot of diameter ~1 mm. This spot is spatially locked on axis by imaging it (with X2 magnification) onto a split photodiode (UDT PIN-Spot/2D) and using the difference signal to servo the laser frequency. The difference amplifier circuit is shown in Fig. 8 and a typical output signal is displayed in Fig. 9. The amplified difference signal is fed into the laser scan circuit (discussed in section III.A.7) in the same manner as the dispersion signal obtained from the sodium cell. The lock is very reliable: <±2 MHz drift over several hours.

Although the optical pumping process itself does not require a magnetic field, the slightest stray field will cause the aligned spins to precess and mix with other magnetic sublevels. Therefore, a small field (~ 4G) is applied along the direction of the laser in order to maintain the alignment. This field does not significantly lift the degeneracy of the various magnetic sublevels, allowing simultaneous pumping from all F=2 m_F levels.

The optical pumping must take place before the first collimating slit in order to avoid decollimation of the atomic beam by the momentum spread associated with deflection by the optical pumping laser. Thus, the atoms must maintain their alignment over a distance of ~ 1 m.

Figure 7

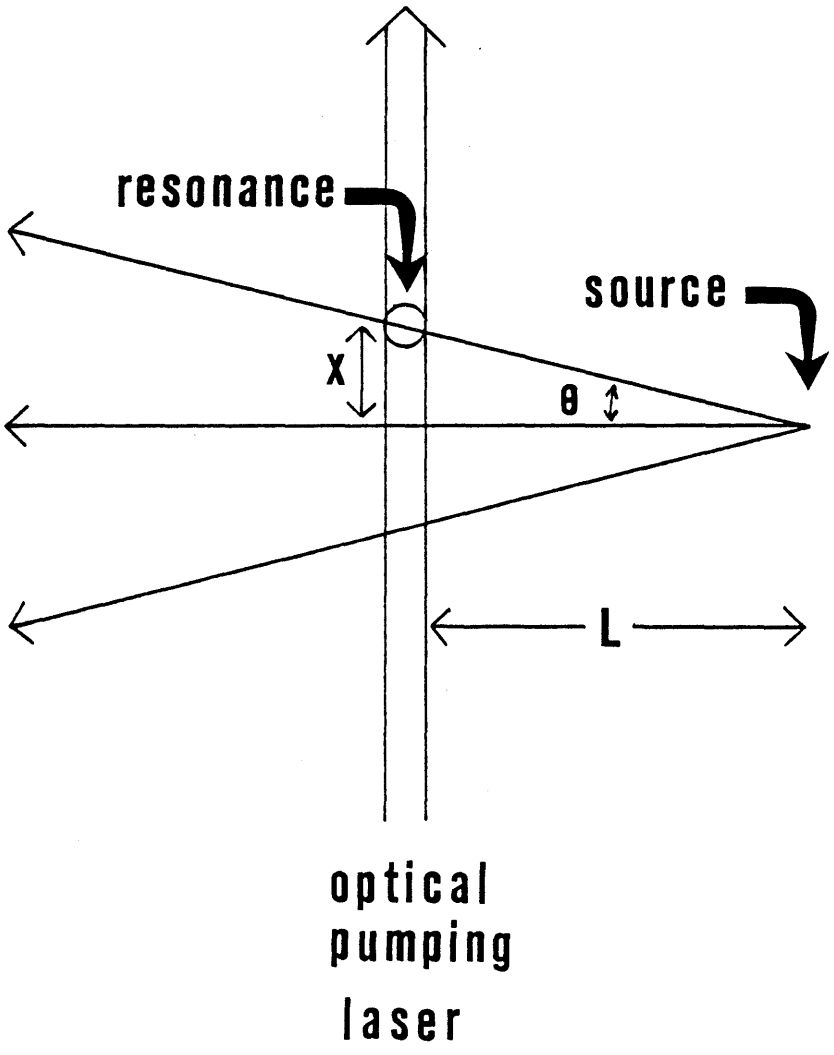

Figure 8

SPLIT PHOTODIODE AMPLIFIER

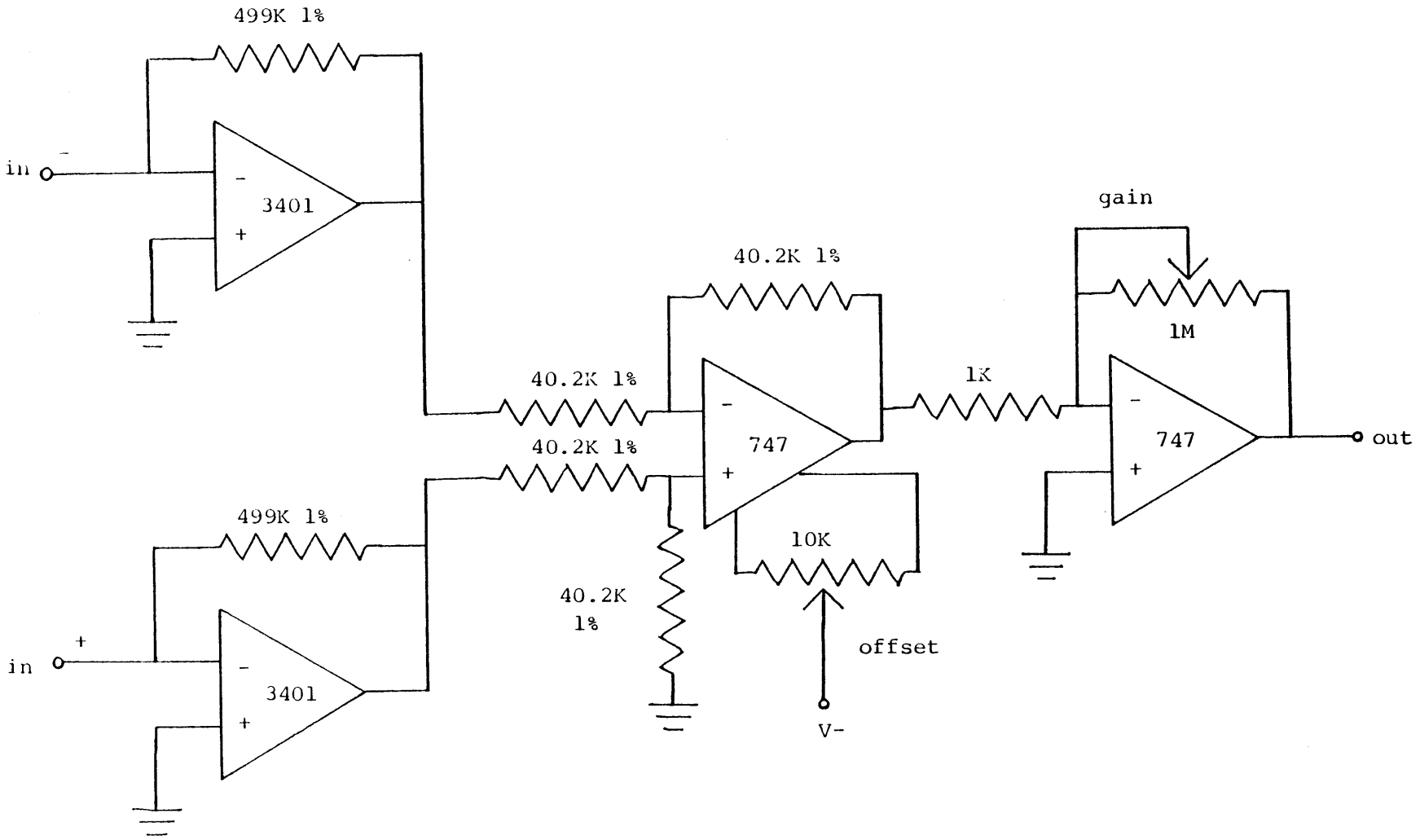

Figure 9

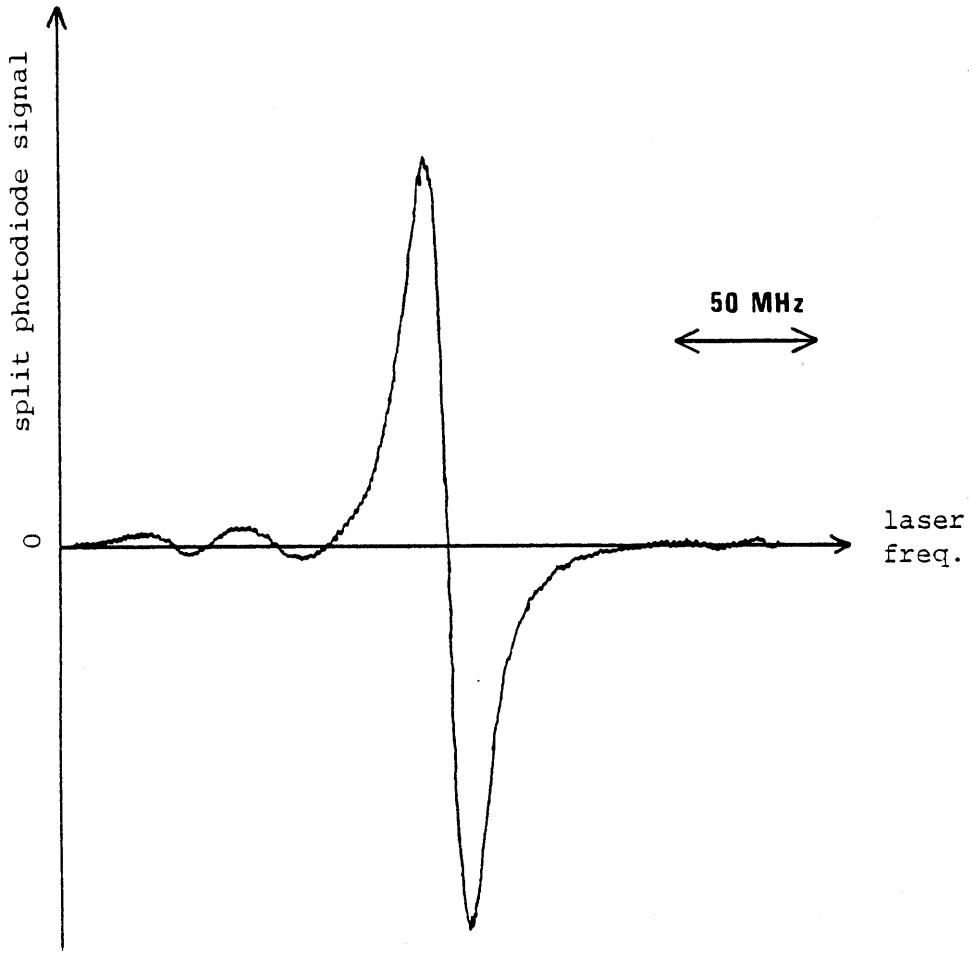

This is accomplished by providing a magnetic field between the optical pumping and interaction regions along which the spins remain aligned. For practical reasons, the field is slowly changed from being along x (i.e. along the laser) in the optical pumping region to being along y (i.e. along the atomic beam) between the two regions and then back to being along x in the interaction region. These field changes are all adiabatic as the rate of change of the field is very slow compared to the spin precession rate.

The magnetic fields are supplied by three orthogonal pairs of coils in the optical pumping and main interaction regions and by two long solenoids along the atomic beam path between the two collimating slits. All of the coils are outside of the vacuum chamber as is the larger solenoid. The smaller solenoid is wound on the extension tube which supports the first slit assembly. Unfortunately the optical pumping region does not sit at the center of its set of coils so the three field directions are not independently controlled, but this interdependence is known. The main interaction region is centered within its coils and an additional set of coils along x can supply ~ 40 G at 5 A, for diagnostic purposes. All of the coils and the larger solenoid supply roughly 2 G/A while the smaller solenoid yields ~ 15 G/A. The currents are supplied by 8 independent constant current supplies, an example of which is shown in Fig. 10. Fields are measured with a Hall probe and set to give $B_x \sim 4$ G, $B_y = B_z = 0$ in the optical pumping and interaction regions, and $B_y \sim 4$ G in the region between (somewhat larger inside the smaller solenoid). It is very important that the field never go to zero if spin flips are to be avoided. The minimum field occurs between the two solenoids, but at ~ 1 G, is still large enough to maintain alignment.

A more serious magnetic field problem arises when the slits are considered. Although nominally non-magnetic (302 stainless steel), they develop a permanent magnetization in their manufacture (they are laser machined). The resulting magnetic field is small (~ 1 G) but the gradients can be very large due to the small slit dimensions (10 μ wide x 13 μ thick). The quantity which is important in maintaining alignment is the characteristic time rate of change of the spin

Figure 10: Magnet Supply

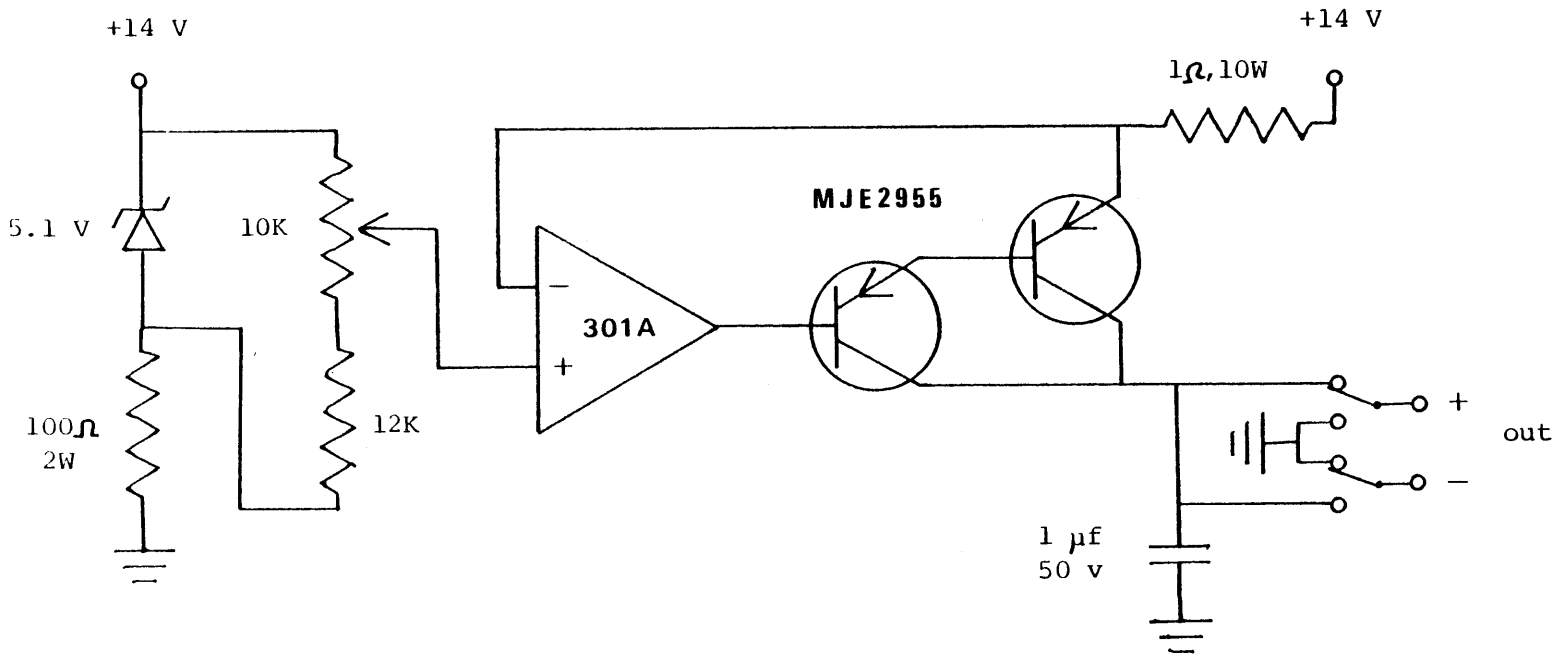

precession rate, $\frac{\dot{\omega}}{\omega} = \frac{\dot{B}}{B}$, relative to the splitting between adjacent magnetic sublevels, $\Delta\omega = \frac{\mu_o B}{2} \approx 2\pi \cdot 2.8\ MHz \approx 1.8x\,10^7\ s^{-1}$ for the F=2 ground state in a field of 4 G. If we assume the field changes by ~1G over a distance of $\sim 10\ \mu$, then $\frac{\dot{B}}{B} \approx 2.5x\,10^7\ s^{-1}$ for an atom traveling at 10^5 cm/sec (assuming an average field of ~4 G). Since $\frac{\dot{B}}{B} > \Delta\omega$, the passage will not be adiabatic and spin flips (so-called Majorana transitions) will likely occur. We have observed that this is indeed the case. We have been able to solve this problem, however, by heating the slits red-hot (while rigidly held between two flat-bottomed ceramic crucibles to prevent deformation) in order to eliminate the magnetization and maintain adiabaticity. Even with these measures, the atomic alignment is degraded somewhat upon passage through the slit; we see all but ~10% of F = 2 atoms in $m_F = 2$ with the slits in, compared to ~5% with the slits out.

5. Deflection Optics

The radiation field which deflects the atomic beam is generated by a Coherent 599-21 scanning single-mode standing-wave dye laser which is situated on an optical shelf attached to the main apparatus. Operating at the peak of the gain curve for R6G dye (sodium D_2 line: 589 nm), a typical output power of 100 mW is obtained with 2.5 W (all lines) of pump power, which is supplied by a Spectra Physics 166 argon ion laser located underneath the main apparatus. The specified linewidth of the dye laser is <1 MHz (rms).

The optical path for the deflecting laser beam is shown in Fig. 11. Beams are picked off from the two surfaces of an anti-reflection coated window (Oriel #4560-3) (~1% each) and sent to the spectrum analyzer and sodium reference cell (described in section (II.A.7)). The optical elements for the deflecting laser beam are mounted on sections of NRC MRL optical rail, including a section in the vacuum chamber which is mounted to the bottom flange of the six-way cross. The

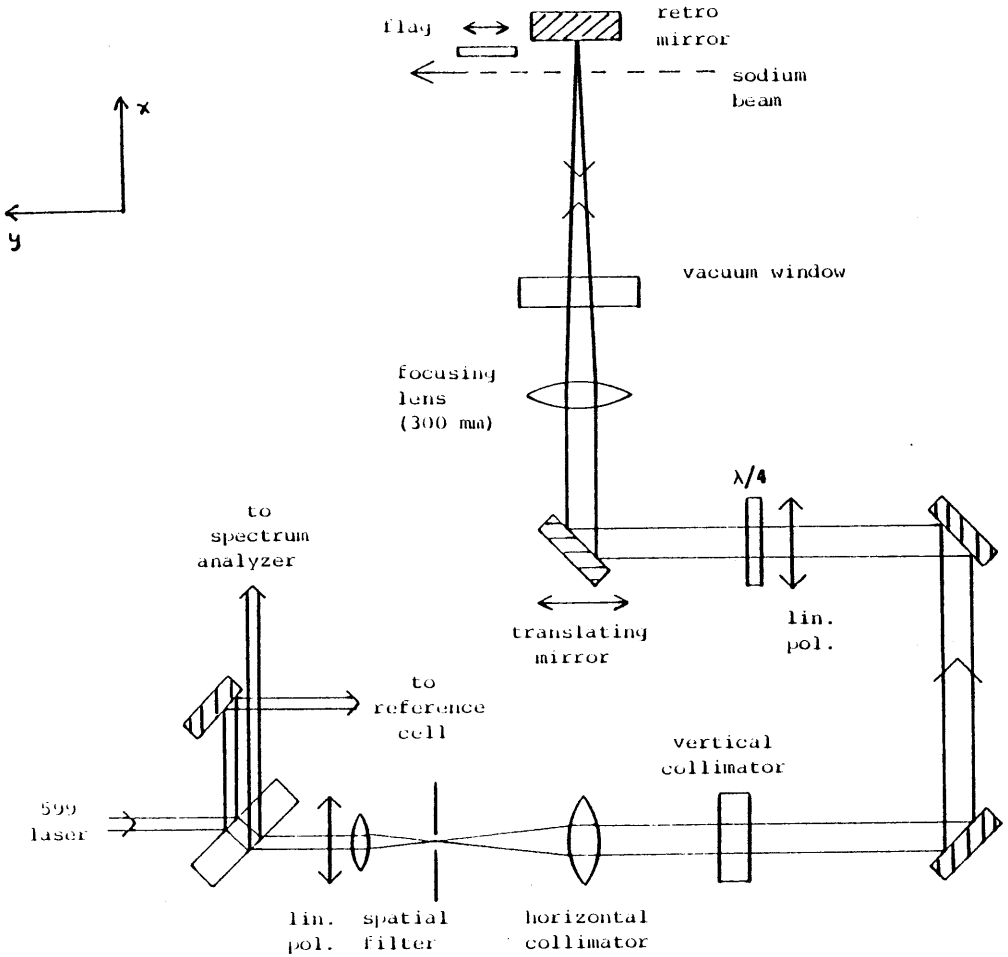

Figure 11: Deflection Optics

use of this rail greatly simplifies the arduous task of optical alignment.

The main portion of the laser beam is spatially filtered (NRC model 900 with 10X objective and 25 μ diameter pinhole) and recollimated. In order to make optimum use of our "ribbon" atomic beam, we use cylindrical optics which allow independent control of the focusing in the two orthogonal directions (horizontal = y = along the atomic beam, vertical = z). The spatially filtered beam is collimated with a pair of crossed cylindrical lenses whose focal lengths determine the major and minor axes of the elliptically collimated beam which results. The horizontal collimator, in conjunction with the final focusing lens, determines the horizontal waist in the interaction region (i.e. the interaction time), as will be discussed below. The vertical collimator determines the vertical extent of the beam in the interaction region and therefore the vertical uniformity and intensity. There is obviously a tradeoff in this regard. A larger vertical waist means a more uniform intensity over the 3 mm high atomic beam but also requires more laser power for a given intensity. As a compromise, we have chosen a 150 mm focal length lens (Melles Griot 01 LCP 166 078) which gives a collimated vertical waist ($\frac{1}{e^2}$ radius of intensity) of 3.6 mm and an intensity which is uniform to within 30% over the 3 mm atomic beam.

The waist in the interaction region is produced by focusing the collimated beam (in the horizontal direction) with a 300 mm focal length cylindrical lens (Melles Griot 01 LCP 137 078). For a collimated (i.e. large waist) Gaussian beam incident on a lens of focal length f, the waist ($\frac{1}{e^2}$ radius of intensity) at the focus is $\omega_o = \frac{f \cdot \lambda}{\pi \omega_H}$ where ω_H is the horizontal waist of the collimated beam (assuming that f is much smaller than the confocal parameter $b_H = \frac{\pi \omega_H^2}{\lambda}$ of the "collimated" beam). We have used two different horizontal collimators to produce two different interaction times: a 40 mm focal length lens (Melles Griot 01 LCP 128 078) and an 80 mm lens (Melles Griot 01 LCP 145 078). The beam parameters for each collimator are displayed in the table below:

collimator	$\omega_H(meas.)$	b_H	$\omega_o(calc.)$	$\omega_o(meas.)$	b_o
40 mm	1.03 mm	5.6 m	55 μ	70 μ	26.1 mm
80 mm	1.90 mm	19 m	27 μ	44 μ	10.3 mm

Here the confocal parameters are calculated from the measured values of the waists.

The beam profiles are measured with an EG&G RL128G Reticon. This is a linear diode array comprised of 128 elements, each 15 μ wide and spaced by 25 μ (center to center). A typical profile (recorded from an oscilloscope trace) is shown in Fig. 12.

Immediately preceding the 300 mm focusing lens, the beam makes a right angle bend by reflecting from a plane mirror at a 45° angle. This mirror is mounted on a translating stage (Daedal #3906) which moves perpendicular to the final direction of the laser beam in order to translate the collimated beam across the surface of the lens. For a translation d, this changes the input angle of the laser by $\theta = \frac{d}{f}$, while leaving the position of the focus fixed. This movement is calibrated in .001" intervals, allowing known angle changes in increments of $\sim 10^{-4}$ *rad.*

The 300 mm focusing lens is situated outside the vacuum for reasons of convenience. The converging beam passes into the vacuum through a $\frac{3}{8}$" thick anti-reflection coated window (CVI BBAR coating: $\sim$.4% per surface). Since we are using such a large f-number optical system (i.e. weakly converging), this window introduces minimal aberration.

The circular polarizer (i.e. linear polarizer followed by an Optics for Research #RZ-$\frac{1}{4}$ -589.6, zero-order quartz, anti-reflection coated $\lambda/4$ plate) should ideally be located as close to the interaction region as possible in order to minimize the polarization effects of dielectric mirrors and other optical elements. However, space limitations required its placement before the last turning mirror. Nevertheless, good circular polarization (>99%) could be obtained in the interaction region by nulling the retroreflected beam passing back through the circular polarizer. This

Figure 12: Laser Profile

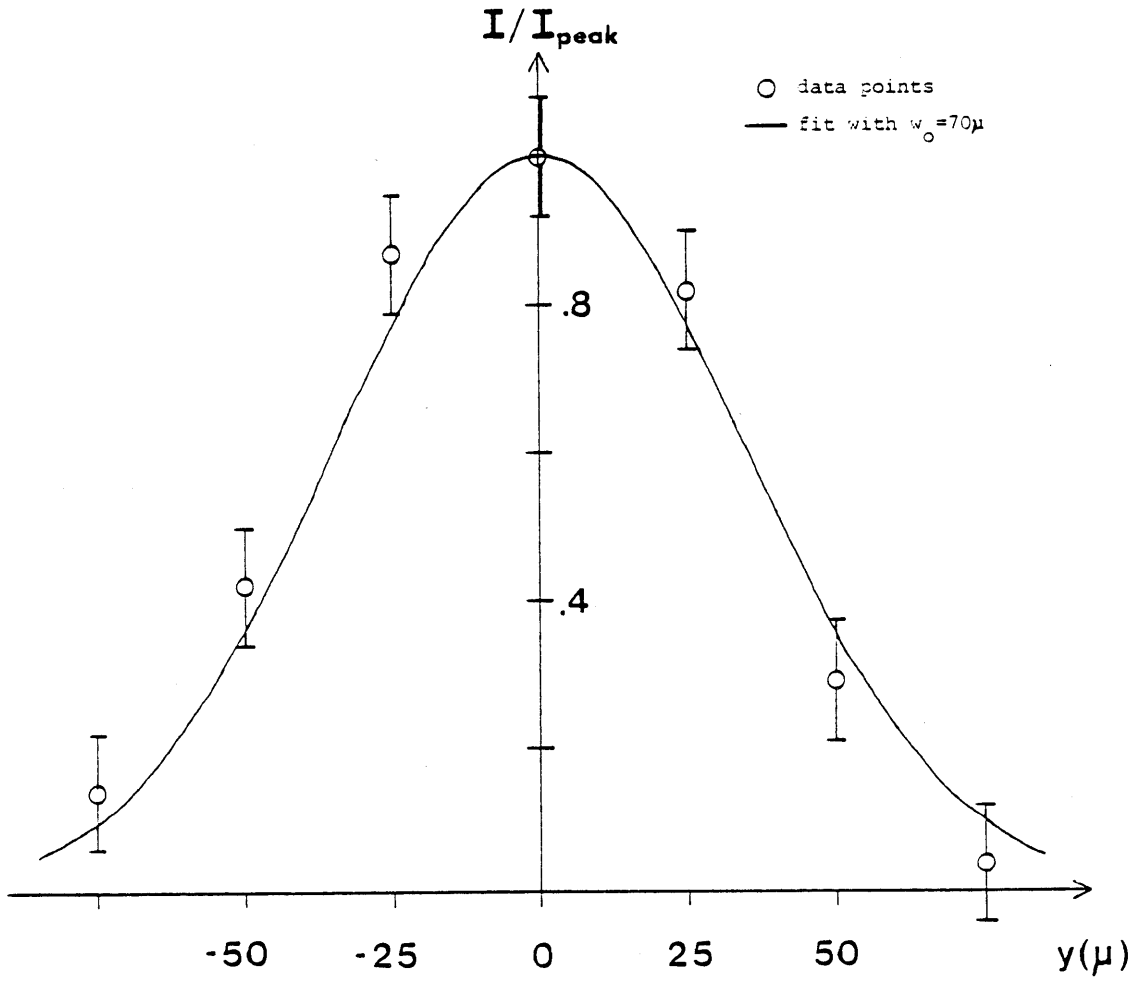

adjustment generally requires both rotation *and* tilt of the $\lambda/4$ plate.

The standing-wave is provided by placing the flat retro mirror (NRC 10D20 BD.1, $\lambda/20$, R>99%) at the focus of the 300 mm focusing lens. This is a type of "cat's-eye" retroreflector discussed in SNY75. A flat mirror (as opposed to a cylindrical reflector) was utilized for ease of alignment and because the larger focused waists we have used would require large radius mirrors situated relatively far from the interaction region, if we wished to image the waist exactly on the atomic beam. For interaction lengths less than $\sim 50\ \mu$ (i.e. ω_o<25 μ) the cylindrical reflector is the preferred solution. The atomic beam passes as close as possible to the mirror (<5 mm), compatible with the placement of a laser beam flag between the two (in order to be able to switch from a standing-wave to a traveling-wave without blocking the atomic beam). The flag is $\frac{1}{32}$" ($\sim$.8 mm) anodized brass which comes to rest flush against a protective ring which protrudes $\sim$.024" ($\sim$.6 mm) from the surface of the mirror. A ferrofluidic feedthrough on the bottom flange allows external control of the shaft which rotates the flag into position. Allowing room for the flag results in the atomic beam being slightly displaced from the focused waist (where the wavefronts are perfectly planar). At a distance x ($<<b_0$) from the waist ω_o, the radius of curvature of the wavefronts is (YAR76):

$$R(x) = x(1+\frac{b_o^2}{x^2}) \approx \frac{b_o^2}{x}$$

Referring to Fig. 13, we see that in traversing the beam (distance = $2\omega_o$), the atom deviates from the curved wavefront by:

$$\Delta \approx \frac{\omega_o^2}{2R} \approx \frac{1}{2\pi} \cdot \frac{x}{b_o} \cdot \lambda$$

If we pick x=5 mm (worst case), this quantity is $\sim\frac{\lambda}{33}$ for the 40 mm collimator and $\sim\frac{\lambda}{13}$ for the

Figure 13: Wavefront Curvature

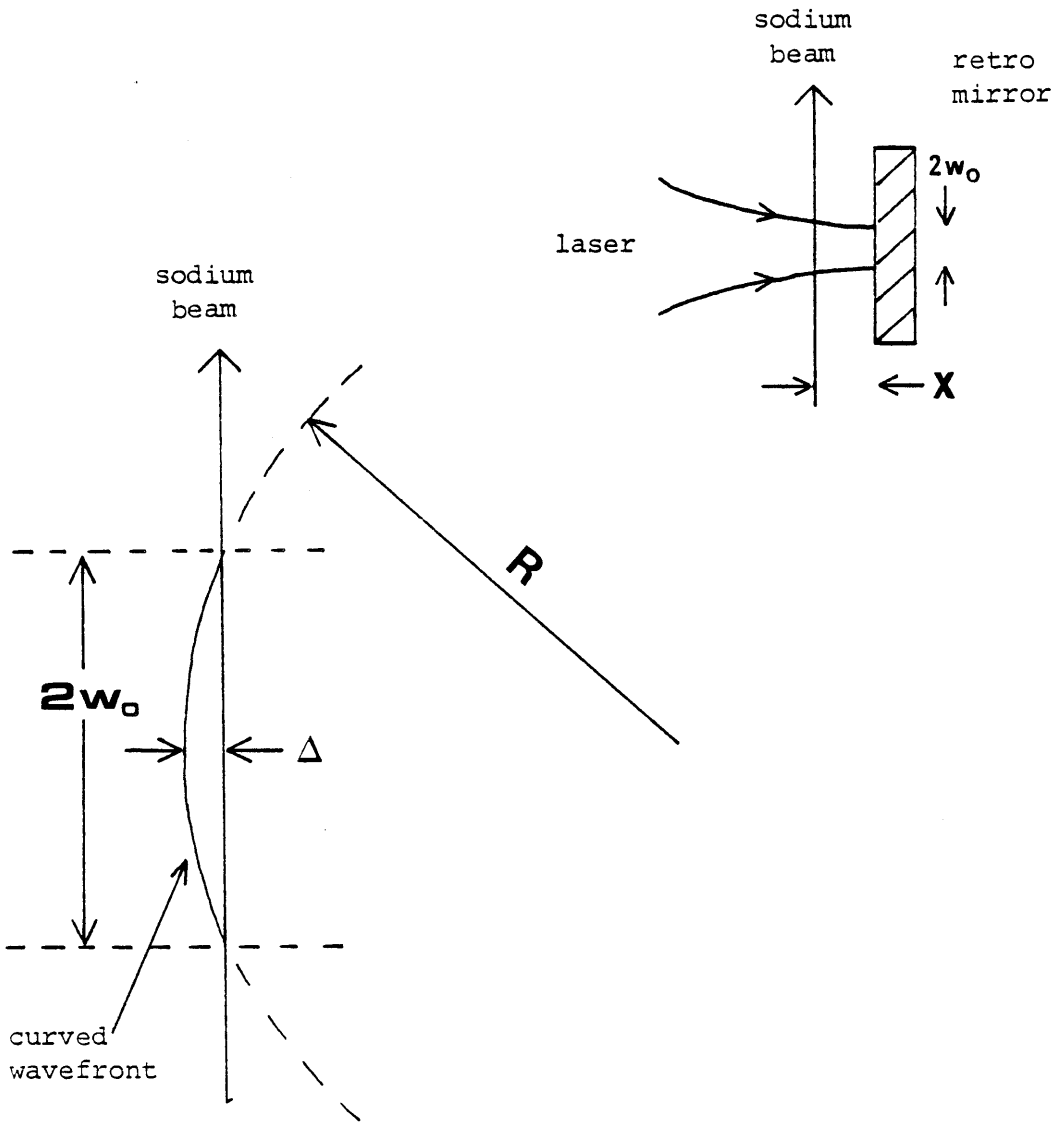

80 mm collimator. So for a given trajectory, the atom does not sample a wide range of intensities (recall that the intensity has a periodicity of $\lambda/2$).

The alignment of the standing wave and its orientation relative to the atomic beam are of critical importance. They can be adjusted somewhat independently with our optical system. The alignment (i.e. overlap) of the incident and retro beams is guaranteed if the corresponding spots are overlapped on the final (300 mm) lens. For a misalignment of 1 mm at this lens, the standing-wave overlap mismatch $\sim 17\ \mu$ at the atomic beam (assuming a distance of 5 mm from the mirror). This coincidence (on the 300 mm lens) of the spots from the incident and retro beams is a good measure of the orthogonality between the mirror and laser beams. If the two spots are offset by a waist radius (ω_B), the mirror is non-parallel to the incident plane wavefronts by an amount λ/π over the focussed waist diameter $2\omega_o$).

The most crucial alignment is that of parallelism between the mirror and the atomic beam. Theoretical calculations require the atom to move much less than an optical wavelength perpendicular to the standing wavefronts while traversing the waist. This places a stringent requirement on the angle of the retro mirror. For a laser diameter of $2\omega_o \approx 100\ \mu$, we require the alignment to be better than $3\text{x}10^{-4}$ rad in order to keep $\Delta x < \frac{\lambda}{20}$. (Recall that the relevant periodicity is that of the intensity: $\frac{\lambda}{2}$). We note that as long as the mirror is parallel to the atomic beam, the standing wavefronts are parallel to the beam. Misalignment of incident and reflected beams simply Doppler shifts both laser beams equally, and reduces the region of standing-wave due to imperfect overlap.

The high resolution mechanical/PZT mirror mount shown in Fig. 14 is used to adjust the parallelism between the standing-wave mirror and the atomic beam. This design utilizes an 80 tpi screw on a 1" lever arm for a "mechanical" resolution of $1.25\text{x}10^{-2}$ rad/turn ($2.5\text{x}10^{-4}$ rad if the fractional turn resolution is $\frac{1}{50}$) and a Jodon SD-20 PZT (4 μ excursion for 2 kV) on a .25" lever

Figure 14: Mirror Mount

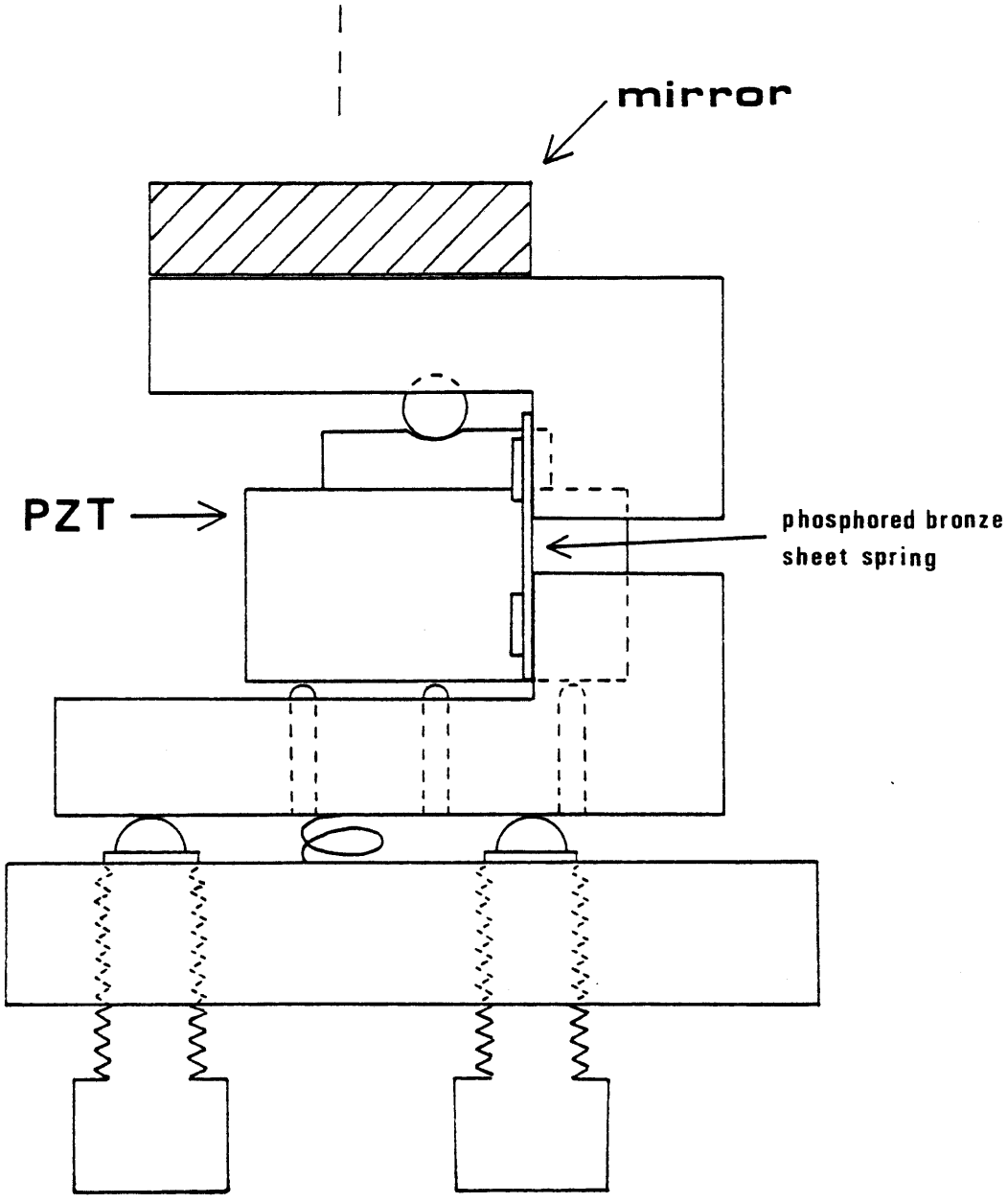

arm for an "electrical" resolution of 3.5×10^{-7} rad/V. The mechanical motion is controlled externally by $\frac{1}{4}$" shafts which feed through ultratorr fittings and are held firmly by a mounted ball bearing. The shafts are coupled to the adjustment screws by a sliding slot arrangement to provide independent wobble-free rotation. The PZT high voltage is supplied by a Bertran PMT-20A/P (Option 3) 2kV supply.

6. Fluorescence Collection

The radiation emitted in the interaction region is a very useful diagnostic for determining parameters of the laser/atomic beam interaction. We have found it most useful for : 1) obtaining perpendicular alignment of the laser and atomic beams; 2) determining the exact atomic resonance; 3) investigating the efficiency of the optical pumping process; and 4) measuring relative atomic flux when optimizing source parameters. We note that this fluorescence would also be of use in determining: 1) the laser waist (if the transit time is short enough to give rise to transients and/or transit time broadening); 2) the absolute laser intensity (by measuring the saturation and/or power broadened line width); and 3) the atomic velocity distribution (using the Doppler shift). The main problem with the current setup is the inability to see the fluorescence when actually doing the experiment. This is due to the low signal level when both collimating slits are in place and the large amount of scattered light present when operating at relatively high power levels.

The fluorescence is collected by the optical tower assembly shown in Fig. 15. A Sears f/1.4 camera lens (f=55 mm) forms an image of the interaction region which in turn is imaged onto the PMT photocathode by a second lens (f=63.5 mm). The use of two lenses allows placement of a baffle in the first image plane to reduce scattered light. In fact, a series of converging and diverging baffles limits the field of view seen by the PMT to a spot ~ 1 mm in diameter and a depth of field of $\sim \pm 3$ mm. The PMT (RCA C31034A) is situated in a cooled (-20 C) and shielded housing (Products for Research #TE-104-RF), resulting in dark counts of ~20 Hz. The

Figure 15: Optical Tower

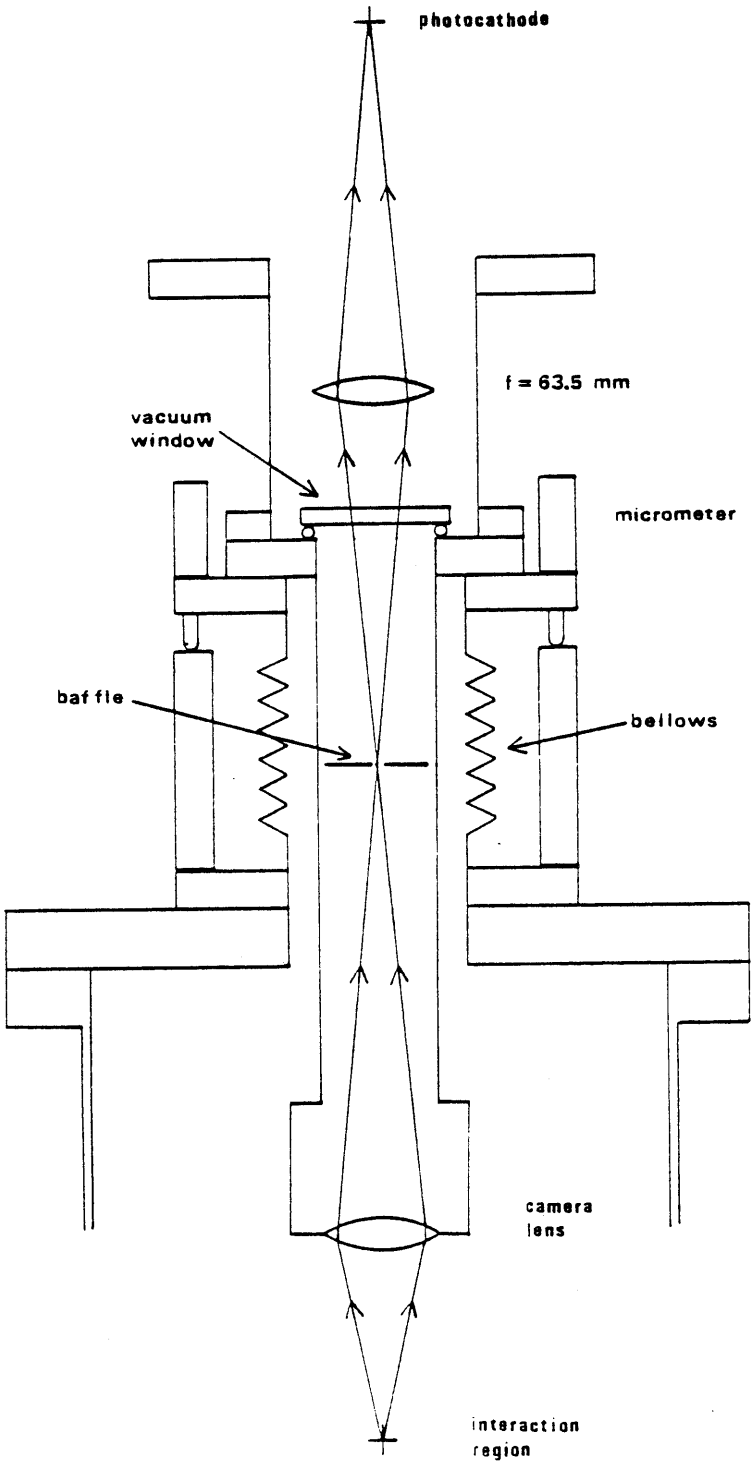

optical tower and PMT are mounted on a spring loaded bellows assembly to allow optimum imaging of the interaction region. The movement is provided by three micrometers equally spaced around the perimeter. A micrometer translation of .001" moves the imaged spot by $\sim 70\ \mu$. The whole assembly can be translated vertically (for focusing) by using all three micrometers.

The overall efficiency of collection is determined by the subtended solid angle ($\sim 1\%$), reflection losses ($\sim 50\%$), and quantum efficiency ($\sim 20\%$) to be about 10^{-3}, assuming optimum alignment.

Scattered light is minimized by eliminating any reflective surfaces from the field of view of the PMT. Most elements of the interaction are either anodized or covered with an anodized shield. The retro mirror is hidden by a baffle on top of the mirror mount which eliminates half of the viewing angle, but the resulting reduction of scattered light is well worth the sacrifice of signal. A $\frac{1}{4}$" high slot just inside the vacuum window serves to eliminate scattered light from the window and reduce the effect of the room lights. The laser beam flag is blackened with soot and partially hidden by a baffle but still gives a fairly large background when obscuring the mirror. The close proximity of the mirror and flag to the interaction region is a definite disadvantage of the flat retroreflector in terms of scattered light.

The PMT is operated at -1.5 kV in pulse counting mode. The pulses are fed to a Mechtronics 511 amplifier/discriminator and then to a pulse-to-voltage converter for display on an x-y recorder.

7. Sodium Reference Cell

We utilize the saturated absorption spectrum in a sodium cell as both a frequency reference and as a means for actively locking a laser to a particular resonance. The cell can serve both lasers simultaneously by using separate optical paths as shown in Fig. 16.

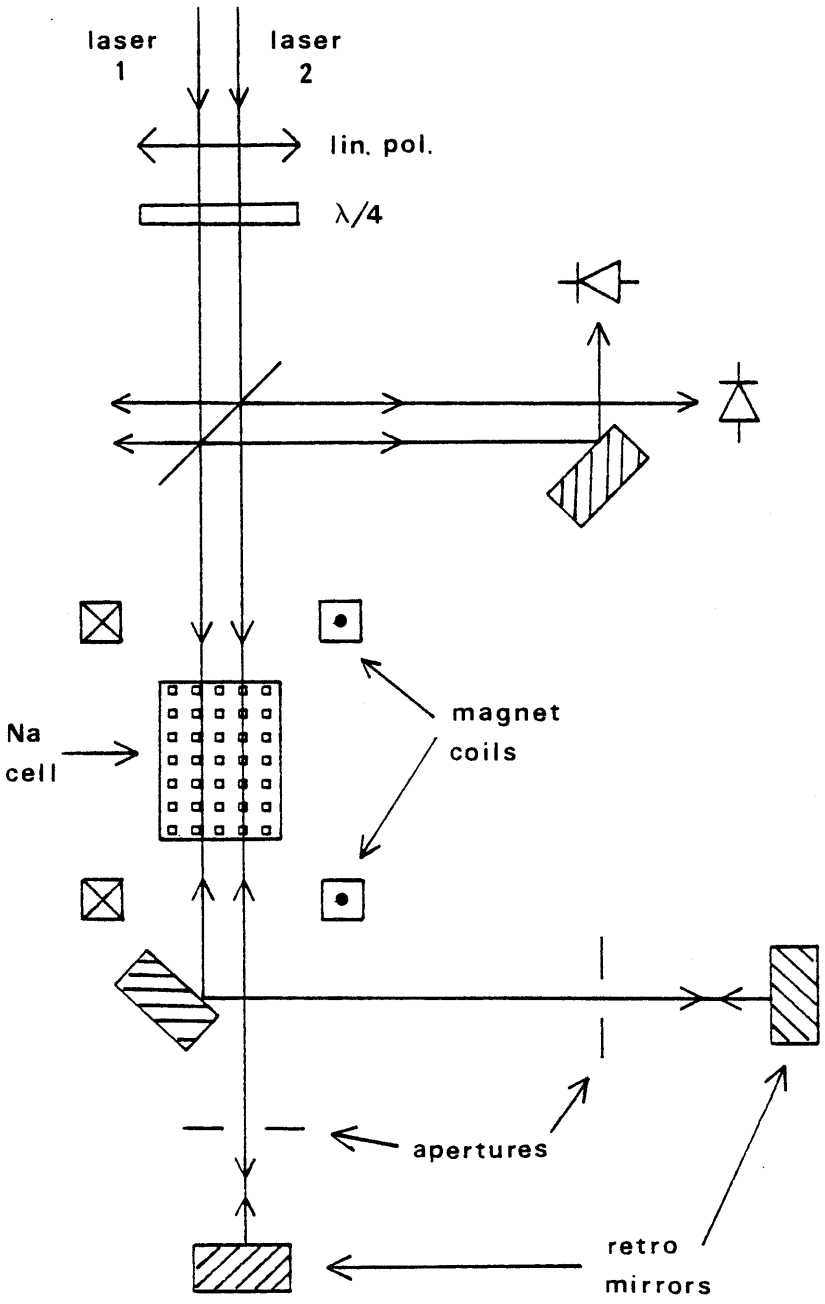

Figure 16: Reference Cell

The cell itself uses a two part design with independent heaters on the reservoir and cell (windows) sections which determine the density and temperature of the vapor, respectively. The reservoir heater requires ~ 13 W to maintain a temperature of ~ 165 *C* (sodium density $\sim 4\text{x}10^{11}$ cm^{-3}) and the cell heater reaches a temperature of ~ 205 *C* (hotter than the reservoir to keep the windows clean) with ~ 23 *W*. Temperatures are monitored with Fenwal GA52P2 thermistors.

Each circularly polarized laser beam is retroreflected to produce a standing wave within the cell. The incident and reflected beams constitute the pump and probe beams, respectively. Probe absorption is measured with a photodiode. The saturated absorption spectrum, consisting of various Lamb-dip and crossover resonances, is easily seen by simply tuning the laser. In order to increase the signal and to obtain electrical signals suitable for frequency stabilization feedback, we modulate the atomic transition frequencies (via the Zeeman shift) with an applied magnetic field, and use phase sensitive detection to yield a derivative curve. This technique has the important advantage that the laser frequency itself is not modulated.

A pair of coils provides the necessary field along the direction of laser propagation (~ 18 G/A). The coils are driven by the circuit shown in Fig. 17 which allows independent control of the DC and AC fields. At a modulation frequency of 200 Hz, the coils (in parallel) have resistive and inductive impedances of $\sim 2\ \Omega$ and $\sim .6\ \Omega$, respectively. Since the transition between the stretched states: $3S_{1/2}$,F=2,m_F=2 $\rightarrow$ $3P_{3/2}$,F'=3,m_F'=3 has a Zeeman shift of 1.4 MHz/G, a peak-to-peak current dither of $\sim .4$ A (peak-to-peak voltage of ~ 1 V)will modulate the resonant frequency by ~ 10 MHz, the natural line width. A DC field of ~ 10 G (~ 1 V across coils) seems to yield the best signals.

The shape of the saturated absorption spectrum is not easily predicted and depends strongly on magnetic field and polarization because of optical pumping effects (PAL79, FBK80, WSP81). Nevertheless, a resonance can usually be identified and its frequency (zero-crossing when using

Figure 17: Magnet Coil Driver

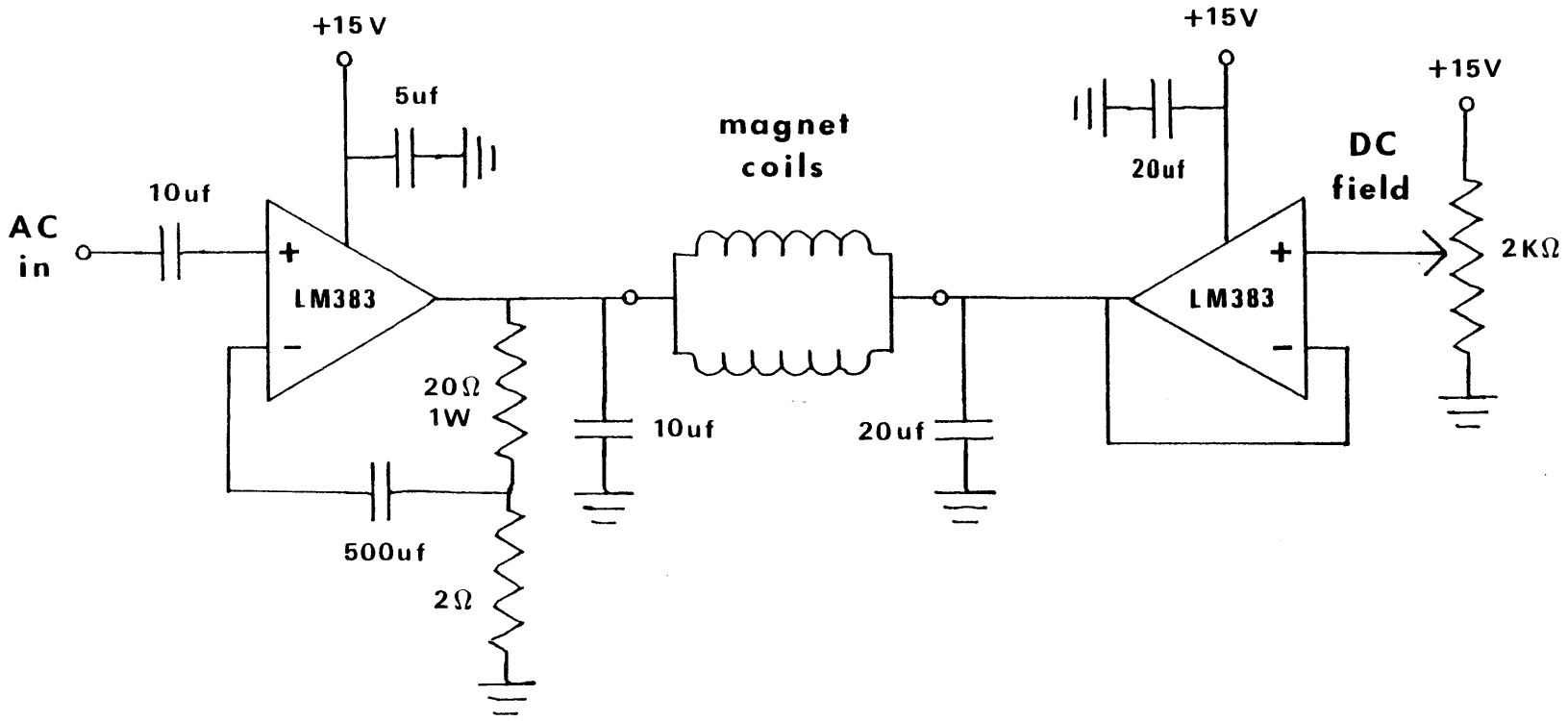

phase sensitive detection) can be shifted (by changing the magnetic field, polarization, or modulation phase) to coincide with the resonance observed in the optical pumping region or main interaction region. An example of a saturated absorption spectrum used in this way is shown in Fig. 18. We note here that good spectra are obtained for incident laser powers of only ~ 1 mW (estimated intensities of ~ 10 mW/cm^2) because of a reduction of the effective saturation intensity by optical pumping effects (FBK80).

The demodulated derivative curves are obtained with either a PAR 128A lock-in amplifier or a combination of Evans modules: phase sensitive detector (#4110) and phase control unit (#4114). If desired, the laser can be locked to the resonance (zero-crossing) using the circuit shown in Fig. 19 resulting in long term drifts of <2 MHz. We note that this is the same circuit used to lock the optical pumping laser with the difference signal from the split photodiode (Section II.A.4). Also, this circuit is used for calibrated manual adjustment of the laser frequency when the servo loop is open.

Figure 18

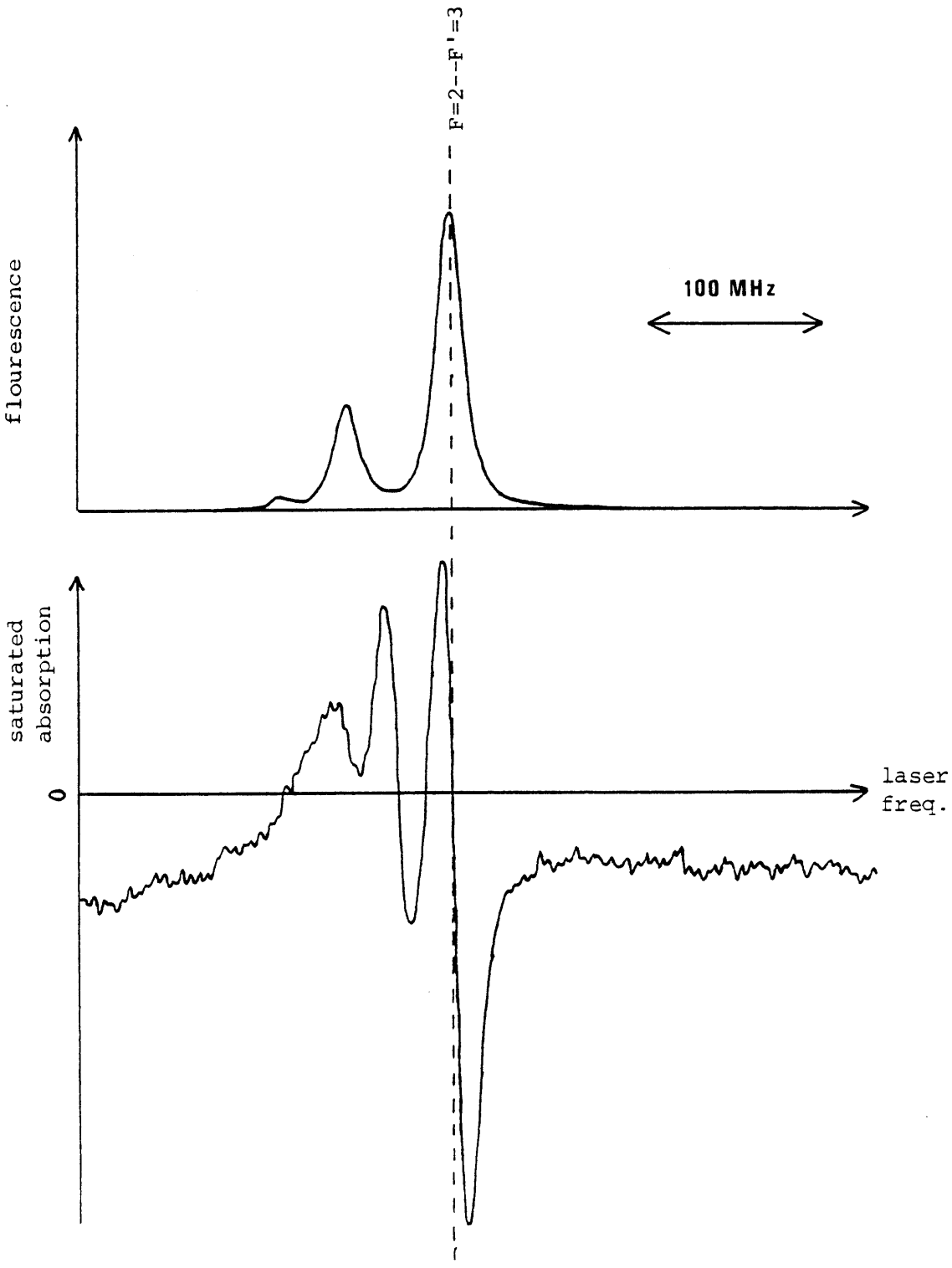
F=2--F'=3
flourescence
100 MHz
saturated
absorption
0
laser
freq.

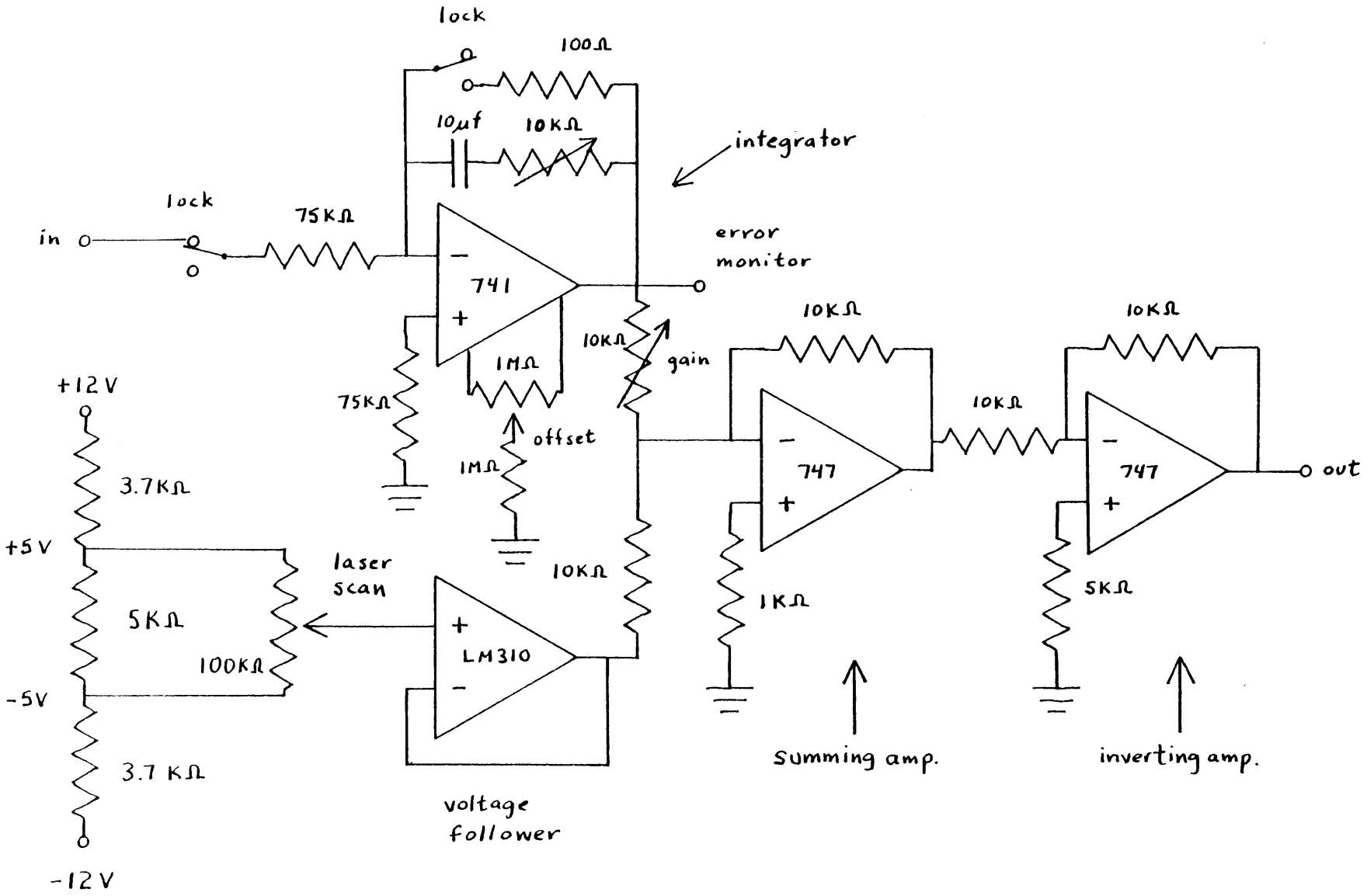

Figure 19: Laser Lock/Scan Circuit

II.B. Operating Procedure

In this section we will describe the general operating procedure for the experiments. In order, we will discuss: 1) sodium source operation, 2) alignment of the atomic beam; 3) optimization of the optical pumping, and 4) alignment of the standing-wave in the interaction region.

1. *Source Operation*

The atomic sodium source requires a great deal of patience in its operation - the warm-up time is typically 4 hours. Similar patience is required in cooling down the source after a run. Attempts to reduce this time are, for the most part, unsuccessful, resulting in clogs of the gas line and/or nozzle.

Typical operating conditions for the source are shown in the table below:

	Nozzle	*Transfer Tube*	*Reservoir*	*Swage Tee (Elbow)*
Current	1.0A	2.0A	1.5A	3.2A
Temperature	660 C	620 C	550 C	570 C

These temperatures are reached by increasing the current in steps of $\sim .25$ A every ~ 30 min. The nozzle should be at ~ 500 C before turning on the other heaters and the reservoir should not be turned on until the transfer tube and swage tee are at $\sim 500\ C$.

The argon carrier gas must be flowing anytime the source is being heated. With the stagnation pressure at 20 psig, typical nozzle throughput is ~ 1 torr $\cdot\ l/s$ with the nozzle cold (25° C) and $\sim .6$ torr $\cdot\ l/s$ with the nozzle at operating temperature. Close monitoring of this flow is essential in preventing clogs. The skimmer must be heated ($\sim 350\ C$ with $\sim 3\ A$) during source operation in order to prevent clogging of its orifice.

During source warm-up, the sodium beam is monitored with the first hot wire detector (HWD#1), where a signal of ~ 30 nA is usually an indication of adequate atomic beam flux. This detector allows optimization of the relative position of the nozzle and skimmer, which is initially set (with the vacuum system at atmospheric pressure) by listening to the rush of argon through the skimmer.

2. *Atomic Beam Alignment*

Alignment of the atomic beam is done in two stages. The first stage is a relatively crude alignment done with the first vacuum system at atmospheric pressure and the detector chamber under vacuum. The second vacuum system (main chamber) may be vented or under vacuum. With the skimmer removed and the detector filament current increased to 50 mA (to make it more visible) a telescope (with cross-hairs) is aligned with the filament and the hole in the source chamber adapter (bulkhead) flange. This line of sight defines the atomic beam axis. The $\frac{3}{16}$" diameter holes (adjacent to the two slits) are then aligned to lie on this axis. The slits are translated into place and their rotation is adjusted for parallelism with the filament (using the rotatable cross-hairs). The last step consists of replacing the skimmer such that it lies exactly on axis.

The second stage of alignment must be done with the atomic beam itself. Fortunately, the alignment obtained with the apparatus vented is maintained upon evacuation, so that only minor "tweaking" is usually required. With the source up to operating temperature (as indicated by the first hot wire detector), the slide valve between the second differential pumping chamber and the main chamber is opened, allowing the sodium beam into the main chamber. With the $\frac{3}{16}$" diameter "collimators" in place, a signal should be present at the second hot wire detector. With the interaction region laser at low power, the fluorescence signal can be seen with the PMT and

optimized by adjusting the optical tower. Obviously, fluorescence measurements are easier with the $\frac{3}{16}$" diameter holes than with the 10 μ slits in place. So, at this point (i.e. before final atomic beam alignment), the optical pumping process is optimized (procedure described in Section II.B.3) and the first stage of alignment of the interaction region optics is carried out (described in Section II.B.4). With these tasks accomplished, the alignment of the atomic beam with the main detector can be completed.

It is important that the detector chamber be cold trapped before the slide valve connecting it to the main chamber is opened. Also, the second slit must be in place to prevent an excessively large signal from reaching the detector. With these measures, exposure of the detector to the beam (i.e. removal of beam flag mounted on the second hot wire detector) should result in a reasonable signal (e.g. 10^4 cts/s, depending on alignment). At this point the ion accelerating voltages are optimized (adjustment of the back plate voltage usually suffices). The detector is then scanned to find the center of the relatively broad (e.g. 500 μ beam profile, where a signal of $\sim 5 \times 10^5$ cts/s should be present. Translation of the first slit into place (optimum position determined by maximum signal with slit #2 and detector fixed) results in a reduction of this signal by a factor of ~ 3 and a substantial decrease in the width of the beam profile.

Rotation of slit #2 is necessary to obtain the narrowest profile (and largest peak signal). Unfortunately, the rotation is accompanied by a small translation, preventing optimization with the detector fixed. The profile must be scanned after each rotation adjustment until the minimum width ($\sim$ 3 steps = 30 μ FWHM) is obtained. Obviously all of the above adjustments must be made with the lasers off. However, final location of the center of the atomic beam profile must be done with the optical pumping laser on and slit #1 translated to compensate for the deflection due to the optical pumping. With attainment of final alignment, collection of deflection data (with the computer) may commence.

3. *Optimization of Optical Pumping*

The optical pumping process is described in detail in Section II.C.1. In the present section we will simply outline the operational procedure for its optimization.

The optical pumping laser is brought over to the experiment via the optical fiber. Stability of the optical pumping relies on optimum coupling into the fiber. The main problem is alignment of the incident laser polarization with the axis of the fiber. Optimum power transmission is relatively independent of this alignment but the output polarization depends critically on it. Misalignment results in large (but relatively slow) variations in the output polarization (seen as variations in power transmitted through a linear polarizer), so optimum rotation of the input end of the fiber is obtained by minimizing these variations. The output end of the fiber is rotated to yield a vertical linear polarization.

The other problem in fiber coupling is the actual mode-matching of the focused beam to the fiber core. This requires very delicate mechanical adjustments but is relatively straightforward with the NRC F-916T precision fiber coupler. Care must be taken to avoid normal incidence reflection from the face of the fiber which can couple back into the laser cavity and disrupt its single-mode operation.

The alignment of the OP (optical pumping) beam with respect to the atomic beam is set by centering it on the hole in the 5-way cross and on the small rear (anti-reflection coated) window. Although the laser lock point shifts by ~ 1.7 MHz/mrad for non-orthogonal alignment, the spatial center of the atomic beam is always in resonance, so this alignment is not critical. However, reasonable alignment ($\sim 10^{-2}$ rad) of the laser beam with the magnetic field is desirable to preserve the $\Delta m = +1$ selection rule for the circularly polarized light.

The polarization of the OP beam is set by temporarily placing a mirror inside the vacuum chamber and reflecting the beam back through the $\lambda/4$ plate and linear polarizer. This combination

acts as an optical isolator, so that good circular polarization is achieved by nulling the retro beam coming back through the linear polarizer. This is done with the apparatus under rough vacuum and the window heater at its usual operating temperature. However, this usually has to be optimized by looking at the optical pumping process itself. The polarization in the interaction region is checked in a similar manner, except that the retro mirror is always present to allow continuous monitoring. We note that this polarization must be readjusted when the laser is switched between the D_1 and D_2 lines.

The OP laser power is measured with a lab built power meter (MOS84). The best results are obtained using ~ 1.5 mW in a ~ 3 mm diameter beam (FWHM) which gives an average intensity of ~ 15 mW/cm^2, slightly in excess of the saturation intensity for the F=2, m_F=2 $\rightarrow$ F'=3, m_F'=3 transition (12.7 mW/cm^2). The use of higher power results in loss to the F=1 ground state via the power broadened F=2 $\rightarrow$ F'=2 transition.

The OP interaction time (3 μsec) results in ~ 70 cycles between the ground and excited state for the nearly saturated transition. This fairly long interaction time may not significantly increase the fraction of F=2 atoms in m_F=+2 (in fact, it may actually increase the loss to F=1 if the polarization is imperfect), but it does provide more deflection for these atoms and prevents a larger fraction of the non-interacting F = 1 atoms from reaching the interaction region (see Section II.C.2).

The magnetic fields in both the OP region and the interaction region are checked with a Hall probe before evacuation of the apparatus. By varying the various field components and noting the changes in the optical pumping signals, it is verified that the field values set in this manner are indeed close to optimum.

The effectiveness of the optical pumping (i.e. the population distribution of the various magnetic sublevels) is measured by monitoring the fluorescence in the interaction region as the

interaction region laser (599) is scanned. As discussed in Section II.C.1, this can be done on either the D_1 or D_2 line. The D_1 line is a more sensitive probe, although both provide useful information. The fluorescence allows us to infer the ground state sublevel populations from measurements of the various transitions between hyperfine states. Care must be taken, of course, to keep the probe laser power low enough to avoid altering the population.

The goal is to transfer all of the F=2 ground state population into m_F=+2. If this is done completely, we would expect to see a single (enhanced) peak replace the three excited state hyperfine peaks which originate from the F=2 ground state of the D_2 line. Using the D_1 line, perfect optical pumping would manifest itself in a null signal for the F=2 ground state, due to the Δm=+1 selection rule. Care must be taken to examine transitions from the F=1 ground state concurrently to ensure that atoms originally in F=2 are not lost to F=1 in the optical pumping process. These points are discussed in more detail in Section II.C.1.

Optical pumping optimization is best performed with the slits out, due to the higher signal levels. However, the efficiency of the process must also be checked with the slits in place. This usually requires a standing-wave probe, as the scattered light from the laser beam flag would contribute a relatively large background signal. Unfortunately, the effects of each slit must be examined separately, as the fluorescent signal level with both slits in place is too low to be of use. It is therefore assumed that the effects of each slit on the optical orientation are independent. As noted in section II.A.4, the effect of the slits is disastrous if they are not demagnetized.

Figures 2, 3, and 4 in Section II.C.1 are examples of the use of the fluorescence in the interaction region to infer the ground state sublevel populations. Using the formulas of Section II.C.1 (based on matrix elements for the various transitions), the various ground state sublevel populations can be estimated. The data shown here are optimized with regard to parameters discussed above. The deleterious effect of the slits is seen in comparing Figs. 2a and 4.

4. *Deflection Optics Alignment*

The alignment and characterization of the standing-wave interaction are the most crucial elements in obtaining and understanding the deflection data. The details of the optical system used are discussed in Section II.A.5. There are basically three stages of alignment: 1) visual alignment done with the apparatus up to air, 2) alignment using the interaction region fluorescence, and 3) final adjustments based on the deflection profiles themselves. These will be discussed in order.

The first step in the visual alignment is to adjust the spatial filter and two cylindrical collimating lenses to obtain a properly directed and collimated beam. Vertically, this beam is adjusted to be parallel to the optical table and to have its center coincide with the center of the atomic beam. Horizontally, the beam is aligned with the center of the optical rail. Collimation is achieved by projecting the beam onto a distant (eg. ~ 5 meters) wall and adjusting the lenses until the beam no longer converges or diverges. The bending mirrors are then positioned to maintain the proper beam directionality (paying special attention to the vertical height and parallelism). The final bending mirror (mounted on a translating stage) is centered in its travel and adjusted to center the beam on the 300 mm focusing lens. This lens is oriented to ensure that the converging beam is centered on the internal optical rail (i.e. is perpendicular to the atomic beam axis), and is positioned 300 mm from the standing-wave retro mirror. This position is adjusted to recollimate the retro beam after passing back through this lens (again by projecting the beam onto a distant wall). At this point the standing-wave mirror is simply adjusted to overlap the incident and retroreflected beams. The $\lambda/4$ plate is set to extinguish this retro and the handedness of the circular polarization is checked to coincide with that of the OP laser.

Alignment of the optical tower is accomplished with a "grain of wheat" light bulb located at the intersection of the laser and atomic beams (inferred from the position of slit #2). With the PMT removed, the bulb is imaged at the position of the photocathode, using the three adjustment

micrometers. If this alignment is done carefully, only small adjustments are required for optimum signal from the atomic beam.

The second stage of optical alignment utilizes the atomic beam fluorescence and is carried out before the optical pumping is implemented (as the optical pumping diagnostics require a reasonably well-aligned standing-wave). The retro mirror is adjusted to superimpose the fluorescent peaks from the incident and retro beams. Overlap of these peaks is an indication of parallelism of the mirror and the atomic beam and is independent of the angle between the incident laser beam and the atomic beam. An example of this overlap is shown in Fig. 1. If the two peaks coincide to within 10 MHz (the natural linewidth), a parallelism of 3×10^{-3} rad is obtained. This is about a factor of 10 greater than the desired (according to Section II.A.5) parallelism, requiring final alignment to be done in conjunction with the deflection profiles themselves.

We note here that the observed fluorescent linewidths always seem well in excess of the 10 MHz natural linewidth. Possible contributions to this width are: 1) Doppler width: ~ 2 MHz if PMT field of is ~ 1 mm diameter (with $\frac{3}{16}$" diameter hole in place); 2) distribution of Zeeman shifts for various transitions: ~ 4 MHz at 4 G, for $\Delta m = +1$ transitions within the F=2 $\rightarrow$ F'=3 transition; and 3) laser linewidth: specified to be ~ 1 MHz. Of course, power broadening contributes at higher power levels.

The fluorescence is also useful for checking the vertical alignment of the laser and the atomic beam. The signal should be maximized when the vertical centers of the laser beam (peak intensity) and atomic beam coincide, if the entire atomic beam is within the depth of field of the optical tower. The initial (visual) alignment does indeed coincide with this maximum.

Alignment of the standing-wave using the fluorescence is usually not precise enough to even *see* any diffraction. This structure is arrived at by situating the detector at an expected diffraction

Figure 1

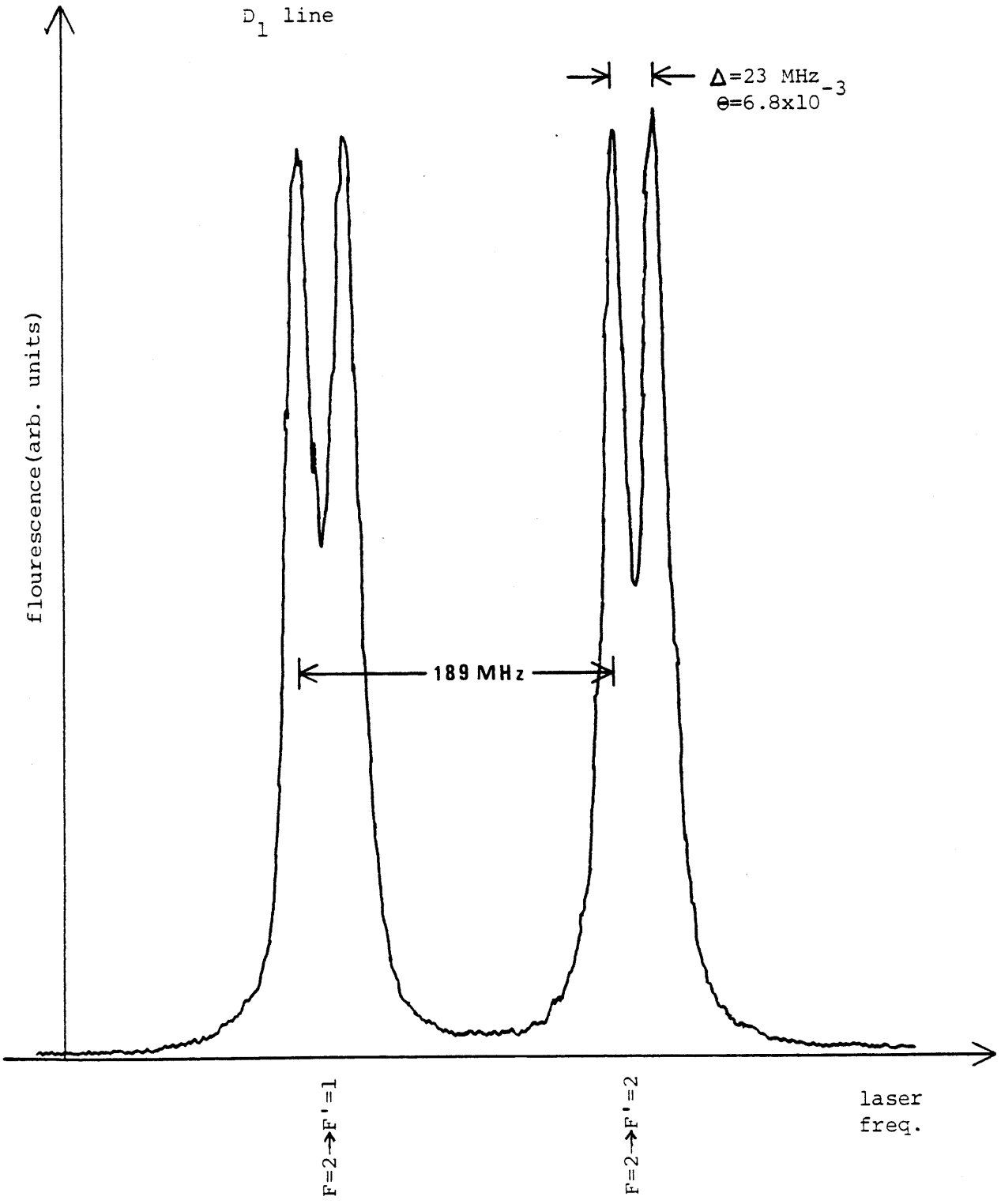
D_1 line
Δ=23 MHz
Θ=6.8x10^{-3}
flourescence(arb. units)
189 MHz
F=2→F'=1
F=2→F'=2
laser freq.

peak (with the laser detuned from resonance) and adjusting the retro mirror (and the input beam angle, to maintain overlap) until a large signal is seen. The detector is then moved to a higher order diffraction peak and the process is repeated. Successive steps become increasingly more sensitive. The symmetry of the pattern is then optimized using the PZT. This is usually done on resonance (where the laser can be locked) to avoid asymmetries due to laser frequency drift. An example of the effect of the PZT on pattern symmetry (on-resonance) is shown in Fig. 2(a). The angle of the mirror differs by $\sim 6 \times 10^{-5}$ rad between successive scans. That the difference between scans is indeed due to standing-wave alignment, and not drift of laser frequency or power, is demonstrated in Fig. 2(b), where successive scans, taken under identical conditions, are superimposed.

The extreme sensitivity of the patterns to mechanical movements of the retro mirror makes systematic variation of the standing-wave alignment very difficult with the present set-up. These variations would be very useful in obtaining optimum alignment and as a means for studying momentum transfer when the field strength varies over the course of the interaction (i.e. when the atomic trajectories traverse the nodes and antinodes of the standing-wave field). In the present experiments, the alignment is assumed optimum when symmetric patterns (with maximum overall deflection) are obtained.

II.C. Optical Pumping

1. *Optical Pumping Process*

Despite its many practical advantages, the sodium atom exhibits an unfortunate (for our purposes) abundance of hyperfine structure (see Fig. 1). Theories based on a two-state system are of limited applicability as the large number of possible transitions does not permit definition of a unique Rabi rate or resonance frequency. Additionally, optical pumping during an interaction can cause a time evolution of population, making the interpretation of results very difficult.

Figure 2

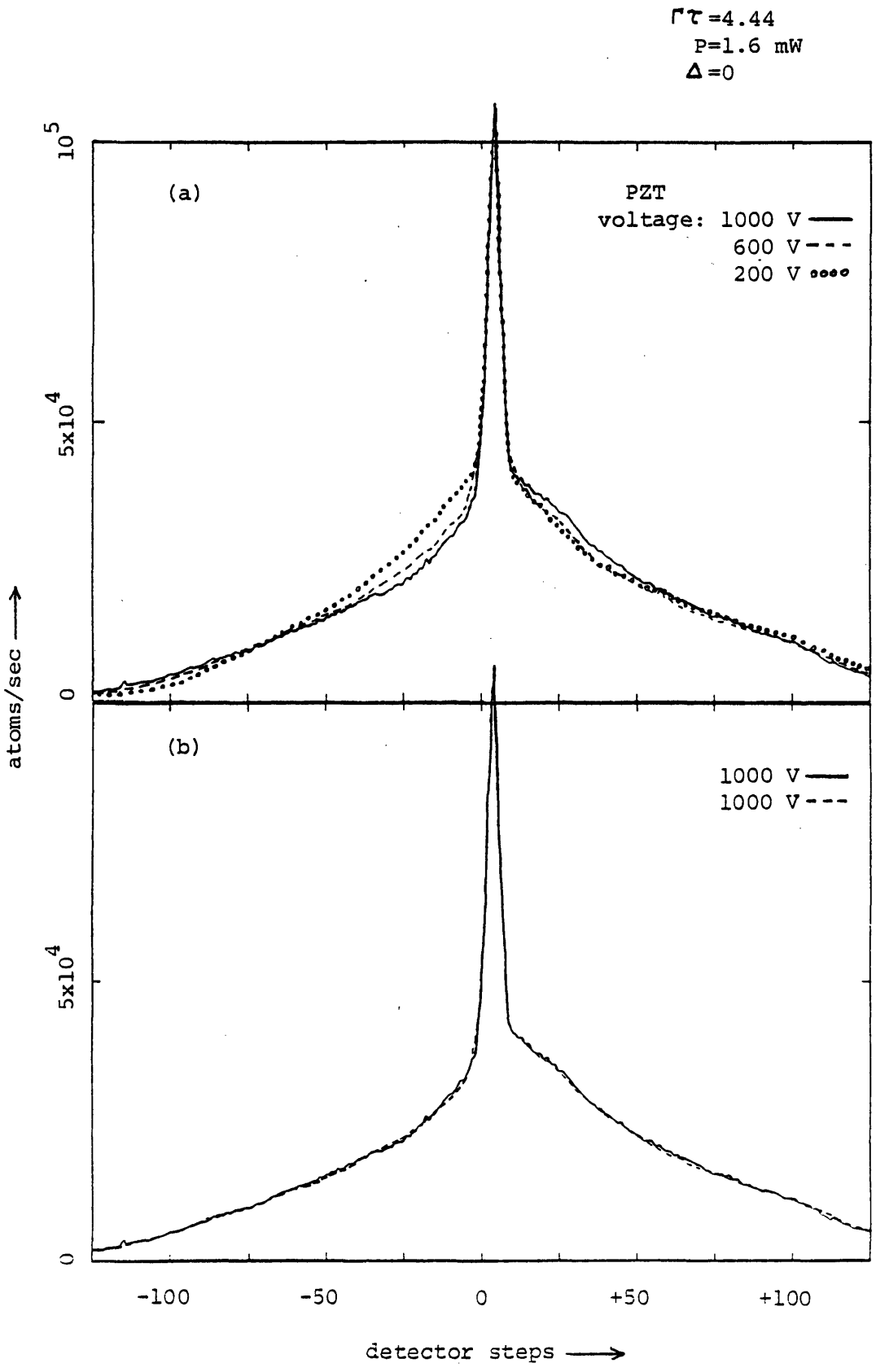
Γτ=4.44
P=1.6 mW
Δ=0
(a)
PZT
voltage: 1000 V
600 V
200 V
(b)
1000 V
1000 V
atoms/sec
10^5
5x10^4
0
5x10^4
0
-100
-50
0
+50
+100
detector steps

Fortunately, the sodium atom can be prepared as a closed two-state system with the use of optical pumping. The basic technique and clever variations have been described by a number of authors (SCS73, ABA74, GEN75, STM83, CUA83, DJK83, MCK85, HES77, HES76, DKB81, HJK81, BAL80, FIH82, CGG77, GWE77). In this section we will briefly describe the technique we have used. The reader is referred to the sources mentioned above, and MCK85 in particular, for more explicit details of the process and the relevant calculations.

The basic idea of the technique is to drive the F=2 → F'=3 transition (of the D_2 line) with circularly polarized light (Δm=+1 selection rule). Repeated excitation eventually results in the accumulation of the F=2 population in the m_F=+2 state, from which the only allowed transition (for Δm=+1) is to F'=3, m_F'=+3. Since decay of this excited state is always back to F=2, m_F=+2, we see that these two state constitute a closed system.

It is important that the optical pumping be done on the F=2 → F'=3 transition, as the F'=3 level cannot decay to F=1. Any atom which decays to F=1 (or is initially in F=1) is lost to the pumping process because of the large energy difference ($\sim$ 1.8 GHz) between the F=2 and F=1 levels. For this reason, care must also be taken to limit the intensity of the optical pumping laser. If the F=2 → F'=3 transition is strongly saturated, then the off-resonant (by $\sim$ 60 MHz) F=2 → F'=2 transition can readily occur, with subsequent decay to F=1.

Calculations by various by various authors (eg. HES76 and MCK85) show that the populations should become stationary after $\sim$ 30 cycles. Under saturated conditions, this corresponds to a pumping time of $\sim$ 1000 ns, or a laser beam diameter of $\sim$ 1 mm (for an atomic velocity of 10^5 cm/sec). We cycle the atoms more times than necessary for alignment, for reasons discussed below.

It is important that the OP laser polarization be circular to a high degree in order to avoid Δm=-1 transitions (Δm=0 transitions are not allowed when the laser propagates along the magnetic

Sodium Hyperfine Structure (from AIV77)

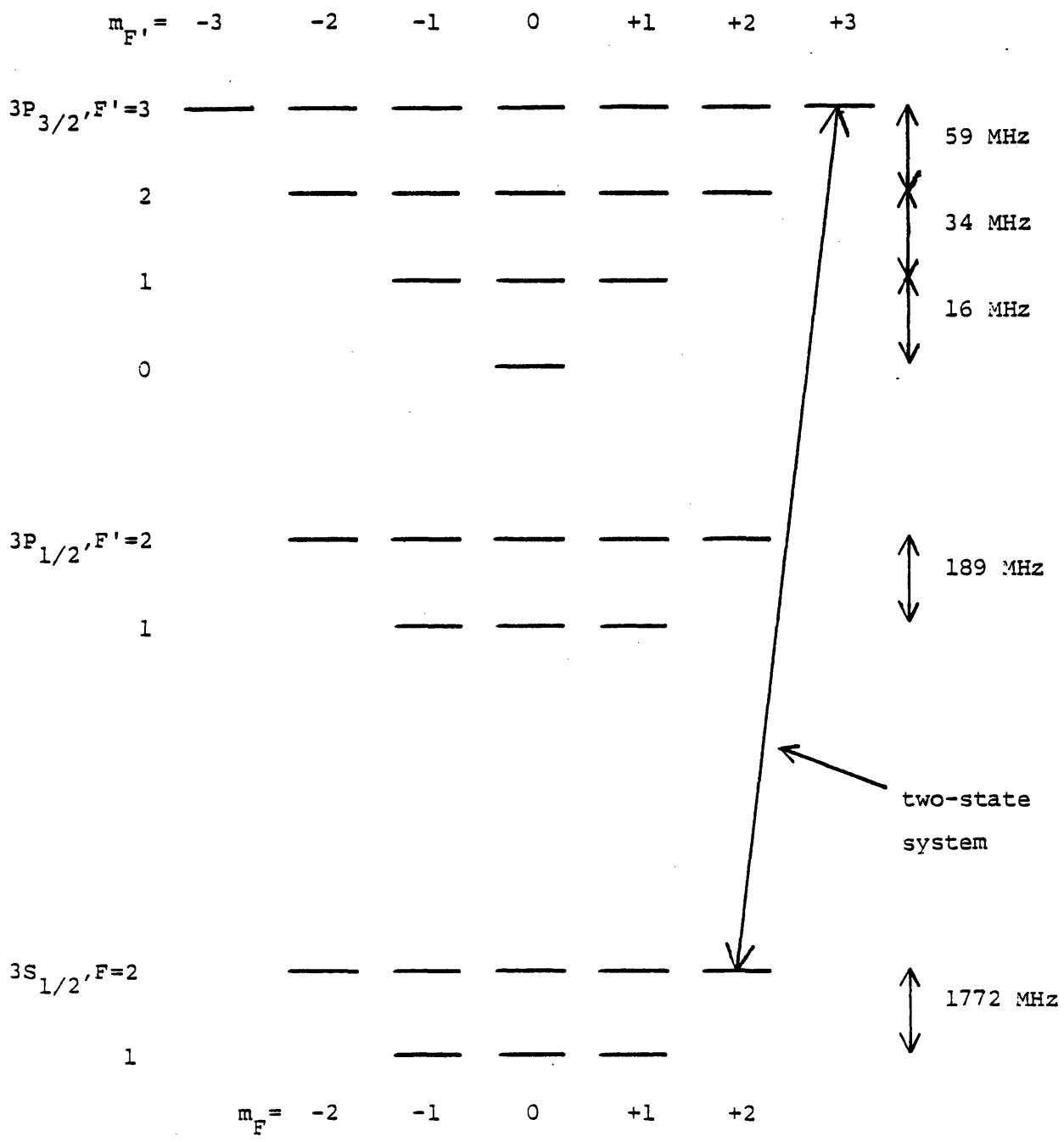

D_1 line: $^3S_{1/2} \rightarrow {}^3P_{3/2}$ 589.0 nm.

D_2 line: $^3S_{1/2} \rightarrow {}^3P_{3/2}$ 589.6 nm.

Figure 1

field) which could lead to loss to F=1. In addition, we use an intensity slightly in excess of saturation, as the Doppler shift due to recoil can become substantial for a large number of cycles (eg. 5 MHz for 100 cycles).

The effectiveness of our optical pumping is determined by probing the population distribution with the interaction region laser. This can be done on either the D_2 or D_1 line. The D_2 line would give a single enhanced peak (from the F=2 ground state) at the F=2 → F'=3 transition frequency if the optical pumping were perfect and we probed with circularly polarized light (Δm=+1). Residual populations in $m_F \neq 2$ and imperfect light polarization are seen as peaks at the F=2 → F'=2 and F=2 → F'=1 transition frequencies. It is reasonable to expect that the largest residual population would be in the F=2, m_F=+1 state, so if we denote this fraction by f_1 (<<1) and the fractional polarization contamination (Δm=−1) by f_p (<<1), examination of the relative transition strengths (squares of matrix elements) in Table 1 leads us to expect the following signals (in arbitrary units) for the D_2 line:

	OP off	*OP on*
F=2 → F'=1	2	$6f_p$
F=2 → F'=2	10	$10f_1+10f_p$
F=2 → F'=3	28	60

Since the indicators of imperfect pumping are small and in the wings of a large signal, we see that the D_2 line is a relatively insensitive probe of the optical pumping process.

If we probe on the D_1 line with circularly polarized light (Δm=+1), we would expect to see no signal for perfect pumping, i.e. the beam should be "transparent". A finite signal for the F=2 → F'=2 transition indicates residual population in m_F=+1 while the F=2 → F'=1 transition is primarily a measure of polarization contamination. The fact that these peaks do not have to compete with

Table 1

Relative Transition Strengths (from PEU83)

			$^3S_{1/2}$							
			F=1			F=2				
		$m_{F'}$ \ m_F	-1	0	+1	-2	-1	0	+1	+2
$^3P_{1/2}$	F'=1	-1	5	5		30	15	5		
		0	5		5		15	20	15	
		+1		5	5			5	15	30
	F'=2	-2	30			20	10			
		-1	15	15		10	5	15		
		0	5	20	5		15		15	
		+1		15	15			15	5	10
		+2			30				10	20
$^3P_{3/2}$	F'=0	0	20	20	20					
	F'=1	-1	25	25		6	3	1		
		0	25		25		3	4	3	
		+1		25	25			1	3	6
	F'=2	-2	30			20	10			
		-1	15	15		10	5	15		
		0	5	20	5		15		15	
		+1		15	15			15	5	10
		+2			30				10	20
	F'=3	-3				60				
		-2				20	40			
		-1				4	32	24		
		0					12	36	12	
		+1						24	32	4
		+2							40	20
		+3								60

the wings of the desired transition (F=2, m_F=+2 → F'=3, m_F'=+3) make the D_1 line the preferred probe. Examination of the transition strengths in Table 1 leads us to expect the following signals (in arbitrary units) for the D_1 line:

	OP off	*OP on*
F=2 → F'=1	10	$30 \cdot f_p$
F=2 → F'=2	10	$10 \cdot f_1 + 10 \cdot f_p$

Examining the D_1 spectra (with no slits in place) shown in Fig. 2a, we see the large reduction in peak height with the optical pumping on. Using the measured ratios of this fluorescence (OP on/OP off) we calculate (according to the above table), f_1=2.1% and f_p=.5%. These numbers are more difficult to obtain from the D_2 spectra shown in Fig. 2b, but this optically pumped spectrum is consistent with the values of f_1 and f_p calculated above.

In probing with the D_1 line, we must ensure that the peak reduction is due to accumulation of atoms in F=2, m_F=+2 and not loss of atoms to F=1. This is checked by comparing scans over transitions from the F=1 level with the OP laser on and off, as shown in Fig. 3 for the D_1 line. Assuming that the atoms lost to F=1 are equally distributed among the various m states, the observed increase of $\sim 10\%$ in fluorescence (with the OP laser on) implies that $\sim \frac{3}{5} \cdot 10\% \approx 6\%$ of the atoms originally in F=2 are lost to F=1.

Atomic fluorescence is seen quite easily with slit #1 *or* slit #2 in place, and with difficulty when both slits are in place. An example is displayed in Fig. 4 where the optical pumping efficiency is shown with slit #2 in place. We note here that the signals with slit #1 in place depend critically on the position of slit #1, due to deflection by the optical pumping laser, and are therefore difficult to interpret. As can be seen in comparing Figs. 2a and 4, the atomic alignment is degraded somewhat upon passage through slit #2. Applying the above analysis for the D_1 line

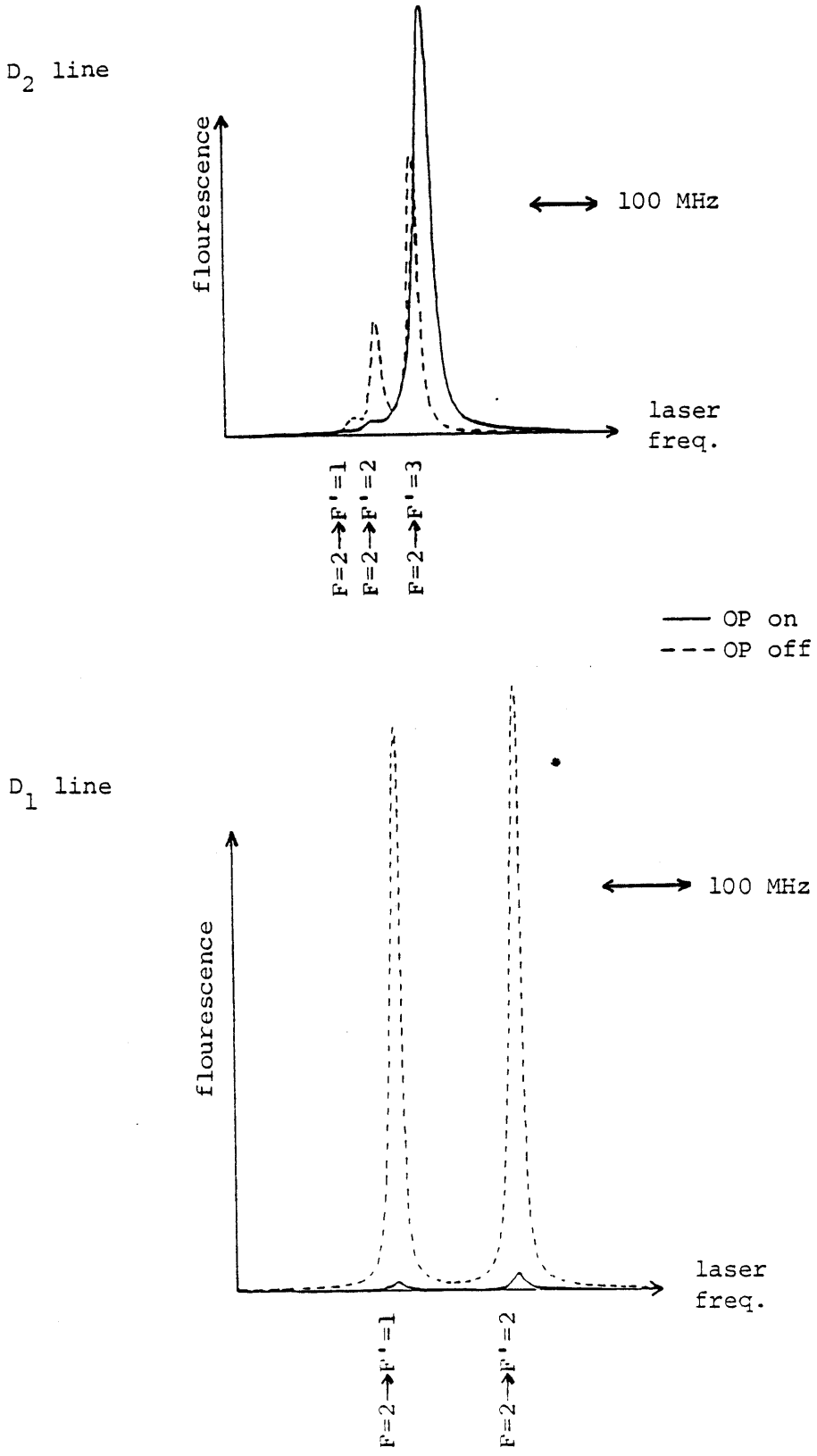
D2 line
flourescence
100 MHz
laser
freq.
F=2→F'=1
F=2→F'=2
F=2→F'=3
OP on
OP off
D1 line
flourescence
100 MHz
laser
freq.
F=2→F'=1
F=2→F'=2

Figure 2

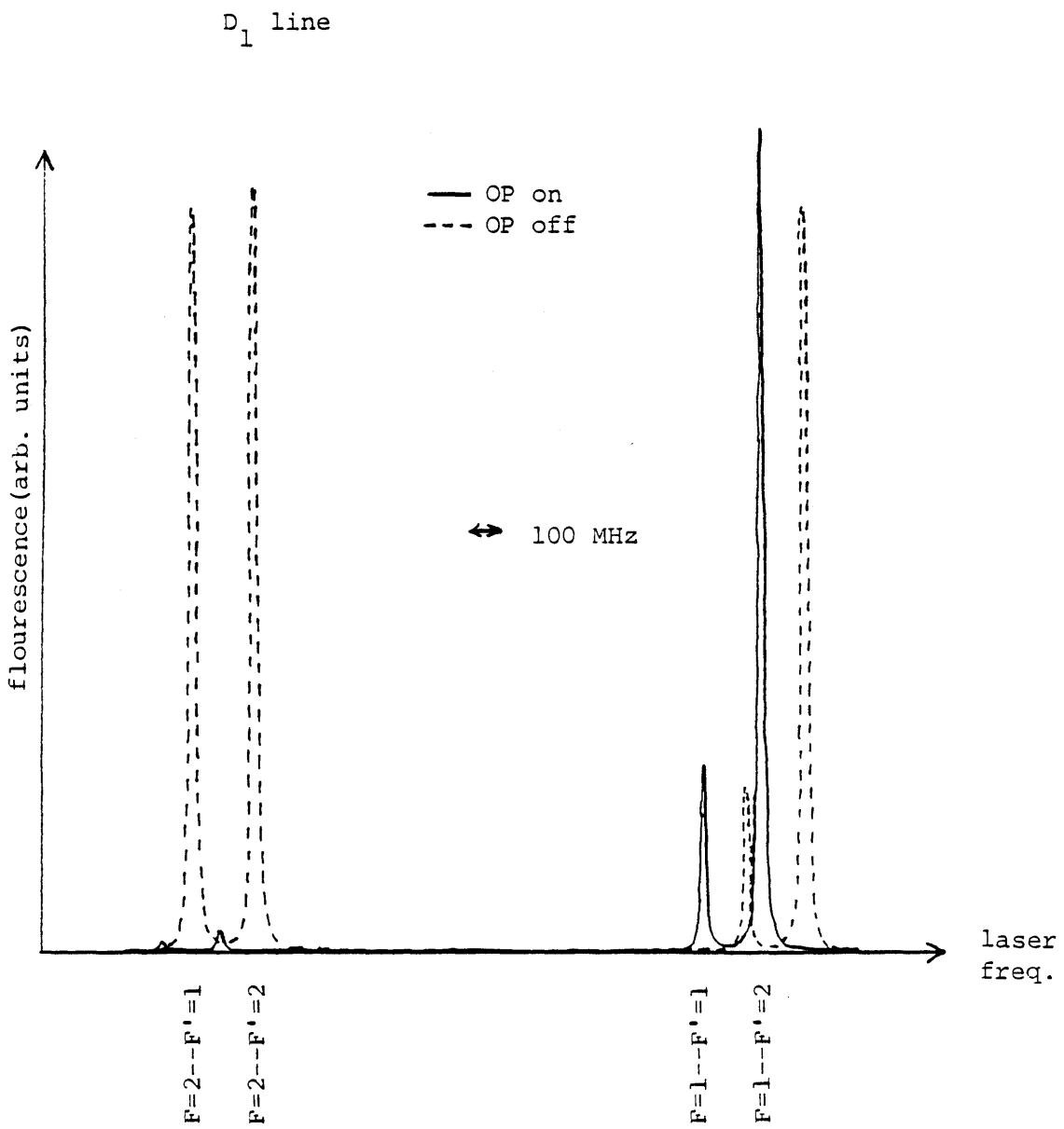
D_1 line
OP on
OP off
100 MHz
flourescence(arb. units)
laser freq.
F=2--F'=1
F=2--F'=2
F=1--F'=1
F=1--F'=2

Figure 3

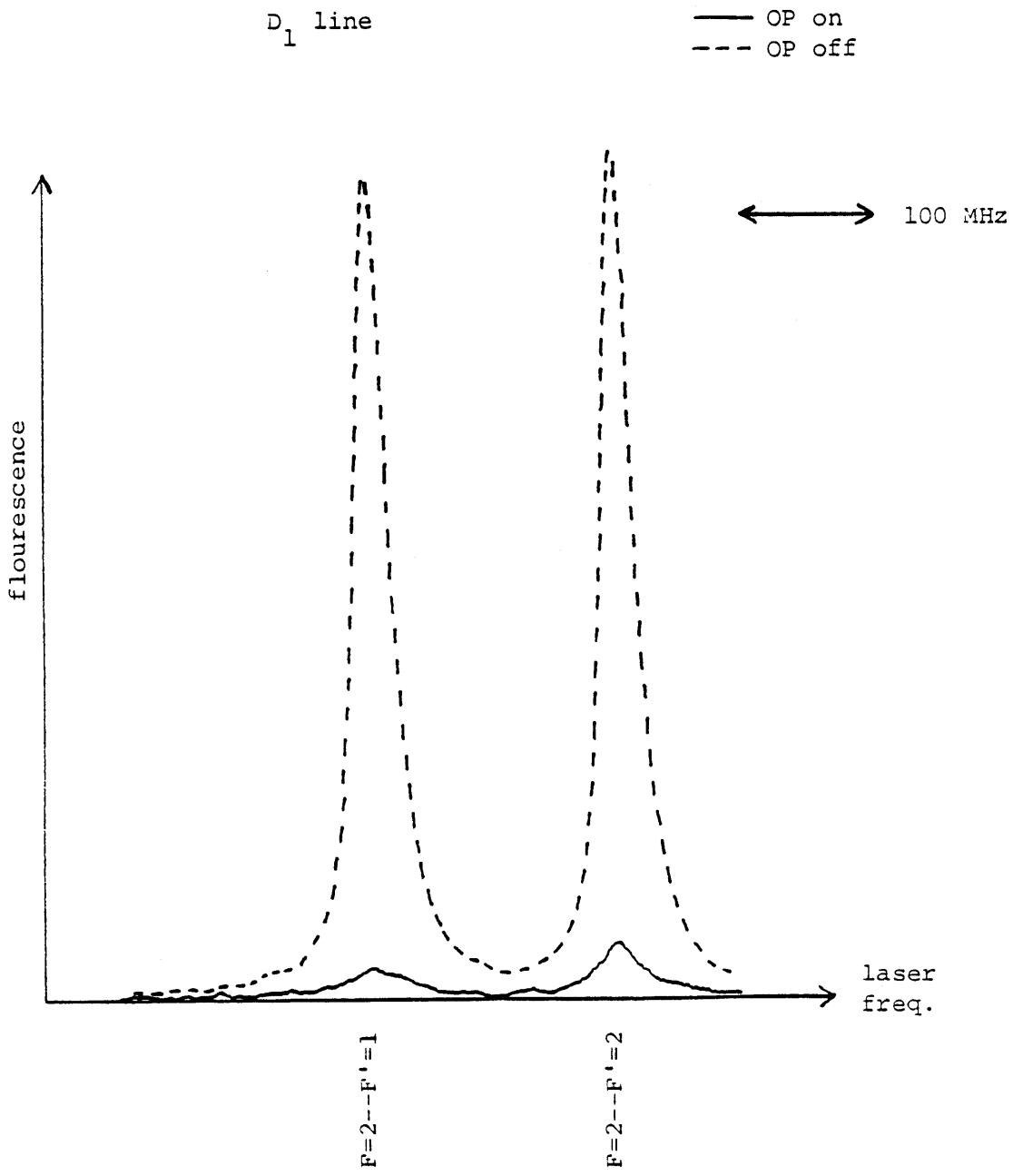
D1 line
OP on
OP off
100 MHz
flourescence
laser
freq.
F=2--F'=1
F=2--F'=2

Figure 4

we obtain f_1=4.6%, and f_p=1.4%. Obviously, the value of f_p should not depend on whether the slit is in place or not. This discrepancy could be due to two simplifying assumptions we have made: 1) we have assumed that only m_F=+1 has residual population and 2) we have ignored the different angular distributions of radiation from the different transitions. The transition strengths shown in Table 1 are strictly valid only if the total (i.e. 4π steradians) fluorescence is collected or if a polarizer at the "magic angle" is used in the collection optics (WAL82). In any case, we can say that >90% of the F=2 atoms are in m_F=+2 with the slits in.

The pumping process discussed above can (in principle) transfer nearly 100% of the F=2 population into m_F=+2. However, the atoms originally in F=1 are unaffected. Since our detector cannot discriminate between F=2 and F=1 atoms (as, for instance, a fluorescence detection scheme could), the F=1 atoms in the beam are a large source of background (on axis), even though they are undeflected (for the most part) in the interaction. As discussed below, we are able to substantially reduce this background.

Our stringent collimation requirements (<1 $\hbar$k) require the optical pumping to be performed before the first slit. As a result, the deflection by the OP laser has a significant effect. With the atomic beam alignment adjusted to account for this deflection, we are able to reduce the number of F=1 atoms reaching the interaction region by a factor of ~ 6 from the statistical fraction of $\frac{3}{8}$. This is described in more detail in the following section.

2. (to be submitted for publication)

Preparation of a Single-State Atomic Beam

by Optical Pumping and Radiative Deflection

George A. Ruff[a)], Phillip L. Gould and David E. Pritchard

Department of Physics and
Research Laboratory of Electronics
Massachusetts Institute of Technology
Cambridge, Massachusetts 02139

A simple technique for producing a single-state sodium atomic beam is described. A single laser both optically pumps the F=2 ground state atoms into m_F=+2 and deflects the pumped atoms away from residual F=1 atoms. Data demonstrating the operational principles are presented, and a practical design for an apparatus based on these principles is described.

Optical pumping of the F, m_F sublevels of an atomic ground state is a useful way to prepare a two-state system in experiments using atomic beams. With sodium, for example, the usual approach (MCK85, CGG77, GWE77) is to drive the F=2 → F'=3 transition (primed quantum numbers refer to the excited state) transition of the D_2 line with circularly polarized light ($\Delta m=+1$ selection rule), causing accumulation of the F=2 atoms in the $m_F=2$ state after ~30 absorption-spontaneous decay cycles. The selection rules for this process leave the F=1 population essentially unchanged, unless the intensity of the pumping light is large enough to cause unwanted (off-resonant) transitions to the F'=2 level. Atomic beams with essentially *all* atoms in the single F=2, $m_F=2$ state have also been achieved (ABA74, SCS73, GEN75, HES77), by using two lasers or two Doppler-tuned beams from a single laser to access the F=1 levels as the F=2 level is being pumped.

We suggest a simple single-state selection technique which uses a single laser to optically pump the F=2 level into $m_F=+2$ and to deflect these pumped atoms away from the unaffected F=1 atoms. Appropriate placement of collimators allows selection of only the F=2, $m_F=+2$ atoms. We present data demonstrating the operational principles of the method, and offer a practical design for an apparatus based on these principles.

A basic schematic of the technique is shown in Figure 1. A supersonic atomic beam from a source aperture in plane S is collimated by two slits of width w. Just before entering the first slit, the atomic beam passes through the optical pumping laser beam, which is oriented perpendicular to the axis defined by the centers of the source aperture and the second slit. The first slit is displaced by distance d_1 from the axis, so that undeflected F=1 atoms which pass through the slit must have left the source plane from a strip of width w_o and off-axis displacement d_o. F=2 atoms from an equal sized but on-axis strip in the source plane can pass through the slit only if they are deflected by an angle θ in the optical pumping region. Assuming for the moment that θ is the same for all F=2 atoms and that the width of the actual source aperture is matched to w_o, the collimated beam emerging from slit 2 will contain only F=2 atoms provided that d_o exceeds w_o.

We have used the arrangement described above to produce a collimated atomic beam for light-deflection experiments reported elsewhere (GRP86). In those experiments, the atoms emerging from slit 2 pass through a second laser beam, and the transverse momentum they receive from this "deflection laser" is measured. To permit resolution of momentum transfers corresponding to single photon absorption, we use 10 μ slits (3 mm high) separated by 87 cm. The remaining geometry was designed to optimize final beam flux rather than to eliminate F=1 atoms. Nevertheless our apparatus clearly discriminates against these atoms.

In our apparatus, the optical pumping laser light crosses the atomic beam at a point 19 cm from the source and 2.8 cm from slit 1. It is produced by a Coherent model 699-21 single-mode ring dye laser, carried to the atomic beam machine via a single-mode polarization-preserving optical fiber, recollimated by a 6X microscope objective to a final Gaussian beam profile with 3 mm FWHM, and circularly polarized by a zero-order quarter wave plate. The power at the atomic beam location is 1.25 mW. Our supersonic atomic beam has a mean velocity of 10^5 cm/s. Under these conditions the expected number of optical pumping cycles, with deflection induced Doppler detuning taken into account, is about 90. This is roughly three times the number needed to produce essentially stable m_F populations.

To analyze the effectiveness of the optical pumping, we use our "deflection laser" to induce fluorescence in the atomic beam at a point just downstream from the second slit. The power of this laser is minimized to avoid perturbing the m_F populations, and one or the other of the collimating slits is removed to allow observation of the induced fluorescence with good signal/noise. The circularly polarized ($\Delta m=+1$) probe beam can be tuned to either the D_1 or D_2 line. The D_2 line, however, is a poor test of imperfect optical pumping because residual populations in $m_F \neq +2$ appear as weak $F=2 \rightarrow F'=1$ and $F=2 \rightarrow F'=2$ peaks in the wing of an enhanced and initially larger $F=2 \rightarrow F'=3$ peak. Consequently, we use the D_1 line $F=2 \rightarrow F'=1$ and $F=2 \rightarrow F'=2$ transitions as indicators of optical pumping effectiveness. For perfect pumping there should be no signal at all in

these transitions (due to the Δ=+1 selection rule). A nonzero F=2 → F'=1 signal indicates residual population in the m_F=+1 sublevel, and a nonzero F=2 → F'=1 signal is primarily a measure of polarization contamination in the probe beam. If we denote by f_1 and f_p, respectively, the small fractional F=2, m_F=+1 population and the small fractional Δm=-1 polarization contamination, examination of the relative transition strengths of the individual hyperfine transitions leads to the following ratios of probe fluorescence for optical pumping on and off:

D_1 line:	OP on/OP off
F=2 to F'=1	$3 f_p$
F=2 to F'=2	$f_1 + f_p$

Our measured fluorescence ratios yield the values f_1 = 4.6% and f_p = 1.4%.

In probing with the D_1 line, we must ensure that the signal reduction is not caused by loss of atoms to F=1. This is checked by measuring fluorescence induced by transitions from the F=1 sublevel. We observe a 10% increase in these signals when the optical pumping is turned on, implying that 6% of the atoms initially in F=2 are lost to F=1. Since transitions to F=1 during optical pumping can not occur from the F'=3 level, it is clear that in the absence of polarization contamination, any transition to F=1 must occur early in the optical pumping process, with the result that atoms transferred to F=1 absorb only a few photons from the optical pumping beam. This suggests that the 10% fluorescence increase we observe would not be seen if both slits were present. When either slit is removed, the range of allowed deflection angles increases sufficiently to permit detection of these F=1 atoms.

When both slits are present, the collimated beam is observed with a hot-wire ionizer and channel electron multiplier detector located downstream from slit 2. With the optical pumping on, the intensity of our collimated beam was observed to depend dramatically on the distance, d_1, of

slit 1 from the axis defined by the centers of the source and slit 2. In our deflection experiments, this distance was set to correspond to a deflection angle of 1.4×10^{-3} rad, or a 50 ħk change in transverse momentum. When the hot wire ionizer was appropriately aligned with the slits, we obtained typical CEM count rates of 675K with the optical pumping on and 107K with it off. Assuming that 3/8 of the latter figure are in F=1 and that no additional F=1 atoms are added by the optical pumping process, the percentage of F=1 atoms in the optically pumped and collimated beam is seen to be 6%. This figure varied between 5% and 7% in the data we have taken.

An independent measure of this F=1 fraction is provided by our data for low power traveling-wave deflection of the atomic beam by the deflection laser. These results are shown in Figure 2. The solid curve is the raw data (after background subtraction and normalization), taken by measuring the CEM count rate as the hot wire ionizer is scanned transversely. Since F=1 atoms do not interact with light from the deflection laser, they appear as a narrow peak at the original beam position. The initially collimated (to .88 ħk FWHM) F=2, m_F=+2 beam is deflected to the right and broadened. The dashed curve shows the result of subtracting the expected undeflected F=1 line profile corresponding to a 6% F=1 fraction.

The nearly complete disappearance of the undeflected peak after the subtraction described above indicates that the 6% F=1 fraction indicated by our hot wire data is correct. Thus the fraction of atoms in F=1 has been reduced by 84%.

As seen in Figure 1, undeflected atoms which pass through the collimator originate in a strip of width w_0 at distance d_0 from the axis in the source plane. For the conditions of our experiment, d_0 is 276 μ. From the atomic beam profile at our hot wire detector with both lasers off and only slit 2 in place, an effective source size of approximately 500 μ (skimmer diameter) is obtained. In light of our +/- 50 μ initial alignment uncertainties, the substantial but yet incomplete F=1 discrimination which we observe is seen to be consistent with the geometry of our apparatus.

It appears practical to construct an apparatus which discriminates completely against F=1 atoms without resorting to collimator slits as narrow as ours. As shown in Figure 1, the key geometrical consideration is that the distance d_o of the source strip for F=1 atoms from the axis be greater than the sum of the half-width of this strip and the radius of the actual source aperture. In principle, this can always be achieved, by sufficiently increasing the deflection angle, θ, and/or the distance between the source and the optical pumping region.

As an illustration, consider a 2.0 mW optical pumping laser beam of 3 mm FWHM Gaussian beam profile. This gives 1.5X saturation intensity at the center of the profile and ensures that only a small fraction of F=2 atoms will be transferred to F=1 during optical pumping. The mean number, N, of photon absorptions is maximized at N=110 if the incident and deflected atoms make equal angles with the laser beam. Given a mean atomic velocity $v=10^5$ cm/s and a 10% velocity spread, the expected mean value and range of deflection angles is θ=3.2+/−.2 mrad. Referring again to Figure 1, we see that the final beam flux is increased if slit 1 is located right at the edge of the optical pumping region, making $l_{12}=l_{01}\equiv l$ and $d_1=2(l/\theta)$. Assuming equal slit widths, w, we find that the source strip for undeflected F=1 atoms has a geometric width w_o=3w, and a displacement $d_o = 2d_1$ from the axis.

Suppose that the actual source has an aperture centered on the axis and having diameter w_a. The condition for complete elimination of F=1 atoms is that this aperture not overlap the F=1 source strip, i.e. that:

$$w_a<4d_1-3w$$

For w_a=500 μ, this is achieved for $w=w_a$ and θ=3.2 mrad if l=62.5 cm. The final beam flux emerging from a system with these dimensions would be approximately 40x greater than that used in our deflection experiments.

We note here that our technique not only provides selection of quantum state, but is also effective in selecting against undesired species (eg. dimers or different isotopes).

References

ABA74 J. Abate, Opt. Commun. 10, 269 (1974).

BAL80 V.I. Balykin, Opt. Commun. 33, 31 (1980).

CGG77 M.L. Citron, H.R. Gray, C.W. Gabel, and C.R. Stroud, Jr., Phys. Rev. A 16, 1507 (1977).

GEN75 H.J. Gerritsen and G. Neinhuis, Appl. Phys. Lett. 26, 347 (1975).

GRP86 P.L. Gould, G.A. Ruff, and D.E. Pritchard, accepted for publication in Phys. Rev. Lett.

GWE77 R.E. Grove, F.Y. Wu, and S. Ezekiel, Phys. Rev. A 16, 1507 (1977).

HES77 I.V. Hertel and W. Stoll, in *Advances in Atomic and Molecular Physics,* Vol. 13, ed. by D.R. Bates and B. Bederson (Academic Press, New York, 1977).

MCK85 J.J. McClelland and M.H. Kelley, Phys. Rev. A 31, 3704 (1985).

SCS73 F. Schuda and C.R. Stroud, Jr., Opt. Commun. 9, 14 (1973).

Figure Captions

Figure 1. Schematic of state selection technique. Atoms from the source plane S are optically pumped and deflected (by an angle θ) by the optical pumping (OP) laser before passing through the two collimating slits.

Figure 2. Deflection profile for our state-selected atomic beam. Solid and dashed lines are the profiles before and after the subtraction for undeflected F=1 atoms, respectively. For reference, the peak probability for the undeflected beam (comprised of F=2 and F=1 atoms) is ~0.26.

Figure 1

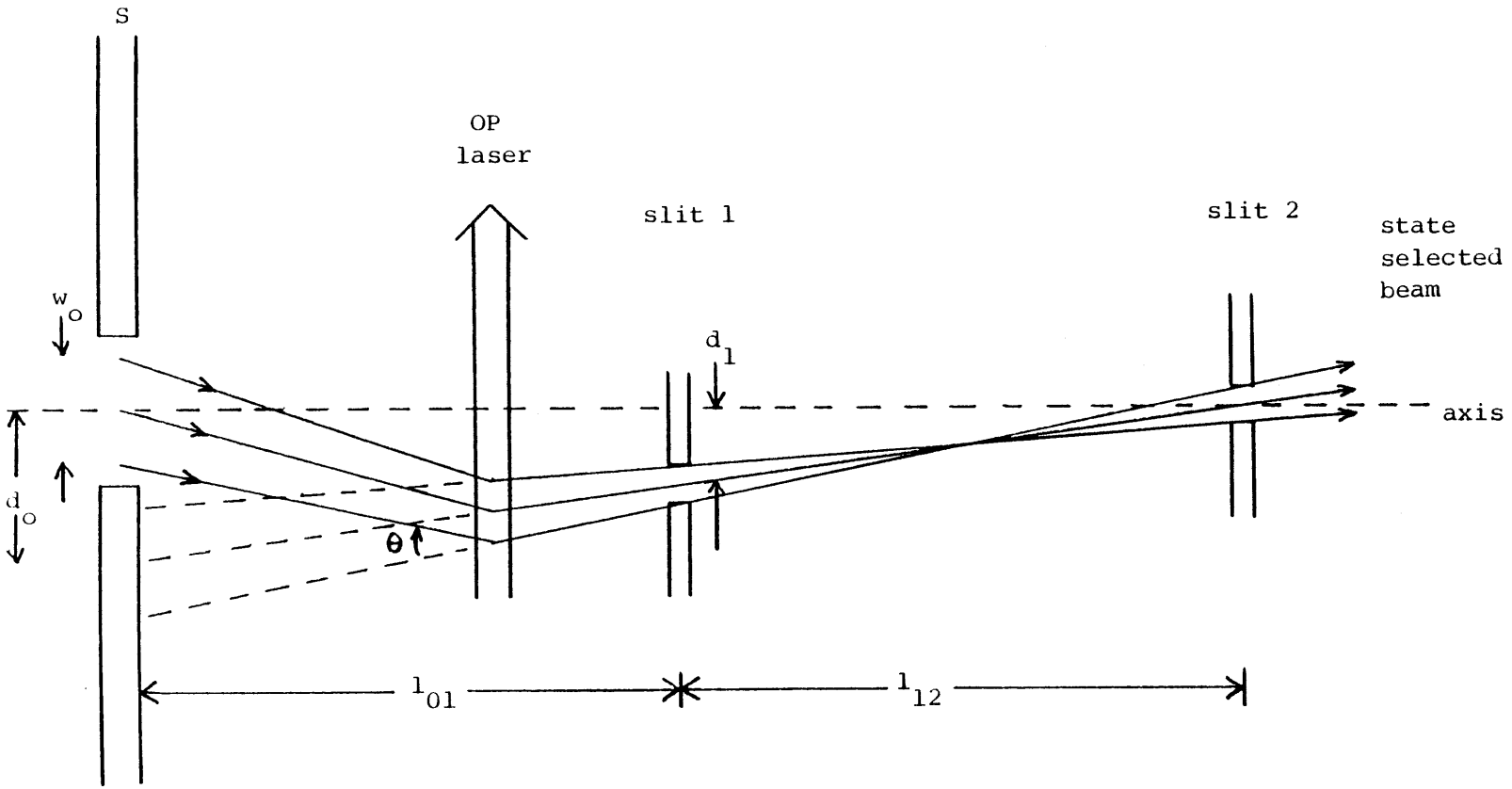
S
OP
laser
slit 1
slit 2
state
selected
beam
w_o
d_1
axis
d_o
θ
l_{01}
l_{12}

Figure 2

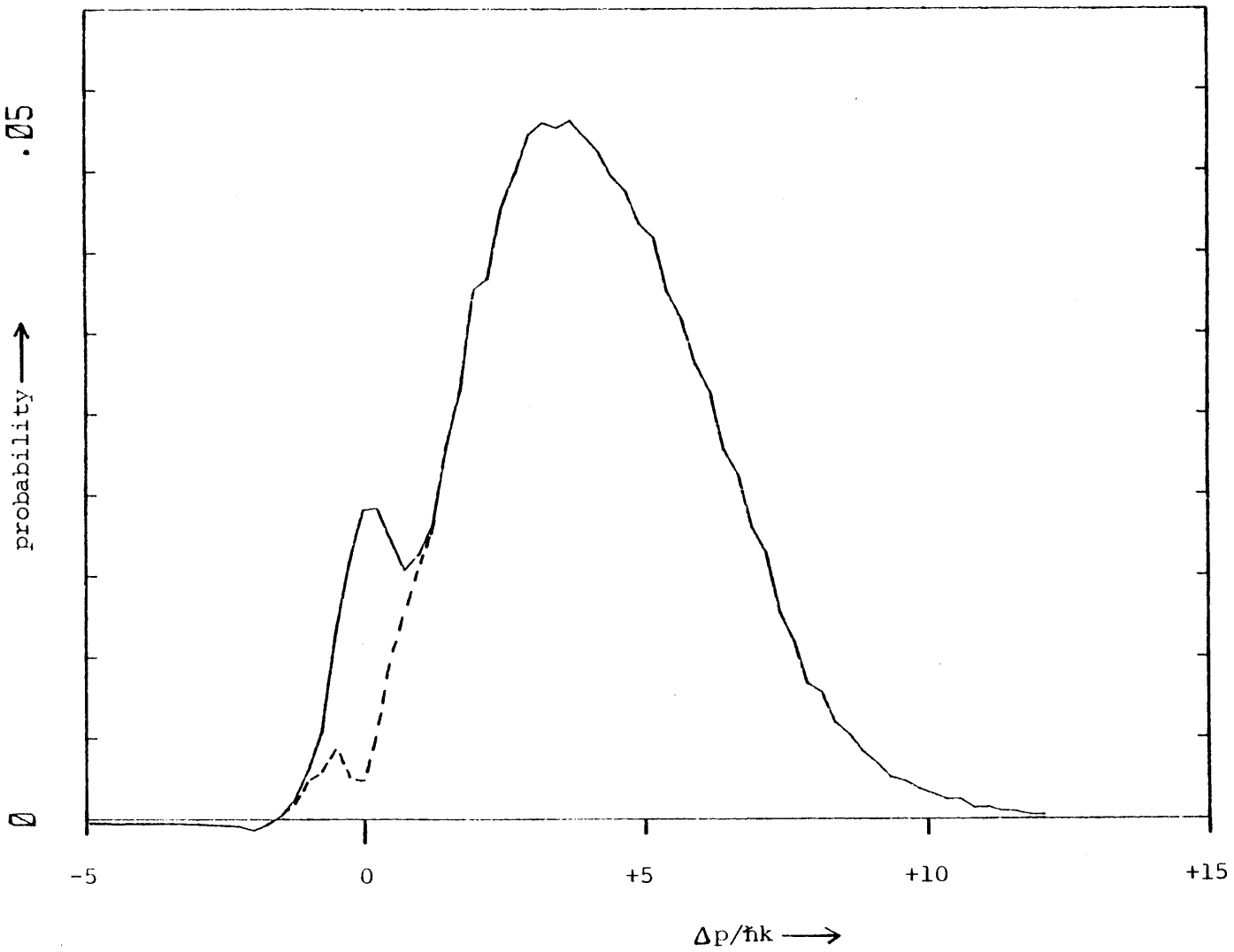

Chapter III. Atomic Beam Diffraction

This chapter describes our experimental observations of atomic beam diffraction - the near-resonant Kapitza-Dirac effect. By operating sufficiently far from resonance, we are able to avoid the effects of spontaneous decay, despite an interaction which lasts for many spontaneous lifetimes. Together with our high momentum resolution ($<\hbar k$), this allows us to observe diffraction into even multiples of $\hbar k$, a phenomenon originally predicted by Kapitza and Dirac (KAD33). The conditions of the experiment: relatively high field; large detuning; adiabatic interaction; two-state system; narrow velocity distribution; and high momentum resolution, permit quantitative comparison with a relatively simply theory.

In Section A we discuss the original prediction of Kapitza and Dirac and briefly review the current status of experiment and theory. The relationship and relevance of our work to this situation is also discussed. A summary of our observations and interpretations is presented in the report which comprises Section B. This manuscript has been accepted (12/13/85) for publication in Physical Review Letters. Section C contains the details of the theoretical calculations which are outlined in Section B. The data analysis and theoretical fits are described in Section D and additional data (which are summarized in Section B) are presented and discussed in Section E.

III.A. Introduction

In 1933, Kapitza and Dirac (KAD33) proposed an experiment in which electrons would be diffracted by the "grating" of a standing light wave (Fig. 1). This idea was motivated by the following remarks (KAD33):

"It is well known that a beam of light falling on a reflecting mirror forms standing waves. This effect has been very beautifully made use of in Lippmann's colour photography process. The standing light waves, in this case, produce a periodic effect in the emulsion of the photographic plate which, when developed, scatters light and produces a similar colour effect. Instead of using a beam of light, it would seem possible to scatter electrons from the emulsion and obtain a reflection of electrons similar to that of a space grating. But it seemed to us that it would be of much greater interest to consider an experiment in which electrons are reflected from the standing waves of

Figure 1

THE KAPITZA-DIRAC EFFECT (from KAD33)

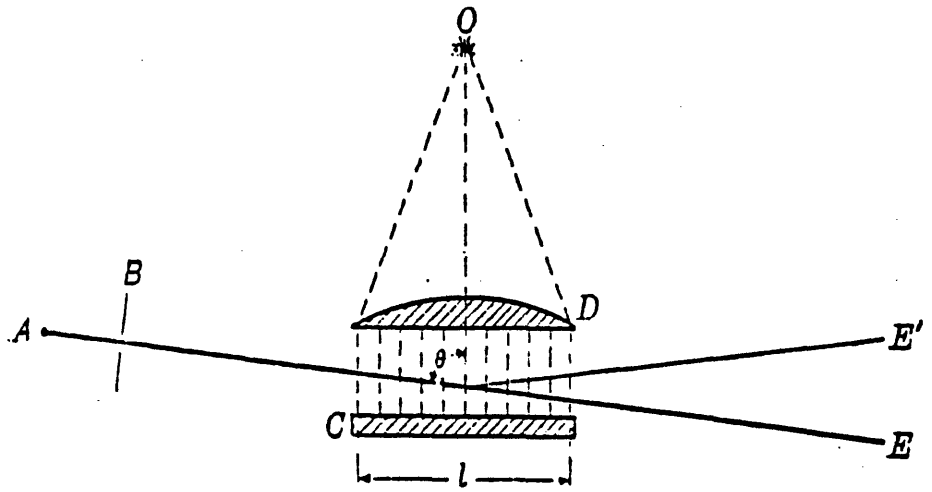

A: electron source
B: aperture
C: mirror
D: lens
E: unreflected beam
E': reflected beam
O: light source

light."

In essence, their proposed experiment would demonstrate the diffraction of electron "waves" by a light "grating" - i.e. the quantum mechanical dual of the well known phenomenon of light waves diffracting from a matter grating. They formulated their idea in terms of stimulated Compton scattering satisfying the Bragg condition.

The original predictions of Kapitza and Dirac were based on the stimulated Compton effect - the process whereby an electron absorbs a photon from one (traveling-wave) component of the standing-wave and is stimulated to re-emit a photon by the other component. The net momentum gained by the electron in this (first-order) process is 2 $\hbar k$ (in the direction of the initial absorption) and the scattering must satisfy the Bragg condition in order that both energy and momentum be conserved. Since the deflection occurs as a result of an absorption/stimulated emission cycle, the momentum transfer proceeds at the rate of these stimulated processes (in the case of electrons, this is proportional to the square of the intensity). Higher order Bragg reflections (or diffraction), with momentum transfer in multiples of 2 $\hbar k$, can also occur, by repeated absorption/stimulated emission cycles.

Unfortunately, Kapitza and Dirac were ahead of their time, as the discovery of the laser was decades away and the light sources available at the time did not have the intensity (or narrow bandwidth) required to observe the predicted effect. In fact, their estimate (based on available light sources) of 10^{-14} for the probability of first order diffraction (i.e. reflection) discouraged even the most optimistic experimentalists.

The advent of the laser revived interest in the idea and several experiments were carried out (SCH67, BRT68, TAM68, PFE68) in an effort to observe the effect. However, the results of these experiments are generally inconclusive due to experimental difficulties associated with the large laser powers ($\sim$ 10MW) and small deflection angles ($\sim 10^{-5}$ rad). It is generally believed that the

effect itself has been observed but that meaningful measurements have not been made (NEI69).

Many theories, both classical (CHT79 and references therein) and quantum mechanical (COM85 and references therein), have expanded on the original idea of Kapitza and Dirac. Unfortunately, the inadequacies of the experimental results have not challenged or verified these theories.

The Kapitza-Dirac effect for neutral atoms was first considered by Altshuler, et. al. (AFB66) who realized that diffraction (or reflection) of atoms could occur as a result of stimulated Rayleigh scattering (cf. stimulated Compton scattering for electrons) in a standing light wave. In addition, it was noted that the resonance enhancement (not possible for electrons) of the scattering cross section should dramatically increase the reflection probability and make higher order diffraction possible. These higher order processes can be viewed as multiphoton absorption/stimulated emission cycles.

Once again, the men with the ideas were ahead of their time. But, with the emergence of the tunable dye laser, momentum transfer to atoms from near-resonant radiation became observable. (This is discussed in greater detail in Chapter 1). Not only is it currently possible to transfer measurable momenta to atoms but it can be done under conditions where stimulated processes dominate over spontaneous ones. We have utilized this resonant enhancement to increase the probability of diffraction, but have operated sufficiently far from resonance to avoid the effects of spontaneous decay. These effects include the loss of coherence between atom and field (KSY85) as well as momentum transfer due to the spontaneously emitted photons (MAN79).

In previous experiments (GKN81, GKN84, GKN85), standing-wave deflection in the absence of spontaneous decay was studied with a pulsed laser in the regime $\Gamma\tau < 1$. However, these efforts suffered from poor momentum resolution and duty cycle problems. The first observation of atomic beam diffraction was reported by Moskowitz, *et al* (MGA83, MGP85) under conditions where

$\Gamma\tau \sim 1$. However, the distribution of atomic states made data analysis rather complicated.

In principle, an on-resonant experiment could be performed with an interaction time short enough to prevent spontaneous decays from occurring during the interaction. The theory for this situation was first worked out in COB78. The result is a quantized momentum distribution with roughly equal likelihood to emerge from the interaction having exchanged an even number of photons with the field (and consequently with the atom in the ground state) or an odd number (and the atom in the excited state). Since atoms emerging from the interaction in the excited state decay well before being detected, all diffraction peaks corresponding to odd integrals of $\hbar k$ would be smeared out by the spontaneous recoil distribution (MAN79, KSY80). Despite this effect, the presence of odd peaks could easily be verified with our present apparatus. This smearing effect has been deconvolved from diffraction data (MGA83, MOS84) but we view the small odd peaks recovered in the deconvolution as resulting from inadequate experimental resolution and uncertainties in the deconvolution procedure. These factors did not allow substantiation of odd peaks (MGP85), despite affirmative interpretations (KSY85).

The major practical problem preventing our observation of odd peaks is that of creating an interaction time short enough to prevent spontaneous decay *during* the interaction (PRG85) when using resonant excitation. This difficulty would be avoided with the use of a pulsed laser, as in GKN81 and GKK84. However, these experiments suffer from duty cycle and resolution problems. Alternatively, a faster atomic beam (attainable with a lighter seed gas) would give a shorter interaction time for a given laser beam diameter, but the angular resolution (i.e. deflection angle per photon) would then be unacceptable.

We argue that in terms of performing an experiments similar to the original idea of Kapitza and Dirac, our off-resonant adiabatic interaction (with momentum transfer in even multiples of $\hbar k$) is better suited than an on-resonant diabatic one. After all, an electron cannot emerge from an

interaction in the excited state!

Before describing the experiment itself, we would like to point out possible applications of this phenomenon, whereby large momentum transfers can occur in the absence of spontaneous emission. In many proposed applications (see Chapter I) for manipulating particles (i.e. atoms and molecules) using radiative forces, spontaneous decays can be very detrimental if they occur to inaccessible states. In fact, isotope separation of barium using traveling wave deflection (BDS74, BDS76) required two lasers due to metastable trapping. Also, efficient traveling wave deflection of sodium (BFP81) required two lasers to deal with optical pumping between ground state hyperfine levels. In the experiments described in this chapter, efficient beam deflection was obtained in the (nearly) complete absence of spontaneous emission. A possible application of this "decay-free" deflection would be for state selection in a molecular beam. If the standing-wave laser were tuned to a transition between two particular molecular levels, the deflected molecules would all be in the lower (rotational, vibrational) level of the transition. If this were attempted with a traveling-wave laser, the atoms initially in the desired ground state would be quickly lost to other ground states by optical pumping.

Another potential application of this effect would be in the realization of an "atomic interferometer" (CDK85). In this case the deflection would be used to separate and recombine an atomic beam, with interference resulting from the spatial coherence maintained between the deflected beams.

III.B. (accepted for publication in Physical Review Letters)

Diffraction of Atoms by Light: The Near-Resonant Kapitza-Dirac Effect

Phillip L. Gould, George A. Ruff,[a)] and David E. Pritchard

Department of Physics and
Research Laboratory of Electronics
Massachusetts Institute of Technology
Cambridge, Massachusetts 02139

We have observed the Kapitza-Dirac effect in the scattering of sodium atoms by a near-resonant standing-wave laser field. The data clearly show diffraction peaks of the atomic momentum transfer at even multiples of the photon momentum. Theoretical predictions for an off-resonant, adiabatic interaction with a two-state system are in reasonable agreement with the data.

Kapitza and Dirac[1] predicted in 1933 that an electron beam would reflect from a standing light wave due to stimulated Compton scattering. Widespread interest in this prediction arose because the phenomenon is the quantum mechanical dual of diffraction of light waves by a matter grating - i.e. it is the diffraction of matter waves from a light grating - and also because it involves a stimulated radiative process. With the advent of the laser, there have been several inconclusive attempts to observe this effect using electrons[2]. As a result, classical[3] and quantum mechanical[4] theories have remained largely unverified.

Following a suggestion[5] that similar diffraction should occur for neutral atoms, we have chosen to investigate this process with an atomic sodium beam. Using light whose frequency is near an atomic resonance makes possible the observation of higher order (i.e. multiphoton) diffraction. Our motivations for performing this experiment include the original interests of Kapitza and Dirac as well as a desire to provide definitive experimental tests to complement the contemporary proliferation of theoretical work on momentum transfer to atoms from radiation[6].

Our experiment, although not the first deflection study with standing-waves[7-11], is the first in which the experimental conditions are sufficiently well defined to permit a clearcut comparison with theory: a velocity selected beam of two-state atoms interacts with a well characterized standing-wave, and the momentum transfer is measured with high resolution. Our results clearly demonstrate the quantization of the momentum transfer in even multiples of the photon's momentum; moreover the amplitudes of the peaks are in good agreement with the predictions for our off-resonant, adiabatic interaction.

Although momentum transfer between an atomic beam and a standing-wave radiation field has received a great deal of theoretical attention[12-19], only Refs. 13 and 18 have considered the combined circumstances of off-resonant excitation and adiabatic travel through the field, and neither has given an expression for amplitudes of even peaks for a smooth field profile.

We now outline a calculation[20] of the momentum transferred to a two-state atom (energy difference $\hbar\omega_o$, dipole moment μ) by a standing-wave electric field with temporal envelope f(t):

$$E(x,t) = 2E_o f(t) \cos kx \cos\omega t \tag{1}$$

The atoms move in the y direction. If their net displacment along x as they traverse the light beam is much smaller than a wavelength, then x becomes a parameter in the time-dependent Schrodinger equation for the ground and excited state amplitudes, a_g and a_e. For f(t) = sech(t/τ), the final (t=+∞) amplitudes for an atom initially (t=-∞) in the ground state can be expressed in terms of hypergeometric functions[21,22] involving the detuning: $\Delta = \omega - \omega_o$, and the peak traveling-wave Rabi rate: $\Omega_o = \frac{\mu E_o}{\hbar}$.

The probability, P_n, that the atom gains transverse momentum $n\hbar k$ from the interaction is obtained by expanding this wavefunction in a Fourier series in x. For n odd (i.e. atom emerges in excited state), we find[13]:

$$P_n = sech^2(\frac{\pi\Delta\tau}{2}) J_n^2(\pi\Omega_o\tau) \qquad n \text{ odd} \tag{2}$$

which is $<10^{-20}$ in our experiment. For n even (i.e. atom emerges in ground state), and for large detuning, we obtain:

$$P_n = J_{n/2}^2(z) = J_{n/2}^2(\frac{\Omega_o^2\tau}{\Delta}) \qquad n \text{ even} \tag{3}$$

Generalizing Eq. 3 to an arbitrary f(t), the argument of the Bessel function becomes:

$$z = \frac{1}{2\Delta} \int_{-\infty}^{\infty} [\Omega_o f(t)]^2 dt \ , \tag{4}$$

which gives the correct result for a square field profile (f(t) = 1 for a time τ) with adiabatic entry and exit and large detuning.[11,18] Thus, for our Gaussian profile: f(t) = $e^{(t/\tau)^2}$, we find:

$$z = (\frac{\pi}{8})^{1/2} \cdot \frac{\Omega_o^2 \tau}{\Delta} \tag{5}$$

Using a summation property for Bessel functions[12], we can calculate the rms momentum from Eq. 3:

$$p_{rms} = [\sum_{n=-\infty}^{\infty} (n\hbar k)^2 P_n]^{1/2} = 2^{1/2} \cdot z \cdot \hbar k \ . \tag{6}$$

The effects of spontaneous decay[19] are avoided by keeping the average number of decays, $\bar{N}$, less than 0.25. This is accomplished by operating off-resonance. $\bar{N}$ is the average (over x) of N(x), the number of decays of an atom entering at a position x. N(x) is the time integral of Γ (the spontaneous decay rate) times the fraction of time spent in the excited state:

$$N(x) = \int_{-\infty}^{\infty} \frac{[2\Omega_o \cos kx \cdot f(t)]^2}{2[2\Omega_o \cos kx \cdot f(t)]^2 + 4\Delta^2 + \Gamma^2} \cdot \Gamma \cdot dt \tag{7}$$

In our experiment a collimated beam of sodium atoms is deflected by a plane standing-wave laser field. The transverse momentum distribution is determined by scanning a detector downstream from this interaction.

Our apparatus is an improved version of the one described in Refs. 9 and 11. Key features are:

1) Momentum resolution (FWHM) of 0.71 $\hbar k$ due to two 10 μm slits and a 25 μm detector spaced by 0.9 m and 1.2 m respectively.

2) Velocity spread of Na beam reduced to 11% FWHM by seeding the Na in an Ar supersonic jet[11].

3) Experimental realization of the two-state system $3^2S_{1/2}$, F=2, m_F=2 $\longleftrightarrow$ $3^2P_{3/2}$, F'=3, m_F'=3 by using optical pumping to transfer 90% of the F=2 atoms into the m_F=2 state and the resulting state-selective radiative deflection to reduce the fraction of atoms in F=1 (or bound together as

dimers) to 6%[23].

4) Well characterized Gaussian laser profile with fine adjustment of parallelism of field nodes and atomic beam.

5) Computer control of detector scan and recording of data - all data reported here were taken with a one second dwell time and 10 μm steps of the detector, corresponding to 0.24 $\hbar k$ of deflection.

The deflecting radiation field was produced by focusing (with a cylindrical lens) the elliptically expanded and circularly polarized Gaussian beam from a single mode dye laser (Coherent 599-21) onto a flat mirror. The focused waists were measured with an EG&G RL-128G Reticon. Waists of $70\mu m$ and $44\mu m$ (e^{-2} radii of intensity) were used, resulting in τ's of ~70 ns and ~45 ns. The collimated vertical waist was 3.6 mm for both cases. The close proximity (~5 mm) of the atomic beam to the flat mirror (relative to the confocal parameter of the focused waist) and precise control of the angle of the mirror (~10^{-5} rad using a PZT) allow realization of a plane standing-wave with wavefronts parallel to the atomic beam. This parallelism, found crucial in this experiment, is an increasingly stringent requirement for longer interaction times since an atom must not move a significant fraction of a wavelength across the standing-wave while traversing the focused waist. The detuning of the deflecting laser, measured using saturated absorption in a sodium cell, was always *below* the F=2→F'=3 resonance to ensure that F=1 atoms did not contribute to the deflection signal.

The experimental results are presented in Figs. 1, 2 and 3, and Table 1. Diffraction patterns for three different values of the parameter z are shown in Fig. 1. The data are corrected for background and undeflected F=1 atoms. The details of these subtractions are derived from a close examination of the raw undeflected beam profile and their effect can be seen in Fig. 1a. All of these scans exhibit a slight displacement of the diffraction peak at +2 $\hbar k$, an isolated artifact due to a reproducible non-linearity in the detector drive. The theoretical curves in Fig. 1b and 1c are

obtained by convolving the result of Eq. 3 with the measured atomic beam profile (FWHM=.71 $\hbar k$) and velocity distribution ($\Delta v/v$ FWHM = 11%).

Table 1 displays parameters for scans taken over a wide range of laser powers and detunings and at two different interaction times. The conversion from laser intensity to Ω_o is:[24] (10 MHz)/(12.7 mW/cm^2). The rms momentum is corrected for small contributions from the finite beam collimation and velocity distribution. We note that the average momentum transferred is almost always less than 0.25 $\hbar k$ indicating excellent overall symmetry of the patterns.

For all data taken, we have had to divide the value of z calculated using Eq. 5 by a factor of 2 to obtain theoretical predictions in good agreement with the experiment. We have confidence that our measured parameters yeild the correct value of z to within 20%, where the principle error arises from uncertainties in determining the absolute laser intensity. At this time, we have no explanation for this discrepancy, which is quite constant in different runs and at the two interaction times studied. Further experimental studies of traveling wave deflection and the effects of optical misalignment are underway in an attempt to determine its origin. The values of z listed in Table 1 and used in Figs. 1 and 2 have been divided by this factor of 2.

The rms momentum for each scan is plotted as a function of z, along with Eq. 6, in Fig. 2. The overall agreement between the theory and our experimental results is reasonable except for the factor of 2.

In our theory the deflection pattern and p_{rms} are determined solely through the parameter z (Eq. 5). We have been able to verify the predicted Δ^{-1} dependence of p_{rms} to within 5% (standard deviation) by restricting attention to data taken within one run (eg. the solid squares in Fig. 2) whose other parameters are held constant. Since Ω_o^2 is proportional to laser intensity, our use of cylindrical optics results in $\Omega_o^2\tau$ being independent of τ at a fixed laser power. Comparing scans from runs B and C (Table 1) with identical values of $\Omega_o^2\tau$ (i.e. laser power) and Δ, we find

values of p_{rms} which agree to within 4% (standard deviation). In addition, this comparison reveals nearly identical diffraction patterns, an example of which is shown in Fig. 3. In general, the agreement between measured and predicted diffraction patterns is improved by choosing the value of z which corresponds (according to Eq. 6) to the measured value of p_{rms}, confirming the predicted Bessel function pattern (Eq. 3).

The sharp quantization of the transferred momentum can be interpreted as the diffraction of the atomic deBroglie waves by the intensity grating of the standing light wave, which diffracts at 2 $\hbar k$ intervals due to its spatial periodicity of $\lambda/2$. In a complimentary view, the $2\hbar k$ periodicity arises from absorption/stimulated emission of photon pairs from the counterpropagating traveling waves. Ironically these complimentary explanations would have been equally unpalatable to a nineteenth century physicist: either the atom must be regarded as a wave or the light as consisting of particles.

In conclusion, we have observed the near-resonant Kapitza-Dirac effect using a beam of sodium atoms and a standing-wave laser field, under conditions where spontaneous emission can be ignored. Individual diffraction patterns are in good agreement with our theoretical predictions and the dependence of the rms deflection on laser power and frequency is consistent with the theory except for the factor of 2.

We gratefully acknowledge the support of the National Science Foundation through grants PHY83-07172-A01 and PHY-8514748 (ROA program). We are also grateful to S. Chan, K. Schwartz, and R. Stoner for technical assistance and to D. Kleppner for critical reading of the manuscript.

References

a) Permanent Address: Department of Physics, Bates College, Lewiston, Maine 04240.

1. P.L. Kapitza and P.A.M. Dirac, Proc. Cambridge Phil. Soc. 29, 297 (1933).

2. H. Schwarz, Z. Phys. 204, 276 (1967); L.S. Bartell, R.R. Roskos, and H.B. Thompson, Phys. Rev. 166, 1494 (1968); Y. Takeda and I. Matsui, J. Phys. Soc. Jpn. 25, 1202 (1968); H. Chr. Pfeiffer, Phys. Lett. 264, 362 (1968).

3. Y.W. Chan and W.L. Tsui, Phys. Rev. A 20, 294 (1979) and references therein.

4. E.A. Coutsias and J.K. McIver, Phys. Rev. A 31, 3155 (1985) and references therein.

5. S. Altschuler, L.M. Frantz and R. Braunstein, Phys. Rev. Lett. 17, 231 (1966).

6. J. Opt. Soc. Am. B 2 (Feature Issue: The Mechanical Effects of Light), Nov. 1985.

7. E. Arimondo, H. Lew, and T. Oka, Phys. Rev. Lett. 43, 753 (1979).

8. V.A. Grinchuk, E.F. Kuzin, M.L. Nagaeva, G.A. Ryabenko, A.P. Kazantsev, G.I. Surdutovich, and V.P. Yakovlev, Phys. Lett. 864, 136 (1981).

9. P.E. Moskowitz, P.L. Gould, S.R. Atlas, and D.E. Pritchard, Phys. Rev. Lett. 51, 370 (1983).

10. V.A. Grinchuk, A.P. Kazantsev, E.F. Kuzin, M.L. Nagaeva, G.A. Ryabenko, G.I. Surdutovich, and V.P. Yakovlev, Sov. Phys. JETP 59, 56 (1984).

11. P.E. Moskowitz, P.L. Gould and D.E. Pritchard, in Ref. 6.

12. R.J. Cook and A.F. Bernhardt, Phys. Rev. A 18, 2533 (1978).

13. A.P. Kazantsev, G.I. Surdutovich and V.P. Yakovlev, JETP Lett. 31, 509 (1980).

14. A.F. Bernhardt and B.W. Shore, Phys. Rev. A 23, 1290 (1981).

15. E. Arimondo, A. Bambini and S. Stenholm, Phys. Rev. A 24, 898 (1981).

16. C. Tanguy, S. Reynaud, M. Matsuoka and C. Cohen-Tannoudji, Opt. Commun. 44, 249 (1983).

17. C. Tanguy, S. Reynaud and C. Cohen-Tannoudji, J. Phys. B 17, 4623 (1984).

18. P.E. Moskowitz, "Diffraction of an Atomic Beam by Standing Wave Radiation", thesis, MIT, 1984 (unpublished).

19. A.P. Kazantsev G.I. Surdutovich, V.P. Yakovlev, and D.O. Chudesnikov, Opt. Commun. 52, 311 (1985).

20. P.L. Gould, thesis, MIT, in preparation.

21. N. Rosen and C. Zener, Phys. Rev. 40, 502 (1932).

22. A. Bambini and P.R. Berman, Phys. Rev. A 23, 2496 (1981).

23. P.L. Gould, G.A. Ruff and D.E. Pritchard, in preparation.

24. M.L. Citron, H.R. Gray, C.W. Gabel, and C.R. Stroud, Jr., Phys. Rev. A16, 1507 (1977).

Figure Captions

Figure 1. Atomic diffraction patterns corresponding to the following scans (listed in Table 1): (a) scan A4, (b) scan A5, (c) scan A3. In (a), the raw (dotted line) and corrected data (solid line) are compared. In (b) and (c), we display the theoretical fits (dashed line), described in the text, and the corrected data (solid line). All curves are normalized. A typical count rate is $\sim 10^6$atoms/sec per scan.

Table 1. Parameters for individual diffraction patterns. Data were taken in three runs. For run A, $\tau = 4.5\Gamma^{-1}$ = 72 ns; run B, $\tau = 4.4\Gamma^{-1}$ = 71 ns; run C, $\tau = 2.8\Gamma^{-1}$ = 45 ns. The scans are listed in the order recorded.

Figure 2. rms momentum vs. z. Data points from Table 1 are depicted by: circles - run A, squares - run B, and triangles - run C. The solid squares represent scans B1, B2, B3, and B4, and their significance is discussed in the text. The dashed line is Eq. (6).

Figure 3. Diffraction patterns for scans B8 (solid line) and C2 (dashed line) from Table 1. The curves correspond to identical laser powers and detunings but different values of τ.

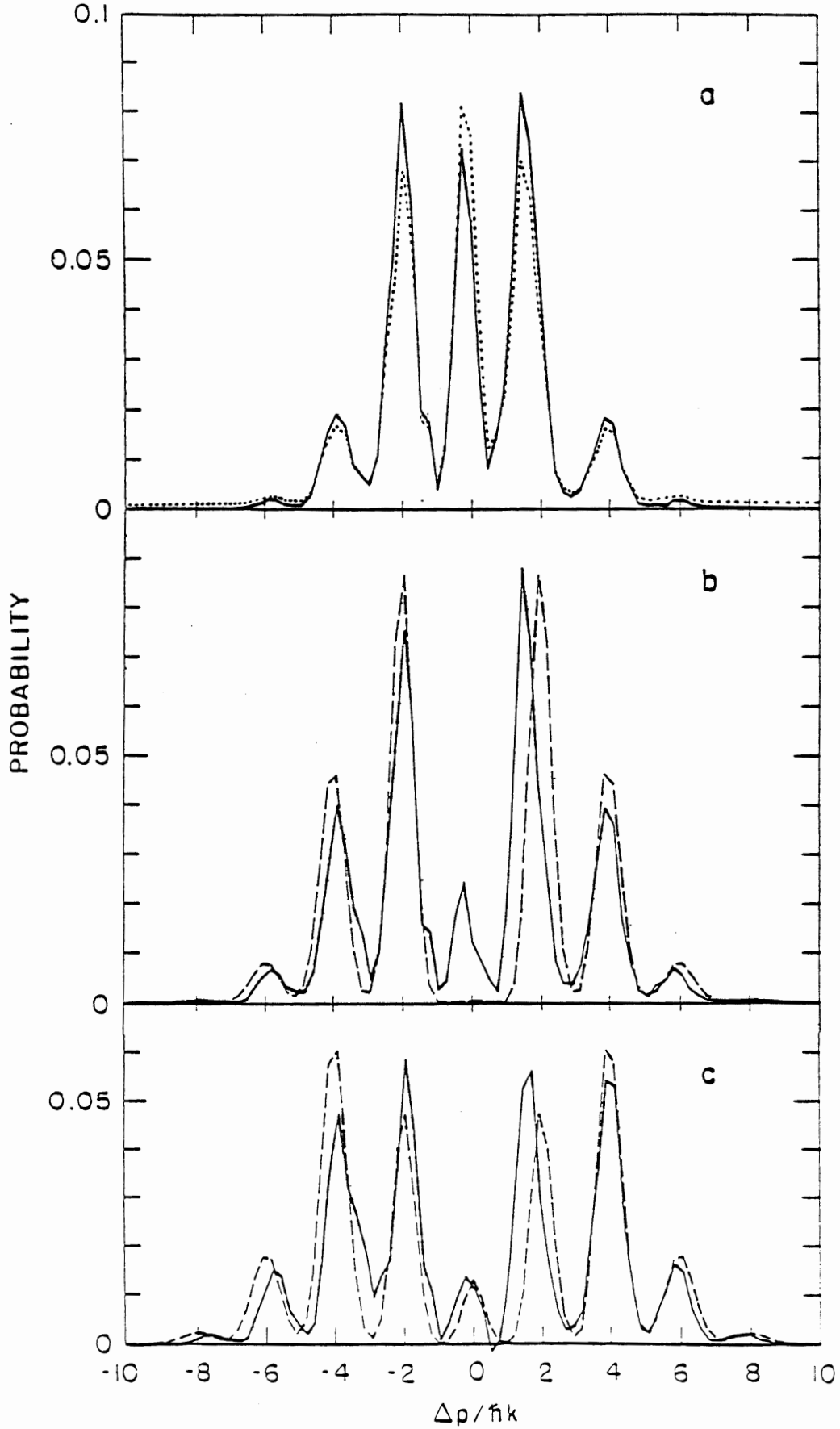

Figure 1

scan	power (mW)	$\Omega_o/2\pi$ (MHz)	$\Delta/2\pi$ (MHz)	$\bar{N}$	z	$\frac{P_{rms}}{\hbar k}$
A1	9.0	135	-444	.24	5.91	7.92
A2	9.0	135	-731	.09	3.59	5.23
A3	9.0	135	-922	.06	2.84	3.59
A4	2.0	64	-349	.09	1.69	2.16
A5	2.0	64	-253	.17	2.33	2.92
A6	0.5	32	-157	.11	0.94	1.21
A7	2.0	64	-349	.09	1.69	1.66
B1	1.6	57	-186	.24	2.48	4.64
B2	1.6	57	-279	.11	1.65	3.01
B3	1.6	57	-372	.06	1.24	2.24
B4	1.6	57	-558	.03	.83	1.52
B5	0.4	28	-93	.24	1.24	1.97
B6	0.4	28	-186	.06	.62	1.10
B7	6.4	114	-372	.24	4.96	8.30
B8	6.4	114	-558	.11	3.31	5.64
B9	6.4	114	-744	.06	2.48	3.94
B10	6.4	114	-930	.04	1.98	3.08
B11	6.4	114	-1116	.03	1.65	2.45
B12	6.4	114	-372	.24	4.96	8.08
C1	6.4	144	-372	.23	4.96	7.61
C2	6.4	144	-558	.11	3.31	5.55
C3	6.4	144	-744	.06	2.48	3.87
C4	6.4	144	-930	.04	1.98	3.52
C5	6.4	144	-1116	.03	1.65	2.58
C6	1.6	72	-186	.23	2.48	4.49
C7	1.6	72	-279	.11	1.65	3.02
C8	1.6	72	-372	.06	1.24	2.39
C9	1.6	72	-558	.03	.83	1.67
C10	0.4	36	-93	.23	1.24	1.96
C11	0.4	36	-186	.06	.62	1.17

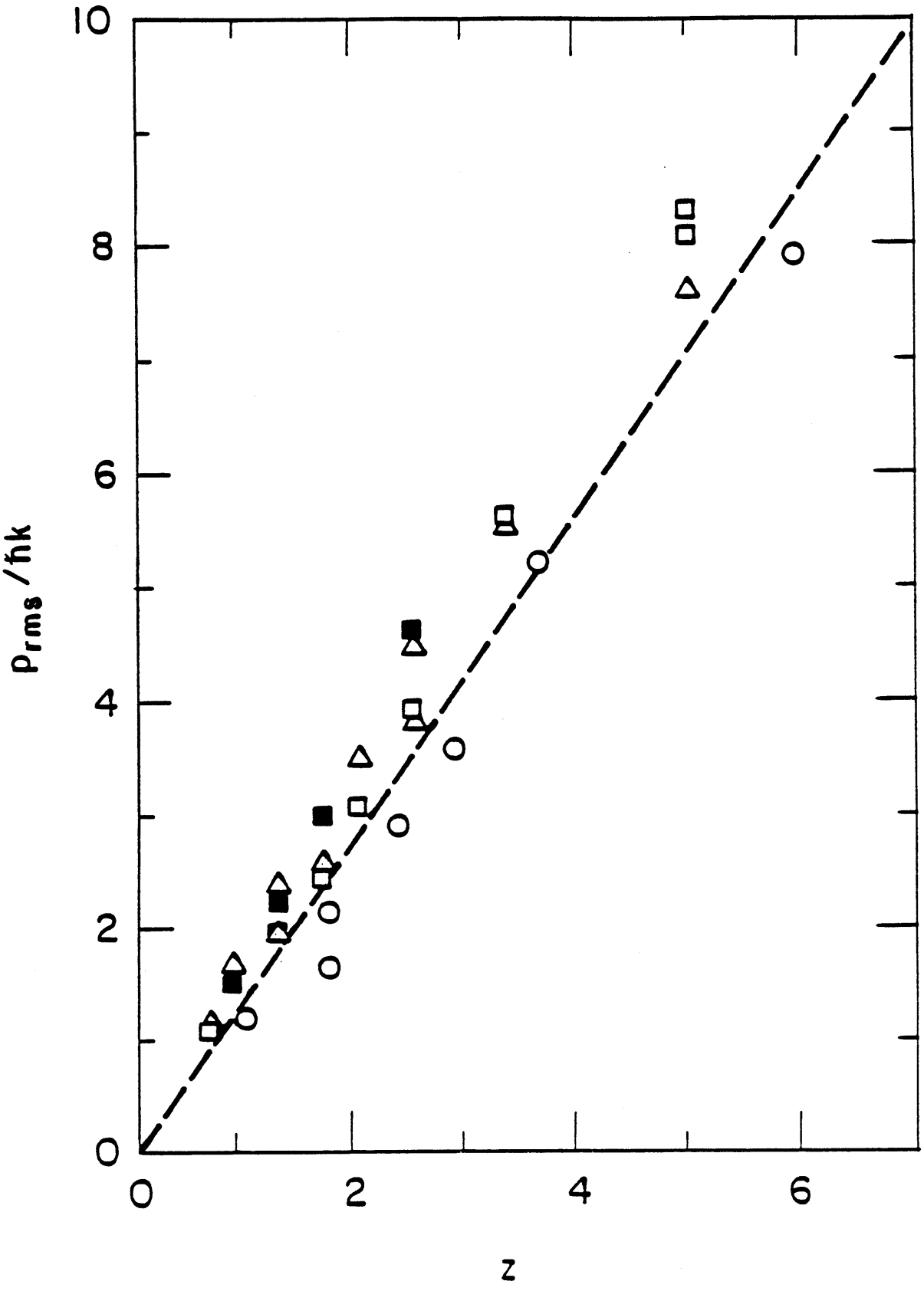

Figure 2

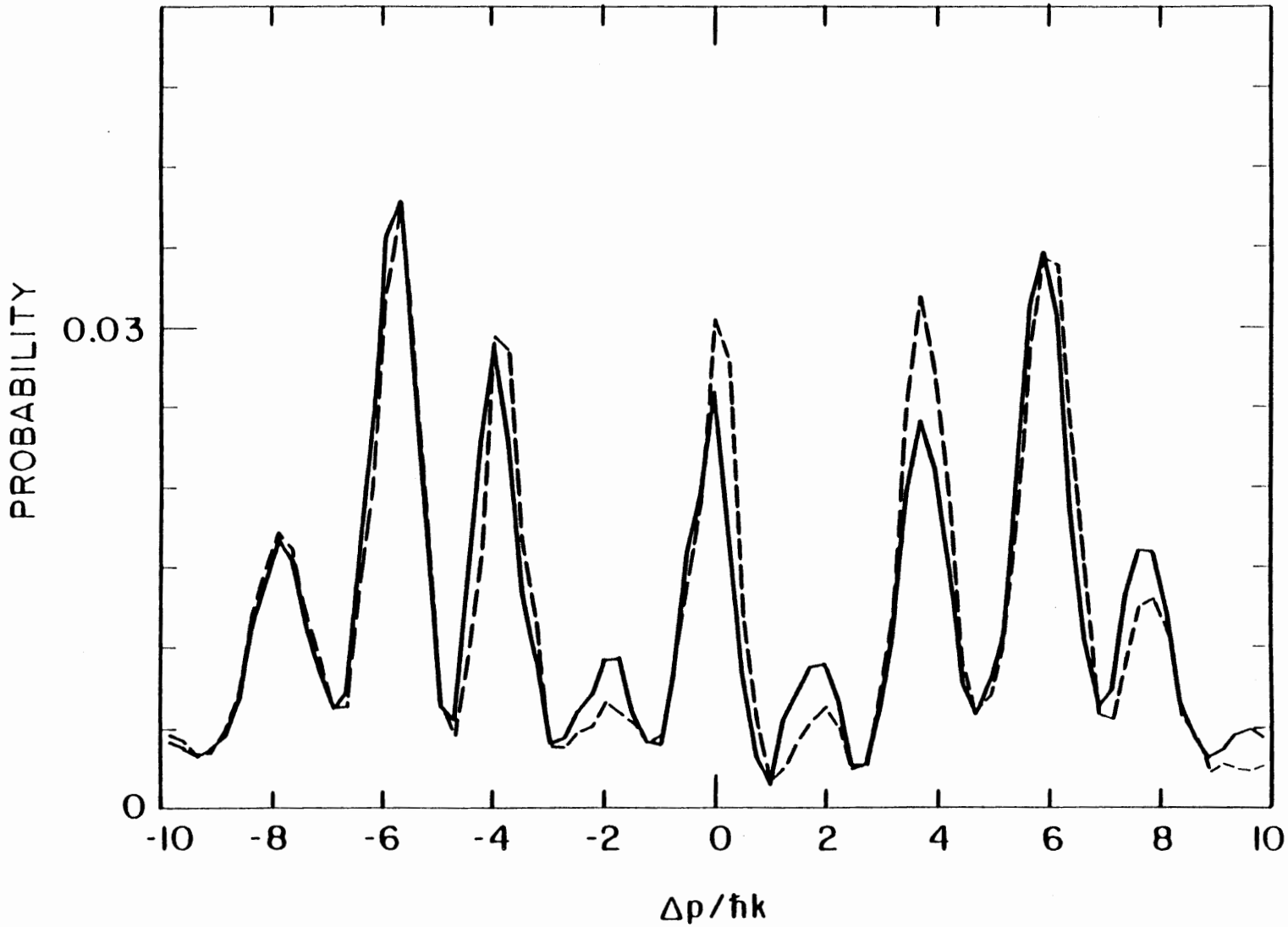

Figure 3

III.C. Detailed Theory of Atomic Diffraction

In this section we consider in detail the theory of standing-wave diffraction in the absence of spontaneous decay. As a first step (Section 1.a), we derive the coefficients of the atomic wave function after interacting with the standing-wave field. A particular functional form of the laser profile (the Rosen-Zener case) allows an analytic solution in terms of hypergeometric functions. Subsequent simplifying assumptions can be made in the limit of large detuning. The momentum distribution is then obtained (Section 1.b) by Fourier transforming the wavefunction. Momentum transfers of odd and even multiples of $\hbar k$ are distinguished and the adiabatic elimination of the odd peaks at large detuning is discussed. The rms momentum transfer is calculated from this momentum distribution in Section 1.c. Generalization of the theory for application to our Gaussian laser profile is carried out in Section 1.d. Finally in Section 2, we justify our neglect of spontaneous decay by calculating the number of spontaneous decays which occur during the interaction.

1. *Momentum Distribution for Adiabatic Off-Resonant Interaction*

a. Wavefunction

We shall consider the interaction of a two-state atom with a near-resonant linearly polarized standing-wave field:

$$\vec{E}(x,t) = 2\hat{\epsilon}_z E_o f(t) \cos kx \cos \omega t \tag{1}$$

where E_0 is the peak electric field due to one of the two traveling waves which form the standing wave, and f(t) expresses the smooth time dependence of the field seen by the atom in its passage through the laser beam along y (y=vt). The time t=0 corresponds to the peak of the field, where f(t=0)=1.

In the following, we will ignore the effects of spontaneous decay. This is justified by keeping $\bar{N}$ (calculated in Section III.C.2) much less than unity.

We will start with the wavefunction in the interaction representation:

$$\Psi(x,t) = a_g(x,t)e^{-iE_g t/\hbar}|g> + a_e(x,t)e^{-iE_e t/\hbar}|e> \tag{2}$$

where the labels g and e denote the ground and excited states, respectively. Here the energy difference between states is $\hbar\omega_o = E_e - E_g$. The interaction Hamiltonian (in the dipole approximation) is $H_{int} = -\vec{\mu}\cdot\vec{E}$, where $\vec{\mu}$ is the atomic dipole moment. The time-dependent Schrodinger equation, in the rotating-wave approximation, yields the following coupled equations for the wavefunction coefficients (LOU83):

$$\frac{da_g}{dt} = -i\Omega_o \cos kx f(t) e^{i\Delta t} a_e \tag{3a}$$

$$\frac{da_e}{dt} = -i\Omega_o \cos kx f(t) e^{-i\Delta t} a_g \tag{3b}$$

Here we have defined Ω_o as the peak on-resonant Rabi rate (assumed real) for one of traveling waves and as the laser detuning from resonance:

$$\Omega_o = \frac{<e|\vec{\mu}|g>\cdot\hat{\epsilon}E_o}{\hbar} \tag{4a}$$

$$\Delta = \omega - \omega_o \tag{4b}$$

Equations 3a and 3b can be decoupled by taking another time derivative and substituting appropriately:

$$\frac{d^2a_g}{dt^2} + [-i\Delta - \frac{\frac{df}{dt}}{f}] \cdot \frac{da_g}{dt} + \Omega_o^2 \cos^2 kx f^2(t) a_g = 0 \tag{5a}$$

$$\frac{d^2a_e}{dt^2} + [i\Delta - \frac{\frac{df}{dt}}{f}] \cdot \frac{da_e}{dt} + \Omega_o^2 \cos^2 kx f^2(t) a_e = 0 \tag{5b}$$

These equations are identical except for the sign of Δ.

A particular functional form of f(t) is especially useful for our purposes, as it allows an analytical solution to Eqn. 5 and is a realistic model for our laser profile (i.e. smooth everywhere but with rapidly decreasing wings). This is the so-called Rosen-Zener case (ROZ32, BAB81):

$$f(t) = sech(t/\tau) \tag{6}$$

The Rosen-Zener solution is arrived at by making the following transformation (i.e. change of variables):

$$w = \frac{1}{2}[\tanh(t/\tau)+1] \tag{7}$$

The time derivatives can be written in terms of derivatives with respect to w:

$$\frac{d}{dt} = \frac{1}{2} \cdot \frac{1}{\tau} sech^2(t/\tau) \frac{d}{dw} \tag{8a}$$

$$\frac{d^2}{dt^2} = -\frac{1}{\tau^2} sech^2(t/\tau) \tanh(t/\tau) \frac{d}{dw} + (\frac{1}{2\tau} sech^2(t/\tau))^2 \frac{d^2}{dw^2} \tag{8b}$$

From the definition of f in Eqn. 6, we find

$$\frac{\frac{df}{dt}}{f} = -\frac{1}{2}\tanh(t/\tau) \tag{9}$$

Substituting Eqns. 7 and 9 into Eqn. 5a, we find (recall that Eqn. 5b is identical to Eqn. 5a if the sign of Δ is reversed):

$$w(1-w)\cdot\frac{da_g^2}{dw^2} + [-i\frac{\Delta\tau}{2} + \frac{1}{2} - w]\cdot\frac{da_g}{dw} + \Omega_o^2\tau^2\cos^2kx\cdot a_g = 0 \tag{10}$$

If we now define:

$$\alpha = -\Delta\tau \tag{11a}$$

$$\beta = \Omega_o\pi cos kx \tag{11b}$$

$$a = -b = \beta \tag{11c}$$

$$c = \frac{1}{2}(i\alpha+1), \tag{11d}$$

Eqn. 10 becomes the hypergeometric equation (ABS72):

$$w(1-w)\frac{d^2a_g}{dw^2} + [c-(a+b+c+1)w]\frac{da_g}{dw} - ab\cdot a_g = 0 \tag{12}$$

The general solution to this differential equation is (ABS72):

$$a_g(w) = A_1 F(a,b,c,;w) + A_2 w^{1-c}F(a-c+1,b-c+1,2-c;w) \tag{13}$$

where F is a hypergeometric function and A_1 and A_2 are constants determined by the initial (boundary) conditions. The initial conditions corresponding to the atom being in the ground state before the interaction are:

$$a_g(t=-\infty) = a_g(w=0) = 1 \tag{14a}$$

$$a_e(t=-\infty) = a_e(w=0) = 0 \tag{14b}$$

Using the fact that F(a,b,c; 0) = 1, we see that

$$A_1 = a_g(0) = 1 \tag{15}$$

In order to solve for A_2, we must transform Eqn. (3a) using Eqn. (7) and the following facts:

$$f(t) = sech(t/\tau) = 2 \cdot w^{1/2}(1-w)^{1/2} \tag{16a}$$

$$\frac{d}{dt} = \frac{1}{\tau} \cdot 2w(1-w) \cdot \frac{d}{dw} \tag{17}$$

The result is:

$$a_e = i(-ab)^{-1/2} w^c (1-w)^{1-c+a+b} \frac{da_g}{dw} \tag{18}$$

The derivatives of the hypergeometric functions are evaluated using the following formulae from ABS72 (15.2.1 and 15.2.4):

$$\frac{d}{dw} F(a,b,c;w) = \frac{ab}{c} F(a+1,b+1,c+1;w) \tag{19a}$$

$$\frac{d}{dw}[w^{1-c} F(a-c+1,b-c+1,2-c;w)] = (1-c) w^{-c} F(a-c+1,b-c+1,1-c;w) \tag{19b}$$

Using the following identity (ABS72 15.3.3):

$$(1-w)^{1-c+a+b} F(a+1,b+1,c+1;w) = F(c-a,c-b,1+c;w) \tag{20}$$

we can express $a_e(w)$ in terms of A_1 and A_2:

$$a_e = -i\frac{(-ab)^{-1/2}}{c} \cdot w_c F(c-a, c-b, 1+c; w) \cdot A_1 \tag{21}$$

$$+ i(-ab)^{-1/2}(1-c)(1-w)^{1-c+ab} F(a-c+1, b-c+1, 1-c; w) \cdot A_2$$

Setting $w = 0$ in Eqn. (21) we obtain:

$$A_2 = -i\frac{(-ab)^{-1/2}}{1-c} \cdot a_e(0) = 0 \tag{22}$$

Using Eqns. (13), (15), and (22), we finally obtain for $a_g(w)$:

$$a_g(w) = F(a, b, c: w) \tag{23}$$

and using Eqns. (21), (15) and (22) we obtain for $a_e(w)$:

$$a_e(w) = -i\frac{(-ab)^{1/2}}{c} \cdot w^c \cdot F(c-a, c-b, 1+c; w) \tag{24}$$

We are interested in the wavefunction at t=+∞(w=1):

$$a_g(1) = F(a, b, c; 1) \tag{25}$$

$$a_e(1) = -i\frac{(-ab)^{1/2}}{c} F(c-a, c-b, 1+c; 1) \tag{26}$$

Despite its simpler appearance, $a_g(1)$ is the more difficult to evaluate, so we'll first consider $a_e(1)$. Using ABS72 15.1.20, we find:

$$F(c-a, c-b, 1+c; 1) = \frac{\Gamma(1+c)\Gamma(1+c-(c-a)-(c-b))}{\Gamma(1+c-(c-a))\Gamma(1-c+(c-b))} \tag{27}$$

$$= \frac{\Gamma(1+\frac{1}{2}+i\frac{\alpha}{2})\Gamma(\frac{1}{2}-i\frac{\alpha}{2})}{\Gamma(1+\beta)\Gamma(1-\beta)}$$

Using some convenient properties of the Γ function, (ABS72 6.1.15, 6.1.30, and 6.1.17), this reduces to:

$$F(c-a,c-b,1+c;1) = \frac{1}{\beta}(\frac{1}{2}+i\frac{\alpha}{2})sech(\pi\frac{\alpha}{2})\sin(\pi\beta) \tag{28}$$

so that $a_e(1)$ becomes:

$$a_e(1) = -isech(\pi\frac{\alpha}{2})\cdot\sin(\pi\beta) \tag{29}$$

$$= -isech(\pi\frac{\Delta\tau}{2})\sin(\pi\Omega_o\pi\cos\omega)$$

In order to evaluate $a_g(1)$, we must perform an asymptotic expansion of the hypergeometric function. This is done using formula 15.7.1 in ABS72:

$$F(a,b,c;w) = \sum_{n=0}^{m}\frac{(a)_n(b)_n}{(c)_n}\cdot\frac{w^n}{n!} + 0(|c|^{-m-1}) \tag{30}$$

where:

$$(a)_n = a(a+1)\cdots(a+n-1);\ (a)_o = 1 \tag{31}$$

This expansion is valid for large $|c|$. Recalling Eqn. 12, we see that our expansion will be valid in the limit of large detuning. Expanding to order m=4 and keeping terms of order $\frac{1}{\alpha^4}$ we obtain:

$$a_g(1) = 1 + (i\frac{2\beta^2}{\alpha}) + \frac{1}{2!}(i\frac{2\beta^2}{\alpha})^2 \tag{32}$$

$$+ \frac{1}{3!}(i\frac{2\beta^2}{\alpha})^3[1+\beta^{-2}-\frac{1}{2}\beta^{-4}]$$

$$+ \frac{1}{4!}(i\frac{2\beta^2}{\alpha})^4[1-11\beta^{-2}-2\beta^{-4}+0\cdot\beta^{-6}] + 0(\alpha^{-5})$$

We note that if $\beta>>1$, this expansion approaches the expansion for the exponential:

$$e^{i(\frac{2\beta^2}{\alpha})} = \sum_{n=0}^{\infty} \frac{1}{n!}(i\frac{2\beta^2}{\alpha})^n \tag{33}$$

Therefore, we will approximate the hypergeometric function by this exponential:

$$a_g(1) = F(\beta,-\beta,\frac{1}{2}(i\alpha+1);1) \approx e^{i(2\beta^2/\alpha)} \tag{34}$$

In order to check the validity of this approximation we have evaluated and compared expansions (30) and (33) for various values of α and $\beta_o = \Omega_o \tau$. If we denote the terms of the expansion in Eqn. 30 (with w=1) by A_n:

$$A_n = \frac{1}{n!}\frac{(a)_n(b)_n}{(c)_n} = \frac{1}{n!}\frac{(\beta)_n(-\beta)_n}{(\frac{1}{2}(1+i\alpha))_n} \tag{35}$$

it can be shown that the following recursion relations hold for the real and imaginary parts of A_n:

$$Re(A_n) = \frac{2}{n}\cdot\frac{(n-1)^2-\beta^2}{(2n-1)^2+\alpha^2}\cdot[(2n-1)Re(A_{n-1})+\alpha Im(A_{n-1})] \tag{36}$$

$$Im(A_n) = \frac{2}{n}\frac{(n-1)^2-\beta^2}{(2n-1)^2+\alpha^2}[(2n-1)Im(A_{n-1})-\alpha Re(A_{n-1})]$$

where $Re(A_0) = 1$ and $Im(A_0) = 0$.

For the exponential, we denote the terms of the expansion in Eqn. 33 by B_n:

$$B_n = \frac{1}{n!}i^n(\frac{2\beta^2}{\alpha})^n \tag{37}$$

The real and imaginary parts obey the following recursion relation:

$$Re(B_n) = -\frac{1}{n}\frac{2\beta^2}{\alpha} Im(B_{n-1}) \tag{38}$$

$$\mathrm{Im}(B_n) = \frac{1}{n}\frac{2\beta^2}{\alpha} \cdot \mathrm{Re}(B_{n-1})$$

with $\mathrm{Re}(B_0) = 1$ and $\mathrm{Im}(B_0) = 0$.

The real and imaginary parts of the sums in Eqns. 30 and 33 have been calculated as a function of x (recall that $\beta=\beta_o \cos kx$), using the recursion relations in Eqns. 36 and 38. An example is shown in Fig. 1 where we compare both real and imaginary parts of the two expansions. For this example, $\alpha = 100$, $\beta_o = 20.1$ and $\frac{2\beta_o^2}{\alpha} = 8.08$, which would be typical for our experimental parameters. The sums for the hypergeometric function (Eqn. 30) and the exponential (Eqn. 33) required ~20 and ~30 terms, respectively, for convergence. The two functions obviously agree very well. We have verified this agreement over the range of parameters corresponding to our experimental conditions.

b. *Momentum Distribution*

Now that we have solved for the wavefunction (Eqns. 29 and 34), we must transform from position to momentum space to determine the momentum distribution. We need to take the Fourier transforms of the coefficients, and since both coefficients are periodic in x, these reduce to Fourier sums. The magnitude squared of the n^{th} order coefficient will be the probability, P_n, that the atom gains momentum $n\hbar k$ from the interaction.

Focusing first on $a_e(1)$:

$$a_e(1) = \sum_{n=-\infty}^{\infty} c_n e^{inkx} \tag{39}$$

The coefficients are easily evaluated using Eqn. 29:

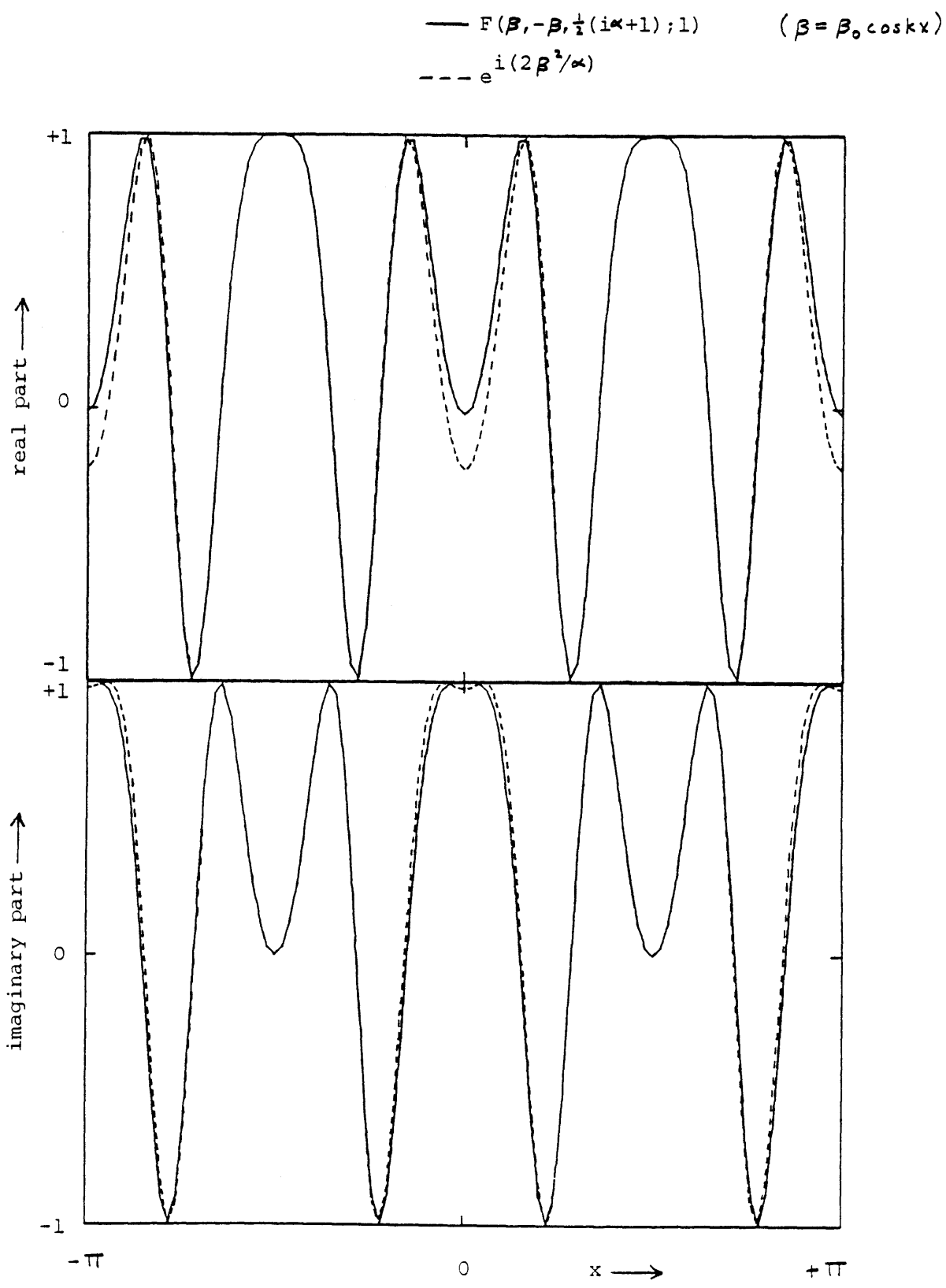
F(β, -β, ½(iα+1); 1)
(β = β₀ cos kx)
e^{i(2β²/α)}
+1
0
-1
real part
+1
0
-1
imaginary part
-π
0
x
+π

Figure 1

$$c_n = \frac{k}{2\pi}\int_{-\lambda/2}^{\lambda/2} a_e(1)e^{-inkx}dx \qquad (40)$$

$$= -isech\,(\pi\frac{\Delta\tau}{2})sin\frac{n\pi}{2}\cdot J_n(\pi\Omega_o\tau)$$

The resulting probability distribution is:

$$P_{e,n} = |c_n|^2 = sech^2(\pi\frac{\Delta\tau}{2})J_n^2(\pi\Omega_o\tau) \quad \text{for } n \text{ odd} \qquad (41)$$

$$0 \quad \text{for } n \text{ even}$$

where the subscript e reminds us that the atom is in the excited state. This expression coincides with the result displayed in KSY80 (note that they define $2\Delta=\omega-\omega_o$ as the detuning). In addition, for $\Delta=0$, the expression reduces to a straightforward generalization of the results of COB78 (noting that $\pi\Omega_o\tau = \int_{-\infty}^{\infty}\Omega_o f(t)dt$). That the probability is non-zero only for odd n results from the fact that the atom must have exchanged an odd number of photons with the standing-wave in order to be in the excited state.

The dependence on Δ simply expresses the degree of adiabaticity. If $\Delta\tau\gg1$, then the passage is adiabatic and the atom has very little chance of emerging from the interaction in the excited state (i.e. of making a transition). Therefore the probabilities for odd numbers of photons exchanged is vanishingly small. This is the case in our experiment. In fact the interaction is so adiabatic that these probabilities are less than 10^{-20} (ignoring, of course, spontaneous decay).

Now turning to $a_g(1)$:

$$a_g(1) = \sum_{n=-\infty}^{\infty} d_n e^{inkx} \qquad (42)$$

where, from Eqn. 34:

$$d_n = \frac{k}{2\pi}\int_{-\lambda/2}^{\lambda/2} a_g(1)e^{-inkx}dx \qquad (43)$$

$$= e^{-i\Omega_o^2\tau/\Delta}e^{i\frac{n\pi}{4}}\cos\frac{n\pi}{2}J_{n/2}(\frac{\Omega_o^2\tau}{\Delta})$$

The probability distribution for the ground state is therefore:

$$P_{g,n} = |d_n|^2 = J_{n/2}^2(\frac{\Omega_o^2\tau}{\Delta}) \text{ for } n \textit{ even} \qquad (44)$$

$$0 \text{ for } n \textit{ odd}$$

We see that being in the ground state implies exchange of an even number of photons, as we would expect. For our purposes (i.e. off-resonant adiabatic interaction), the probabilities in Eqn. 41 are totally negligible, so the diffraction pattern is determined entirely by Eqn. 44. Thus we can drop the state label and write:

$$P_n = J_{n/2}^2(\frac{\Omega_o^2\tau}{\Delta}) \text{ for } n \textit{ even} \qquad (45)$$

$$0 \text{ for } n \textit{ odd}$$

An example of this distribution is shown in Fig. 2 (z is the argument of the Bessel function).

c. *RMS momentum*

From this distribution (Eqn. 45), we can calculate the mean square momentum transferred using a summation property for Bessel functions (COB78):

Figure 2: Momentum Distribution

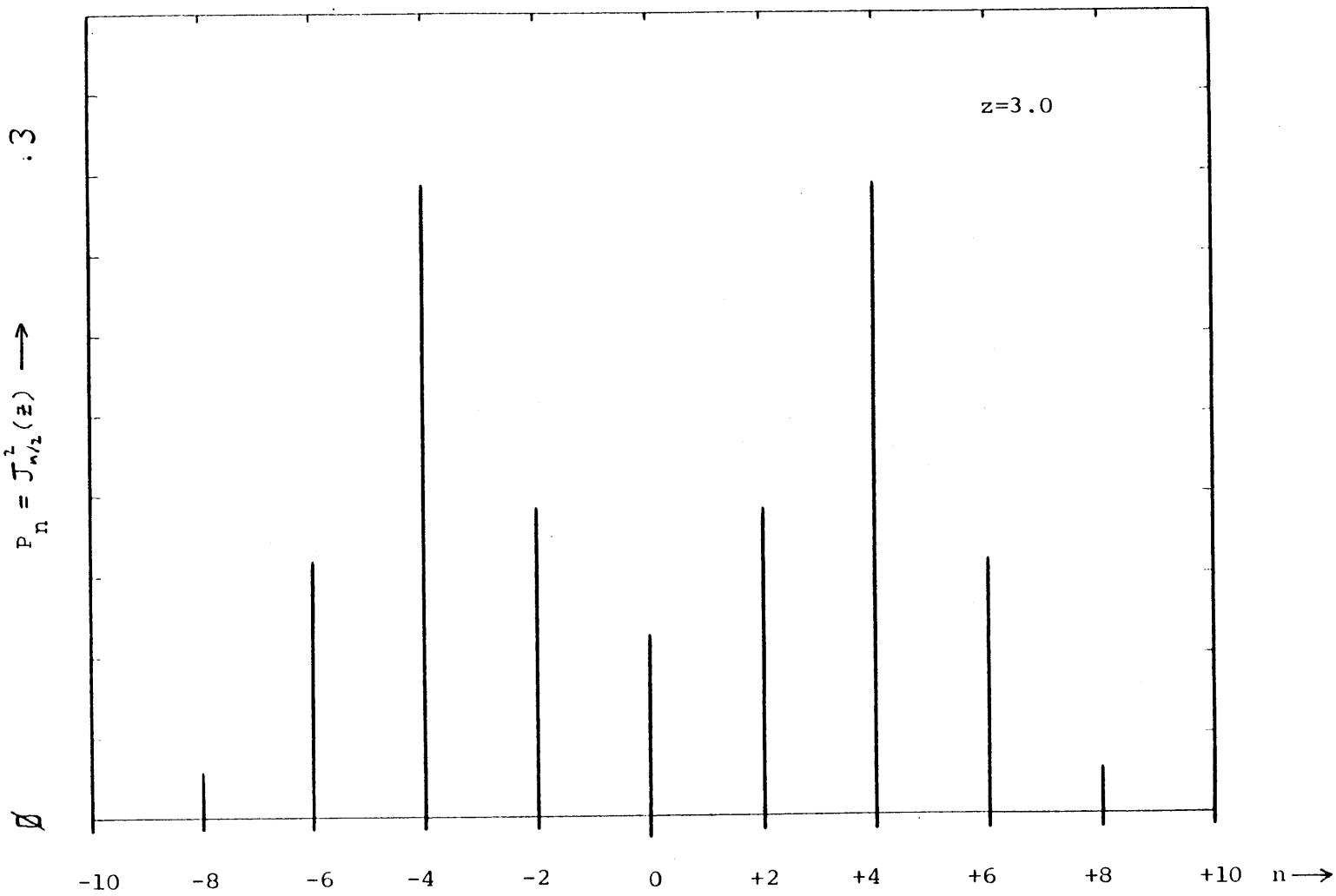

$$\langle p^2 \rangle = \sum_{n=-\infty}^{\infty} (n\hbar k)^2 P_n \tag{46}$$

$$= (\hbar k)^2 \sum_{n\ even} n^2 J_{n/2}^2 \left(\frac{\Omega_o^2 \tau}{\Delta}\right)$$

$$= (\hbar k)^2 2 \cdot \left(\frac{\Omega_o^2 \tau}{\Delta}\right)^2$$

The rms momentum is therefore:

$$p_{rms} = 2^{1/2} \left(\frac{\Omega_o^2 \tau}{\Delta}\right) \cdot \hbar k \tag{47}$$

It is interesting that the deflection (diffraction) pattern and the rms momentum are both characterized by a single parameter: $\frac{\Omega_o^2 \tau}{\Delta}$.

d. Generalization to Gaussian Profile

Although the sech(t/τ) profile is qualitatively similar to our experimental Gaussian field profile (except its wings fall off less rapidly), it would be desireable to extend the theory to an arbitrary laser profile in order to be able to make quantitative comparisons between experiment and theory. In MOS84 and MGP85, the case of a "top-hat" profile:

$$f(t) = 1 \quad \text{for } 0 < t < \tau \tag{48}$$

$$0 \quad \textit{otherwise}$$

is considered using the dressed atom formalism. Under the asssumption that the atom enters and exits the field adiabatically (i.e. assuming adiabatic "wings" for the profile in Eqn. 48, which do not contribute to the deflection), an expansion of the phase of the dressed atom wavefunction in the small parameter $\frac{\Omega_o^2}{\Delta^2}$ yields the following probability distribution (Eqn. 55 in MOS84, Eqn. 17 in MGP85):

$$P_n \approx J_{n/2}^2(\frac{\Omega_o^2 \tau}{2\Delta}) \quad \text{for } n \text{ even} \tag{49}$$

$$= 0 \quad \text{for } n \text{ odd}$$

The argument of the Bessel functions, which we will denote as z, is simply related to the accumulated phase difference between the two dressed states. We can express this as an integral over the interaction:

$$z = \int_{-\infty}^{\infty} \frac{(\Omega_o f(t))^2}{2\Delta} dt \tag{50}$$

If we now apply this formula to the case of the sech(t/τ) profile, we obtain:

$$z = \int_{-\infty}^{\infty} \frac{(\Omega_o sech(t/\tau))^2}{2\Delta} dt = \frac{\Omega_o^2 \tau}{\Delta} \tag{51}$$

which is identical to the result obtained via the Rosen-Zener solution (i.e. Eqn. 45). This gives us confidence in extending this formula to our measured Gaussian profile:

$$f(t) = e^{-(t/\tau)^2} \tag{52}$$

where τ is the transit time for the $\frac{1}{e^2}$ radius of intensity. For this profile:

$$z = \int_{-\infty}^{\infty} \frac{1}{2\Delta} (\Omega_o e^{-(t/\tau)^2})^2 dt = (\frac{\pi}{8})^{1/2} (\frac{\Omega_o^2 \tau}{\Delta}) \tag{53}$$

Therefore, we can write the momentum distribution as:

$$P_n = J_{n/2}^2(z) \quad \text{for } n \text{ even} \tag{54}$$

$$= 0 \quad \text{for } n \text{ odd}$$

with z (for a Gaussian profile) given by Eqn. 53.

Obviously, the expression for the rms momentum (Eqn. 47) is valid for any value of z:

$$p_{rms} = 2^{1/2} z \cdot \hbar k \tag{55}$$

2. *Average Number of Spontaneous Decays*

In the preceding section (III.C.1), we neglected the effects of spontaneous decay of the excited state. This is justified if the average number of spontaneous decays occurring during the interaction, $\bar{N}$, is much less than unity, even if the interaction time is much longer than the natural lifetime.

Using the standing-wave electric field defined in Eqn. 1 and the accompanying definition of Ω_o (Eqn. 4a), we can express the fraction of time spent in the excited state by an atom at position x and time t as (LOU83):

$$\rho(x,t) = \frac{(2\Omega_o f(t)\cdot \cos kx)^2}{2(2\Omega_o f(t)\cdot \cos kx)^2 + 4\Delta^2 + \Gamma^2} \tag{56}$$

This atom will undergo spontaneous decays at a rate:

$$R(x,t) = f(x,t)\cdot \Gamma, \tag{57}$$

so that in traversing the interaction (at a fixed value of x), the atom will undergo an average number of spontaneous decays:

$$N(x) = \int_{-\infty}^{\infty} dt\ R(x,t) \tag{58}$$

Since the atom has an equal probability of entering the field at any value of x, we must average N(x) over x to obtain $\bar{N}$, the average number of spontaneous decays occurring during the interaction:

$$\bar{N} = \frac{2}{\lambda}\int_{-\lambda/4}^{\lambda/4} dx\ N(x) \tag{59}$$

The integration interval is $\frac{\lambda}{2}$, the period of ρ. Using Eqs. 56-59 and reversing the order of integration, we obtain:

$$\bar{N} = \Gamma\cdot\int_{-\infty}^{\infty} dt\cdot\frac{2}{\lambda}\int_{-\lambda/4}^{\lambda/4} dx\cdot\frac{1}{2}\cdot\frac{\gamma_o^2 f^2(t)\cos^2 kx}{\gamma_o^2 f^2(t)\cos^2 kx+1} \tag{60}$$

where

$$\gamma_o^2 = \frac{2(2\Omega_o)^2}{4\Delta^2+\Gamma^2}$$

Evaluating the x integral yields:

$$\bar{N} = \frac{1}{2}\Gamma\cdot\int_{-\infty}^{\infty} dt\,[1-(\gamma_o^2 f^2(t)+1)^{-1/2}] \tag{61}$$

For our Gaussian profile: $f(t) = e^{-(t/\tau)^2}$ the result reduces to:

$$\bar{N} = \Gamma\tau\cdot\int_{o}^{\infty} dz\ \frac{(\gamma_o^2 e^{-2z^2}+1)^{1/2}-1}{(\gamma_o^2 e^{-2z^2}+1)^{1/2}} \tag{62}$$

For γ_o<<1 (e.g. Δ> >Ω_o,Γ), this can be approximated:

$$\bar{N}\sim\Gamma\tau\cdot\frac{1}{4}\left(\frac{\pi}{2}\right)^{1/2}\cdot\gamma_o^2 = (2\pi)^{1/2}\cdot\Gamma\cdot\frac{\Omega_o^2\tau}{4\Delta^2+\Gamma^2} \tag{63}$$

Obviously, the condition $\bar{N}$< <1 is fulfilled (even for $\Gamma\tau$>1) when the value of γ_o (i.e. $\frac{\Omega_o}{\Delta}$) is sufficiently small. In addition, we see that $\bar{N}$ is proportional to $\Omega_o^2\tau$ in this case. With our use of cylindrical optics, $\Omega_o^2\tau$ is proportional to laser power and independent of τ at a fixed laser power (see section III.E).

The result of performing the integral in Eq. 62 numerically is shown in Fig. 3. Saturation is

Figure 3

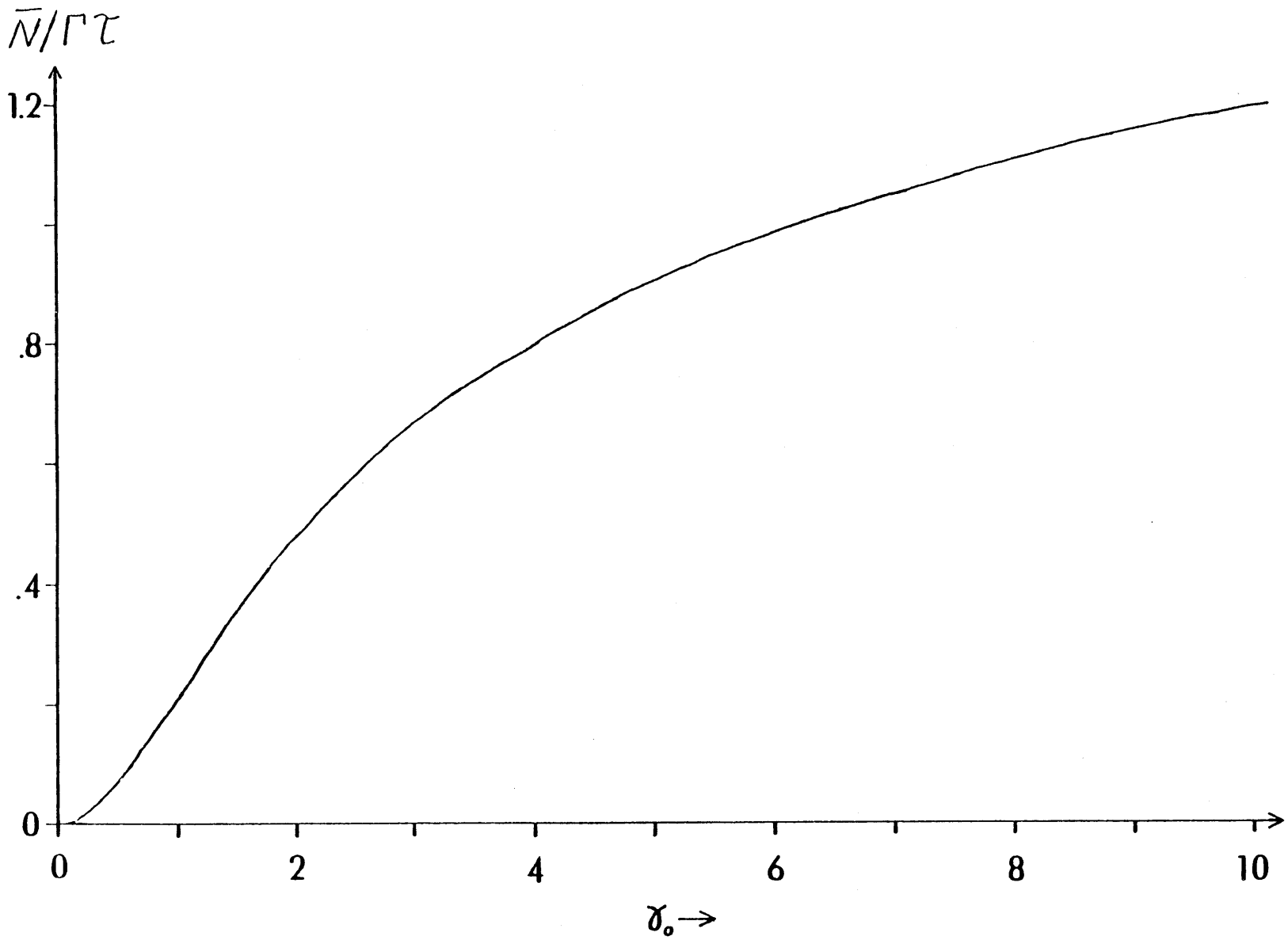

evident at large values of γ_o but $\bar{N}$ does not asymptotically approach a maximum value. This is due to incomplete saturation in the vicinity of the standing-wave nodes and in the wings of the Gaussian profile.

We note here that this calculation of $\bar{N}$ (Eq. 62) gives the spontaneous diffusion coefficient calculated in section IV.C.1 if one realizes that each spontaneous photon contributes $\frac{2}{5}(\hbar k)^2$ to the mean squared momentum.

III.D. Data Analysis

Meaningful comparisons between experiment and theory require careful analysis of the data in order to account for the non-ideal aspects of the experiment; these data may then be compared with theoretical predictions which account for the experimental conditions and resolution. In order to prepare our data for comparison with theory, computer programs were written to eliminate the effects of atomic flux changes, background signal, and undeflected F=1 atoms from the raw data. Theoretical predictions for the momentum distributions (based on measured parameters of the interaction) were then convolved with the finite atomic beam profile and velocity distribution, thereby allowing a direct comparison with the analyzed data. The overall procedure leading to this comparison is depicted schematically in Fig. 1. The details of this procedure will be discussed below.

The data must first be translated from the logarithmic form stored by the data-taking routine into a linear form for further manipulation. It is important that the appropriate magnification be used when the data are recorded to avoid loss of accuracy in the translation.

All data files are then normalized (sum of ordinates = 1) in order to eliminate the effect of atomic flux variation between scans. The variation during a scan is not a major problem due to the fairly rapid scan time (~5 min. for 251 data points). The data taking routine has a limited file size

Figure 1

DATA ANALYSIS FLOWCHART

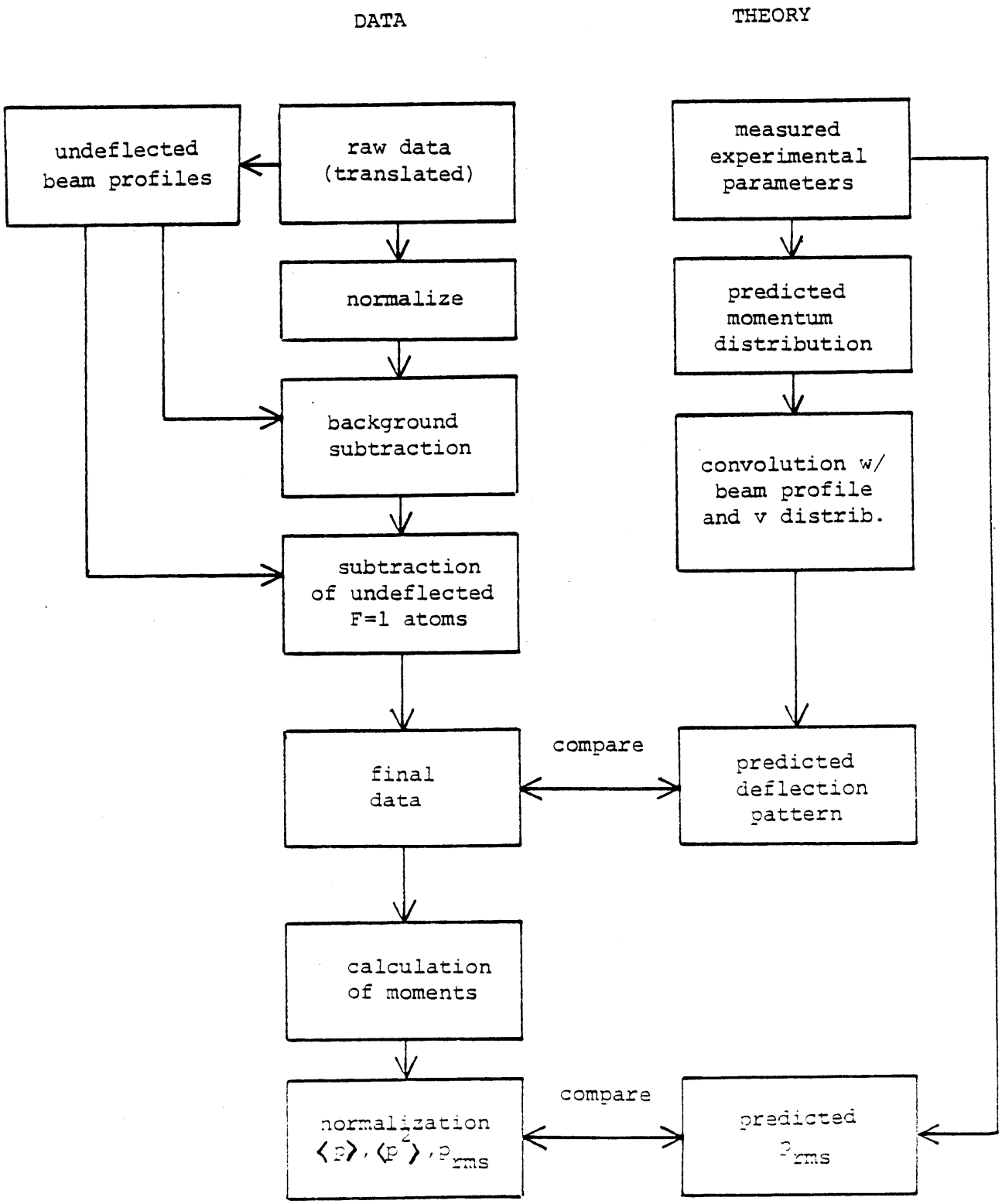

(251 points), so some data, taken under conditions of large deflection, were truncated without recording all deflected atoms. In these cases, the normalization must be modified to account for these unrecorded atoms by interpolating the total signal level from preceding and succeeding scans. Obviously these scans do not yield useful values of p_{rms} but their general shape is interesting nevertheless.

The undeflected atomic beam must be characterized for each run, as the atomic beam alignment (i.e. slit rotation), background level, and optical pumping efficiency do exhibit some variation between runs.

The width of the undeflected beam is a required parameter in the theoretical convolution. The FWHM is measured and a corresponding Gaussian profile is assumed. An example of this Gaussian and the measured profile it represents are shown in Fig. 2. Deflection data in this thesis were taken with two values of this FWHM: .71 $\hbar k$ and .88 $\hbar k$.

The background level is determined by examining the wings of the undeflected beam profile. Blocking the atomic beam almost completely eliminates the background, leading us to believe that its major source is low angle scattering of atoms out of the collimated beam by background gas. The shape of the wings also supports this hypothesis. Proportionality of background and collimated beam is automatically taken care of by normalizing all scans (including the undeflected beam) before background subtraction. The effect of our background subtraction procedure on a typical deflection pattern is shown in Fig. 3.

After background subtraction and subsequent renormalization, the contribution of undeflected atoms in the F=1 ground state must be accounted for. This is done by comparing the undeflected beam profiles with the optical pumping laser on and off. The corresponding signal levels yield the fraction of F=1 atoms in the collimated beam (see Section II.C.2). The undeflected beam profile is multiplied by this fraction and subtracted from each deflection profile. Obviously,

Figure 2 : Undeflected Beam Profile

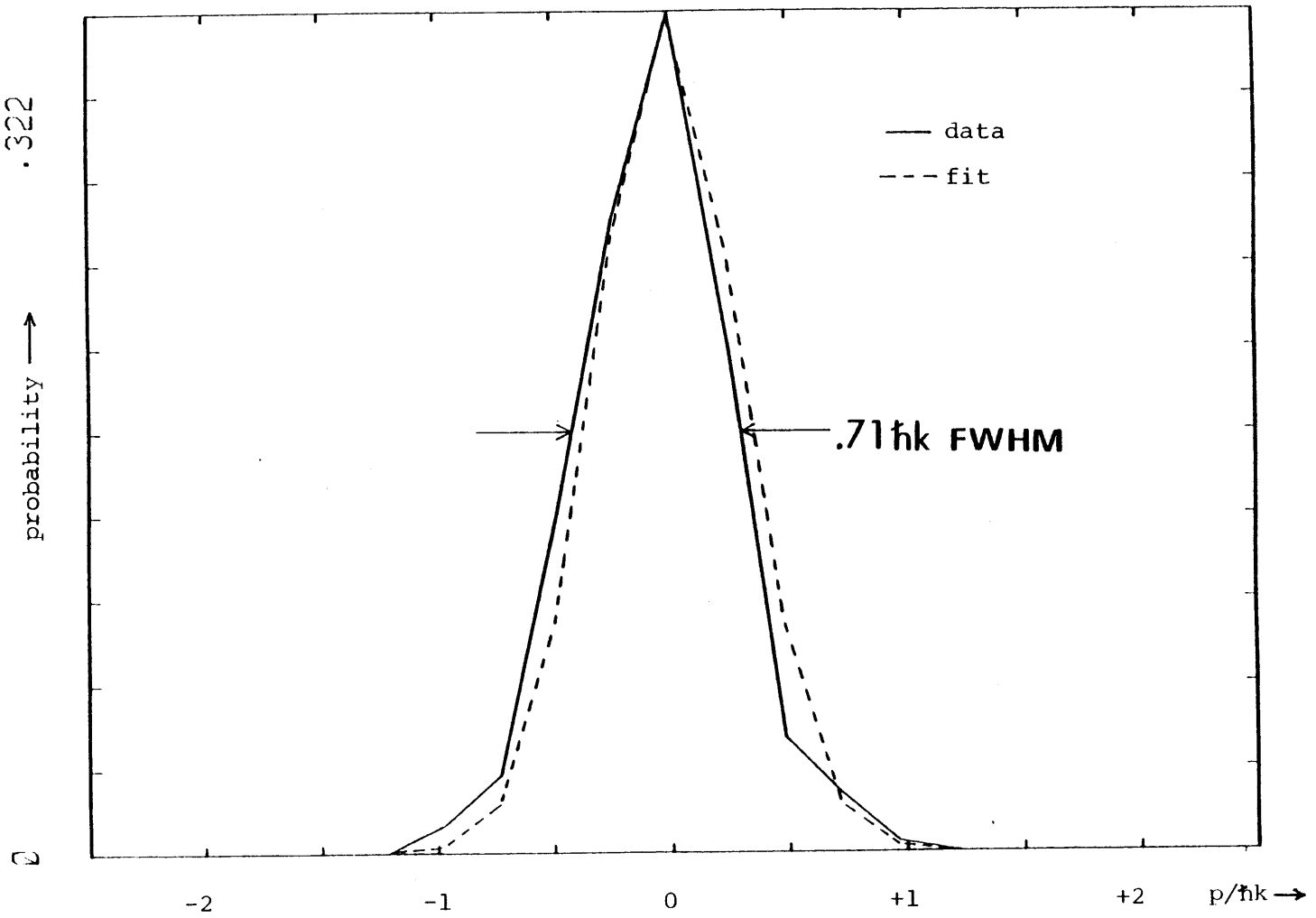

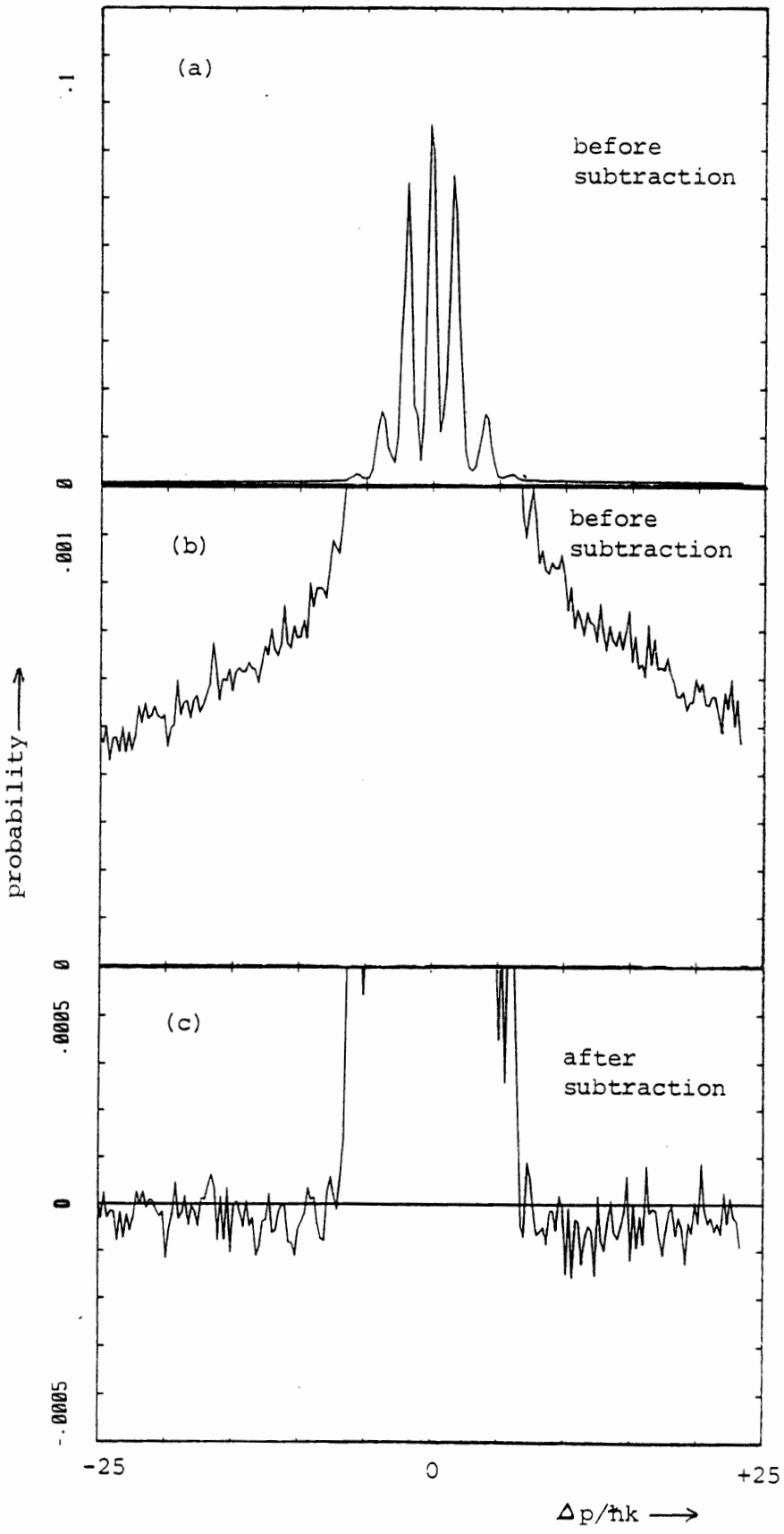

Figure 3: Background Subtraction

this procedure assumes that the F=1 atoms are completely undeflected. Account of finite F=1 deflection is described in Section IV.D where the effect is significant. The final data file is obtained by normalizing the file which results from the F=1 subtraction.

The various moments of the deflection pattern are calculated by simply summing the appropriate elements of the final data file. Two parameters must be specified: the center point of the scan and the conversion from detector steps to photon momentum. The center point is determined from the peak of the undeflected beam profile and is constant during a run. The conversion is calculated from the known apparatus geometry and the average atomic velocity (which is determined by the nozzle temperature). The moments which are calculated include: 1) the normalization (zeroth moment); 2) the average momentum (first moment); and 3) the mean squared momentum (second moment). The sums are truncated at the points where the momentum distribution goes to zero in order to avoid possible effects of incomplete background subtraction. Validity of this truncation is ensured by checking that the moments do not change when more points are included in the sum. The average momentum transfer is a good indication of the overall symmetry of a standing-wave deflection profile and is obviously crucial for traveling-wave deflection experiments. The mean squared momentum yields the rms (root mean squared) momentum for comparison to theoretical predictions.

Theoretical momentum distributions are generated by convolving the predicted probability distribution (Eq. 54 of Section III.C), with the undeflected atomic beam profile and the atomic velocity distribution. The beam profile is assumed to be a Gaussian with a width determined from the measured FWHM. Thus, the probability that an atom (in the undeflected beam) has momentum between t and t + dt (where t is in photon units) is:

$$P(t)dt = \left(\frac{2}{\pi}\right) \cdot \frac{1}{t_o} \cdot e^{-2(t/t_o)^2} dt \qquad (1)$$

where $2t_o$ is the $\frac{1}{e^2} \rightarrow \frac{1}{e^2}$ width (i.e. $t_o = .85 \cdot$ FWHM).

The velocity distribution of the beam is also assumed to be Gaussian, so that the probability for an atom to have longitudinal velocity between v and v + dv is:

$$P(v)dv = (\frac{2}{\pi})^{1/2} \cdot \frac{1}{\alpha} \cdot e^{-2(\bar{v}-v)^2/\alpha^2} dv \qquad (2)$$

where v is the average velocity and 2α is the $\frac{1}{e^2} \rightarrow \frac{1}{e^2}$ width of the distribution. This width ($\Delta v/v$ = 11% FWHM, α/v = .935 for our operating conditions) was measured in previous experiments (MOS84). We note that we have not included any powers of v in Eq. 2 as these would make little difference for our relatively narrow distribution.

Denoting the probability of acquiring momentum n (in photon units) by P_n, we obtain the final probability of detecting an atom at a position between s and s + ds as:

$$P(s)ds = (\frac{2}{\pi}) \cdot \sum_{n=-\infty}^{\infty} P_n \frac{[n \cdot s \cdot (\alpha/v)^2 + t_o^2]}{[s^2(\alpha/v)^2 + t_o^2]^{3/2}} \cdot \exp[-2\frac{(n-s)^2}{s^2(\alpha/v)^2 + t_o^2}] \qquad (3)$$

where we have essentially convolved together the effects of Eqs. 1 and 2, noting that the position at the detector is *inversely* proportional to the longitudinal velocity for a given transverse momentum. The variable s is the position at the detector in units of $(\hbar k/mv) \cdot l$, where l is the distance from the interaction region to the detector.

Despite its apparent complexity (most of it concerns the normalization!), Eq. 3 is really quite easy to understand. It is simply a sum of Gaussians which are centered at positions corresponding to integral numbers (n) of photon momenta. Each Gaussian is weighted by P_n. The Gaussian width is the combined width due to the initial momentum spread (t_o) and the spread ($s(\alpha/v) \approx n(\alpha/v)$) due to the velocity distribution. This latter width increases with increasing deflection, as we would expect.

The values of P_n are calculated from the Bessel function distribution (Eq. 54) arrived at in Section C. The value of z is determined from experimentally measured parameters according to

Eq. 53 (Section C). An example of the effects of the convolution on the momentum distribution is shown in Fig. 4. For this example, the collimation width is .71 ħk (FWHM) and $\Delta v/v$ = 11% FWHM. It is seen that peaks at larger n have a decreased height and increased width, due to the velocity distribution. In fact, the decreasing momentum resolution eventually washes out diffraction structure at large momentum transfers.

The rms momentum transfer is calculated from z according to Eq. 55 of Section C. The effects of the finite beam collimation and velocity distribution on the measured value of p_{rms} are estimated by comparing the prediction of Eq. 55 with the value calculated directly from the convolved profile with the algorithm described earlier in this section. These small corrections are then subtracted from the measured values of p_{rms}.

III.E. Additional Data

A summary of our atomic beam diffraction data is presented in Section B (Figs. 1,2,3 and Table 1). In the present section, we will display and discuss additional data which satisfy our criterion ($\bar{N}$<0.25) for ignoring spontaneous decay.

Diffraction patterns are shown in Figs. 1 and 2 for three values of detuning at a fixed laser power and interaction time. For Fig. 1, the power is 1.6 mW ($\Omega_o/2\pi$ = 57 *MHz*) and τ = 71 *ns*, while for Fig. 2, the power is 9.0 mW ($\Omega_o/2\pi$ = 135 *MHz*) and τ = 72 ns. Due to non-optimum slit rotation for this particular run, the resolution (FWHM of undeflected beam) is .88 ħk for Fig. 1 instead of the optimum value of .71 ħk obtained in Fig. 2. This accounts for the difference in contrast between the two sets of data.

We see that for all scans the overall envelope is a symmetrical two-peaked structure, in accord with classical predictions (MGA83, MOS84, MGP85, KSY80). The overall spread of the beam (measured quantitatively as p_{rms}) is seen to increase as the laser detuning is decreased. In fact, for the scans of Fig. 1 (including an additional scan, not shown, with Δ = -558 MHz), p_{rms} is

Figure 4: Convolution

vertical bars: Bessel function distribution

solid curve: convolution

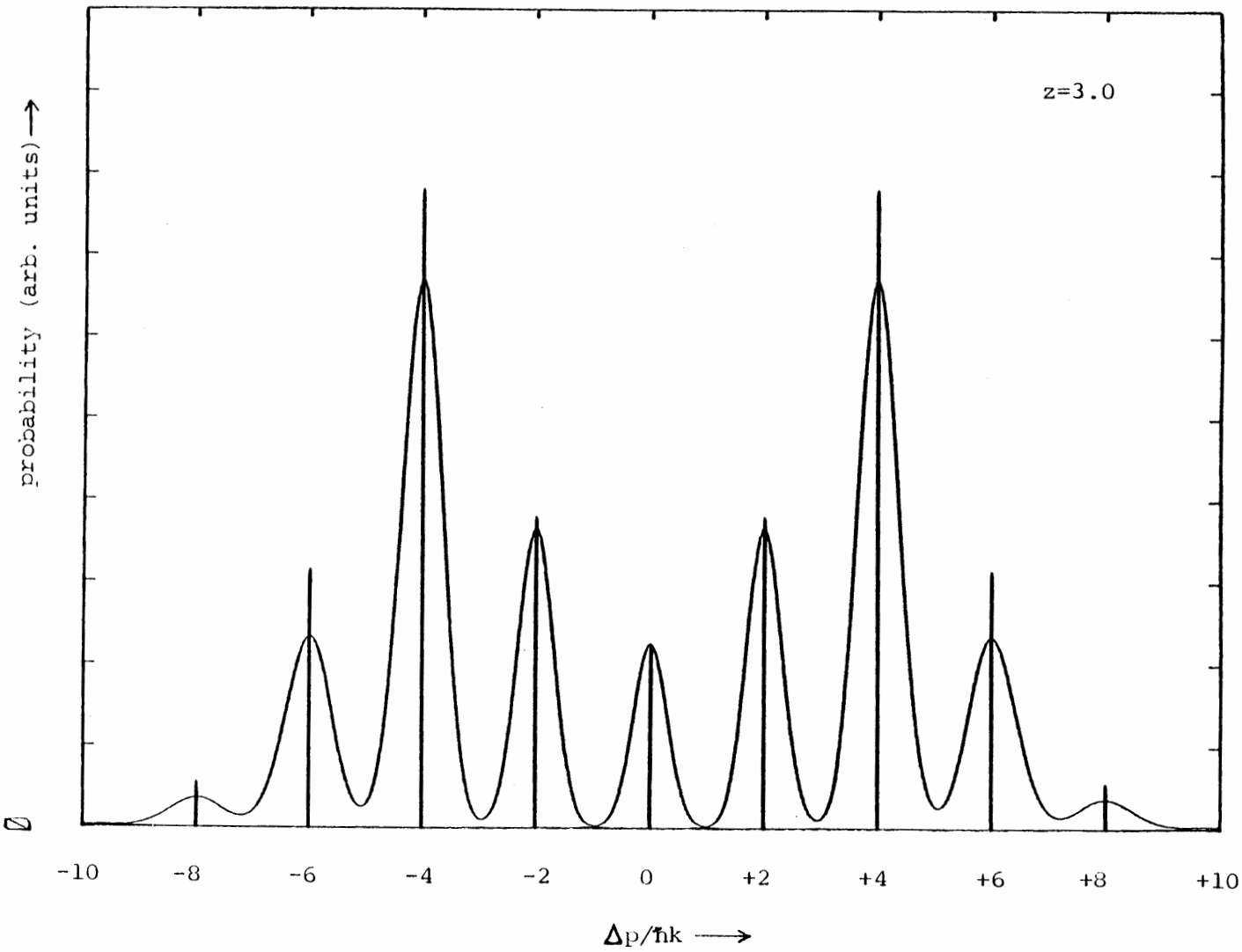

Figure 1

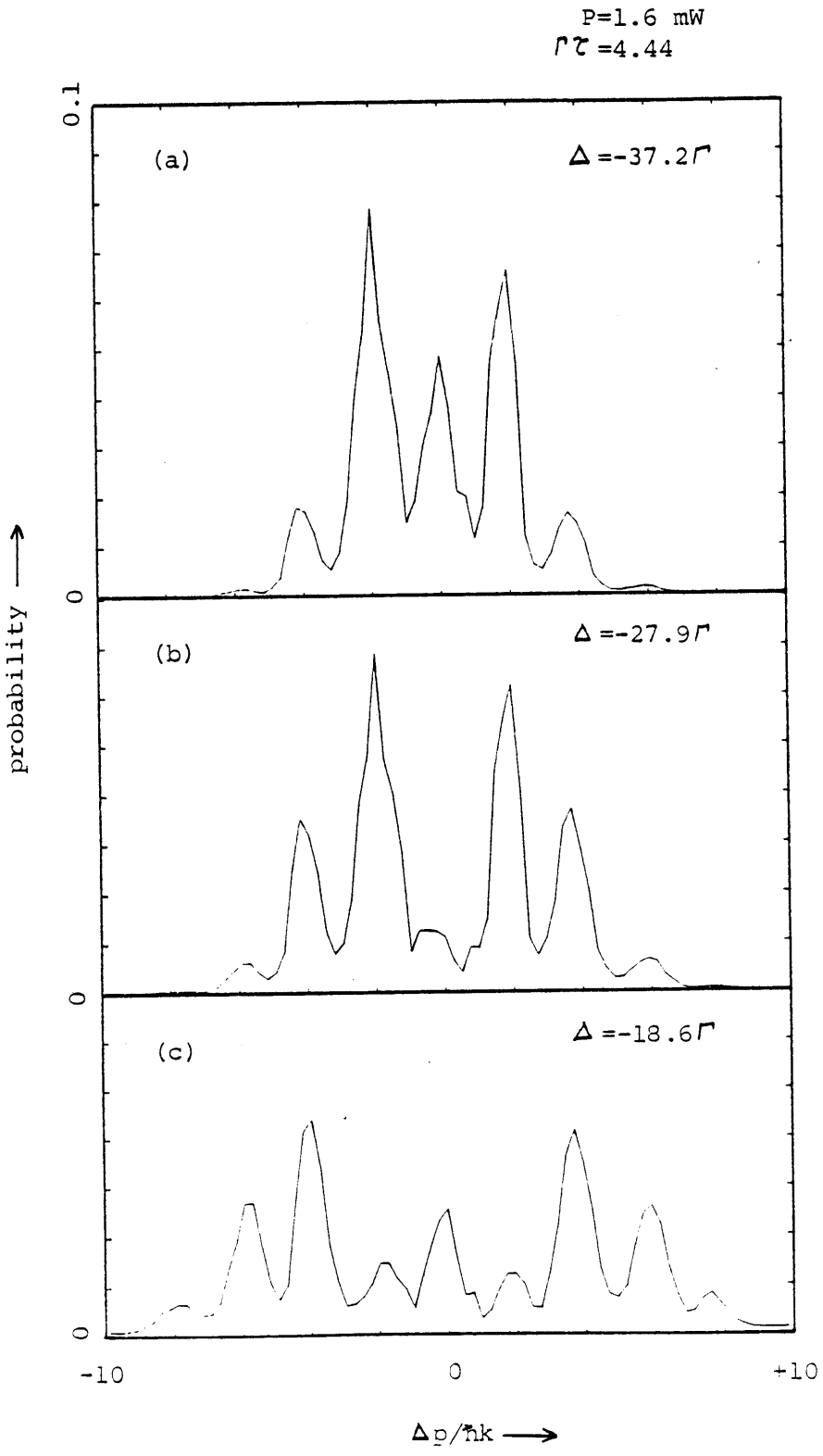
P=1.6 mW
Γτ =4.44
0.1
(a)
Δ =-37.2Γ
probability ⟶
0
(b)
Δ =-27.9Γ
0
(c)
Δ =-18.6Γ
0
-10
0
+10
Δp/ħk ⟶

Figure 2

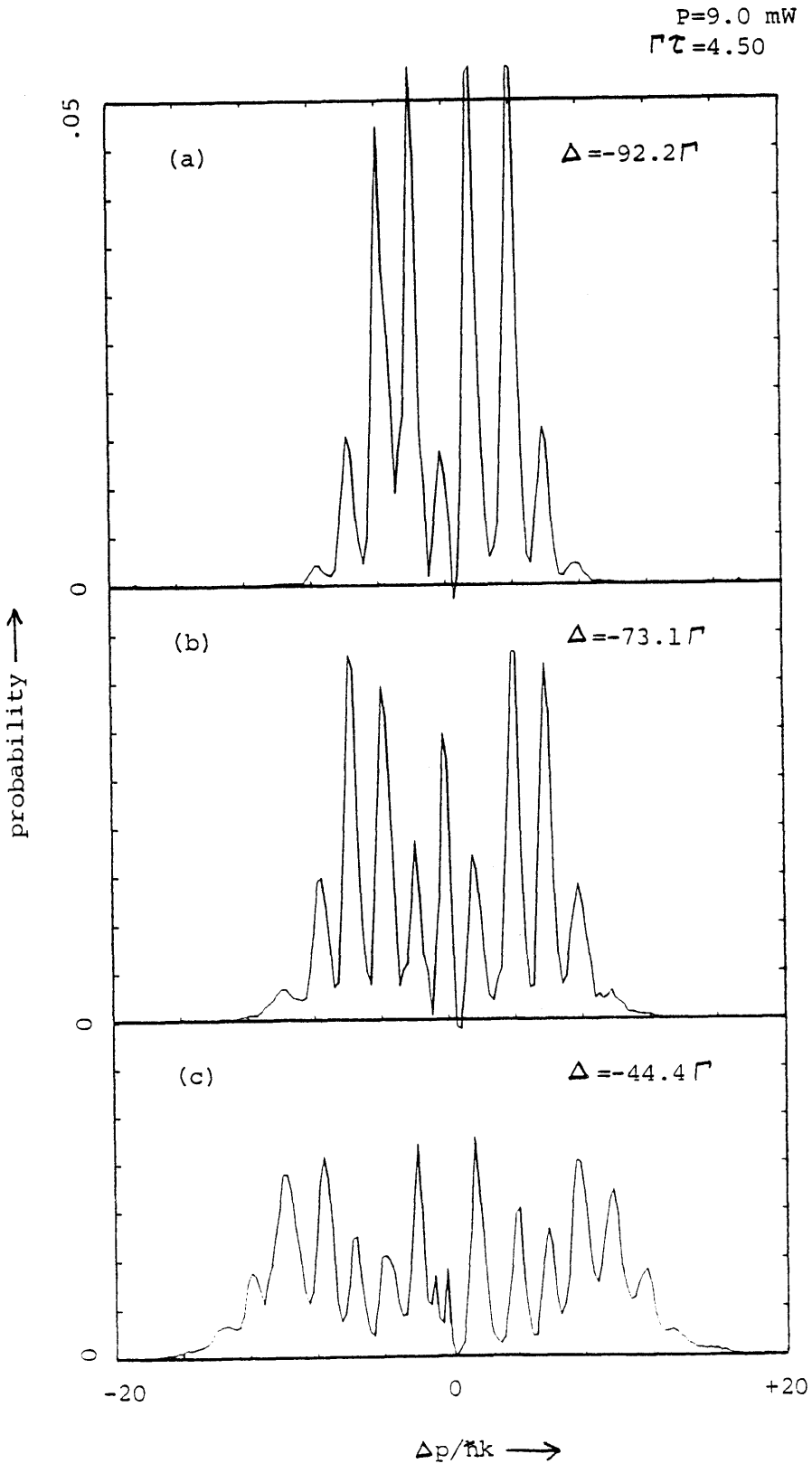
P=9.0 mW
Γτ=4.50
.05
0
(a)
Δ=-92.2Γ
(b)
Δ=-73.1Γ
(c)
Δ=-44.4Γ
probability
-20
0
+20
Δp/ħk

inversely proportional to Δ (see Eqs. 55, 53 of Section C) to within 1.4% (standard deviation). These four scans are represented by the solid squares, in Fig. 2 of Section III.B. For the three scans of Fig. 2, this proportionality to Δ^{-1} is confirmed to 7.5%. For all diffraction data taken, the Δ^{-1} dependence (at a fixed Ω_o and τ) is verified to within 5.1%.

The diffraction structure in all scans of Figs. 1 and 2 is obviously very pronounced. Since the interaction is always adiabatic and $\bar{N}$ is kept less than 0.25, the recoil associated with spontaneous decay has a negligible effect for these data. The diffraction into even multiples of $\hbar k$ is due solely to absorption/stimulated emission cycles. If one focuses on a particular diffraction peak (eg. $+6\hbar k$ in Fig. 2) and follows its evolution as the detuning is changed, one sees an oscillation in the probability (note that all scans within a figure are to scale). Bessel functions exhibit this type of oscillation as their argument is changed with their order fixed (if argument < order). These oscillations were also observed experimentally by fixing the detector at a diffraction peak and scanning the laser frequency.

The subtraction (in the data analysis) of undeflected F=1 atoms from the central ($0\hbar k$) peak can give the appearance of added structure in this region (eg. negative probability!). This is strictly an artifact due to slight mismatches of the individual points of these very sharp peaks. For the scans of Fig. 2, the power is high enough to give a small probability deflection (into $\pm 2\,\hbar k$) of F=1 atoms. This is seen in Fig. 2c where the peaks at $\pm 2\,\hbar k$ seem anomalously high, at the expense of the peat at $0\hbar k$.

Since our optical system utilizes cylindrical optics, the focused intensity and interaction time (i.e. focused waist) are inversely proportional for a fixed laser power. Since Ω_o^2 is proportional to intensity, we see that the product $\Omega_o^2\tau$ is independent of τ (for a fixed power). The parameter z, which is proportional to $\Omega_o^2\tau$ (see Eq. 53, Section C), determines not only the rms momentum, but the deflection pattern as well. Thus, we would expect that scans taken at different values of τ, but a

fixed laser power (and detuning), would yield identical values of p_{rms} and have identical momentum distributions. The rms momenta agree to within 3.5% (standard deviation) for all pairs of scans which differ only in τ. Verification of pattern coincidence is demonstrated in Fig. 3 where three such pairs (corresponding to three different powers and detunings) are displayed. Agreement within each pair is seen to be excellent.

Although the measured values of p_{rms} do not agree quantitatively with the theoretical prediction, we do verify the Bessel function distribution (Eq. 54 of Section C) for the diffraction patterns. If we choose a value of z based on the *measured* value of p_{rms} (according to Eq. 55 of Section C: $p_{rms} = (2)^{1/2} \cdot z \cdot \hbar k$), then the predicted distribution (convolved with the atomic beam profile and velocity distribution) agrees very well with the measured patterns. Examples of these fits, for three different laser powers, are shown in Fig. 4. (Additional fits appear in Fig. 1 of Section B.) The overall agreement is seen to be quite good. The largest discrepancy is seen to be in the central region of the scan taken at highest power (scan c). Again this is likely due to our F=1 subtraction process, which does not account for any deflection of these atoms.

Figure 3

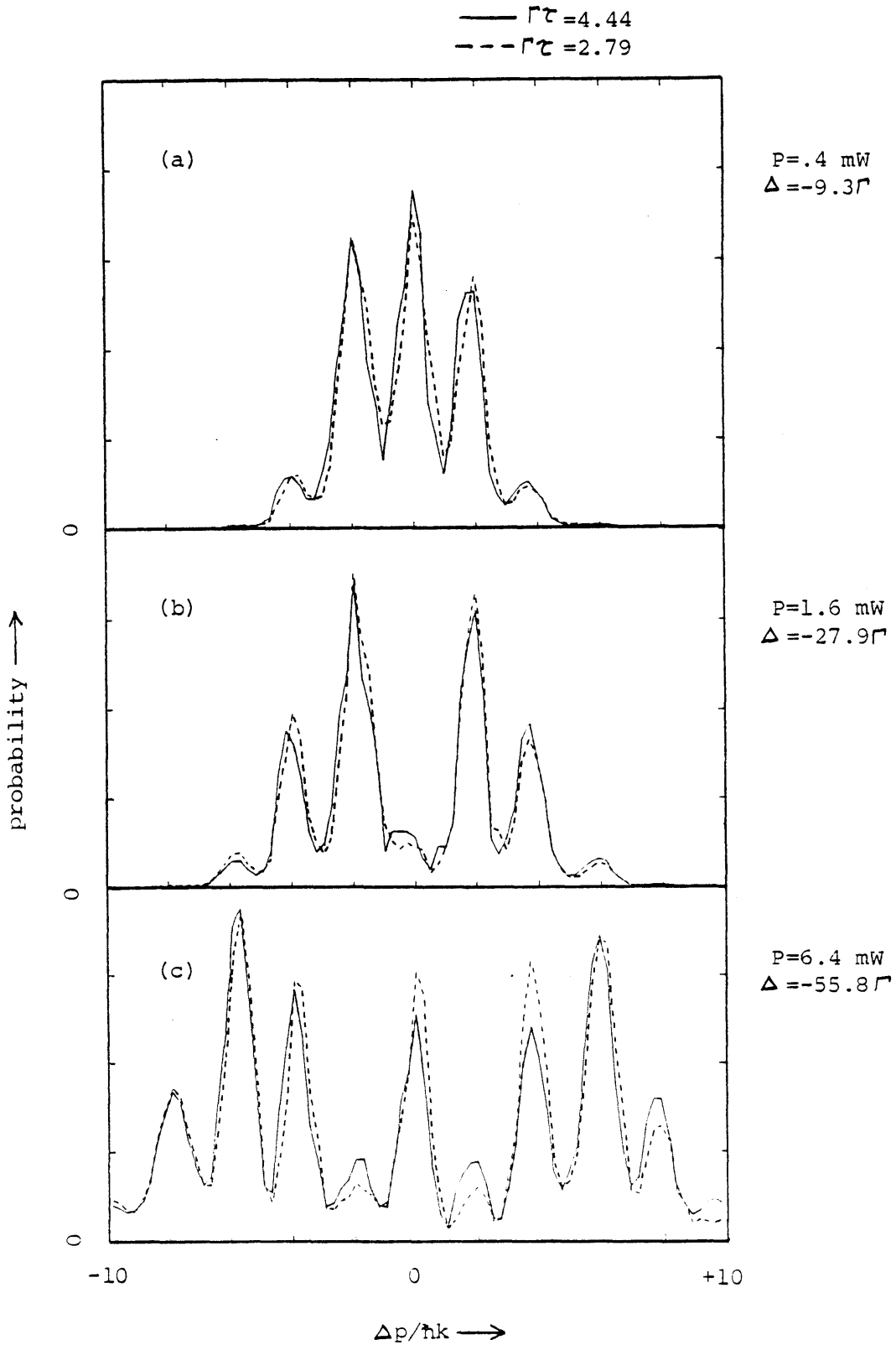
Γτ =4.44
Γτ =2.79
(a)
P=.4 mW
Δ =-9.3Γ
(b)
P=1.6 mW
Δ =-27.9Γ
(c)
P=6.4 mW
Δ =-55.8Γ
probability
0
0
0
-10
0
+10
Δp/ħk

Figure 4

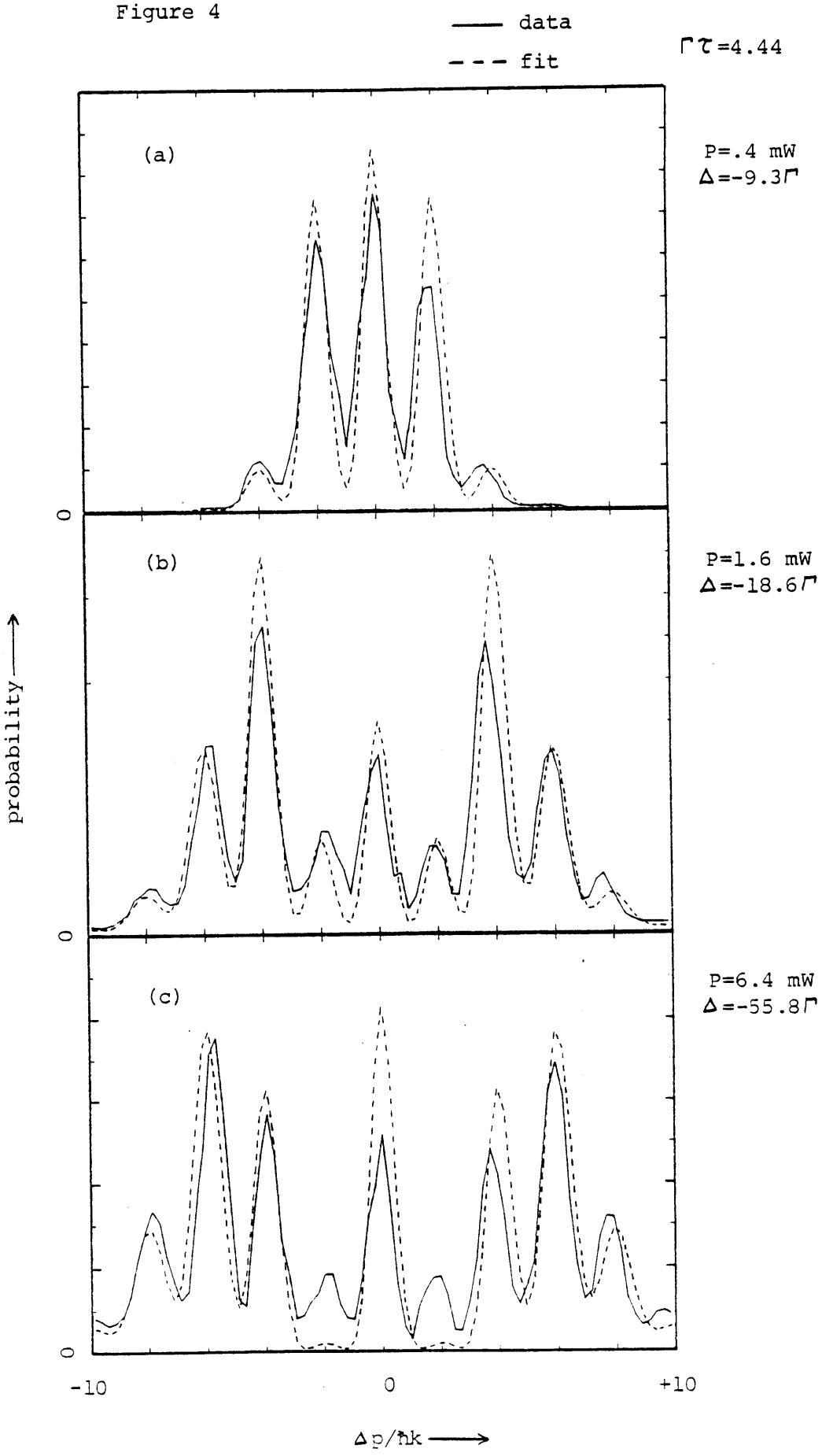
data
fit
Γτ=4.44
(a)
P=.4 mW
Δ=-9.3Γ
(b)
P=1.6 mW
Δ=-18.6Γ
(c)
P=6.4 mW
Δ=-55.8Γ
probability
0
0
0
-10
0
+10
Δp/ħk

Chapter IV. Induced Forces and Induced Diffusion

This chapter describes our study of momentum transfer to atoms from induced processes occurring in a standing-wave field under conditions where spontaneous emission plays an important role. This is in contrast to Chapter III, where the off-resonant nature of the excitation allowed us to ignore spontaneous decay. Here the effects of spontaneous emission are two-fold: primarily, it disrupts the phase relationship between the atomic dipole and the applied field, causing a diffusion of the atomic momentum. Secondly, the distribution of recoils from spontaneous decay smears out an otherwise discrete (in units of $\hbar k$) momentum distribution.

In section A, the induced force and induced momentum diffusion are briefly described, along with past experiments, motivation for the present experiments, and possible applications. Section B is a summary of our experimental investigations which will be submitted for publication. The theory outlined in section B is presented in more detail in section C. Additional data, including the transition region from diffraction to diffusion, are contained in section D.

IV.A. Introduction

As discussed in Chapter I, there are two types of radiative forces on atoms: the spontaneous (or scattering) force and the induced (or dipole or gradient) force. The spontaneous force is the microscopic analog of classical radiation pressure and exists when there is net propagation of field energy (eg. in a traveling plane wave). The induced force, on the other hand, arises from the spatially dependent potential energy of the atomic dipole moment in the field, and is present only when there is a field gradient. Spontaneous decays cause fluctuations in these forces, leading to diffusion of the atomic momentum.

Most experimental efforts on radiative forces have focused on the spontaneous force (see Chapter I for references) because of the relative experimental simplicity and ease of interpretation. The induced force, on the other hand, has not been subject to detailed quantitative investigation,

despite the large amount of theoretical attention it has received and the rich variety of phenomena which are predicted (see Chapter I for references). This is due in part to the experimental difficulties involved in creating and characterizing a strong field gradient.

Using the large gradients present in a standing-wave field, we have made measurements of the induced force and the fluctuations in this force (induced diffusion) resulting from spontaneous decay. These experiments were motivated by a desire to: 1) provide definitive tests of the many theories of the induced force and induced diffusion; and 2) study the effect of a stochastic process (spontaneous decay) on a coherent interaction (diffraction).

The induced force has been observed in previous studies, but experimental conditions did not allow definitive measurements. To our knowledge, the results we present in this chapter are the first quantitative measurements of the induced force and its fluctuations (induced diffusion).

Experiments have been performed (BFA78, PFB80) using the radial intensity gradient of a copropagating laser beam to focus an atomic beam. However, a quantitative analysis was not possible because of ambiguities in the interaction time. Several experiments have also been carried out using a standing-wave. Grinchuk et. al. (GKN81, GKK84, GKN85) and Moskowitz et. al. (MGA83, MGP85) have reported measurements in the regime $\Gamma\tau<1$ (where spontaneous decay is negligible), as discussed in Section III.A. Arimondo, et. al. (ALO79) measured the deflection of a sodium beam by a resonant standing-wave laser using an interaction time long enough to allow many spontaneous decays. However their rms momentum transfer varied with laser power (P) as $P^{1/4}$ instead of $p^{1/2}$, as predicted. Subsequent analyses have either misinterpreted (MIN81, TRC84), incorrectly explained (KSY81), or been unable to explain (ABS81) these results.

The induced force has many potential applications in the field of trapping, cooling, and manipulating atoms. The fact that it can be made arbitrarily large (i.e. it does not saturate) makes it particularly appealing for situations which would benefit from large forces (eg. atom slowing

and/or trapping). Induced diffusion, on the other hand, is usually a nemesis to atom manipulation because it is a heating mechanism. Hence its understanding is crucial for the successful use of radiative forces to control atomic motion.

IV.B. (to be submitted for publication)

Observation of Momentum Transfer to Atoms by Induced Processes in a Standing-Wave Laser Field

Phillip L. Gould,[a] George A. Ruff,[b] Jean-Louis Picque,[c]
Richard E. Stoner,[d] Peter J. Martin and David E. Pritchard

Department of Physics and
Research Laboratory of Electronics
Massachusetts Institute of Technology
Cambridge, Massachusetts 02139

We report on measurements of the momentum transfer to an atomic sodium beam due to induced processes occurring in a near-resonant standing-wave radiation field. In our experiment, the strong atomic saturation and large intensity gradients of the standing-wave result in momentum transfer dominated by the induced force and induced momentum diffusion. The effects of spontaneous diffusion are also evident in our data. Our results are in general agreement with theoretical predictions but differ quantitatively by a factor of two.

With the advent of the tunable dye laser, there has been a great deal of theoretical and experimental interest in the forces exerted on atoms by near-resonant radiation (JOS85). Radiative forces divide naturally into two types: the spontaneous force and the induced force. The spontaneous force is due to absorption followed by spontaneous emission and is always directed along the incident laser beam. The induced force occurs in inhomogeneous fields and is a result of the interaction between the induced atomic dipole moment and the intensity gradient. This "gradient" or "dipole" force can also be explained by absorption and stimulated emission of photons into different spatial modes. The important features of this induced force are that it can be made arbitrarily large by increasing the laser intensity (in contrast to the spontaneous force which saturates) and that it can occur in the absence of spontaneous emission.

Both types of forces exhibit quantum fluctuations due to the randomizing effects of spontaneous emission. Fluctuations in the spontaneous force are due to the recoil distribution of the spontaneously emitted photons as well as fluctuations in the number of photons absorbed and emitted. Fluctuations in the dipole (induced) force are not so easily understood but are generally explained as the interaction of a fluctuating dipole (due to spontaneous emission) with the intensity gradient. Both types of fluctuations may be described in terms of momentum diffusion coefficients in conjunction with a Fokker-Planck type equation for the momentum distribution.

In this article, we present quantitative observations of the induced force and induced diffusion and demonstrate the effects of spontaneous diffusion. Our high resolution measurements of the deflection of a two-state, velocity selected atomic beam by a well-defined laser standing-wave allow us to make quantitative comparisons to theoretical predictions. Our results are in general agreement with the theory but differ quantitatively by a factor of two.

The spontaneous force has been studied experimentally (BFP81) and the influence of fluctuations has been observed (BFA80,WHC85). Induced forces have been observed in the rf

(BEL67) and microwave (HIG75) spectral regions, and in the optical domain, experiments have been performed using the radial field gradient of a focused Gaussian waist (BFA78) and the strong intensity gradients present in a standing-wave field (ALO79, GKN81, MGA83, GKK84, MGP85). In general, these experiments have been only qualitative in nature in that they have been performed on systems with distributions of velocity and/or internal state. Recently, we have reported (GRP86) on a quantitative study of these forces in the regime where spontaneous decay effects are negligible. These results were interpreted as the diffraction of the atomic deBroglie waves by the standing-wave light "grating". The results presented in the present article represent the first quantitative measurements of the induced force and induced momentum diffusion, i.e. the fluctuations of the induced force.

Many proposals for trapping neutral atoms with laser light rely on the use of the induced force and are adversely affected by the accompanying fluctuations. These fluctuations (induced diffusion) are a heating mechanism which can limit the confinement time. Our measurements have allowed independent observation of these two phenomena and our measurements are in general agreement with existing theory.

The theory of standing-wave deflection of an atomic beam in the regime where many spontaneous decays occur during the interaction has been investigated by several authors (TRM83, TRC84, MIN81, KSY81). In this regime, the deflection profile is determined by the average force and its fluctuations (momentum diffusion). The standing-wave electric field is taken to be:

$$E(x,t) = 2E_o f(t)\cos kx \cos\omega t \qquad (1)$$

Where f(t) describes the time dependence of the field amplitude due to the atom's passage (along $\hat{y}$) through the laser beam with velocity v. We will assume a Gaussian laser profile: $f(t) = e^{-(t/\tau)^2}$, where τ is the transit time for the $\frac{1}{e^2}$ radius of intensity.

For a two-state atom (energy difference $\hbar\omega_o$) interacting (via dipole moment μ) with the electric field of Eq. 1, there are three relevant frequencies: the spontaneous decay rate Γ ($\Gamma/2\pi$ = 10 MHz for the sodium D_2 line), the laser detuning $\Delta = \omega - \omega_o$, and the peak Rabi rate: $\Omega_o = \frac{\mu E_o}{\hbar}$, due to one of the two traveling waves which combine to form the standing wave. Defining a resonance parameter $r = \frac{\Gamma^2}{\Gamma^2+4\Delta^2}$ and a saturation parameter $s(x,t) = s_o \cdot f^2(t)\cos^2 kx$, with $s_o = \frac{8\Omega_o^2}{\Gamma^2+4\Delta^2}$, the induced dipole force is (TRM83, TRC84):

$$F(x,t) = -\frac{\hbar\Delta}{2(1+s)} \cdot \frac{ds}{dx} \tag{2}$$

and the contributions to the momentum diffusion coefficient, $D = D_I + D_S$, from induced processes (D_I) and spontaneous recoil (D_S) can be written (COO80c, GOA80, COO80d, TRM83):

$$D_I(x,t) = \frac{\hbar^2\Gamma}{16s(1+s)^3}\left(\frac{ds}{dx}\right)^2\left[1+(4r-1)s+3s^2+\frac{s^3}{r}\right] \tag{3a}$$

$$D_S(x,t) = \frac{\hbar^2 k^2}{10}\Gamma \cdot \frac{s}{1+s} \tag{3b}$$

We note that on resonance (Δ=0) the induced diffusion coefficient reduces to:

$$D_I(x,t;\Delta=0) = \frac{\hbar^2\Gamma}{16s} \cdot \left(\frac{ds}{dx}\right)^2 \tag{4}$$

Considering an atom crossing the standing-wave at a point x, the induced force (Eq. 2) will impart an average transverse momentum, $p_F(x)$, to the atom over the course of the interaction. In addition, the dispersion of the atomic momentum, $p_D^2(x)$, will increase as a result of momentum diffusion (Eq. 3). Solution of the Fokker-Planck equation (TRM83) yields a Gaussian momentum transfer distribution centered at $p_F(x)$ with rms width $p_D(x)$. If we assume that x changes much less than λ during the interaction, the average value and dispersion of the atomic momentum are given by:

$$p_F(x) = \int_{-\infty}^{\infty} F(x,t)dt \tag{5a}$$

$$p_D^2(x) = p_I^2(x) + p_s^2(t) = 2\int_{-\infty}^{\infty} (D_I(x,t)+D_S(x,t))dt \tag{5b}$$

where we have separated the contributions to the dispersion from induced and spontaneous diffusion. If the extent (along x) of the atomic beam is $> > \lambda$ and the initial momentum distribution is much narrower than the distribution of momentum transfers (determined by Eq. 5), the final momentum distribution P(p) is a sum (i.e. average over x) of Gaussians centered at $p_F(x)$ and having dispersion $p_D^2(x)$ (TRM83):

$$P(p) = \frac{2}{\lambda}\int_{-\lambda/4}^{+\lambda/4} dx \cdot [2\pi p_D^2(x)]^{-1/2}\exp[-(p-p_F(x))^2/2p_D^2(x)] \tag{6}$$

The rms momentum transfer, p_{rms}, is easily calculated from this momentum distribution:

$$\begin{aligned} P_{rms}^2 &= \int_{-\infty}^{\infty} dp \cdot p^2 \cdot P(p) \\ &= \frac{2}{\lambda} \cdot \int_{-\lambda/4}^{\lambda/4} dx\,(p_F^2(x)+p_D^2(x)) \\ &= \overline{p_F^2} + \overline{p_I^2} + \overline{p_S^2} \end{aligned} \tag{7}$$

where the contributions from the dipole force, induced diffusion, and spontaneous diffusion have been separated. The relative contributions of the three terms are plotted as functions of detuning in Fig. 1. On resonance, the force term vanishes while the diffusive terms are maximized; whereas for $\Delta > \Omega_o$, the diffusive terms vanish more rapidly than the force term. Therefore, momentum transfer measurements at small and large values of Δ are primarily observations of the diffusive and force terms, respectively.

In fact, the two diffusive processes can also be distinguished because the spontaneous recoil contributes negligibly to the rms momentum, manifesting itself in the blurring of an otherwise

discrete momentum distribution. Since the dipole force and induced diffusion account for momentum exchanged in absorption and stimulated emission, the projection of this momentum along the laser axis (for a plane standing-wave) is quantized in integral multiples of $\hbar k$. Spontaneous recoil, however, has a continuous momentum distribution along the laser axis.

The experiment was performed using a previously described apparatus - we refer the reader to GRP86 for details. Observations of the induced force and induced (and spontaneous) diffusion were carried out by operating off-resonance and on-resonance, respectively.

Experimental results are shown in Figs. 2 and 3. Deflection profiles for on-resonance and off-resonance excitation are displayed in Fig. 2. These data have been corrected for background and undeflected F=1 atoms. The latter subtraction is the cause for the apparent "structure" in the center of the profile.

Two qualitative differences are immediately obvious. Firstly, for $\Delta = 0$ (Fig. 2a), the probability distribution is a relatively smooth function of momentum as a result of the blurring effect of spontaneous recoil. This blurring does not occur off-resonance (Fig. 2b) because the average number ($\bar{N} = \frac{5}{2}\cdot\overline{p_s^2}/(\hbar k)^2$) of spontaneous decays occurring during the interaction is less than unity. We note that the condition $\Gamma\tau >> 1$ is not sufficient to ensure that $\bar{N} >> 1$, when operating off-resonance. We would not expect the Fokker-Planck treatment to remain valid in this regime. The diffraction structure is due to interference of the translational states of the atom - information which is lost when probabilities, instead of amplitudes, are summed in Eq. 6. The induced force, as a classical concept, does not account for wave-like properties of the atom.

Substantial deflection can occur in this regime: $\bar{N} < 1$, as we have demonstrated in GRP86, because the dipole force falls off more slowly ($\alpha \frac{\Omega_o^2}{\Delta}$) than $\bar{N}(\alpha \frac{\Omega_o^2}{\Delta^2})$ in the limit of large Δ (as seen in comparing the corresponding contributions in Fig. 1). In comparing Figs. 2a and 2b,

(which have the same value of τ), we see that the transition from diffraction to diffusion is determined by $\bar{N}$ and not simply $\Gamma\tau$, as assumed in TRC84.

The second obvious difference is in the envelopes of the two profiles. The on-resonant profile (Fig. 2a) is a single-peaked structure centered at zero momentum, while off-resonance (Fig. 2b), the envelope exhibits the predicted (TRM83, TRC84) two-peaked, symmetric, "rainbow" structure, due to a stationary point (as a function of x) in the force (Eqn. 2) at its maximum value. The dashed lines in Fig. 2 are the theoretical fits according to Eq. 6. We have not convolved the finite atomic beam collimation (.88 $\hbar k$ FWHM) and velocity distribution ($\Delta v/\bar{v}$ = 11% FWHM) into these fits as their effects are minimal on these smooth distributions. For these fits, we have divided the value of Ω_o^2 determined from experimental parameters by a factor of two. The reason for this discrepancy is not clear at this time, but we note its similar appearance in GRP86.

The rms momentum transfers for two values of laser power and two values of τ are plotted as a function of Δ in Fig. 3. The data are corrected for small contributions to the rms momentum from the finite beam collimation and velocity distribution. The theoretical fits in Fig. 3 are derived from Eq. 7, where again we have divided the value of Ω_o^2 by a factor of 2 in order to obtain good agreement with the data.

The expression for p_{rms} (Eq. 7) can be simplified for the cases $\Delta = 0$ (using Eq. 4) and $\Delta << \Omega_o$ (i.e. $s_o << 1$):

$$p_{rms} = ((2\pi)^{1/2} \cdot \frac{\Omega_o^2 \tau}{\Gamma})^{1/2} \cdot \hbar k \qquad \text{for } \Delta = 0 \tag{7a}$$

$$p_{rms} = \frac{1}{2} \cdot (\pi)^{1/2} \cdot \frac{\Omega_o^2 \tau}{\Delta} \cdot \hbar k \qquad \text{for } \Delta >> \Omega_o \tag{7b}$$

(We note that Eq. 7b is the same expression for p_{rms} obtained in GRP86 where attention was restricted to large detunings). In both limits ($\Delta = 0$, $\Delta >> \Omega_o$) we see that p_{rms} depends on the

product $\Omega_o^2\tau$, and since Ω_o^2 is proportional to laser intensity, our use of cylindrical optics (GRP86) results in this product being independent of τ at a fixed laser power. This is verified by the data shown in Fig. 3, where values of p_{rms} for a fixed laser power but different value of τ are seen to coincide in these limits.

In conclusion, we have observed and measured the induced (dipole) force and its associated fluctuations (induced diffusion) by deflecting an atomic beam with a standing-wave laser field. Far from resonance, the fluctuations are negligible and diffraction structure persists, contrary to theoretical predictions based on the Fokker-Planck equation. On resonance, the induced force vanishes but its fluctuations give rise to substantial momentum transfer in a random direction (i.e. "heating"). In addition, fluctuations of the spontaneous force have been observed (for $\Delta = 0$) by their blurring effect on an otherwise discrete momentum distribution. All measurements are in agreement with theoretical predictions except for a factor of two in the absolute intensity.

We gratefully acknowledge the support of the National Science Foundation through grants PHY83-07172-A01 and PHY-8514748 (ROA program).

References

a) Current Address: Electricity Division, Center for Basic Standards, National Bureau of Standards, Gaithersburg, Maryland.

b) Permanent Address: Department of Physics, Bates College, Lewiston, Maine 04240.

c) Permanent Address: Laboratoire Aime Cotton, Centre National de la Recherche Scientifique, F-91405 Orsay, France.

d) Current Address: Department of Physics, University of Colorado, Boulder, Colorado 80309.

ALO79 E. Arimondo, H. Lew and T. Oka, Phys. Rev. Lett. 43, 753 (1979).

BEL67 M. Bloom, E. Enga, and H. Lew, Can. J. Phys. 45, 1481 (1967).

BFA78 J.E. Bjorkholm, R.R. Freeman, A. Ashkin, and D.B. Pearson, Phys. Rev. Lett. 41, 1361 (1978).

BFA80 J.E. Bjorkholm, R.R. Freeman, A. Ashkin, and D.B. Pearson, Opt. Lett. 5, 111 (1980).

BFP81 J.E. Bjorkholm, R.R. Freeman, and D.B. Pearson, Phys. Rev. A 23, 491 (1981), and references therein.

COO80c R.J. Cook, Phys. Rev. Lett. 44, 976 (1980).

COO80d R.J. Cook, Phys. Rev. A 22, 1078 (1980).

GKK81 V.A. Grinchuk, E.F. Kuzin, M.L. Nagaeva, G.A. Ryabenko, A.P. Kazantsev, G.I. Surdutovich, and V.P. Yakovlev, Phys. Lett. 864, 136 (1981).

GKN84 V.A. Grinchuk, A.P. Kazantsev, E.F. Kuzin, M.L. Nagaeva, G.A. Ryabenko, G.I. Surdutovich and V.P. Yakovlev, Sov. Phys. JETP 59, 56 (1984).

GOA80 J.P. Gordon and A. Ashkin, Phys. Rev. A 21, 1606 (1980).

GRP86 P.L. Gould, G.A. Ruff, and D.E. Pritchard, to be published in Physical Review Letters.

HIG75 R.M. Hill and T.F. Gallagher, Phys. Rev. A 12, 451 (1975).

JOS85 J. Opt. Soc. Am. B 2 (Feature Issure: The Mechanical Effects of Light), Nov. 1985.

KSY81 A.P. Kazantsev, G.I. Surdutovich, and V.P. Yakovlev, J. Phys. (Paris) 42, 1231 (1981).

MGA83 P.E. Moskowitz, P.L. Gould, S.R. Atlas, and D.E. Pritchard, Phys. Rev. Lett. 51, 370 (1983).

MGP85 P.E. Moskowitz, P.L. Gould and D.E. Pritchard, J. Opt. Soc. Am. B 2, 1784 (1985).

MIN81 V.G. Minogin, Opt. Commun. 37, 442 (1981).

TRC84 C. Tanguy, S. Reynaud, and C. Cohen-Tannoudji, J. Phys. B 17, 4623 (1984).

TRM83 C. Tanguy, S. Reynaud, M. Matsuoka and C. Cohen-Tannoudji, Opt. Commun. 44, 249 (1983).

WHC85 Y.Z. Wang, W.G. Huang, Y.D. Cheng, and L. Liu, in *Laser Spectroscopy VII,* edited by T.W. Hansch and Y.R. Shen (Springer-Verlag, New York, 1985).

Figure Captions

Figure 1. Contributions to the total mean squared momentum (solid line) from the induced force (dashed line), induced diffusion (dotted line), and spontaneous diffusion (dashed-dotted line). For these plots $\Omega_o/2\pi$ = 20 MHz and τ = 71 ns.

Figure 2. Deflection profiles (solid line) and theoretical fits (dashed line) for Δ = 0 (a) and Δ = 46.5 MHz (b). For both curves, $\Omega_o/2\pi$ = 20 MHz and τ = 71 ns.

Figure 3. rms momentum vs. Δ for two values of laser power: P = 1.6 mW (upper set of curves) and p = .4 mW (lower set of curves). Data points are depicted by: crosses - τ = 71 ns; open circles - τ = 45 ns. The solid and dashed lines of each set are the theoretical fits for τ = 71 ns and τ = 45 ns, respectively. Values of $\Omega_o/2\pi$ are: 40 MHz (upper solid curve); 51 MHz (upper dashed curve); 20 MHz (lower solid curve); and 25.5 MHz (lower dashed curve).

Figure 1

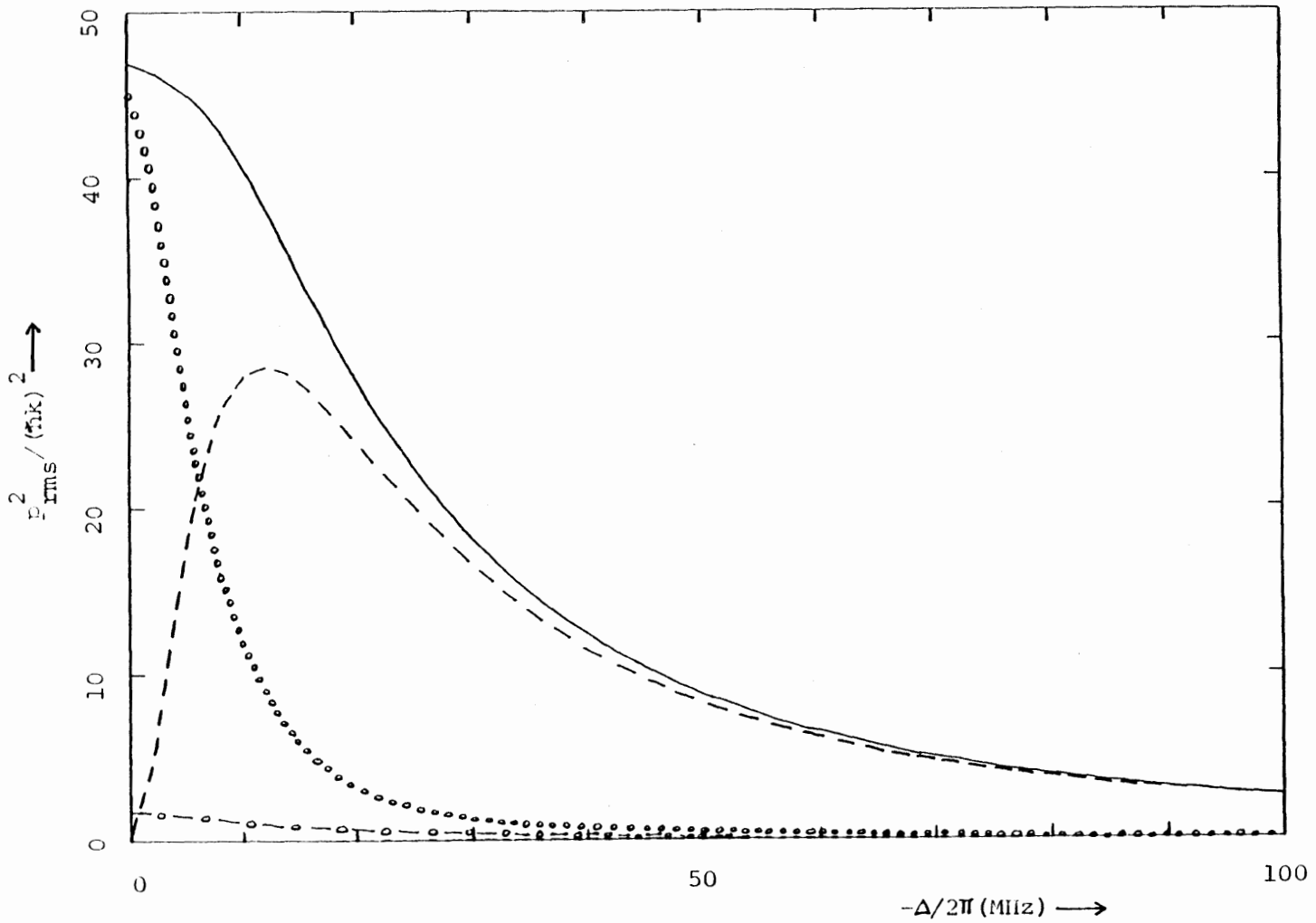

Figure 2

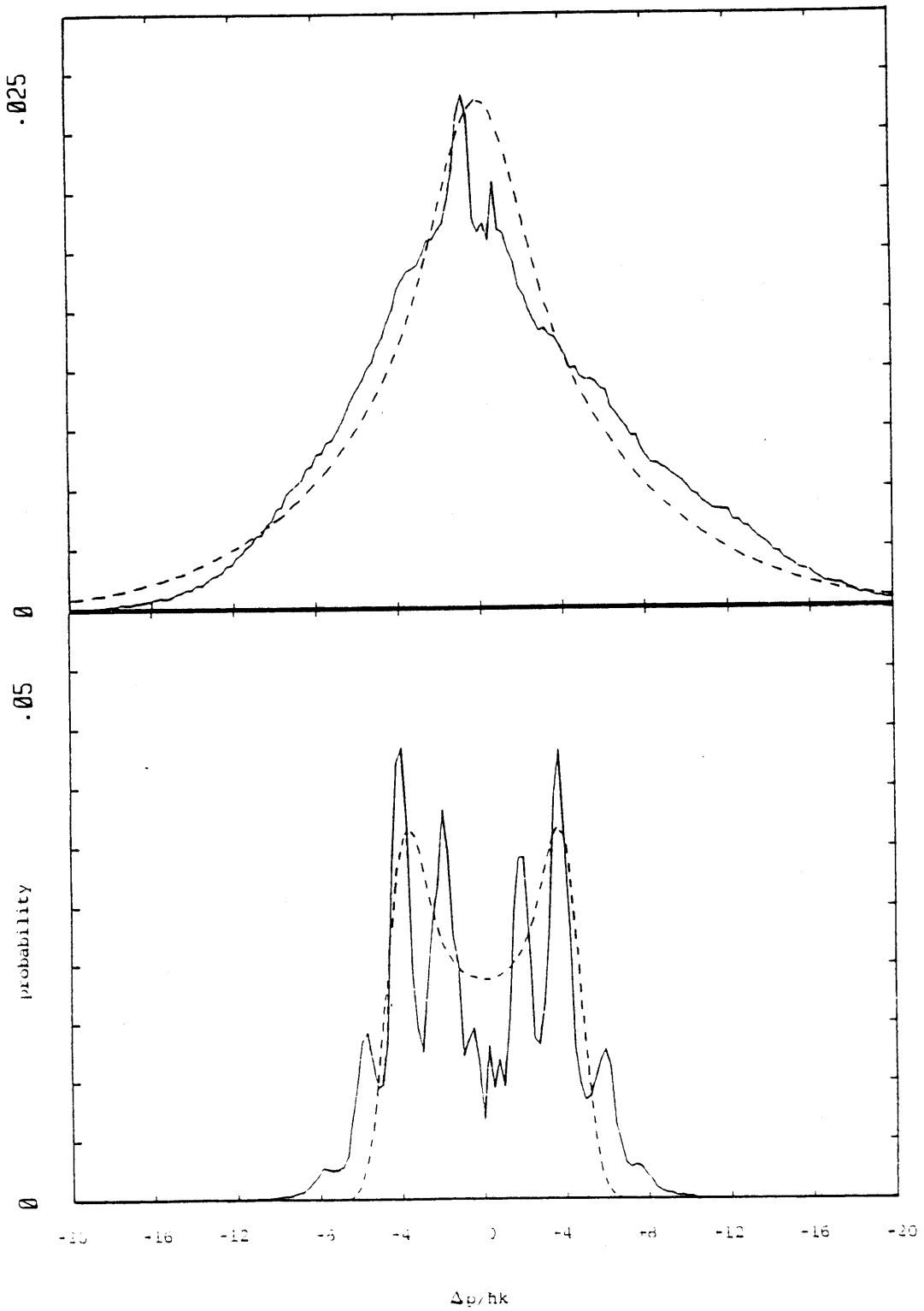

Figure 3

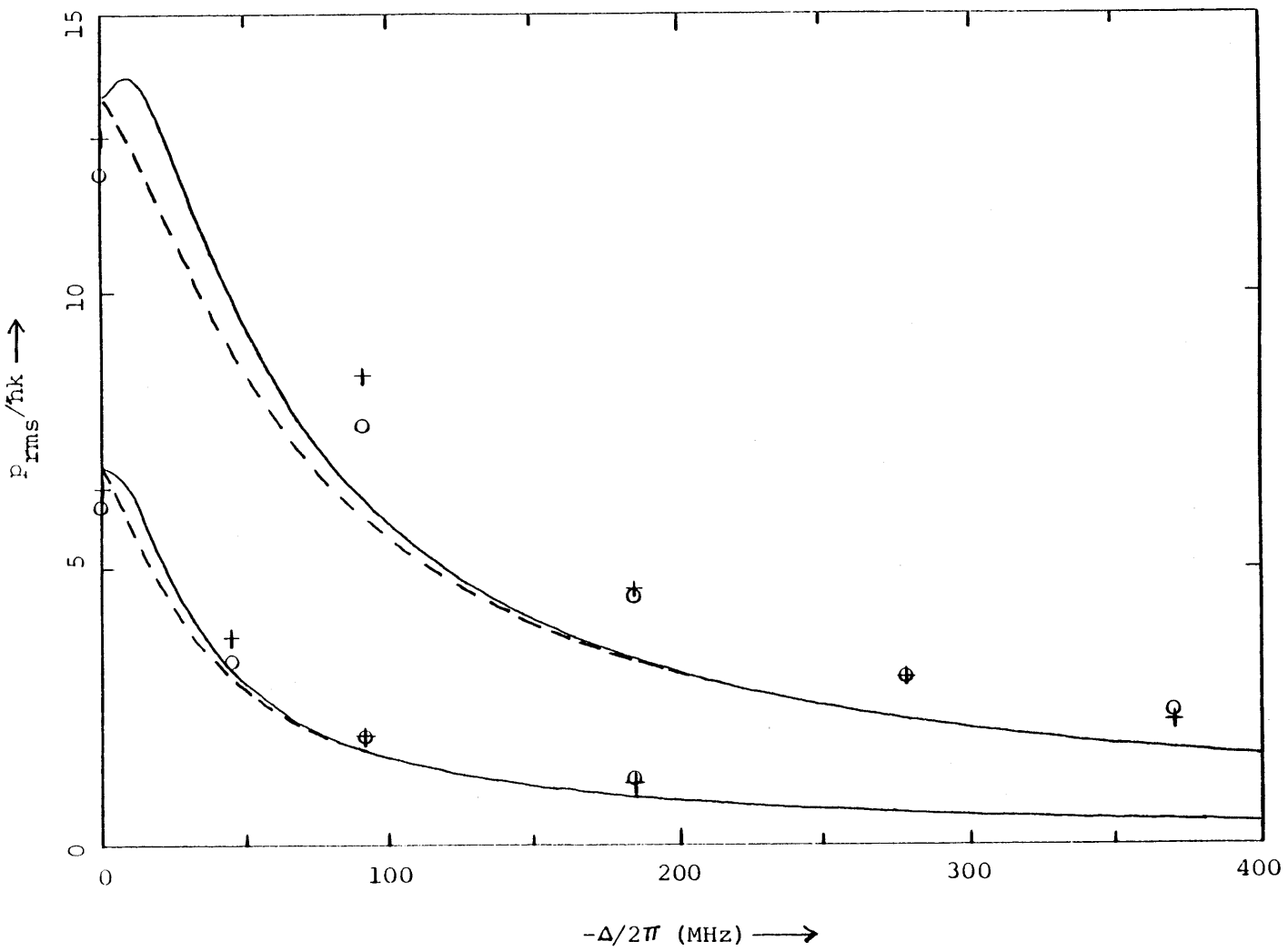
15
10
5
0
0
100
200
300
400
$\rho_{rms}/\hbar k \longrightarrow$
$-\Delta/2\pi$ (MHz) $\longrightarrow$

IV.C. Detailed Theory of Deflection

In this section we consider the deflection of an atomic beam by an orthogonal standing-wave field in the regime where many spontaneous decays occur during the interaction. In this regime the momentum distribution evolves according to a Fokker-Planck equation in which the induced force and momentum diffusion coefficient determine the average change and spread in the atomic momentum, respectively.

In Section 1, we will use the solution of this Fokker-Planck equation which is appropriate for our Gaussian laser profile to generate deflection profiles (i.e. momentum distributions) for various values of detuning. The rms momentum transfer is calculated and its dependence on detuning is examined in Section 2. Sections 3 and 4 discuss the limits of exact resonance and large detuning, respectively. The limitations of the theory in describing our data are pointed out in Section 5.

1. *Deflection Profiles*

Deflection profiles will be calculated for a highly collimated (momentum spread $<\hbar k$) atomic beam, with spatial extent $>\lambda$ (in accordance with the uncertainty principle), crossing a standing-wave electric field:

$$E(x,t) = 2E_o f(t)\cos kx \cos\omega t. \tag{1}$$

Here, f(t) expresses the temporal envelope of the field due to the atom's passage (along y) through the laser profile. The dipole force (F) and momentum diffusion coefficient ($D=D_I+D_S$) can be expressed (COO80c, COO80d, GOA80, TRM83, TRC84):

$$F(x,t) = -\frac{\hbar\Delta}{2(1+s)}\cdot\frac{ds}{dx} \tag{2}$$

$$D_I(x,t) = \frac{\hbar^2\Gamma}{16s(1+s)^3}\left(\frac{ds}{dx}\right)^2\left[1+(4r-1)s+3s^2+\frac{s^3}{r}\right] \tag{3}$$

$$D_S(x,t) = \frac{\hbar^2 k^2}{10} \cdot \Gamma \cdot \frac{s}{1+s} \tag{4}$$

Here we have defined the saturation parameter s(x,t)and the resonance parameter r:

$$s(x,t) = s_o f^2(t)\cos^2 kx, \tag{5a}$$

$$s_o = \frac{8\Omega_o^2}{\Gamma^2+4\Delta^2}, \tag{5b}$$

$$r = \frac{\Gamma^2}{\Gamma^2+4\Delta^2}. \tag{5c}$$

The quantities Γ, Δ, and Ω_o refer to the spontaneous decay rate, the laser detuning ($\omega-\omega_o$), and the peak traveling-wave Rabi rate ($\frac{\mu E_o}{\hbar}$), respectively. We have separated the contributions to the diffusion coefficient ($D=D_I+D_S$) from induced processes (D_I) and spontaneous recoil (D_S) in Eqns. 3 and 4, respectively. We restrict attention to our experimentally measured Gaussian profile:

$$f(t) = e^{-(t/\tau)^2} \tag{6}$$

where τ is the transit time for the $\frac{1}{e^2}$ radius of intensity.

In the following, we will make use of the Wigner phase-space distribution w(x,p,t), which is discussed in detail in COO80d. Its similarity to the classical phase-space distribution (i.e. joint probability distribution for position and momentum), recommends it to the current application. It has the property that its integral over momentum (position) space yields the probability density for position (momentum).

Defining τ as the characteristic time of the interaction, the condition $\Gamma\tau >> 1$ corresponds to the atom remaining in the field for many spontaneous lifetimes. If this is the case, it is shown (COO80d, JAS80, LEM81, MIN82) that the Wigner distribution obeys a Fokker-Planck type equation:

$$[\frac{\partial}{\partial t} + F(x,t)\frac{\partial}{\partial p} - D(x,t)\frac{\partial^2}{\partial p^2}]w(x,p,t) = 0 \tag{7}$$

In Eq. 7, we have ignored the "free flight" term ($\frac{\partial}{\partial x}$). This is based on the assumption that the atom does not move appreciably along the standing-wave during the interaction (thereby making x a parameter in the equation). Validity of this assumption requires negligible translation (due to deflection) during the interaction as well as a high degree of parallelism between the incident atomic beam and the standing-wave nodes. Both of these conditions become harder to fulfill at longer interaction times. If we define $p_F(x,t)$ as the time integral of the force:

$$p_F(x,t) = \int_{-\infty}^{t} F(x,t)dt \tag{8}$$

and $p_I^2(x,t)$, $p_S^2(x,t)$, and $p_D^2(x,t)$ as twice the time integral of the induced, spontaneous, and total diffusion coefficients, respectively,

$$p_I^2(x,t) = 2\int_{-\infty}^{t} D_I(x,t)dt \tag{9a}$$

$$p_S^2(x,t) = 2\int_{-\infty}^{t} D_s(x,t)dt \tag{9b}$$

$$p_D^2(x,t) = p_I^2(x,t) + p_S^2(x,t) = 2\int_{-\infty}^{t} D(x,t)dt \tag{9c}$$

then the formal solution to Eqn. 7 is (TRM83):

$$w(x,p,t) = \int dq w(x,p-q,t=-\infty)G(x,q,t) \tag{10}$$

where:

$$G(x,q,t) = [2\pi p_D^2(x,t)]^{-1/2}\exp[-(q-p_F(x,t))^2/2p_D^2(x,t)] \tag{11}$$

Thus we see that the distribution at time t is obtained by convolving the initial ($t=-\infty$) distribution with the Green's function (or "propagator") G, which describes the momentum transfer process.

Physically, we interpret this propagator as follows: at time t, an atom at position x with initial momentum q, has had its momentum changed by an average amount $p_F(x,t)$ (due to the dipole force) with a dispersion about that average of $p_D^2(x,t)$ (due to momentum diffusion).

If the initial distribution is a plane-wave: well localized in momentum (i.e. to $<<\hbar k$) but unlocalized in x (i.e. to $>>\lambda$), then the propagator can be brought outside the integral in Eq. 10:

$$w(x,p,t) = G(x,p,t) \cdot X(x,t,=-\infty) \tag{12}$$

Here, $X(x,t=-\infty)$ is the initial probability distribution for position, assumed to be relatively constant over many λ. The momentum distribution at time t, P(p,t), is obtained by integrating the Wigner distribution over x. Since G is periodic in x (with period $\lambda/2$) and X is constant over many λ, the integral reduces to an average of G over a period:

$$P(p,t) = \frac{2}{\lambda}\int_{-\lambda/4}^{\lambda/4} dx G(x,p,t) \tag{13}$$

We are interested in the distribution at t = $+\infty$:

$$P(p) \equiv P(p,t=+\infty) \tag{14}$$

$$= \frac{2}{\lambda}\int_{-\lambda/\infty}^{\lambda/\infty} dx\,[2\pi p_D^2(x)]^{-1/2}\exp[-(p-p_F(x))^2/2p_D^2(x)]$$

We have adopted the convention here of dropping the explicit time dependence for t = $+\infty$, i.e. $p_F(x) \equiv p_F(x,t=+\infty)$, etc. Examining Eq. 14, we see that the distribution of momentum transfers is a sum (i.e. average over x) of Gaussians, each centered at $p_F(x)$ and having a dispersion of $p_D^2(x)$. (We note that we are defining the dispersion to be the difference between the mean square and the square of the mean.)

Examples of deflection profiles calculated from Eq. 14 are shown in Fig. 1. The three profiles represent three values of detuning (Δ=0, -5Γ, -10Γ) and a fixed value of $\Omega_o(5\Gamma)$ and $\tau(5\Gamma^{-1})$. We

Figure 1: Deflection Profiles

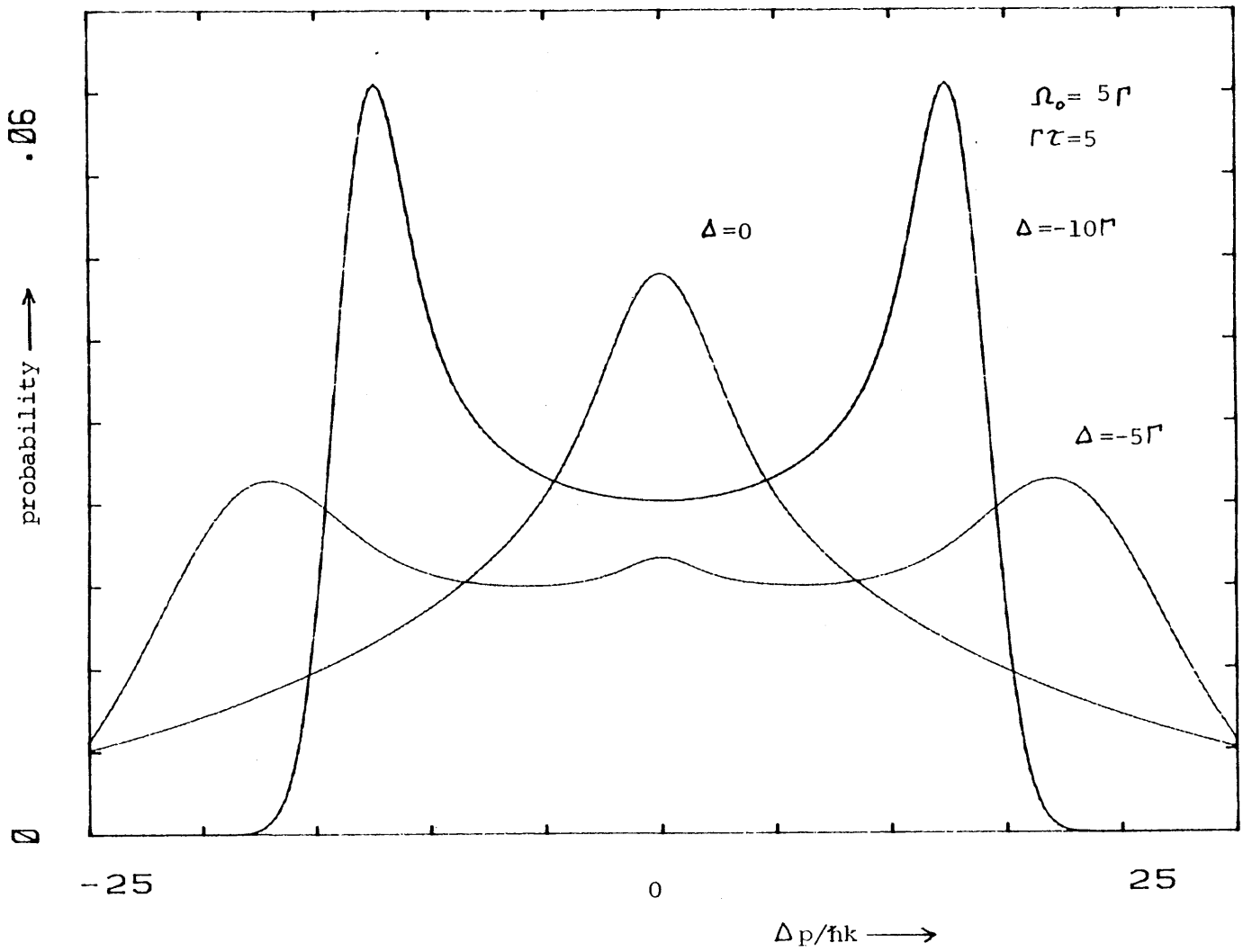

note that the calculation of each of these profiles requires a double numerical integration: the first is an integral over the laser profile (i.e. t) to determine $p_F(x)$ and $p_D(x)$, and the second is an integral over the standing-wave (i.e. x) to determine P(p).

The profiles in Fig. 1 are qualitatively different depending on whether the excitation is resonant or off-resonant. For $\Delta = 0$, the profile is a single-peaked structure, while for $\Delta \neq 0$, a symmetric two-peaked structure is obtained. On resonance the dipole force vanishes, so that the Gaussians which are are all centered on p = 0. The resulting deflection profile is not Gaussian, however, since the width of each Gaussian in the sum depends on x. Off-resonance, the location of the center of each is a function of x. The force is stationary (with respect to x) at its maximum (and minimum) values, so that the corresponding momentum is heavily weighted in the average over x. This gives rise to the symmetric "rainbow" structure seen in the off-resonant deflection profiles (TRC84).

2. RMS Momentum

For many purposes, the rms momentum transfer provides a convenient summary of the interaction. It is calculated from the momentum distribution (Eq. 14 of Section 1):

$$p_{rms}^2 = \int_{-\infty}^{\infty} dp \cdot p^2 \cdot P(p) \tag{1}$$

$$= \int_{-\infty}^{\infty} dp \cdot p^2 \cdot \frac{2}{\lambda} \int_{-\lambda/4}^{\lambda/4} dx \cdot G(x,p)$$

Reversing the order of integration yields:

$$p_{rms}^2 = \frac{2}{\lambda} \int_{-\lambda/4}^{\lambda/4} dx \, [p_I^2(x) + p_S^2(x) + p_F^2(x)] \tag{12}$$

$$= \overline{p_I^2} + \overline{p_S^2} + \overline{p_F^2}$$

where the over-bar indicates an average over x. Each of these quantities is a double integral (over t (Eqs. 8 and 9) and x). For p_I^2 and p_S^2 we can reverse the order of integration:

$$\overline{p_I^2} = \int_{-\infty}^{\infty} dt \cdot \frac{2}{\lambda} \int_{-\lambda/4}^{\lambda/4} dx \cdot 2 \cdot D_I(x,t) \tag{3a}$$

$$\overline{p_S^2} = \int_{-\infty}^{\infty} dt \cdot \frac{2}{\lambda} \int_{-\lambda/4}^{\lambda/4} dx \cdot 2 \cdot D_S(x,t) \tag{3b}$$

The integrals over x can be done analytically:

$$2\bar{D}_I = \frac{1}{16}\hbar^2 k^2 \cdot \Gamma(1+\gamma^2)^{-3/2} \cdot \tag{4}$$

$$\{-96\delta^2 - 160\gamma^2\delta^2 + \gamma^4(11+4r-15/r)$$

$$+ (1+\gamma)^{1/2}[96\delta^2 - 4\gamma^2(6-7/r) + 4\delta^4/r]\}$$

$$2\bar{D}_S(t) = \frac{1}{10} \cdot \hbar^2 k^2 \Gamma \cdot [1-(\gamma^2+1)^{-1/2}] \tag{5}$$

Here we have defined $\gamma^2 = s_0 \cdot f^2(t)$ as the time-dependent saturation parameter and $\delta = \Delta/\Gamma$ as the dimensionless detuning. The values of $\overline{p_I^2}$ and $\overline{p_S^2}$ are then obtained by a numerical integration over t. Unfortunately, the order of integration cannot be reversed for $\overline{p_F^2}$, so a double numerical integration must be performed.

The results of these numerical integrations are shown in Fig. 1 of Section B, where we have plotted, as a function of Δ, the contributions to p_{rms}^2 from the dipole force ($\overline{p_F^2}$), induced diffusion ($\overline{p_I^2}$), and spontaneous ($\overline{p_S^2}$) as well as their sum. We see that near resonance (i.e. when the atom spends a substantial fraction of time in the excited state), diffusion dominates the momentum transfer. However, off-resonance, the dipole force becomes the sole contributor.

3. *Simplifications for* $\Delta = 0$

For resonant excitation, we can use a more intuitive approach to the problem of induced diffusion, based on the concept of a fluctuating force. This fluctuating force is the result of stochastic changes of "dressed state" caused by spontaneous decay (COO80d, GOA80, DAC85).

The dressed atom formalism is discussed very extensively by many authors (COH68, COR77, KNM80) and is especially suited to the problem of an atom in a strong standing-wave field (MOS84, MGP85). Considering the atom plus field as a single system (i.e. "dressing" the atom with the field), the two eigenstates ("dressed states") are time varying superpositions of the ground and excited states. When $\Delta = 0$, these dressed states (denoted + and -) are 50/50 superpositions of ground and excited states. Alternatively, the ground and excited states are 50/50 superpositions of the two dressed states. When an atom in a particular dressed state undergoes a spontaneous decay, it winds up in the ground state, which is immediately projected onto the dressed basis. Thus, the atom is equally likely to be in either dressed state following the decay.

If we make the simplifying assumption of a "tophat" intensity distribution (i.e. f(t) = 1 for a time τ), the dressed atom energy eigenvalues are (MOS84, MGP85):

$$U_{\pm} = \pm\hbar\,\Omega_o \cos kx \tag{1}$$

Viewing this position dependent energy as a potential, the force on an atom in a particular dressed state is:

$$F_{\pm} = -\frac{d}{dx}U_{\pm} = \pm F_o \tag{2}$$

where $F_0 = \hbar k\,\Omega_o \sin kx$. We see that the fluctuating force is simply due to changes in the sign of the force caused by random changes of dressed state.

If we consider the fluctuating force F(t) to have a characteristic time scale of fluctuations τ_f, the time average of F(t) over an interval $>>\tau_f$ will vanish:

$$\langle F \rangle = \frac{1}{\tau}\int_{o}^{\tau} d\tau' F(\tau') = 0 \tag{3}$$

Since $F(t) = \frac{d}{dt}p(t)$, we can express the momentum as the time integral of the force:

$$p(t) = \int_{-\infty}^{t} d\tau' F(\tau') \tag{4}$$

We are interested in the time average (over $>>\tau_f$) of the time rate of change of the square of the momentum (i.e. kinetic energy):

$$\left\langle \frac{1}{2}\frac{d}{dt}p^2(t) \right\rangle = \langle F(t)\cdot p(t)\rangle \tag{5}$$

$$= \frac{1}{\tau}\cdot\int_{o}^{\tau} d\tau' F(\tau')p(\tau')$$

Using Eq. 4, this becomes:

$$\left\langle \frac{1}{2}\frac{d}{dt}p^2 \right\rangle = \frac{1}{\tau}\int_{o}^{\tau} d\tau' F(\tau')\int_{-\infty}^{\tau'} d\tau'' F(\tau'')$$

Reversing the order of integration and assuming the problem to be stationary (i.e. that time averaged quantities are constant), we obtain:

$$\left\langle \frac{1}{2}\frac{d}{dt}p^2 \right\rangle = \int_{-\infty}^{o} d\tau' \langle F(0)\cdot F(\tau')\rangle \tag{6}$$

Thus, we see that the problem reduces to evaluating the time correlation function of the fluctuating force. Realizing that the force fluctuates between $+F_o$ and $-F_o$ with an average time between spontaneous decays of $2\tau_s$ ($\tau_s = \Gamma^{-1}$ is the excited state lifetime), this integral is easily evaluated:

$$\left\langle \frac{1}{2}\frac{d}{dt}p^2 \right\rangle = F_o^2\cdot 2\tau_s \tag{7}$$

$$= (\hbar k)^2\Omega_o^2\sin^2 kx\cdot 2\tau_s$$

Since the time average in Eq. 7 simply smooths out the fluctuations while the time derivative refers to the macroscopic time evolution, we can interchange the two. Also, we must average over x, as the atom is equally likely to enter the field at any value of x. Thus, the rms momentum of the deflected beam should increase according to:

$$\frac{d}{dt} \cdot p_{rms}^2 = 2(\hbar k)^2 \Omega_o^2 \cdot \tau_s \tag{8}$$

For the case of a constant intensity for a time τ we find:

$$\begin{aligned} p_{rms} &= (2)^{1/2} \hbar k \cdot (\Omega_o^2 \tau_s \tau)^{1/2} \\ &= (2)^{1/2} \hbar k \cdot ((\frac{\Omega_o}{\Gamma})^2 \Gamma \tau)^{1/2} \end{aligned} \tag{9}$$

For comparison with our previous results, we set $\Delta = 0$ (i.e. r = 1) and f(t) = 1 in Eq. 4 of Section 2:

$$\begin{aligned} 2\bar{D}_I(t) &= \frac{1}{16}(\hbar k)^2 \Gamma \cdot 4\gamma^2 \\ &= \frac{1}{4}(\hbar k)^2 \Gamma \cdot \frac{8\Omega_o^2}{\Gamma^2} \\ &= 2(\hbar k)^2 (\frac{\Omega_o}{\Gamma})^2 \Gamma \end{aligned} \tag{10}$$

Since $p_{rms}^2 = 2\bar{D}_I \tau$ for our "tophat" interaction (ignoring spontaneous diffusion), we find

$$p_{rms} = (2)^{1/2} \hbar k ((\frac{\Omega_o}{\Gamma})^2 \Gamma \tau)^{1/2} \tag{11}$$

This is in exact accord with the result obtained in Eq. 9 by utilizing the concept of a fluctuating force.

4. *Simplifications for* $\Delta > > \Omega_o$

In the limit $\Delta > > \Omega_o$, the average number , $\bar{N}$, of spontaneous decays which occur during the interaction goes to zero (see Section III.C.2). Thus, we would expect the rms momentum

calculated (assuming $\bar{N} << 1$) in Section III.C.1 (Eq. 55) to be valid in this limit. This is indeed the case, as will be shown below.

Examination of Fig. 1 in Section IV.B shows that the deflection is dominated by the dipole force in the limit of large detuning (i.e. $\Delta >> \Omega_o$):

$$p_{rms}^2 \approx \overline{p_F^2} \tag{1}$$

Recalling the definition of $p_F(x)$ from Eq. 8 in Section IV.C.1 (for t = $+\infty$):

$$p_F(x) = \int_{-\infty}^{\infty} F(x,t)dt \tag{2}$$

and expanding F (Eq. 2, Section IV.C.1) in powers of $\frac{\Omega_o}{\Delta}$, we find

$$\begin{aligned} F(x,t) &\approx -\frac{\hbar\Delta}{2} \cdot \frac{8\Omega_o^2}{4\Delta^2} \cdot f^2(t) \cdot \frac{d}{dx}(\cos^2 kx) \\ &\approx \hbar k \cdot \frac{\Omega_o^2}{\Delta} \cdot f^2(t) \cdot \sin 2kx \end{aligned} \tag{3}$$

to order $(\frac{\Omega_o}{\Delta})^2$. Obviously, $p_F(x)$ is obtained by integrating F(x,t):

$$p_F(x) = \hbar k \cdot \frac{\Omega_o^2}{\Delta} \cdot \sin 2kx \int_{-\infty}^{\infty} f^2(t)dt \tag{4}$$

and p_{rms} is calculated from the trivial average of p_F^2 over x:

$$p_{rms} \approx (2)^{-1/2} \hbar k \cdot \frac{\Omega_o^2}{\Delta} \cdot \int_{-\infty}^{\infty} f^2(t)dt \tag{5}$$

If we write this as:

$$p_{rms} = (2)^{1/2} \hbar k \cdot \int_{-\infty}^{\infty} \frac{(\Omega_o f(t))^2}{2\Delta} dt \tag{6}$$

we see that this is identical to the prediction of the theory developed in Section III.C.1 (Eq. 55 and

50):

$$p_{rms} = (2)^{1/2}\hbar k \cdot z$$

$$= (2)^{1/2}\hbar k \cdot \int_{-\infty}^{\infty} \frac{(\Omega_o f(t))^2}{2\Delta} dt$$

and that this result is independent of the functional form of f(t).

We note in passing that if we look at the propagator G (Eq. 11 in section IV.C.1) for $\Delta > > \Omega_o$ and take the limit $\Gamma \rightarrow 0$ (i.e. no damping), we get the classical momentum distribution derived in MGA83 and KSY80. This is an expected result as the limit $\Gamma \rightarrow 0$ corresponds to no spontaneous decay and hence no momentum diffusion. However, the classical distribution contains none of the diffraction structure (i.e. interference) predicted in Chapter III, since it is based on a formalism in which probabilities, instead of amplitudes, are added. In other words, the process is analyzed classicaly in terms of particle trajectories and omits the effects of interference between atoms scattered with the same final momentum which results from the wave-like properties of the incident atoms.

5. Limitations of the Theory

The theory developed above (Section IV.C.1) is based on the assumption that the atom spends many spontaneous lifetimes in the interaction (i.e. $\Gamma\tau > > 1$). However, the more appropriate parameter is $\bar{N}$, the number of spontaneous decays (i.e. randomizing events) which occur during the interaction (calculated in Section III.C.2). With relatively small detunings from resonance, the conditions $\bar{N} < < 1$ and $\Gamma\tau > > 1$ are obtainable simultaneously. We would certainly not expect the Fokker-Planck treatment to be valid in this case.

Another limitation of the theory is that, even in the absence of momentum diffusion, the

momentum transfer is based on the concept of a force. This concept is inherently classical and cannot give rise to diffraction structure such as we have seen experimentally.

Finally, we would like to comment on the validity of the impulse approximation (i.e. that the atom does not move appreciably *along* the standing-wave during the interaction). As a practical matter, this is a difficult condition to meet (especially at longer interaction times), requiring high quality optics and very accurate alignment. However, assuming these demands can be met, there is the more fundamental problem of the translation (during the interaction) due to the deflection. For a sodium atom which gains a momentum Δp (in units of $\hbar k$) by interacting with a constant force for a time τ (in units of Γ^{-1}), the change in x over the course of the interaction will be:

$$\Delta x/\lambda \sim 4x\,10^{-4}\,\Delta p\cdot\tau \qquad (1)$$

For example, if τ = 10 and Δp = 30 (our maximum scan range), then $\Delta x/\lambda \sim .11$. Recalling that the intensity of the standing-wave has a periodicity $\lambda/2$, we see that this effect is not negligible. Since the on-resonance deflection can be very large (for high power and long τ), we must operate at relatively low power to avoid this effect. However, this results in $\bar{N} < 1$ for off-resonance scans, thereby preventing a good test of the theory (which is valid for $\bar{N} > > 1$) off-resonance.

IV.D. Additional Data

In this section we will present data which could not be included in Section IV.B because of space limitations. These data are reduced in the manner described in Section III.D except that the subtraction to account for F=1 atoms is performed slightly differently. For these data, the convolution procedure (described in Section III.D) is used to generate a deflection pattern for the F=1 atoms which is subtracted from the data. This deflection pattern is based on the theory of Section III.C assuming equally populated F=1 sublevels and ignoring the excited state hyperfine splittings (since the detunings are very large). The transition strength (proportional to the square of the matrix element) is calculated as an average over the ground state sublevels accounting for all

possible $\Delta m = +1$ transitions. Since all data are taken with the laser tuned to the red of the F=2 → F'=3 transition (i.e. away from transitions from F=1), the deflection of F=1 atoms is minimal, yielding significant population in $\pm 2\hbar k$ diffraction peaks only at the highest power levels. The fact that the deflection patterns shown in this section are so spread out (and become smooth on resonance) makes these F=1 atoms more evident than in data presented in Chapter III. These atoms do not contribute significantly to the rms momentum in either case. An example of the effect of this F=1 subtraction is shown in Fig. 1. We see once again that this subtraction gives rise to anomalous structure in the central region of the deflection pattern. For this example, the laser power is relatively high (6.4 mW) and the total fraction of atoms in F=1 is 6.3%.

Deflection patterns are displayed in Figs. 2-7 for three values of laser power (P=.4 mW, 1.6 mW, 6.4 mW), two different interaction times (τ = 71ns, 45 ns), and various laser detunings. For all of these scans, the resolution (FWHM of undeflected beam) is .88 $\hbar k$. The quantity $\bar{N}$, the average number of spontaneous decays occurring during the interaction, is calculated for each scan by the method described in Section III.C.2.

For each of these figures the qualitative change in the deflection pattern as resonance is approached is quite obvious. Off-resonance, the patterns are almost entirely diffractive, as we would expect for $\bar{N}<1$. On-resonance, however, we have $\bar{N}>1$ and the diffraction is completely washed out by spontaneous recoil. An exception to this is seen in Fig. 3(c), where we see a slight residual diffraction pattern superimposed on the smooth curve. For this example we have $\bar{N}$ = 3.35. Recalling (Section IV.B or MAN79) that each spontaneous photon adds $\frac{2}{5}(\hbar k)^2$ to the mean squared momentum, we find a total mean squared momentum of $1.34(\hbar k)^2$ due to

Figure 1

Subtraction of F=1 Atoms

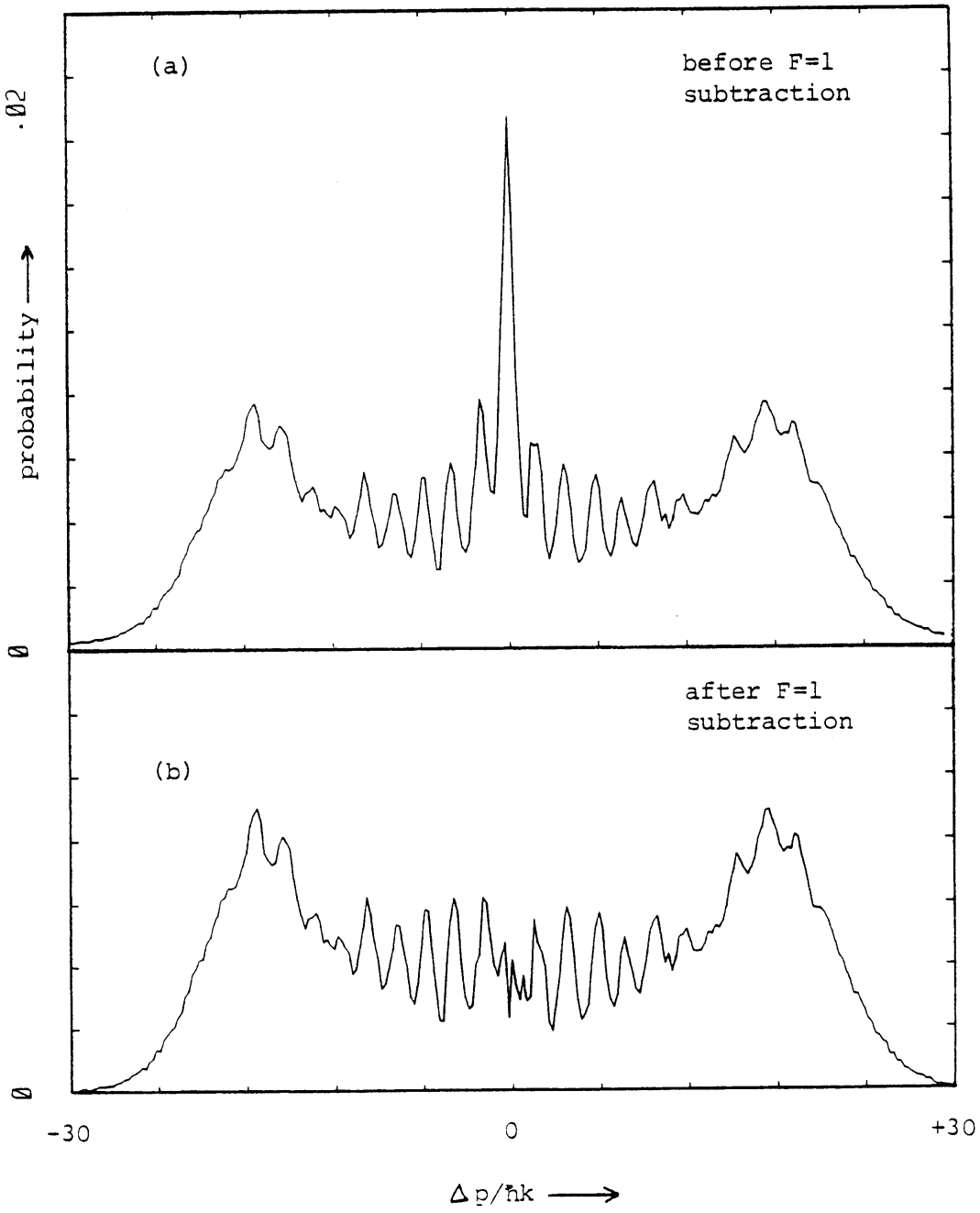

Figure 2

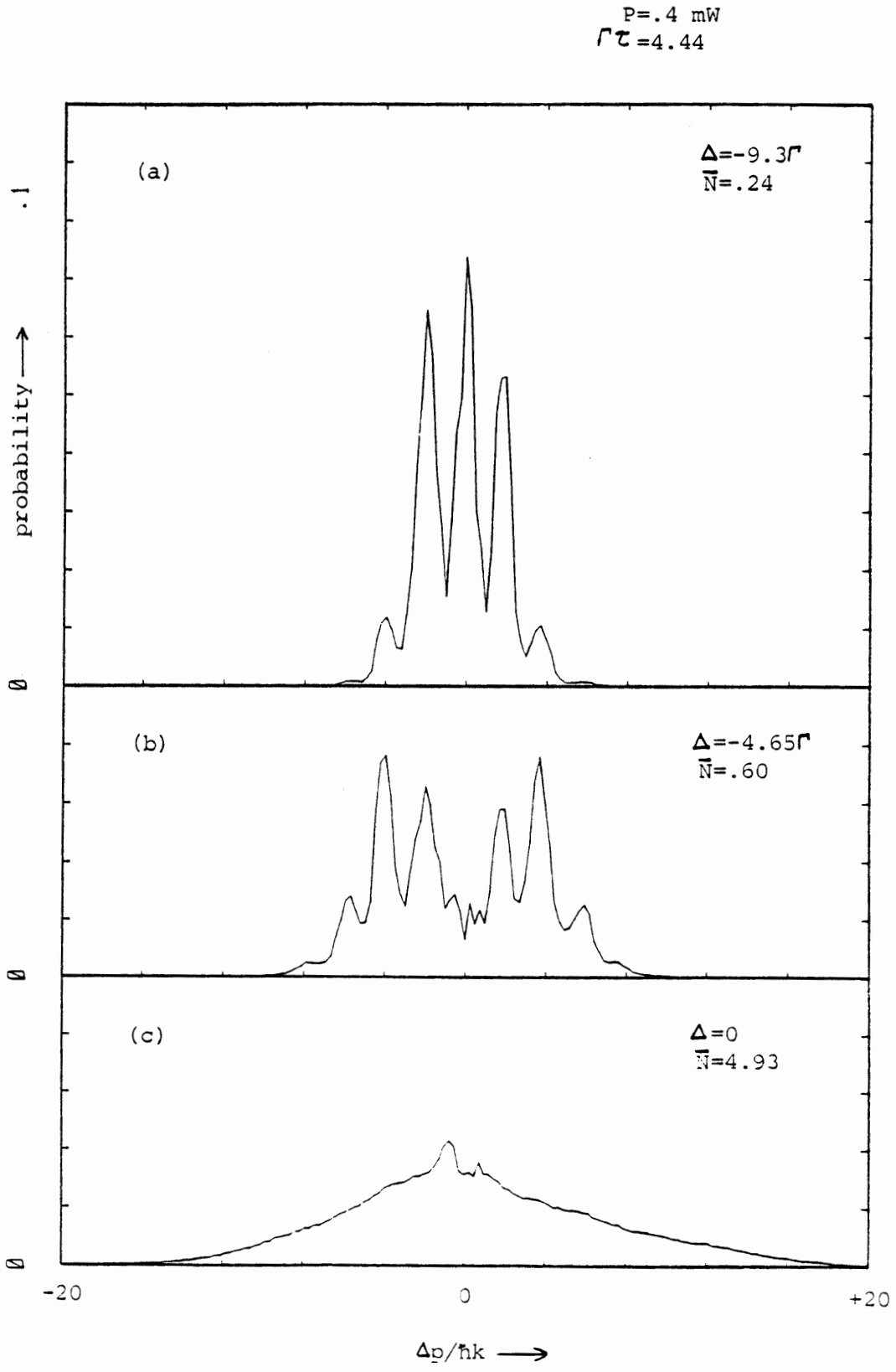
P=.4 mW
Γτ=4.44
(a)
Δ=-9.3Γ
N̄=.24
(b)
Δ=-4.65Γ
N̄=.60
(c)
Δ=0
N̄=4.93
probability
.1
0
0
0
-20
0
+20
Δp/ħk

Figure 3

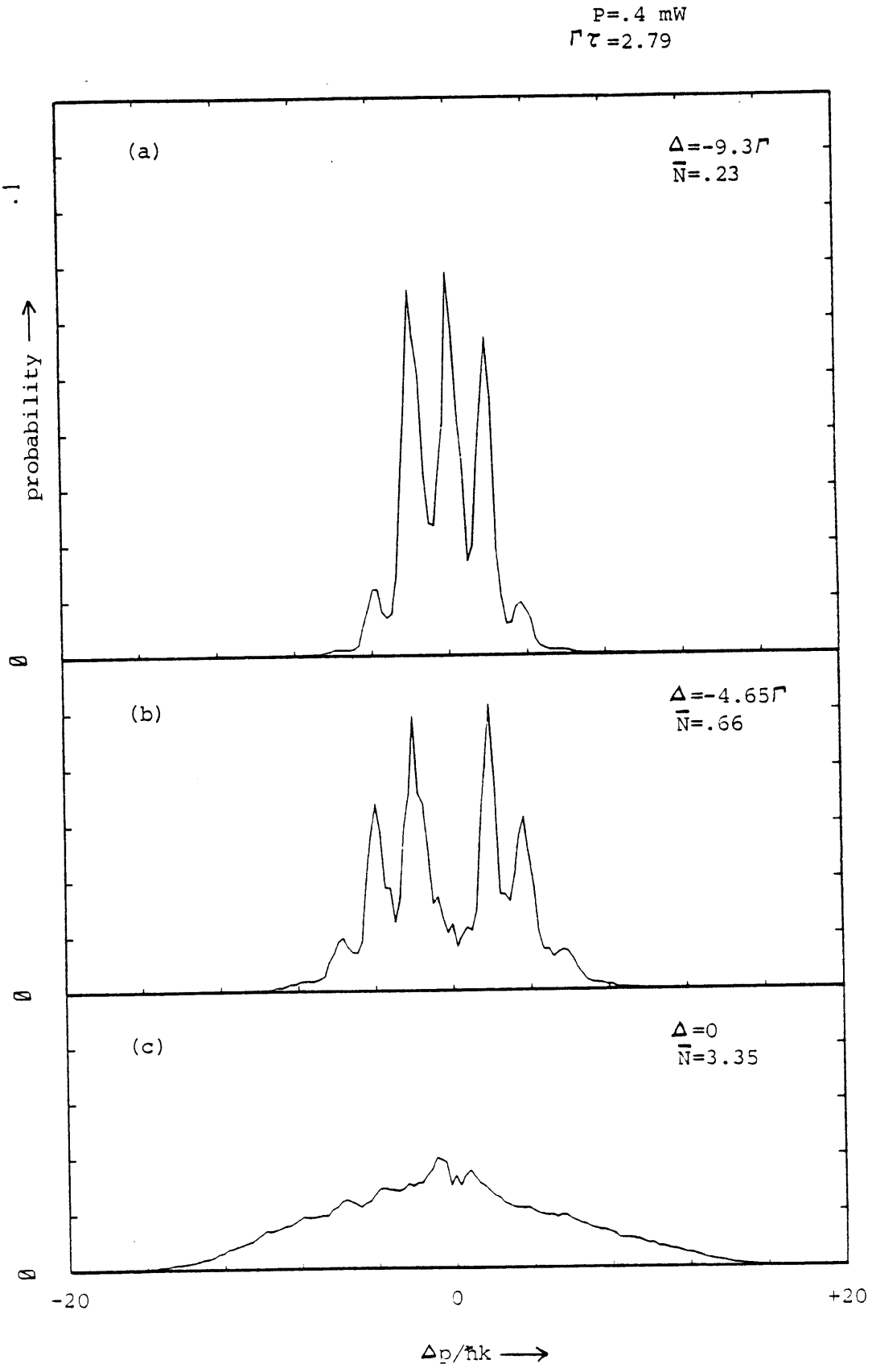
P=.4 mW
Γτ=2.79
(a)
Δ=-9.3Γ
N̄=.23
(b)
Δ=-4.65Γ
N̄=.66
(c)
Δ=0
N̄=3.35
probability
.1
0
0
0
-20
0
+20
Δp/ħk

Figure 4

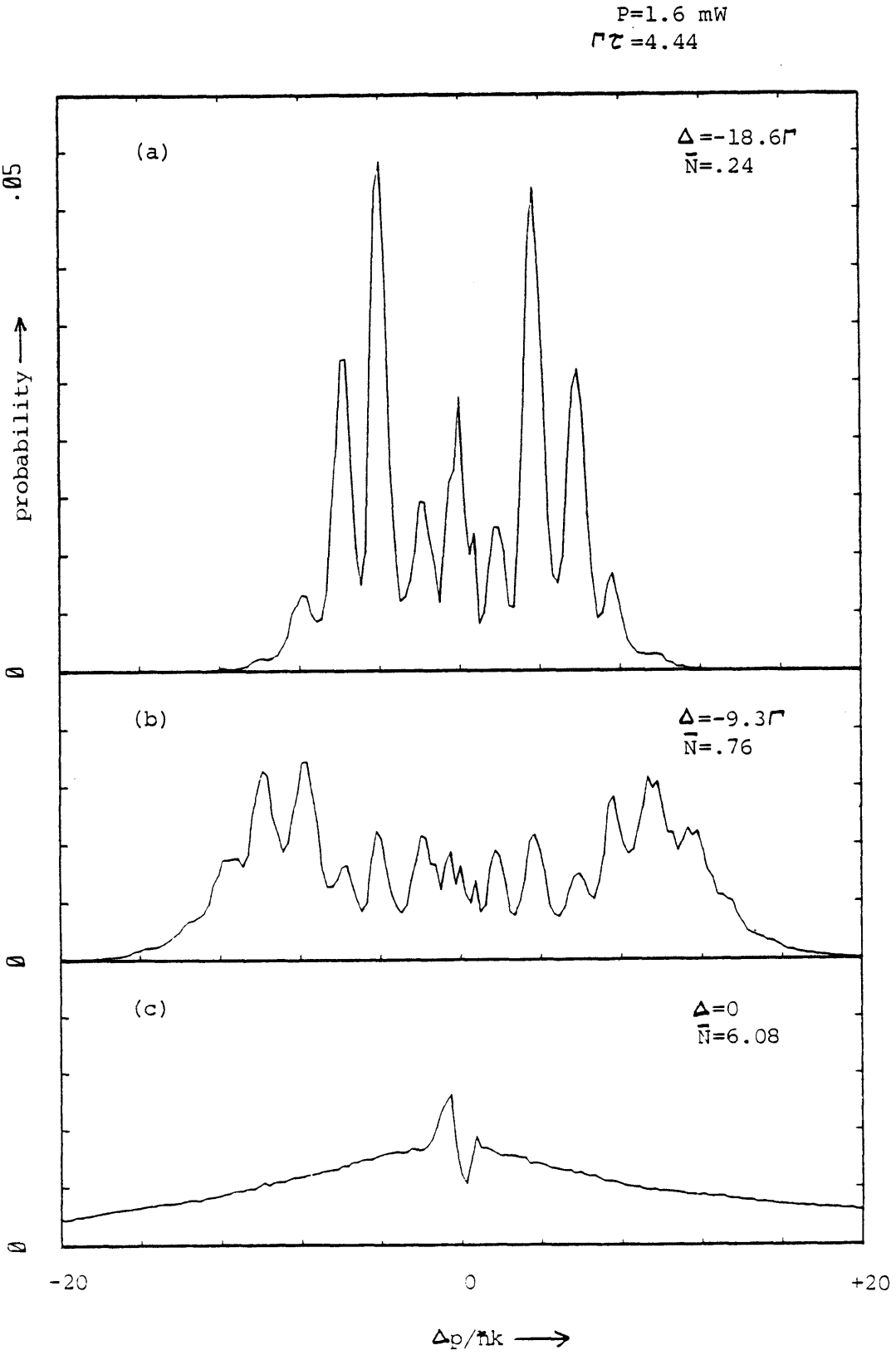
P=1.6 mW
Γτ=4.44
(a)
Δ=-18.6Γ
N̄=.24
(b)
Δ=-9.3Γ
N̄=.76
(c)
Δ=0
N̄=6.08
.05
0
0
0
probability
-20
0
+20
Δp/ħk

Figure 5

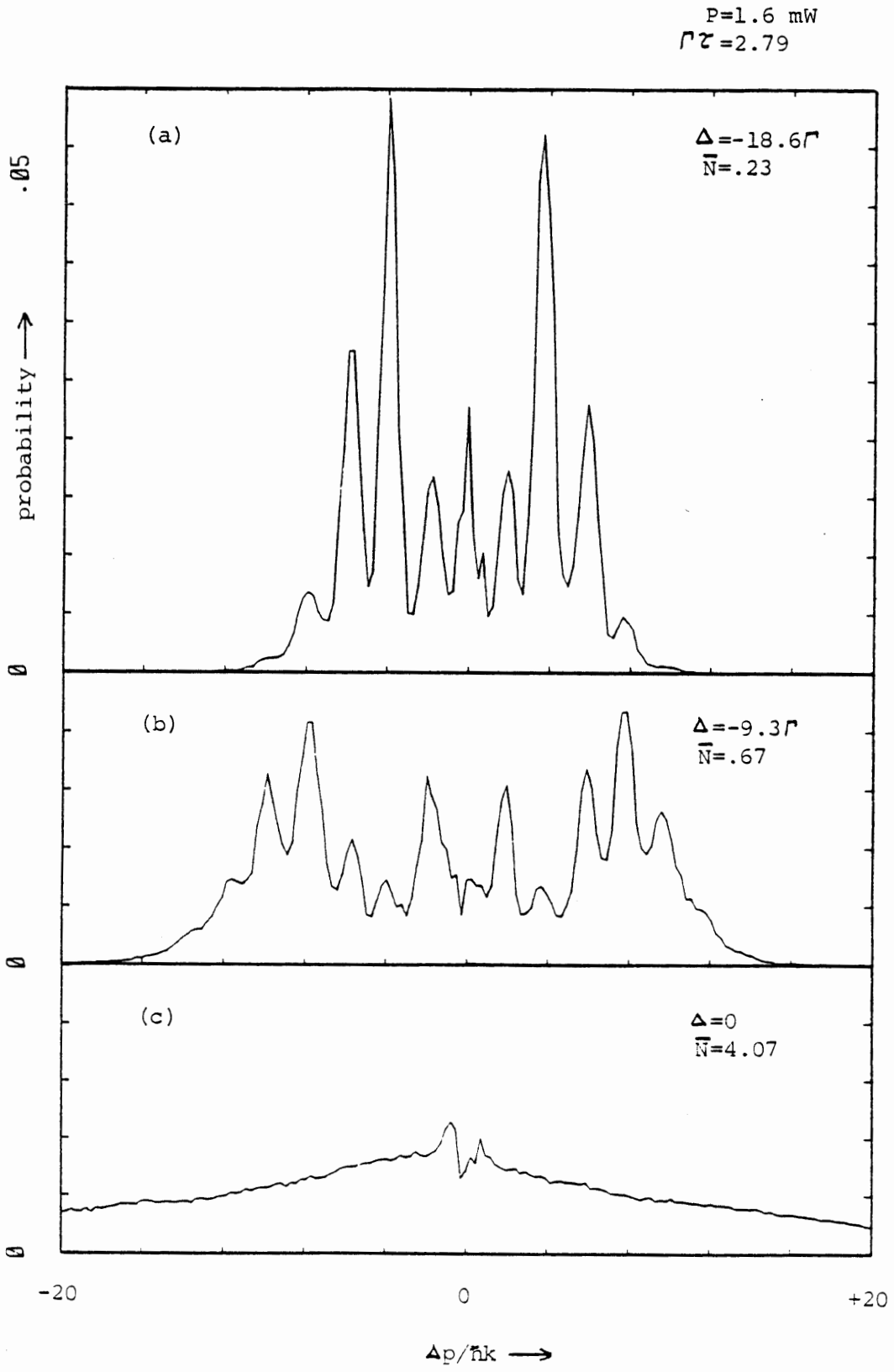
P=1.6 mW
Γτ=2.79
(a)
Δ=-18.6Γ
N̄=.23
(b)
Δ=-9.3Γ
N̄=.67
(c)
Δ=0
N̄=4.07
.05
0
probability ⟶
-20
0
+20
Δp/ħk ⟶

Figure 6

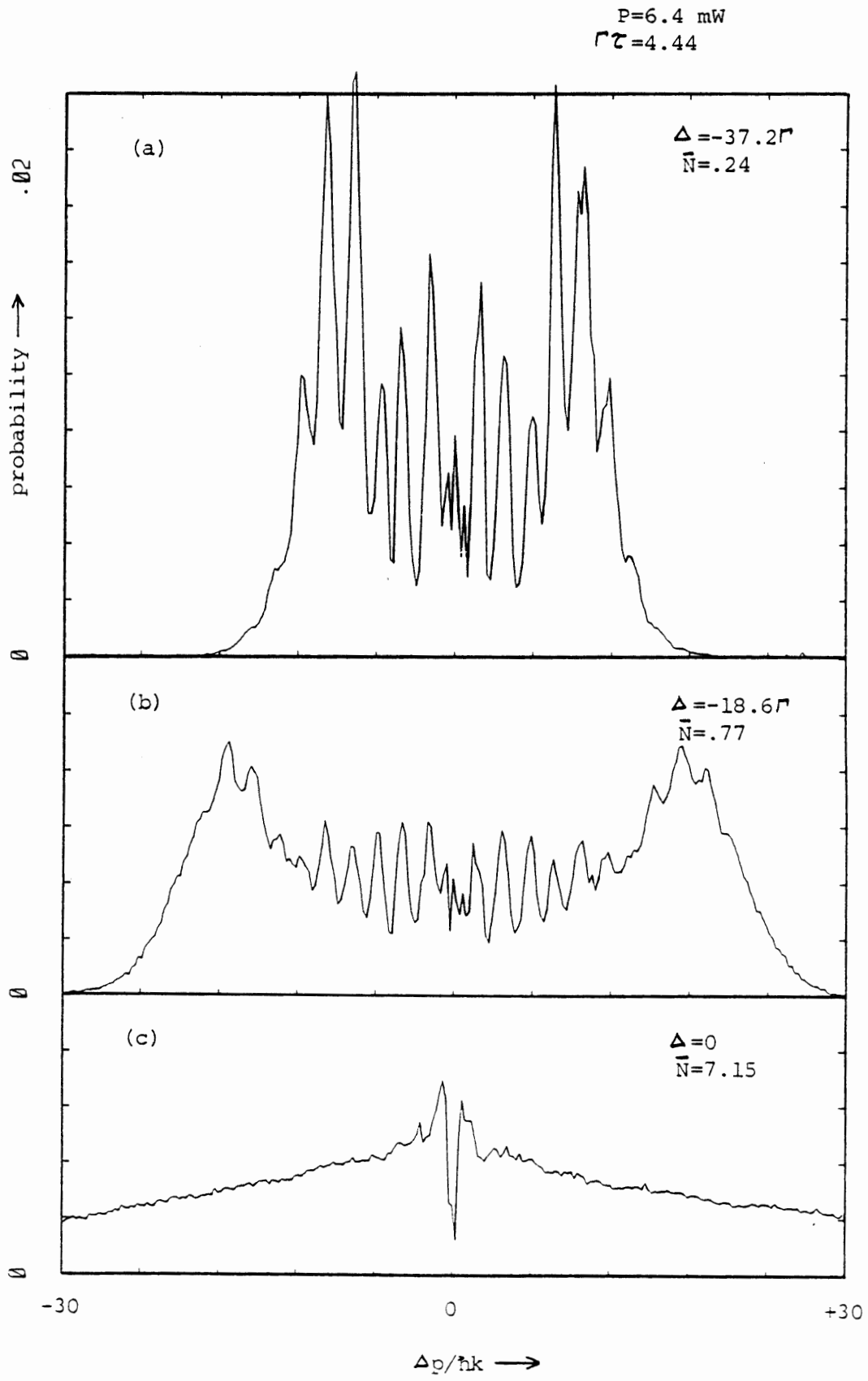
P=6.4 mW
Γτ=4.44
(a)
Δ=-37.2Γ
N̄=.24
(b)
Δ=-18.6Γ
N̄=.77
(c)
Δ=0
N̄=7.15
probability ⟶
.02
0
0
0
-30
0
+30
Δp/ħk ⟶

Figure 7

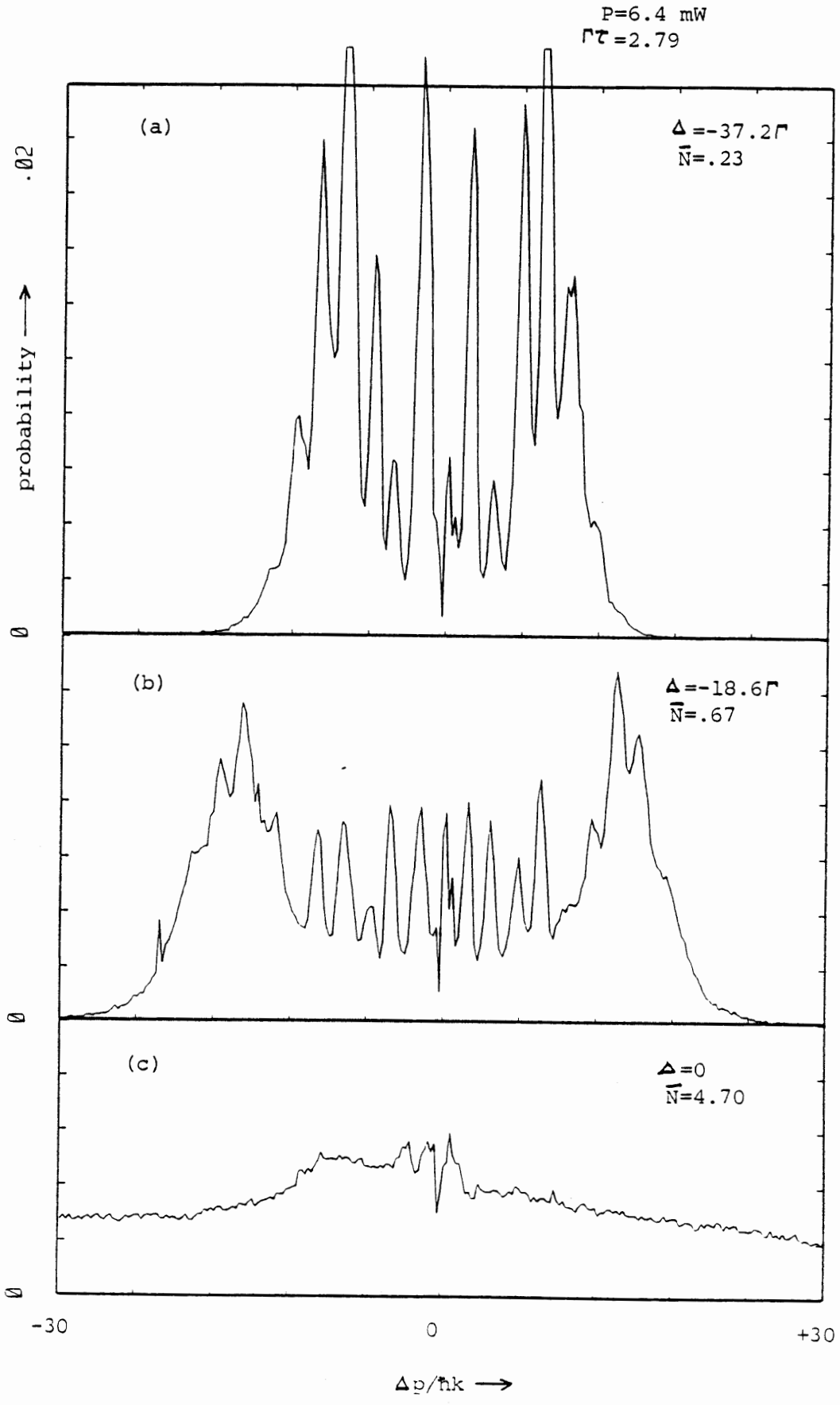
P=6.4 mW
Γτ=2.79
(a)
Δ=-37.2Γ
N̄=.23
.02
probability ⟶
0
(b)
Δ=-18.6Γ
N̄=.67
0
(c)
Δ=0
N̄=4.70
0
-30
0
+30
Δp/ħk ⟶

spontaneous decay. Mandel (MAN79) has shown that for traveling-wave deflection, the momentum distribution (for a given number of decays) is well approximated by a Gaussian when $\bar{N}>3$. If we assume that each diffraction peak is broadened in this manner, we obtain a total mean squared momentum width (including collimation width) of $1.48(\hbar k)^2$. This Gaussian has a FWHM of 2.86 $\hbar k$, which is not much larger than the 2 $\hbar k$ separation of diffraction peaks.

The off-resonance deflection profiles display the same general two-peaked structure seen in the Kapitza-Dirac data. In fact, some of the off-resonant scans shown in this chapter were analyzed in Chapter 3 (if they have $\bar{N}< 0.25$). We note the definite persistence of diffraction, in sharp contrast to the theoretical curves (Section IV.C.1) for off-resonant excitation.

The rms momentum transferred is calculated for each scan by the method described in Section III.D. The high power, on-resonance scans are cut-off and do not yield meaningful values of p_{rms}. In Fig. 3 of Section IV.B, we plot rms momenta vs. detuning for laser powers of .4 mW and 1.6 mW and τ = 71 ns and 45 ns. Also plotted are the theoretical predictions for these cases. However, for these fits, we have divided the calculated (from measured parameters) value of Ω_o^2 by a factor of two in order to obtain reasonable agreement with the data. Although the origin of this discrepancy is not certain, classical calculations (in the limit of large detuning) seem to indicate that the rms momentum can be substantially reduced by a slight non-parallelism of the atomic beam and standing wave fronts without affecting the symmetry or shape of the momentum distribution. This could explain the fact that the profiles (especially off-resonance) seem to have the expected shape but differ consistently from theory in terms of the overall deflection.

Theoretical fits to actual deflection profiles are shown in Figs. 8-10 (also in Fig. 2 of Section IV.B). Once again, we have divided the values of Ω_o^2 by a factor of two for these fits. The on-resonance profiles seem to describe the data reasonably well except that the measured "wings" (i.e. large Δp) seem to fall off faster than predicted. If the criterion $\Delta x << \lambda$ were not satisfied, either

Figure 8

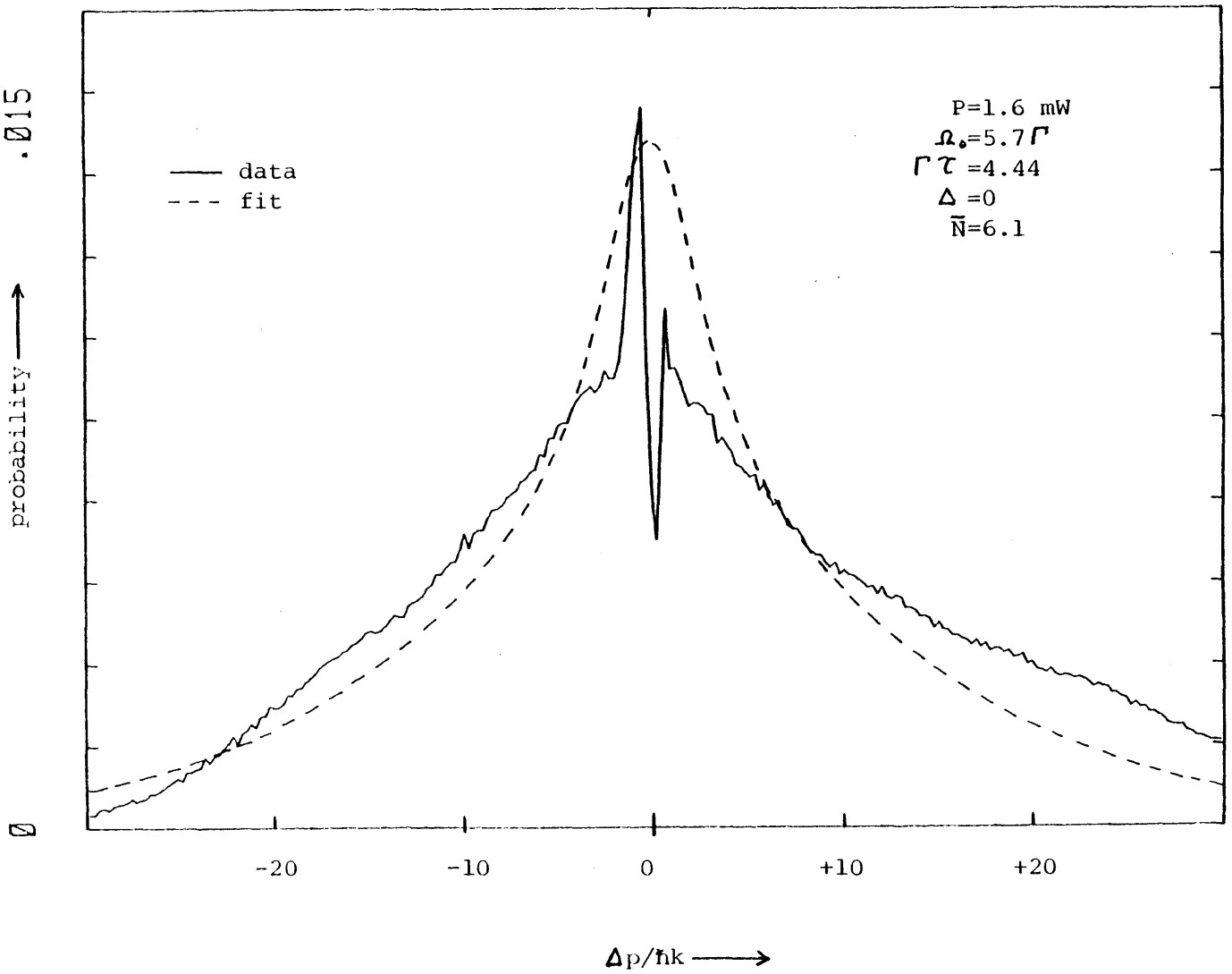
.Ø15
Ø
probability
data
fit
P=1.6 mW
Ω₀=5.7Γ
Γτ =4.44
Δ =0
N̄=6.1
-20
-10
0
+10
+20
Δp/ħk

Figure 9

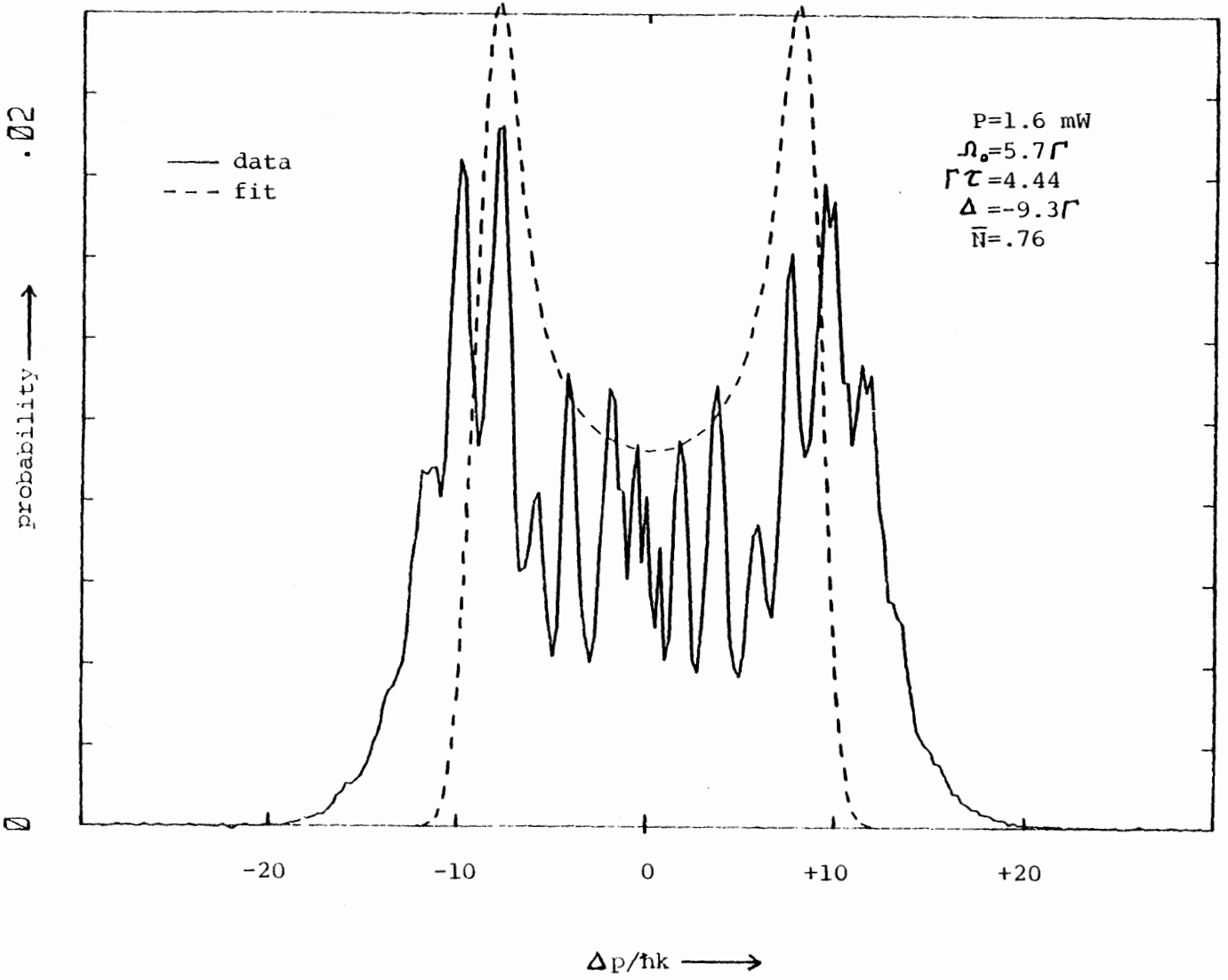
.02
probability
0
data
fit
P=1.6 mW
Ω_o=5.7Γ
$\Gamma\tau$=4.44
Δ=-9.3Γ
$\bar{N}$=.76
-20
-10
0
+10
+20
$\Delta p/\hbar k$

Figure 10

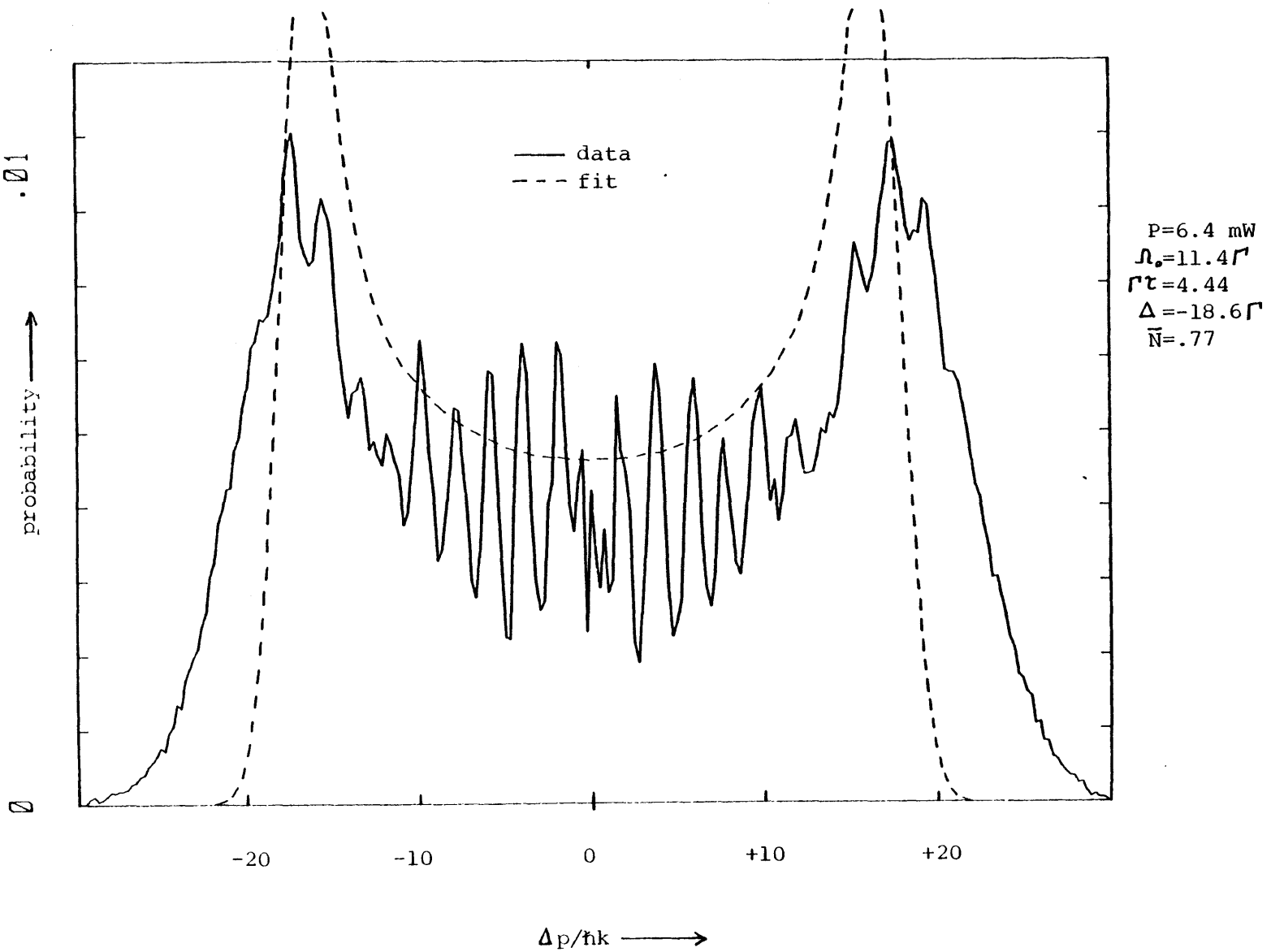
data
fit
probability
.01
0
-20
-10
0
+10
+20
Δp/ħk
P=6.4 mW
Ω₀=11.4Γ
Γτ=4.44
Δ=-18.6Γ
N̄=.77

due to: 1) slight misalignment (i.e. non-parallelism) of the standing-wave with respect to the atomic beam; or 2) significant deflection induced translation during the interaction, then atoms would be subject to a range of electric fields (i.e. values of x) throughout the course of the interaction. As a result, no atom would experience the largest or smallest diffusion coefficient over the entire interaction, and the widths of the Gaussians summed (Eq. 14 of Section IV.C.1) to determine the deflection profile would exhibit less variation and tend towards the average value. This would lead to a more Gaussian-like profile and faster falloff in the wings. Off-resonance, the prediction seems to describe the envelope of the momentum distribution reasonably well but completely misses the pronounced diffraction structure.

Finally, we would like to present some data which demonstrate the striking transition from diffraction to diffusion as the detuning is decreased to zero. Unfortunately, these data are of limited quantitative use due to an uncertainty of ±20 MHz in the detunings (cf. ±5 MHz for other data shown in this chapter) and the large fraction of atoms which are deflected outside of the scan range. Resolution for these scans is .71 $\hbar k$ (FWHM) and data analysis was conducted in the same manner as for data shown previously. Once again, fine structure at small momentum transfers is due to our F=1 subtraction procedure.

In Fig. 11, the diffraction structure is seen to wash out gradually as $\bar{N}$ increases with decreasing detuning. Even for $\bar{N}$>2, there is still some diffraction structure evident.

Figure 11

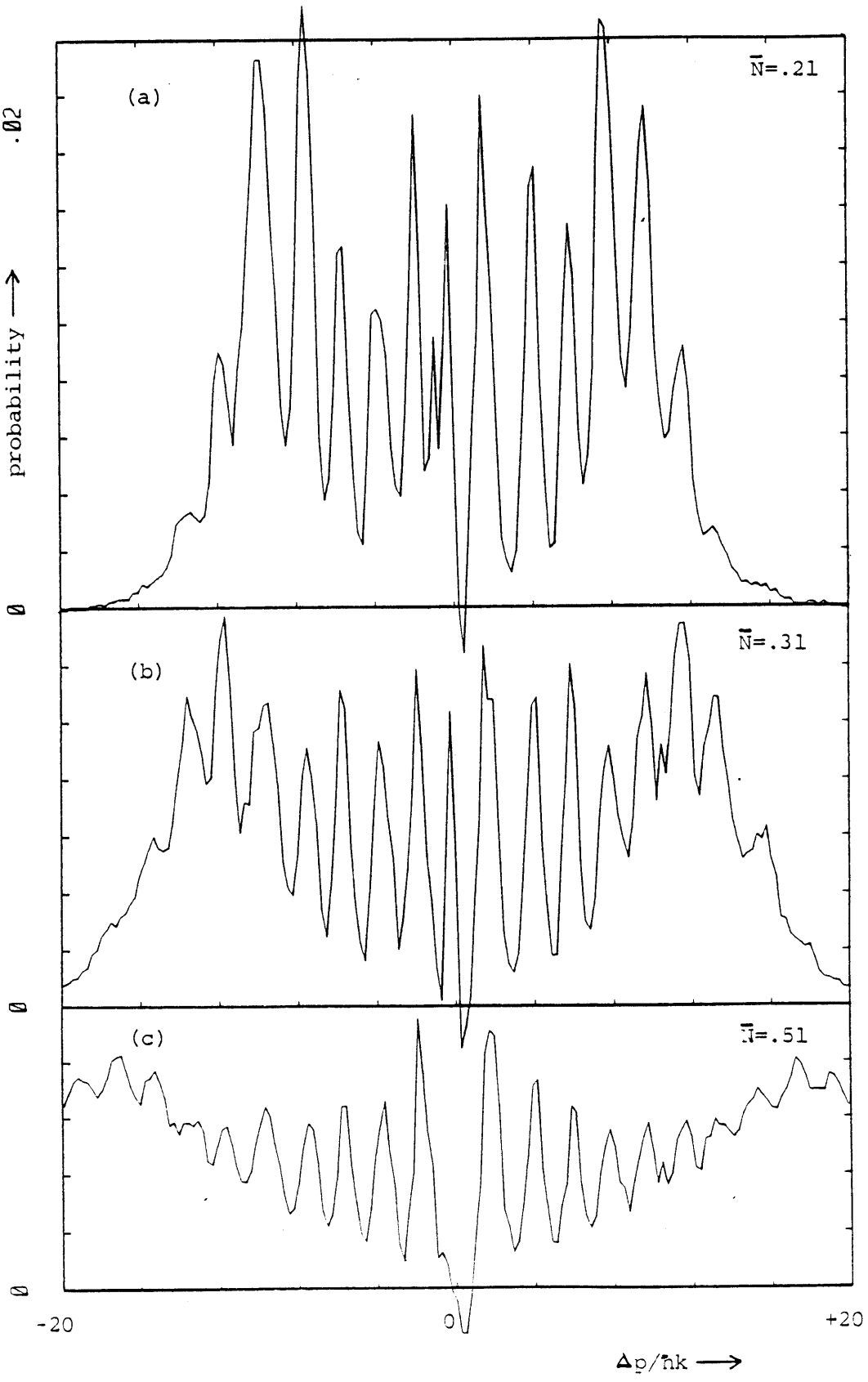

Figure 11 (cont.)

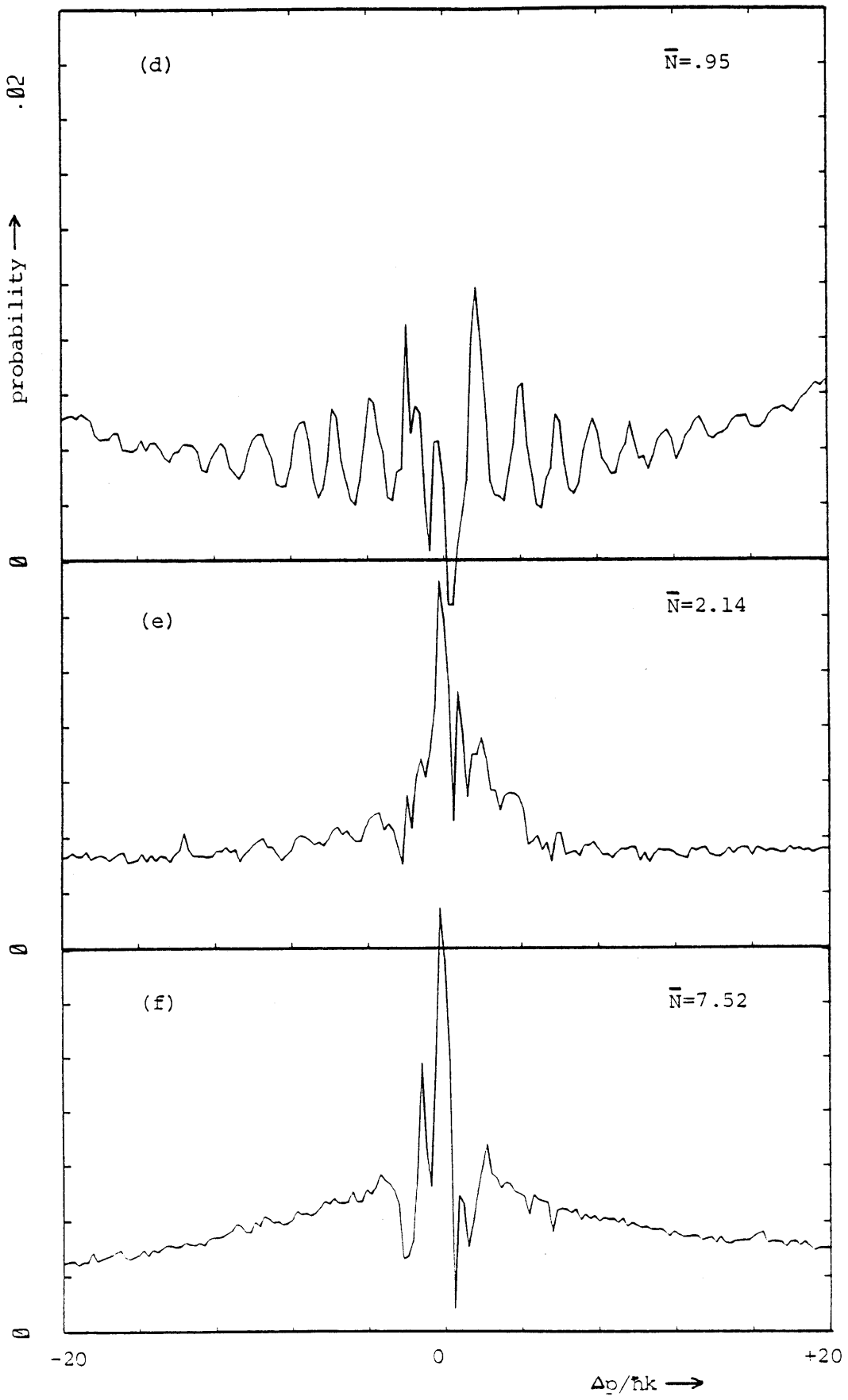

References

ABA74 J. Abate, Opt. Commun. 10, 269 (1974).

ABS72 M. Abramowitz and I.A. Stegun, *Handbook of Mathematical Functions,* (Dover, New York, 1972).

ABS81 E. Arimondo, A. Bambini and S. Stenholm, Phys. Rev. A 24, 898 (1981).

AFB66 S. Altshuler, L.M. Frantz, and R. Braunstein, Phys. Rev. Lett. 17, 231 (1966).

AIV77 E. Arimondo, M. Inguscio, and P. Violino, Rev. Mod. Phys. 49, 31 (1977).

ALO79 E. Arimondo, H. Lew and T. Oka, Phys. Rev. Lett. 43, 753 (1979).

AND74 J.B. Anderson, in *Molecular Beams and Low Density Gasdynamics,* edited by P.P. Wegener (Marcel Dekker, New York, 1974).

ASH70 A. Ashkin, Phys. Rev. Lett. 25, 1321 (1970).

ASH78 A. Ashkin, Phys. Rev. Lett. 40, 729 (1978).

ASH80 A. Ashkin, Science 210, 1081 (1980).

BAB81 A. Bambini and P.R. Berman, Phys. Rev. A23, 2496 (1981).

BAL80 V.I. Balykin, Opt. Commun. 33, 31 (1980).

BDS74 A.F. Bernhardt, D.E. Duerre, J.R. Simpson, and L.L. Wood, Appl. Phys. Lett. 25, 617 (1974).

BDS76 A.F. Bernhardt, D.E. Duerre, J.R. Simpson, and L.L. Wood, Opt. Commun. 16, 169

(1976).

BES81 A.F. Bernhardt and B.W. Shore, Phys. Rev. A 23, 1290 (1981).

BFA78 J.E. Bjorkholm, R.R. Freeman, A. Ashkin, and D.B. Pearson, Phys. Rev. Lett. 41, 1361 (1978).

BFP81 J.E. Bjorkholm, R.R. Freeman, and D.B. Pearson, Phys. Rev. A23, 491 (1981).

BJF80 J.E. Bjorkholm and R.R. Freeman, Comments Atom. Mol. Phys. 10, 31 (1980).

BIR76 G.A. Bird, Phys. Fluids 19, 1486 (1976).

BLM85 V.I. Balykin, V.S. Letokhov, V.G. Minogin, Y.V. Rozhdestvensky, and A.I. Sidorov, J. Opt. Soc. Am. B 2, 1776 (1985).

BRT68 L.S. Bartell, R.R. Roskos, and H.B. Thompson, Phys. Rev. 166, 1494 (1968).

CDK85 V.P. Chebotayev, B.Y. Dubetsky, A.P. Kazantsev, and V.P. m Yakovlev, J. Opt. Soc. Am. B 2, 1791 (1985).

CGG77 M.L. Citron, H.R. Gray, C.W. Gabel, and C.R. Stroud, Jr., Phys. Rev. A 16, 1507 (1977).

CHB85 S. Chu, L. Hollberg, J.E. Bjorkholm, A. Cable, and A. Ashkin, Phys. Rev. Lett. 55, 48 (1985).

CHT69 Y.W. Chan and W.L. Tsui, Phys. Rev. A 20, 294 (1979).

CLL76 R. Campargue, A. Lebehot, and J.C. Lemonnier, in *Rarified Gas Dynamics, Vol. 51, Pt. II, Progress in Astronautics and Aeronautics,* edited by J.L. Potter (Amer. Inst. of Aeronautics and Astronautics, 1976).

COB78 R.J. Cook and A.F. Bernhardt, Phys. Rev. A 18, 2533 (1978).

COH68 C. Cohen-Tannoudji, Cargese Lectures in Physics 2, ed. by M. Levy (Gordon and Breach, New York, 1968), p. 347.

COM85 E.A. Coutsias and J.K. McIver, Phys. Rev. A 31 3155 (1985).

COO79 R.J. Cook, Phys. Rev. A 20, 224 (1979).

COO80c R.J. Cook, Phys. Rev. Lett. 44, 976 (1980).

COO80d R.J. Cook, Phys. Rev. A 22, 1078 (1980).

COO81 R.J. Cook, Comments Atom. Mol. Phys. 10, 267 (1981).

COR77 C. Cohen-Tannoudji and S. Reynaud, J. Phys. B10, 345 (1977).

CUA83 J.T. Cusma mand L.W. Anderson, Phys. Rev. A 28, 1195 (1983).

DAC85a J. Dalibard and C. Cohen-Tannoudji, J. Phys. B. 18, 1661 (1985).

DAC85b J. Dalibard and C. Cohen-Tannoudji, J. Opt. Soc. Am. B2, 1707 (1985).

DAT56 S. Datz and E.H. Taylor, J. Chem. Phys. *25,* 389 (1956).

DEV80 J.M.M. van Deventer, Ph.D. Thesis, Utrecht (1980), unpublished.

DGK78 G.A. Delone, V.A. Grinchuk, A.P. Kazantsev and G.I. Surdutovich, Opt. Commun. 25, 399 (1978).

DJK83 W. Dreves, H. Jansch, E. Koch, and D. Fick, Phys. Rev. Lett. 50, 1759 (1983).

DKB81 W. Dreves, W. Kamke, W. Broermann, and D. Fick, Z. Phys. A 303, 203 (1981).

EBH85 W. Ertmer, R. Blatt, J.L. Hall, and M. Zhu, Phys. Rev. Lett. 54, 996 (1985).

EIN17 A. Einstein, Physik. Zs. 18, 121 (1917), translated in D. ter Haar, *The Old Quantum Theory,* (Pergamon Press, Oxford, 1967), p. 167-183.

FBK80 M.S. Feld, M.M. Burns, T.V. Kuhl, P.G. Pappas, and D.E. Murnick, Opt. Lett. 5, 79 (1980).

FIH82 A. Fischer and I.V. Hertel, Z. Phys. A 304, 103 (1982).

FRI33 O.R. Frisch, Z. Phys. 86, 42 (1933).

GEN75 H.J. Gerritsen and G. Neinhuis, Appl. Phys. Lett. 26, 347 (1975).

GKK84 V.A. Grinchuk, A.P. Kazantsev, E.F. Kuzin, M.L. Nagaeva, G.A. Ryabenko, G.I. Surdutovich, and V.P. Yakovlev, Sov. Phys. JETP 59, 56 (1984).

GKN81 V.A. Grinchuk, E.F. Kuzin, M.L. Nagaeva, G.A. Ryabenko, A.P. Kazantsev, G.I. Surdutovich, and V.P. Yakovlev, Phys. Lett. 864, 136 (1981).

GKN85 V.A. Grinchuk, E.F. Kuzin, M.L. Nagaeva, G.A. Ryabenko, A.P. Kazantsev, G.I. Surdutovich, and V.P. Yakovlev, J. Opt. Soc. Am. *B* 2, 1805 (1985).

GOA80 J.P. Gordon and A. Ashkin, Phys. Rev. A 21, 1606 (1980).

GWE77 R.E. Grove, F.Y. Wu, and S. Ezekiel, Phys. Rev. A 16, 1507 (1977).

HAB77 A.H.M. Habets, Ph.D. Thesis, Technische Hogeschool Eindhoven, (1977), unpublished.

HES76 I.V. Hertel and W. Stoll, J. Appl. Phys. 47, 214 (1976).

HES77 I.V. Hertel and W. Stoll, in *Advances in Atomic and Molecular Physics,* Vol. 13, ed. by

D.R. Bates and B. Bederson (Academic Press, New York, 1977).

HJK81 D. Hils, W. Jitschin, and H. Kleinipoppen, Appl. Phys. 25, 39 (1981).

HLW79 A. Herrmann, S. Leutwyler, L. Woste, and E. Schumacher, Chem. Phys. Lett. 62, 444 (1979).

JAS80 J. Javanainen and S. Stenholm, Appl. Phys. 21, 35 (1980).

JDW80 B. Jaduszliwer, R. Dang. P. Weiss, and B. Bederson, Phys. Rev. A 21, 808 (1980).

JIT84 W. Jitschin, Appl. Phys. B 33, 7 (1984).

JLP73 P. Jacquinot, S. Liberman, J.-L. Picque and J. Pinard, Opt. Commun. 8, 163 (1973).

JOS85 J. Opt. Soc. Am. B 2 (Feature Issue: The Mechanical Effects of Light), Nov. 1985.

KAD33 P.L. Kapitza and P.A.M. Dirac, Proc. Cambridge Phil. Soc. 29, 297 (1933).

KAM65 M. Kaminsky, *Atomic and Ionic Impact Phenomena on Metal Surfaces,* (Academic Press, NY, 1965), p. 98-135.

KAS75 A.P. Kazantsev and G.I. Surdutovich, JETP Lett. 21, 158 (1975).

KAZ78 A.P. Kazantsev, Sov. Phys. Usp. 21, 58 (1978).

KNM80 P.L. Knight and P.W. Milonni, Phys. Rep. 66, 21 (1980).

KSY80 A.P. Kazantsev, G.I. Surdutovich, and V.P. Yakovlev, JETP Lett. 31, 509 (1980).

KSY81 A.P. Kazantsev, G.I. Surdutovich, and V.P. Yakovlev, J. Physique 42, 1231 (1981).

KSY85 A.P. Kazantsev, G.I. Surdutovich, V.P. Yakovlev, and D.D. Chudesnikov, Opt. Commun.

52, 311 (1985).

LEB10 P.N. Lebedev, Ann. d. Phys. 32, 411 (1910).

LEM81 V.S. Letokhov and V.B. Minogin, Phys. Rep. 73, 1 (1981).

LOU83 R. Loudon, *The Quantum Theory of Light* (Oxford, New York, 1983).

MAN79 L. Mandel, J. Opt. (Paris) 10, 51 (1979).

MCK85 J.J. McClelland and M.H. Kelley, Phys. Rev. A 31, 3704 (1985).

MGA83 P.E. Moskowitz, P.L. Gould, S.R. Atlas, and D.E. Pritchard, Phys. Rev. Lett. 51, 370 (1983).

MGP85 P.E. Moskowitz, P.L. Gould, and D.E. Pritchard, J. Opt. Soc. Am. B 2, 1784 (1985).

MIG84 A.L. Migdall, Ph.D. Thesis, MIT (1984), unpublished.

MIN81 V.G. Minogin, Opt. Commun. 37, 442 (1981).

MIN82 V.G. Minogin, Sov. Phys. JETP 53, 1164 (1982).

MOS84 P.E. Moskowitz, Ph.D. Thesis, MIT (1984), unpublished.

NEI69 M.M. Nieto, Am. J. Phys. 37, 162 (1969).

NHT80 W. Neuhauser, M. Hohenstatt, P.E. Toschek and H.G. Dehmelt, Phys. Rev. A 22, 1137 (1980).

PAL79 M. Pinard, C.G. Aminoff, and F. Laloe, Phys. Rev. A 19, 2366 (1979).

PEU83 B.W. Peuse, Ph.D. Thesis, MIT (1983), unpublished.

PFB80 D.B. Pearson, R.R. Freeman, J.E. Bjorkholm, and A. Ashkin, Appl. Phys. Lett. 36, 99 (1980).

PFE68 H. Chr. Pfeiffer, Phys. Lett. 264, 362 (1968).

PIV72 J.-L. Picque and J.-L. Vialle, Opt. Commun. 5, 402 (1972).

PMP85 J. Prodan, A. Migdall, W.D. Phillips, I. So, H. Metcalf, and J. Dalibard, Phys. Rev. Lett. 54, 992 (1985).

PPM85 W.D. Phillips, J.V. Prodan, and H.J. Metcalf, J. Opt. Soc. Am. B 2, 1751 (1985).

PRG85 D.E. Pritchard and P.L. Gould, J. Opt. Soc. Am. B 2 1799 (1985).

RAM56 N.F. Ramsey, *Molecular Beams,* (Oxford Univ. Press, London, 1956).

ROZ32 N. Rosen and C. Zener, Phys. Rev. 40, 502 (1932).

SCH67 H. Schwarz, Z. Phys. 204, 276 (1967).

SCS73 F. Schuda and C.R. Stroud, Jr., Opt. Commun. 9, 14 (1973).

SER80 J.A. Serri, Ph.D. Thesis, MIT (1980), unpublished.

SNY75 J.J. Snyder, Appl. Opt. 14, 1825 (1975).

STE78 S. Stenholm, Phys. Rep. 43, 151 (1978).

STM83 D.G. Steel and R.A. McFarlane, Opt. Lett. 8, 33 (1983).

SWW72 R. Schieder, H. Walther and L. Woste, Opt. Commun. 5, 337 (1972).

TAM68 Y. Takeda and I. Matsui, J. Phys. Soc. Jpn. 25, 1202 (1968).

TRC84 C. Tanguy, S. Reynaud, and C. Cohen-Tannoudji, J. Phys. B17, 4623 (1984).

TRM83 C. Tanguy, S. Reynaud, M. Matsuoka, and C. Cohen-Tannoudji, Opt. Commun. 44, 249 (1983).

WAL82 R.E. Walkup, Ph.D. Thesis, MIT (1982), unpublished.

WHC85 Y.Z. Wang, W.G. Huang, Y.D. Cheng, and Z. Liu, in *Laser Spectroscopy VII,* edited by T.W. Hansch and Y.R. Shen (Springer-Verlag, New York, 1985).

WII64 K.R. Wilson and R.J. Ivanetich, "Surface Ionization of Na, Rb, LiI, and NaI, on W, Re, and Pt-W", University of California Radiation Laboratory Report UCRL-11606, August 25, 1964.

WII81 D.J. Wineland and W.M. Itano, Phys. Lett. 82*A*, 75 (1981).

WSP81 R. Walkup, A. Spielfiedel, W.D. Phillips, and D.E. Pritchard, Phys. Rev. A 23, 1869 (1981).

YAR76 A. Yariv, *Introduction to Optical Electronics,* (Holt, Rinehardt and Winston, New York, 1976).

Acknowledgments

I would like to thank all of those people who made this work possible. Phil Moskowitz taught me the "ropes" and was responsible for the construction of the early version of the apparatus. His willingness to share his considerable lab (and other) experience is appreciated. The assistance of Rick Stoner, Pete Martin, So Kuen Chan, and Katie Schwarz on the project is also appreciated. I would also like to thank my good friends George Ruff and Jean-Louis Picque for their very productive visits to the lab and continued interest in the experiments. Warren Moskowitz and Eric Raab provided helpful laser "tweaking" and Tom Scott, Robert Weisskoff, George Welch and Brian Stewart were always willing to help with computer problems. Discussions with Mike Kash were always helpful and greatly appreciated.

I would especially like to thank Andrea Gelinas for her expert and efficient help in preparing the thesis itself. Thanks are also extended to Dan Kleppner for the use of the laser printer.

Obviously, this work would not have been possible without the financial support and supervision provided by Dave Pritchard. I would also like to thank him personally for his enthusiastic approach to science, his willingness to share his knowledge of physics, and his friendly encouragement throughout the course of this work.

Finally I would like to thank my family for their constant love and support throughout my long educational career.

For all you do, this Bud's for you!